The Dissertation Committee for Ali Emad Abu-Yosef certifies that this is the approved version of the following dissertation:

Development of Non-Contact Passive Wireless Sensors for Detection of Corrosion in Reinforced Concrete Bridge Decks

Committee:

Sharon L. Wood, Supervisor

Dean P. Neikirk

Harovel G. Wheat

Todd Helwig

Jinying Zhu

Development of Non-Contact Passive Wireless Sensors for Detection of Corrosion in Reinforced Concrete Bridge Decks

by

Ali Emad Abu-Yosef, B.S.C.E.; M.S.E.

Dissertation

Presented to the Faculty of the Graduate School of

The University of Texas at Austin

in Partial Fulfillment

of the Requirements

for the Degree of

Doctor of Philosophy

The University of Texas at Austin

December 2013

Dedication

To my parents for their unconditional love and endless support

Acknowledgements

I would like to begin by expressing my sincere appreciation for Dr. Sharon Wood, whose invaluable advice, never-ending assistance, and constant support made this dissertation possible. Her diligent effort, insightful guidance, and attentive encouragement helped me become a better researcher and engineer. The lessons I have learned from our interactions will forever shape my character and career. Working with Dr. Wood has been one of the most wonderful opportunities that I have ever had. I admire her as an exceptional mentor and as an excellent friend. I am truly honored to have worked under her supervision.

I am grateful to Dr. Dean Neikirk and his research group in the Electrical Engineering Department for their tremendous help with everything inductive and all that is RF. I cannot express enough gratitude and thanks for Dr. Harovel Wheat for all she has taught me about the exciting science of corrosion and for generously allowing me to occupy her lab space for months. I thank my committee members Dr. Todd Helwig and Dr. Jinying Zhu for their insight, feedback, and for taking the time to guide me through my dissertation. Randy Poston, Justin Norvell, and Dylan Freytag of WPD & Associates are to be thanked for kindly allowing me to use the GECOR equipment.

I greatly appreciate the financial support from the Technology Innovation Program of the National Institute of Standards and Technology that made this project possible. I would like to thank the TIP project manager, Mr. Gerald Castellucci, for his guidance and feedback.

I have been very fortunate to work with a great team of researchers that I admire in many ways. I would like to give special thanks to Dr. Praveen Pasupathy for his integral role in the development of the NC sensor and the reflectometer reader and for all his great ideas which always emerged after long caffeine-powered meetings. I am also appreciative of Dr. Jinyoung Kim for volunteering to spend long hours interrogating the corrosion sensors and for our memorable discussions. Jason Harlan came at a critical time of this research and spent numerous hours in the sweltering Texas heat interrogating the

sensors. I am very thankful for his work and I wish him the best of luck in his academic endeavors.

Now on to the NIST-TIP gang of graduate students: Dr. Jeremiah Fasl, Vasilis Samaras, and Matt Reichenbach. It has been a tremendous pleasure to work with y'all. Your friendship made the dirty, back-breaking, dehydrating days in the lab and in the field seem a whole lot better and dare I say "enjoyable". I will forever cherish our memories in the lab, in soccer fields, and in conference trips. I would like to also thank the numerous remarkable graduate students of FSEL for making the last few years nourishing and exciting. I have made many lifetime friends here, and as we all eventually go our own way I wish you the best.

The extensive lab work would not have been possible without the help of the lab technical staff: Blake Stasney, Dennis Fillip, Andrew Valentine, David Braley, Eric Schell, and Mike Wason. I am grateful for all of your great assistance and for the invaluable lab lessons. On the administration side, my deepest gratitude goes to Barbara Howard, Jessica Hanten, and Michelle Damvar whose help navigating the treacherous waters of purchasing and travel logistics was priceless.

I would like to express my eternal thanks to Greisy. Your love and encouragement helped me through the research lows and pushed me to get the job done.

I reserve my deepest gratitude for my parents, brothers, and sister. Despite the distance, you have always been by my side. Your endless love and support has allowed me to get where I am today. Thank you.

Development of Non-Contact Passive Wireless Sensors for Detection of Corrosion in Reinforced Concrete Bridge Decks

Ali Emad Abu-Yosef, Ph.D

The University of Texas at Austin, 2013

Supervisor: Sharon L. Wood

Corrosion of embedded reinforcement is the leading form of deterioration affecting the integrity of reinforced and prestressed concrete bridge members around the world. If undetected, corrosion can limit the service life of the bridge and lead to expensive repairs. The research team at the University of Texas at Austin has developed a new class of passive wireless corrosion sensors. The noncontact (NC) sensor platform provides an economical and nondestructive means for detecting corrosion initiation within concrete. The sensor is powered through the inductive coupling to an external mobile reader that can be handheld or mounted on a vehicle. It is envisioned that the four-dollar sensor will be embedded in concrete during construction and interrogated sporadically over the service life of the structure. The sensor output can be used to detect corrosion initiation within concrete and is expected to enhance the quality information collected during qualitative routine bridge inspections.

The NC sensor prototype consists of a resonant circuit that is inductively coupled to a sacrificial transducer. Corrosion of the sacrificial element alters the measured sensor response and is used to detect corrosion within concrete. Electrochemical evaluations were conducted to ensure that the sacrificial element exhibited identical response as the reinforcement steel. In addition, the results of extensive experimental parametric studies were used in conjunction with circuit and electromagnetic finite element models to optimize the NC sensor design.

Long-term exposure tests were used to evaluate the reliability of the passive noncontact sensors. Sensors were embedded in reinforced concrete specimens and successfully detected the onset of corrosion in the adjacent reinforcement. Unlike the traditional corrosion evaluation methods, such as half-cell potentials, the sensors output was insensitive to environmental variations.

Table of Contents

List of Tables

List of Figures

CHAPTER 1

Introduction

1.1 THE CASE FOR STRUCTURAL HEALTH MONITORING OF BRIDGES

The highway system in the United States is the backbone of the nation's economy and of paramount importance for its national security and future growth. This vital transportation system relies on more than 600,000 bridges that act as the critical links and the core infrastructural components needed for daily traffic. A large percentage of these bridges have exceeded their intended design life and have shown evidence of deterioration and damage (ASCE 2013). As of 2012, approximately one in four bridges in the US highway bridge inventory was considered to be either structurally deficient or functionally obsolete (FHWA 2012). Furthermore, an estimated $76 billion is needed to repair and eliminate the current deficiencies in the nation's bridge inventory (ASCE 2013). However, current federal and private funding for infrastructure maintenance constitutes a small fraction of the investment needed (LePatner 2010). Hence, due to the limited budgets and continuous growth of demand, transportation officials and bridge owners face a serious infrastructure crisis where the growing maintenance needs for existing bridges have far outpaced the available resources.

With such large inventory of deficient bridges, transportation officials are challenged with the difficult task of allocating repair funds and prioritizing maintenance projects based on the overall needs of the highway system. Such decisions are currently based on the information collected during routine bridge inspections. Current regulations mandated by the National Bridge Inspection Standards require bridges longer than 20 ft to be inspected at least once every two years (Code of Federal Regulations 2004). However, current state-of-practice for the majority of bridge inspections relies primarily on cursory documentation of visible signs of deteriorations (Ryan, et al. 2012). Hence, the information collected can only identify bridges that exhibit significant levels of damage (Moore, et al. 2001). As a result, costly repairs and expensive replacement projects become the only viable solution to avoid catastrophic failures or unforeseen loss of service (Somerville 2008). Furthermore, the allocation of resources and personnel needed to conduct the scheduled inspections can become a financial burden for bridge owners and a constraint for the bridge management system (Branco and De Brito 2004). Hence, such a qualitative bridge assessment paradigm does not allow for early intervention and leads to misallocation of funds (Hearn, et al. 2002).

Due to the obvious need for reliable assessment techniques that aids the decision making process, the integration of modern structural health monitoring (SHM) techniques became necessary (Hearn, et al. 2002). SHM has been used successfully for decades in the aerospace industry and has been an integral part of the inspection and monitoring processes of aircrafts (Staszewski, Boller and Tomlinson 2004). Furthermore, reliable SHM utilization have been shown to enable early detection of structural distress and consequently SHM can lower the overall life-cycle costs of a structure through the use of preventive remedial measures and economical repairs (Somerville 2008). Hence, SHM can play a major role in developing a successful infrastructure management program in the United States.

However, the employment of SHM as a reliable tool for the assessments needed for the nation's bridge management program has numerous challenges (Farrar and Worden 2007). Bridges are different as each bridge is unique in size, design, age, boundary conditions, level of exposure to environmental conditions, and traffic density. Hence, the task of identifying the sources of damage using monitoring techniques and SHM is a complex task (Brownjohn 2007). Real-time health monitoring systems have been deployed successfully in signature projects (Ko and Ni 2005); however, the costs of their installation, maintenance, and interpretation are prohibitive for usage in ordinary civil structures.

An emerging alternative to real-time SHM for civil applications is the use of passive sensor technology for damage identification and deterioration monitoring (Lynch and Loh 2006). This class of sensors are wireless in nature, does not contain any on-board processing hardware, and does not depend on a battery source (Finkenzeller 2003). Hence, passive sensors are inexpensive and can operate indefinitely. Furthermore, the wireless nature of the passive sensors lowers the cost of monitoring and expedites the installation process.

1.2 Corrosion Detection in RC Bridge Decks and the Potential for SHM

Since the introduction of steel reinforcement to concrete in the late 1800's, reinforced concrete has become the most widely used material in the construction of civil infrastructure. The data from the National Bridge Inventory indicate that more than 65% of the bridges in the US are built using either reinforced or prestressed concrete (FHWA 2012). In addition, the majority of the deck area in US bridges is constructed using reinforced concrete.

The marriage between the high tensile strength of reinforcement steel and the insulating nature of the concrete medium became an inexpensive and durable alternative for modern construction. Reinforcing steel is electrochemically unstable and tends to corrode under atmospheric exposure; however, the alkalinity of the concrete provides a protective environment for the steel (Bertolini, et al. 2004). However, chloride penetration and carbonation initiate the corrosion process within the concrete and can accelerate the deterioration of the structure (Hansson 1984). Consequently, the exposure to marine environments and the use of deicing salts on highway bridges put reinforced concrete bridge decks and substructures at a high risk of corrosion damage.

Reinforcement corrosion is the leading cause of deterioration affecting the integrity of reinforced concrete structures around the world. A study conducted by British Cement Association (1997) indicated that more than 70% of the deterioration observed in bridges and more than 35% of the damage reported in parking structures is due to corrosion of the reinforcement. As a result, governments around the world spend billions of dollars to maintain the aging bridges and delay the onset of corrosion damage

(Broomfield 2007). In the United States, the annual direct cost of corrosion damage on reinforced concrete highway bridges was estimated to be $4 billion (Koch, et al. 2001). Chase and Laman (2000) reported that the cost of repairing and maintaining deteriorated concrete bridge decks is over $1 billion annually. Furthermore, the indirect costs resulting from road closures and traffic delays were estimated to be at least ten times the direct repair costs (Somerville 2008).

Corrosion of embedded reinforcing bars is a complex phenomenon that is mainly dependent on the quality of the concrete, the degree of exposure to chlorides and CO_2, and time. Modern building codes and construction standards have attempted to improve the quality of the construction materials and reduce the corrosion risk by reducing the permeability of the concrete (ACI 222R 2010). However, the economic pressure for stronger materials and faster construction has lead to lower concrete durability and quality resulting from early age cracking (Mehta and Burrows 2001). A study by the International Concrete Repair Institute estimated that the annual cost of the repair of concrete structures in the U.S. was more than $18 billion (Emmons and Sordyl 2006).

Corrosion is a time-dependent process and the ensuing degradation can take decades before any signs of damage become visible. The final corrosion product occupies six to ten times the original volume of steel (Bertolini, et al. 2004). A theoretical representation of the service life of a reinforced concrete structure exposed to corrosion is shown in Figure 1-1. The expansion in the volume of iron induces tensile stresses in the surrounding concrete, which results in cracking. The ensuing cracks provide a direct path for moisture and oxygen, hence, the corrosion process accelerate. The process continues at a higher rate resulting in either spalling of the concrete cover or planar delamination parallel to the concrete surface. Figure 1-2 shows corrosion-induced damage in a concrete bridge pier. If the structure is not repaired, corrosion will proceed at higher rates leading to a significant loss in the reinforcement cross section, which will result in limiting the serviceability of the structure (Bertolini, et al. 2004). In extreme cases, catastrophic and sudden failures leading to deadly structural collapses caused by reinforcement corrosion have been reported (Woodward and Williams 1988, Poston and West 2005, Johnson, Couture and Nicolet 2007, Covino, et al. 1999).

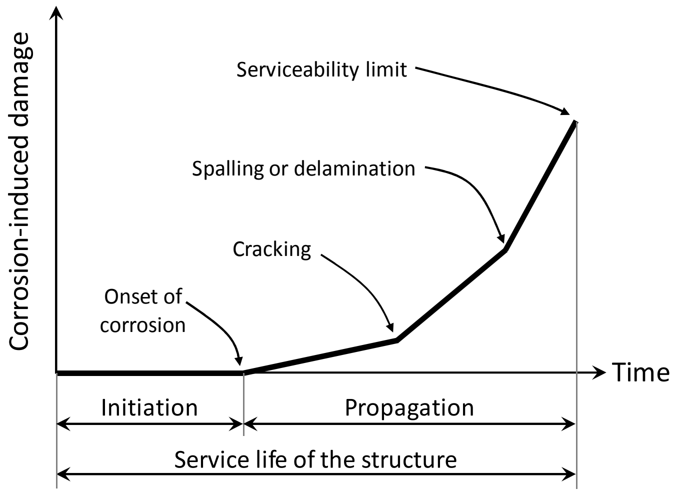

Figure 1-1: Schematic representation of corrosion-induced damage in reinforced concrete members

Figure 1-2: Concrete spalling due to rebar corrosion (Courtesy of Kevin Folliard)

The embedded nature of reinforcement corrosion makes the task of detecting the corrosion activity very difficult. To this end, bridge owners rely on non-destructive evaluation (NDE) techniques to assess the presence, extent and rate of corrosion damage (Gannon and Cady 1992). Highway agencies in the U.S. still rely primarily on visual and sounding techniques to identify corrosion damage in reinforced concrete bridges (Branco and De Brito 2004). To date, the chain-drag method remains the most commonly used techniques for corrosion inspections (Ryan, et al. 2012). In the last few decades, a number of novel technologies were developed to assess corrosion detection within concrete. Ground Penetrating Radar (GPR) and Infrared Thermography have shown great potential for improving the nature and quality of information collected during bridge inspections (Halabe, et al. 1997). However, both methods require professional processing and are their output is hard to interpret (Bertolini, et al. 2004).

The visual and acoustical inspection techniques only detect delaminations and concrete spalling resulting from substantial corrosion damage. At that level of corrosion damage, expensive deck replacements and costly repairs become the only feasible maintenance alternatives (Branco and De Brito 2004). In contrast, early detection of the corrosion activity allows remedial or preventive measures to be taken which can significantly reduce the life-cycle costs of the structure (Somerville 2008). Researchers have shown that the application of chemical penetrating sealers and waterproofing overlays can delay the corrosion process by inhibiting additional chloride diffusion and moisture penetration (Broomfield 2007). However, such repair techniques are only feasible if corrosion was detected during the initiation stage (Richardson 2002). Polder et al. (2012) reported that the direct cost of extensive corrosion repairs or full replacements is 12 to 40 times higher than the cost associated with the application of hydrophobic overlays. In addition, these preventive repair measures can be conducted with relatively limited lane closure and little interruption to the daily traffic (Weyers, et al. 1993, Hearn, et al. 2002, Polder, et al. 2012). Hence, it is clear that a shift to a more proactive bridge management paradigm is needed to better allocate the resources of the transportation authority and the utilization of cost-effective repair techniques (Russell 2004, Emmons and Sordyl 2006).

1.3 Scope of Research

The National Institute of Standards and Technology (NIST) sponsored a research project entitled, "Development of Rapid, Reliable and Economic Methods for Inspection and Monitoring of Highway Bridges." The primary goal of the project was to develop novel technologies and data interpretation methodologies that will provide transportation officials with reliable quantitative information regarding bridge performance. The technologies are envisioned to complement the qualitative data obtained during scheduled inspections. The research project addressed the monitoring of the two main deterioration mechanisms affecting the durability of modern highway bridges: (1) fatigue and the ensuing crack growth in fracture-critical steel bridges, and (2) corrosion of steel reinforcement in highway bridge decks. The first research task was to develop a reliable wireless sensor network that enables long-term, maintenance free monitoring of strains and crack growth rates in fracture-critical steel bridges. Details regarding the wireless strain nodes and the algorithms developed to interpret the strain data collected during monitoring can be found in Fasl (2013).

The main objective of the research presented in this dissertation is to develop a class of passive wireless sensors that enables the early detection of corrosion initiation in reinforced concrete bridge decks. The sensors are designed to complement routine bridge inspections and provide reliable information regarding the corrosion state within the concrete medium. The sensor relies on a radio frequency (RF) communication technology for the wireless data transfer. The evolution of the sensor design was based on the threshold passive corrosion sensor previously developed at the University of Texas at Austin (Wood and Neikirk 2009). The work presented explores the development of a new passive corrosion sensor design and examines the reliability of the sensor performance through long-term exposure tests and extensive studies in a variety of environmental conditions. The results of those studies are used to identify design limitations and provide recommendations that will allow for successful implementation in the field.

Chapter 2 contains a literature review of bridge inspection practices and examines the advantages and limitations of traditional corrosion monitoring techniques. In addition, existing commercial wireless corrosion sensors, as well as sensors under development, are discussed. The properties of all these systems are used to identify the attributes required for the development of a reliable sensor platform that can be adopted for use in ordinary concrete bridges. Finally, examples of RF-based wireless sensors that are used for a number of applications and have influenced the design of the corrosion sensor are also described.

The concept of the non-contact (NC) corrosion sensor prototype is introduced in Chapter 3. A brief description of the component of the passive sensor platform is provided. The results of extensive parametric studies are then used to fabricate the NC sensor prototype. In addition, the sensitivity of the sensor response to environmental variations and corrosion development is also examined. A circuit model of the NC sensor platform was developed to examine the influence of the different design parameters on the acquired sensor response. Furthermore, an electromagnetic finite element model of the inductively coupled components was created to complement the circuit model and provide a better understanding of the sensor behavior. The details and findings of both models are provided in Chapter 3.

The NC sensor employs an inductively coupled sacrificial transducer to detect corrosion within the surrounding concrete medium. Hence, the reliability of the NC sensor relies on the selection of sacrificial elements that exhibit electrochemical properties that are similar to those of the adjacent reinforcement. A detailed electrochemical investigation exploring the corrosion tendencies of the sacrificial element and samples of reinforcement steel was performed. The corrosion response of the samples was obtained for a number of mediums exhibiting electrochemical properties similar to those observed in concrete members. The experimental program and the results of the electrochemical investigation are discussed in Chapter 4.

A preliminary evaluation of the reliability of the NC sensor and its ability to detect corrosion initiation within concrete is demonstrated in Chapter 5. To this end, long-term exposure testing of NC sensors embedded in reinforced concrete prisms was performed. The sensors were interrogated regularly and traditional electrochemical corrosion monitoring techniques were also used to assess the corrosion risk. At the end of the exposure period, physical autopsy was conducted and the reliability of the sensor output was compared to the observed corrosion damage. The sensor readings were also used to evaluate the sensitivity of the embedded sensors to variations of the environmental conditions.

The small size of the reinforced concrete prisms used for the preliminary evaluation of the reliability of the NC sensors (Chapter 5) did not allow for assessing the sensitivity of the embedded sensors to different levels of chloride exposure. In addition, the spatial coverage of the NC sensors and their sensitivity to the size and location of cracks could not be evaluated. To this end, NC sensors were embedded in large-scale reinforced concrete specimens that resemble sections of a bridge deck. The large-scale specimens were subjected to regular moisture cycles of either salt or tap water solutions for more than 19 months. In addition to regular sensor interrogations, half-cell and linear polarization measurements were conducted. At the end of the exposure period, the specimens were autopsied. The signals of the sensors were compared to the observed conditions of the reinforcement. The construction details of the large-scale specimens and the description of the experimental program is provided in Chapter 6. The results of the long-term test are reported in Chapter 7 along with a detailed analysis of the sensor reliability compared to traditional corrosion monitoring techniques.

Chapter 8 examines the sensing layer of the NC sensor design. Slight adjustments to the sacrificial element enabled the detection of different threshold levels of corrosion damage within concrete. Such modifications are expected to allow for a versatile and adaptable deployment of the NC sensor platform without a significant addition to the cost. Furthermore, the development of two multi-threshold NC sensor designs is introduced.

In addition, the results of the long-term exposure tests have indicated that crack-induced localized corrosion can affect the measure response of the NC sensors. To mitigate this problem, a modification to the transduction layer was developed. The results of a long-term chlorides exposure tests demonstrated that the placement of an inexpensive diffusion layer on the surface of the sensor can mitigate the localized corrosion problem. Details of the localized corrosion phenomenon and the diffusion layer concept are discussed in Chapter 8.

Finally, Chapter 9 summarizes the conclusions and observations of this research project and provides recommendations for future research.

CHAPTER 2

Background and Literature Survey

2.1 OVERVIEW

The corrosion process in reinforced concrete members is a complex phenomenon. Typical structural member designs examine the interaction between external loads and the strength of structural members. However, corrosion deterioration is a ternary problem that is dependent on the concrete quality, the external exposure, and time (Seim 2010). The complex interaction between the three factors makes the corrosion activity within concrete members hard to predict, prevent, and detect. In addition, while the passive oxide layer that forms on a steel surface embedded in concrete hinders the corrosion activity, the natural electrochemical instability of the steel-concrete interface and age-induced deterioration of the concrete will eventually initiate corrosion (ACI 222R 2010). Consequently, the time needed to initiate the corrosion activity and the time needed for the corrosion-induced damage to cause cracking, spalling, and eventually limit the serviceability of the structure is highly variable. Melchers and Li (2009) reported numerous cases where extensive corrosion damage in reinforced concrete bridge decks was observed after less than 10 years of service. The same study indicated that the time needed for the initiation of the corrosion activity (chloride ingress) ranged between 2 and 35 years for bridges exposed to marine environments or regular exposure to de-icing salts. Recently, a nine-year old 26-story residential building constructed with post-tensioned concrete slabs was demolished due to corrosion damage initially observed at the prestressing anchors (Freytag, et al. 2012). In contrast, a large number of reinforced concrete structures have performed adequately throughout their service life and did not exhibit any signs of corrosion damage.

For transportation authorities, the corrosion issue is hard to handle. Unless a serious amount of damage has already occurred, visual inspections do not provide accurate information regarding the corrosion state and its progress (Branco and De Brito 2004). In addition, the initial stage of the corrosion process (ingress of chlorides and breakdown of the passive layer) is invisible to the naked eye and cannot be detected by the commonly used visual inspections (Raupach, Reichling, et al. 2012). Consequently, current inspection practices can only enable corrosion detection once damage has already developed into the propagation stage. Hence, the required aggressive measures for protection and repair become necessarily expensive and disruptive to daily traffic (Polder, et al. 2012). Thus, transportation officials are in desperate need for a reliable corrosion inspection program that enables early detection and can be adopted for use in everyday concrete bridges with minimal increase to inspection costs (Emmons and Sordyl 2006).

In addition, the ternary nature of the corrosion process makes the ensuing damage localized in nature and, hence, hard to locate (Gannon and Cady 1992). The hidden nature of the initial damage and the uneven moisture and chloride accumulation makes the spatial distribution of the corrosion activity impossible to predict. Hence, presence, rate, and the extent of the corrosion activity are highly variable over any bridge deck surface (Gucunski, et al. 2010). Due to the spatial variability of the corrosion phenomenon, a reliable inspection program should examine the entire surface of the bridge deck to identify the locations of corrosion-induced deterioration. However, such detailed damage surveys can become tedious and expensive to conduct (Polder, et al. 2012). Hence, the development of low-cost, rapid, and reliable corrosion detection techniques that can complement regular inspections are critical for a successful infrastructure management program.

Current non-destructive corrosion monitoring and damage detection techniques can be classified into two main categories: (1) delamination surveys and (2) electrochemical evaluation techniques. The first is used to locate regions of the bridge deck where internal delamination and excessive cracking are present. In contrast, the electrochemical evaluation techniques are typically used to assess the risk of corrosion activity and the rate of deterioration. Recently, a number of promising technologies that employ wired or wireless embeddable sensors have been reported in literature. Some of these technologies are currently under development while others have been placed in reinforced concrete structures and are currently in service.

Section 2.2 examines sounding techniques currently used by transportation officials to conduct delamination surveys. The electrochemical evaluation techniques, the limitations of their use, and the difficulties of interpreting the measured data are presented in Section 2.3. The use of embedded electrochemical sensors for real-time monitoring of the corrosion activity within concrete is discussed in Section 2.4. Finally, Section 2.5 examines a number of embedded passive sensor technologies that have been reported in literature. The section concentrates on sensor designs that utilize wireless radio frequency (RF) technology for power exchange and data transfer.

2.2 DELAMINATION SURVEYS

The tensile stresses resulting from the expansive corrosion products cause cracking in the surrounding concrete (Broomfield 2007). These cracks create fracture planes that can either be parallel to the concrete surface (delamination) or V-shaped (spalling). The type of fracture plane is dependent on the clear cover and reinforcement spacing (Bertolini, et al. 2004). Corrosion-induced cover spalling can be detected visually and is easily identified by bridge inspectors. However, planar delaminations remain hidden and continue to grow as corrosion proceeds. Delamination surveys are critical for avoiding catastrophic structural failures and preventing the sudden spalling of large concrete masses that can result in property damage and even human injuries (Mays 1992).

In general, delamination surveys rely on the reflection or interference of mechanical waves (acoustic or stress) to locate anomalies within the concrete (ASTM D 4580 2007). The sounding method is the most commonly used approach for locating delaminations on bridge decks (Gannon and Cady 1992, Yehia, et al. 2008). Delamination surveys using the sounding method produce a binary output (delamination/ no delamination). Delaminations are identified if a hollow sound is heard when the concrete surface is struck by a hammer. Intact concrete produces a sharp, ringing sound. Hollow sounding concrete is marked and recorded in the inspection documents (Ryan, et al. 2012). For large areas, such as bridge decks, a steel chain can be dragged across the surface to locate delaminations (Figure 2-1). The dimensions and size of the equipment used in the sounding surveys are specified in ASTM D4580 (2007), which provides a full description of the test method. ASTM D4580 has been widely adopted by the transportation authorities in the United States.

ACI 222R (2010) reported that sounding was the best method for measuring delaminations in terms of accuracy, and repeatability. However, the surveys are tedious, time-consuming, and require traffic control and road closures. To date, the sounding surveys are still conducted manually, thus, the experience of the inspector is crucial for the success of the delaminations survey (Yehia, et al. 2008). Inspector fatigue and desensitization to the ringing sound were reported as key obstacles to the success of inspections (ACI 222R 2010). In addition, the quality of the survey results can be affected by the noise of nearby traffic and the presence of water within the delamination plane (Broomfield 2007). Furthermore, sounding cannot be used on bridge decks with asphalt overlays or concrete toppings (ASTM D 4580 2007).

Figure 2-1: Chain drag test (NCHRP 2004)

Recent developments in nondestructive evaluation techniques, such as: ground penetrating radar (Maser, et al. 2012), impact-echo (Kee, et al. 2012) and infrared thermography (Clark, McCann and Forde 2003) have shown great potential for improving the quality of the information collected during delamination surveys (Vaghefi, et al. 2012). The equipments needed for such techniques can be vehicle-mounted and the damage surveys have the potential to be conducted at highway speeds and with minimal interruption to traffic (Gucunski, et al. 2010). However, the output produced by the novel techniques is difficult to interpret and requires extensive processing. Furthermore, the equipment needed is relatively expensive and the results are on average less accurate than the chain drag test (Scott, et al. 2003, Broomfield 2007). In addition, the novel techniques are only capable of locating delaminations and excessive cracking produced by severely corroded reinforcement. Hence, the investment required to employ such delamination survey methods does not lead to savings on needed repairs. Consequently, these methods were not widely adopted by transportation officials for use in routine bridge inspections (Yehia, et al. 2008).

2.3 ELECTROCHEMICAL EVALUATION TECHNIQUES

Corrosion is an electrochemical process consisting of two half-cells reactions. A half-cell is defined as a metal submerged in a solution of its ions (electrolyte). Corrosion cells include an anodic and a cathodic reaction cells. Oxidation usually occurs at the anode where the metal dissolves producing free electrons. The electrons move to the cathode and reduce water and oxygen producing hydroxide ions (Jones 1996).

In order to drive the electrons toward the cathode, a difference in electrochemical potential is needed. The unbalance in potential is usually the catalyst for corrosion initiation (Pourbaix 1973). Each metal has a unique electrochemical potential that describes its willingness to lose electrons in a certain environment. Nobel metals exhibit higher positive potentials and tend to act as cathodes. Metals with low potentials tend to dissolve (corrode) and act as anodes when connected to more nobel metals (Jones 1996). Table 2-1 lists the standard electrochemical potentials for a number of metals.

Table 2-1: Standard electrochemical potentials of metals (Jones 1996)

	Metal-Metal ion	Electrode Potential vs. Hydrogen (Volts)
More Nobel	$Pt\text{-}Pt^{+2}$	+1.20
	$Ag\text{-}Ag^{+}$	+0.80
	$Hg\text{-}Hg^{+2}$	+0.78
	$Cu\text{-}Cu^{+2}$	+0.34
	$H_2\text{-}H^{+}$	0.00
	$Fe\text{-}Fe^{+2}$	-0.44
More Active	$Zn\text{-}Zn^{+2}$	-0.76
	$K\text{-}K^{+}$	-2.93

When two cells are connected, an equilibrium potential difference (E_{corr}) is established and this difference in potential can be measured using a voltmeter. For example, when a silver-silver sulphate half-cell is connected to a zinc-zinc sulphate are connected (Figure 2-2), the zinc (more active) dissolves into its solution and becomes the corrosion anode. If a voltmeter is connected to the cell it will measure a corrosion potential of 1.56 V ((+0.8V) – (-0.76V)). The electrochemical potential values are affected by the concentrations of ions in the electrolyte solution, temperature, and electrical connection (Bertolini, et al. 2004). The potential measured provides an indication regarding the susceptibility of the system to corrode and does not provide any information regarding the rate of corrosion. The corrosion rate is dependent on the rate of ion transfer between the two cells.

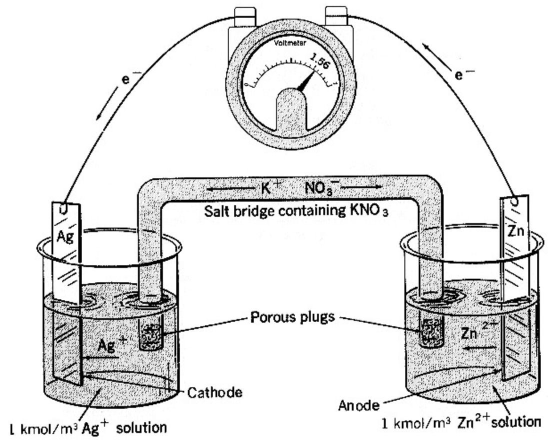

Figure 2-2: Electrochemical cell (Jones 1996)

2.3.1 Half-Cell Potential Mapping

The half-cell potential method is an invaluable and cost-efficient tool for indicating the risk of corrosion activity. The potential is a thermodynamic measure of the ease of removing electrons from the metal with no external polarization (Jones 1996). Hence, the method measures the willingness of embedded steel to corrode, but does not provide any information about the rate of corrosion (ACI 222R 2010).

In reinforced concrete, the unbalance in electrochemical potential is created by the localized depassivation resulting from chloride infiltration (Bertolini, et al. 2004). In order to measure the half-cell potential of embedded reinforcement, a reference half-cell is used (electrode). A reference electrode consists of a piece of nobel metal immersed in a stable solution of its ions (Ansuini and Dimond 1994). In theory, any nobel metal with a known standard potential can be used to assess corrosion risk in concrete. However, only three standard reference electrodes are typically used in practice; copper/copper sulphate (CSE), silver/silver chloride (Ag/AgCl) and mercury/mercuric acid (saturated calomel)

(Broomfield 2007). The difference in potential between the embedded rebar and the reference electrode is then used to identify the corrosion activity within concrete.

In order to measure the corrosion potential in a reinforced concrete member, the rebar is electrically connected to a high-impedance DC voltmeter which is attached to a reference electrode (Figure 2-3). The reference electrode is placed over a wet sponge and moved along the surface of the concrete while the voltage readings are recorded. The voltage values are typically negative. Passive reinforcement generally exhibits more nobel voltage readings (less negative). Theoretically, more negative potentials are recorded in regions where active corrosion occurs due to the thermodynamic nature of the anode region.

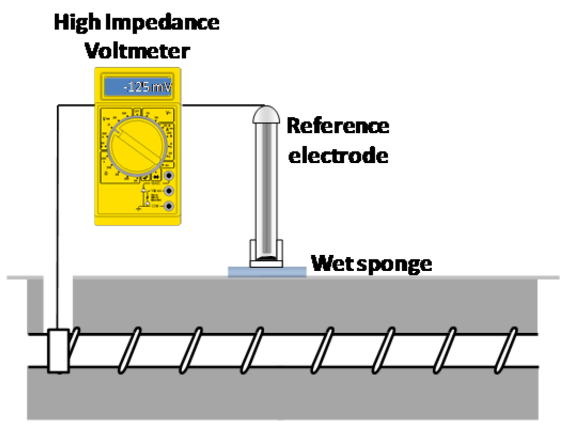

Figure 2-3: Schematic of a half-cell potential measurement of steel in concrete

In a bridge deck inspection, the potential readings are typically taken on a predefined grid. The rebar is exposed at the two opposite corners of the deck and the electrical connectivity is checked. Then, the reference electrode is moved over the grid points and the voltage is recorded. The data are typically presented as a contour map with the most negative potential peaks indicating anode locations. ASTM C876 provides a classification of corrosion risk based on the measured potential values (Table 2-2). The suggested limits were devised empirically from the results of a research study that examined 120 reinforced concrete bridge decks from 33 states (Kliethermes 1972). Hence, the classification limits are only applicable for uncoated steel reinforcement

(Broomfield 2007). However, research and practical experience have shown that the assessment of the corrosion risk in bridges is best achieved by examining the spatial variation of the corrosion potentials rather than the sole use the absolute potential values and dependence on the suggested ASTM risk limits (Andrade, Alonso and Gulikers, et al. 2004, Gu, Carter, et al. 1996, Elsener, et al. 2003). In order to ensure a correct interpretation of half-cell readings, some practitioners suggest exposing the rebar in regions of the deck that exhibit the most negative potentials to eliminate any unconsidered variables (Gannon and Cady 1992, Poursaee and Hansson 2009).

Table 2-2: ASTM C876 criteria for the corrosion risk of steel in concrete

Corrosion Risk	Copper/Copper Sulphate	Silver/ Silver Chloride	Calomel
Low (<10% risk)	> -200 mV	>-100 mV	>-130
Moderate risk	-200 to -350	-100 to -250	-130 to -280
High Risk	<-350 mV	<-250 mV	<-280 mV
Severe Corrosion (>90% risk)	<-500 mV	<-400 mV	<-430 mV

The half-cell method can only identify regions with a high probability of active corrosion. Hence, the measurements have a rather qualitative nature (Huang, Chang and Wu 1996). Furthermore, Feliu et al. (1996) have shown that half-cell potentials provide a poor indication of the corrosion rate. Broomfield et al. (1994) demonstrated that the half-cell potentials can become misleading due to concrete carbonation or saturation. Furthermore, the potential is affected by many factors that need to be considered when the data are being interpreted. For example, potentials are typically very negative in saturated concrete (underwater conditions), where oxygen is absent and corrosion is inhibited (Ansuini and Dimond 1994, Broomfield 2007). On the other hand, nobel potentials can be measured in active reinforcement if the concrete is dry or contain corrosion inhibitors (Gu and Beaudoin 1998, ACI 222R 2010). In addition, the method cannot be used in bridge decks that have asphalt overlays or impervious membranes (Bertolini, et al. 2004).

In addition, the thermodynamic nature of half-cell measurements makes it dependent on a number of factors. Changes in the degree of carbonation, chloride levels, concrete resistivity, concrete quality, cover depth, presence of cracks, ambient temperature and relative humidity, and oxygen concentration were shown to affect the corrosion potential values differently and to variable extents (Poursaee and Hansson 2009, Andrade, Alonso and Gulikers, et al. 2004, Bertolini, et al. 2004, Andrade and Castillo 2003, Elsener, et al. 2003, Carino 1999, Pourbaix 1973, Martinez, et al. 2008). Hence, the main drawback of the half-cell method is the susceptibility of the measured potentials to shift either to more positive or more negative potentials due to external factors that may not be related to the extent or severity of the corrosion activity (Poursaee and Hansson 2009).

2.3.2 Linear Polarization Resistance

The linear polarization resistance (LPR) is the only reliable method for estimating the corrosion rate of reinforcement steel (ACI 222R 2010). Corrosion rate represents the amount of steel dissolving in the anode (Jones 1996). By measuring the electric current (rate of electron production) at the anode, the corrosion rate can be calculated using Faraday's law of metal loss. However, electric current measurements cannot be performed as directly as half-cell potentials. The LPR technique relies on the findings of Stern and Geary that states that "the ratio of the potential deviation to the applied current density is inversely proportional to the corrosion current density" (Figure 2-4) (Jones 1996). The LPR theory can be summarized by the following equations:

$$R_p = \frac{\Delta E}{\Delta i}$$ ***Equation 2-1***

$$x = \frac{11x10^6 \cdot B}{R_p \cdot A}$$ ***Equation 2-2***

where, x is the corrosion rate in µm/year, R_p is the polarization resistance, ΔE is the potential change due to the application of Δi, B is a constant and A is the surface area of the polarized steel.

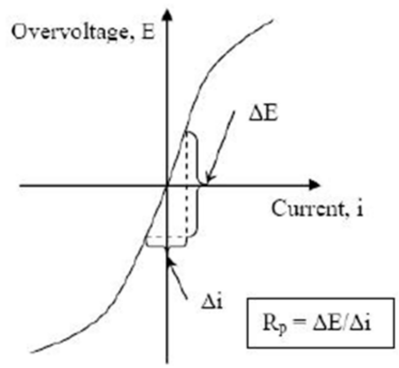

Figure 2-4: Plot of linear polarization resistance (Jones 1996)

The LPR equipment is a sophisticated arrangement of reference electrodes, auxiliary electrode and a low voltage DC current supply (Figure 2-5). The measurement is conducted by polarizing a known area of steel with an electric current applied through the auxiliary electrode. The potential change is measured using the reference electrode. The current is increased monotonically until the corrosion potential changes by ±25 mV. Within this small overvoltage range, the polarization curve is assumed to be linear and the Stern-Geary formula is accurate (Jones 1996).

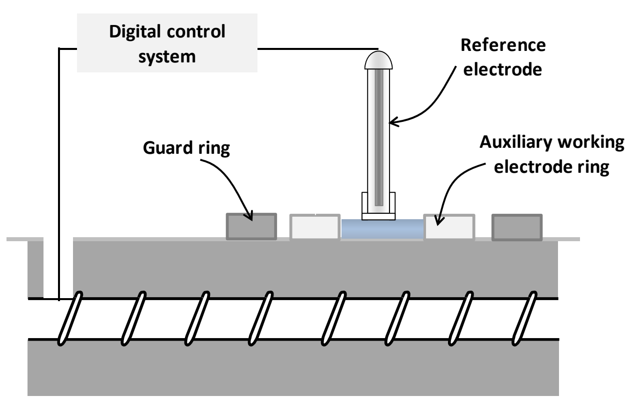

Figure 2-5: Schematic of a Linear Polarization system

For bridge inspections, the LPR equipment is connected to the reinforcement in a manner similar to the half-cell measurements. A DC connection is made between the reinforcement cage and the LPR equipment. Then the electrode assembly is placed over a wet sponge and positioned over the concrete surface. Unlike half-cell measurements, the LPR readings are slow and may take up to ten minutes per reading. Hence, maintenance engineers typically acquire half-cell maps and then perform the LPR measurements in regions identified with high risk of corrosion risk (Gannon and Cady 1992). A number of researchers have suggested the criteria listed in Table 2-3 to classify the corrosion damage within concrete (Feliu, Gonzalez and Andrade 1996, Broomfield 2007, Broomfield, Rodriguez, et al. 1994). The suggestions were based on laboratory investigations and the limit values were shown to provide relatively good correlation with damage observed in real structures.

Table 2-3: Corrosion criteria based on measured corrosion rate using LPR

Corrosion Risk	**i_{corr} (μA/cm^2)**
Passive Condition	< 0.1
Low Corrosion	0.1-0.5
Moderate	0.5-1.0
High Corrosion	>1.0

The corrosion rate of embedded steel is variable and continuously changes with time (ACI 222R 2010). Furthermore, corrosion rates are very sensitive to temperature changes and seasonal variations (Grantham, Herts and Broomfield 1997, Martinez, et al. 2008, Andrade, Alonso and Sarria 2002). The temperature affects the corrosion rate directly as it alters the available heat energy, which controls the oxidation rate. The corrosion rate is also affected by relative humidity and the concentration of chlorides in the concrete solution (Millard, et al. 2001, Angst, et al. 2011). The latter factors influence the ease of ion transfer between the anode and cathode regions. In addition, Martinez et al. (2008) demonstrated the sensitivity of the measured corrosion rates to the type of instrument used. Nygaard et al. (2009) have also shown that due to the large rebar area being polarized, the LPR method fails to accurately locate regions of localized corrosion and the rates measured near pitting locations generally resembles passive rebar values.

The previous discussion demonstrates an important feature of LPR measurements: corrosion rates obtained by the LPR method are instantaneous and reflect the corrosion condition at the time of the measurement (Scully 2000). Hence, the reliance on a single set of measurements to calculate section losses can lead to erroneous conclusions. In addition, a major difficulty in obtaining accurate corrosion rates is the need to identify the actual surface area of the polarized steel (Grantham, Herts and Broomfield 1997, Bertolini, et al. 2004). Furthermore, the LPR equipment is relatively expensive and requires continuous maintenance and care, hence, the method is rarely used in traditional bridge inspections (ACI 222R 2010).

2.3.3 Concrete Electrical Resistivity

The electrical resistivity of the concrete cover has a major influence on the rate of ion exchange and corrosion rate (Gowers and Millard 1999). The resistivity is strongly affected by the quality of the concrete, the moisture content, and the chloride ion concentration. The method provides a qualitative comparison of the concrete quality in a structure. Researchers reported that concretes with electrical resistivity higher than 20 kΩ-cm exhibit very low permeability, hence, exhibit low risk of corrosion (Bertolini, et al. 2004, Carino 1999).

The measurements are conducted using a four-probe resistivity meter (Wenner Probe) and does not require any connection to the embedded steel (Gowers and Millard 1999). The probes are placed on a wet sponge and positioned directly over the surface of concrete. The machine applies a predefined low frequency AC current at the end probes and measures the voltage between the inner probes (Figure 2-6). Ohm's law is then used to calculate the electric resistivity of concrete. This technique does not measure the corrosion rate, activity, or provide an indication of the ensuing damage. The resistivity measurements merely provides an indication of the concrete quality (ACI 222R 2010).

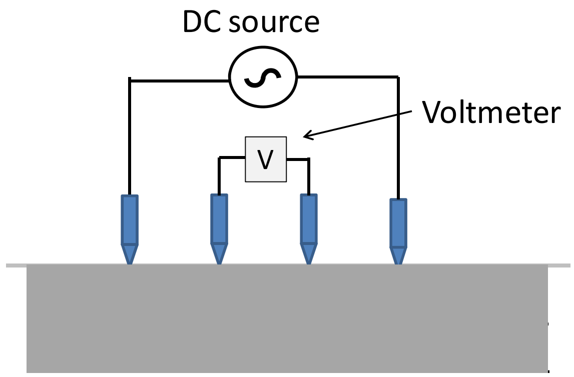

Figure 2-6: Schematic of the four probe resistivity meter

2.4 EMBEDDED ELECTROCHEMICAL SENSORS FOR CORROSION MONITORING

A number of novel sensor platforms have been developed for real-time monitoring of corrosion initiation and propagation within concrete members. This class of sensors employs traditional electrochemical evaluation techniques to assess the corrosion risk and current densities. The sensors are permanently embedded in concrete during construction or repair projects and are placed adjacent to reinforcement bars (McCarter and Vennesland 2004). The embeddable nature of the sensors provides the most direct representation of the actual corrosion state within concrete. Furthermore, the placement of the sensors in concrete reduces the interface effects and eliminates the sensitivity of the electrochemical measurements for ambient conditions. To date, the embedded electrochemical sensors require a wired connection and are typically linked to a central data acquisition system. Numerous embedded corrosion monitoring technologies have been reported in literature and have shown a potential for reliable corrosion monitoring (Broomfield, Davies and Hladky 2002, Raupach and Schiebl 2001, McCarter and Vennesland 2004, Lu and Ba 2011, Pease, et al. 2011). The following paragraphs describe two embeddable wired sensors that are currently available commercially.

2.4.1 SensCore Concrete Corrosion Monitoring Sensor

The SensCore corrosion monitoring sensor by RocTest allows the monitoring of corrosion initiation and progression within concrete structures (Figure 2-7). The sensor also provides real-time data on concrete humidity and temperature (RocTest 2013). SensCore consists of four mild steel sensing rebars that are connected to a reference stainless steel support. The sensing rebars are placed at four different depths. The sensor measures the corrosion rate at each sensing rebar and can be used to monitor the rate of ingress of the chloride front. The rates measured in the sensing rebars are used to assess the level of corrosion risk and estimate the corrosion rate in adjacent reinforcement. The embedded sensors are wired to a datalogger which located in the vicinity of the structure. The datalogger can then be used to transmit the data wirelessly or through wires to a central data collection unit. Recently, a total of eight SensCore sensors were installed in the newly constructed I35-W replacement bridge in Minneapolis where they are being used to measure chloride penetration in the bridge deck (RocTest 2013). However, due to the inability to interpret the data provided by the datalogger, the SensCore output became obsolete for this bridge monitoring application (French, et al. 2012).

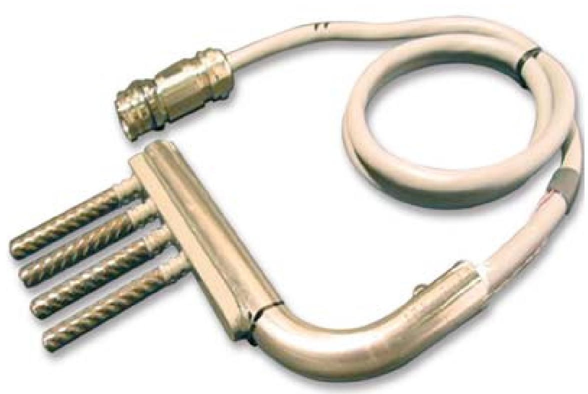

Figure 2-7: SensCore Corrosion Sensor (RocTest 2013)

2.4.2 Embedded Corrosion Instrument (ECI-1)

The ECI-1 sensor was developed by Virginia Technologies Inc. to provide an early warning of the corrosion activity within concrete (2013). The sensor assembly combines a complex arrangement of electrodes and an onboard microcontroller. ECI-1 sensor monitors simultaneously five key indication of corrosion activity including linear polarization resistance, half-cell potential, chloride ion levels, concrete resistivity, and medium temperature. Hence, the sensor output provides a comprehensive assessment of the corrosion process allowing for reliable diagnosis of the corrosion problem and the rate of the corrosion activity (Reis and Gallaher 2006). It should be noted that all the electrochemical evaluation measurement are conducted on sacrificial sensing low-carbon steel rebar section that is part of the sensor assembly. The ECI-1 employs a digital communication through a wired sensor network. Hence, the sensors communicate continuously to an external datalogger which controls the frequency of the measurements and transmits the data to a central data management center (Reis and Gallaher 2006).

The ECI-1sensor assembly is relatively large in size and the manufacturer suggests examining its effect on the structural performance. In addition, the cost of the unit is relatively high ($1000 (Fortner 2003)) and the cost of sensor installation, powering the datalogger, and wire connections also add to the overall system cost.

Figure 2-8: ECI-1Sensor (Virginia Technologies Inc. 2013)

2.4.3 Limitations of Embedded Real-Time Electrochemical Sensor Systems

The sensor technologies described in this section have the potential for providing comprehensive and direct signals regarding the state of corrosion within concrete. The use of embedded electrodes eliminates the environmental issues affecting traditional electrochemical evaluation methods (McCarter and Vennesland 2004). Furthermore, the ability to provide early warning of chloride ingress enables preventive repairs and mitigation measures to be used and also monitor the quality of the repairs used. However, the embedded sensors can only indicate the corrosion state in the concrete medium surrounding the sensor (Broomfield 2007). Hence, the sensor output cannot be generalized to provide conclusions regarding the corrosion state within an entire structure being monitored. In addition, the commercially available sensors are relatively expensive, which restricts their use to applications that require a limited number of embedded sensors. The installation, wiring, and maintenance costs also prohibit the wide deployment of this technology. Hence, transportation officials have been hesitant to use the embedded monitoring technologies for ordinary bridges and the sensors have only been used in signature structures (French, et al. 2012).

Furthermore, the corrosion rates and half-cell potentials acquired using the embedded corrosion sensors are measured across sacrificial low-carbon steel rebars. While the corrosion behavior of the sensing rebars should be similar to the steel reinforcement used, the frequent polarization of the sensing rebars alters their electrochemical characteristics in the long term, leading to the possibility of erroneous measurements in the future (Bertolini, et al. 2004). In addition, these sensors rely on cables and electric wiring to supply power and transfer data. The wires are typically connected to external data collection equipment or dataloggers. Hence, the wires penetrate the surface of the concrete and can provide direct access for deleterious contaminants and moisture into the concrete medium. As a result, the sensor assembly can lead to faster corrosion initiation within the concrete structure being monitored.

The main drawback of real-time monitoring of corrosion within civil structures pertains to the data management aspect. Corrosion of steel reinforcement requires years and even decades to initiate and form (Melchers and Li 2009). Hence, the continuous acquisition of corrosion data and statistics, while academically seems interesting, does not provide any benefit to the bridge owners. In contrast, the economical investment needed to maintain the embedded sensor systems and the costs of data interpretation can become a big burden for the infrastructure management program. Consequently, the use of theses real-time monitoring technologies has been limited to signature structures and for short-term monitoring of repairs. The same drawback affects the wide adoption passive monitoring technologies such as acoustic emissions for corrosion monitoring applications (Yoon, Weiss and Shah 2000).

2.5 PASSIVE RF BASED SENSORS FOR CIVIL INFRASTRUCTURE APPLICATIONS

Civil infrastructures provide a unique challenge for SHM engineers. The large scale of the structures being monitored and the catastrophic consequences of localized deterioration make the development of a reliable health monitoring system a complex task. In addition, the time required for the deterioration to start affecting the structural performance varies depending on the deterioration mechanism and the degree of exposure to the aggressive environmental conditions. Wired sensor technologies are typically associated with higher initial costs due to installation costs. Hence, a number of wireless sensor and sensor network technologies have been developed recently to monitor the structural performance of bridges and buildings (Lynch and Loh 2006). However, the wireless monitoring sensors have a finite life due to the use of portable power sources to allow for a wireless communication. While a number of promising energy harvesting technologies have been developed, the majority of these harvesters are in their early development stages and, to date, may not be suitable for long-term applications (Dierks 2011). Hence, novel design concepts that address the issue of the finite sensor life are needed for long-term deployment in civil infrastructures.

Many researchers in the field of SHM have proposed employing radio frequency (RF) wireless technologies for powering and interrogating embedded passive sensors (Lynch and Loh 2006). The technology has been used successfully in chemical and biological applications (Steinberg and Steinberg 2009, Ong, et al. 2002, Zhang, Pasupathy and Neikirk 2011, Garcia-Canton, Merlos and Baldi 2007). RF sensors rely on the wireless communication between remote readers and the sensors using near-field inductive coupling. Hence, the passive sensors can only provide information if the external reader in present making the sensors ideal for threshold sensing applications. The sensors are battery-free and their designs typically do not contain any onboard processing capabilities. Therefore, the sensors are much simpler in design and significantly less expensive to fabricate and operate compared with active real-time wireless monitoring sensors.

2.5.1 RF- and RFID-Based Sensors for Structural Health Monitoring Applications

A number of RF prototype sensors were developed to monitor the changes in structural strains or to memorize peak strains or displacements at the location of sensor embedment. Mita and Takahira (2002) developed an RFID based sensor that memorizes maximum strains through the use of a sacrificial buckling wire. The change in the geometry of the buckling wire alters the frequency response of the embedded sensor. This change in frequency become stable and it is only changed if higher strains were applied. Similarly, a resonant RF sensor that monitors changes in strain by measuring the shifts in the frequency response induced by changes in the geometry of the coil antenna was developed by Chuang, Thomson, and Bridges (2005). Alternatively, Jia and Sun (2006) proposed the use of a thick capacitive layer that is composed of a strain sensitive material to monitor strain changes. The sensing layer acts as a capacitive transducer that is coupled with a planar inductor. Deformation in the sensing capacitor alters the system capacitance leading to a shift in the self-resonant frequency of the sensor. Similarly, Yi et al. (2011) proposed the use of a novel design that employs folded patch RFID-based antennas to act as smart-skin sensors. The antenna employs a special substrate material that is connected to an RFID tag. The planar antenna sensors are attached to the surface of metallic structures and the strain-induced change in geometry alters the frequency response measured.

RF-based sensors have also been developed for a number of applications other than strain monitoring. Novak et al. (2003) proposed a state sensor design that enables the detection of crack initiation or growth in welded steel connections. The sensor employs an electronic article surveillance (EAS) tag for data communication. The tag is connected to two sensing copper strips that are positioned over potential crack locations. Rupture of the sensing strips alters the frequency response of the sensor and is indicative of crack formation. In addition, passive wireless sensor designs were also developed to monitor the curing of concrete after casting through monitoring changes in water content (Ong, et al. 2008) and concrete conductivity (Kim 2013).

2.5.2 RF- and RFID-Based Sensors for Corrosion Monitoring in Concrete Structures

While passive wireless sensors can be deployed for monitoring numerous phenomena pertaining to civil structures, the field of corrosion monitoring within concrete structures can benefit tremendously from this class of sensors (Agrawal, et al. 2009). The corrosion process is slow and the propagation of damage may require years or decades. Hence, the use of the battery-free sensors ensures that the sensors will operate throughout the service life of the structure. Furthermore, the integration of sensor interrogations with routine bridge inspections limits the operating costs and eliminates the need to store, analyze, and interpret the continuous data output typically generated in real-time monitoring systems. In addition, corrosion of steel reinforcement can be identified through the use of threshold level damage identification. Corrosion initiation is typically associated with reaching critical levels of chloride concentrations and cracking of the surrounding concrete is also associated with a threshold level of rebar section loss.

Hence, the use of state passive sensors that alter the response once a threshold level is reached can be feasible and advantageous. The following paragraphs provide a brief summary of the RF-based sensors for corrosion detection and monitoring applications that are available commercially or are currently under development.

2.5.2.1 Smart Pebble™

A wireless sensor based on RFID technology for monitoring chloride concentrations in bridge decks was developed by SRI International and the California Department of Transportation (Watters, et al. 2003). The Smart Pebble™ sensor employs an RFID MCRF202 microchip that enables the wireless interaction with a remote reader. The microchip is connected to a 300-turn coil resulting in an inherent resonant frequency of 125 kHz. The sensor assembly contains two electrochemical electrodes (an ion-selective electrode and a reference electrode) that produce a half-cell potential voltage. The value of the voltage produced is dependent on the chloride ion concentration. Once a threshold voltage is reached, the binary response is switched. Due to its reliance on electric potential changes, the Smart Pebble™ response is highly dependent on temperature. Furthermore, the electrochemical cell is subject to temporal drifts as electrolyte solutions within the electrochemical cell are expected to dry out with time. Fortner (2003) reported that the 1.5-in.-diameter Smart Pebbles™ are expected to cost $100 per unit and allow for monitoring chloride ingress for depths that are as large as 4.0 in.

2.5.2.2 Smart Aggregate

Cain et al. (2003) have also developed a passive RFID-based wireless sensor to monitor corrosion in reinforced concrete. The smart aggregate sensor employs a low-power microcontroller and two antenna coils. One of the coils is used for power collection while the second is used for data communication. The sensor employs a thermometer and a resistance meter transducers. The thermometer is used to monitor temperature evolution during the curing of fresh concrete. The resistance transducer is used to assess the resistivity of the concrete in the deck. Hence, corrosion is detected by monitoring the changes in concrete resistivity due to chloride presence. The Smart Aggregate design was envisioned to cost approximately $50 and last for over 50 years (Cain, et al. 2003).

2.5.2.3 RF-Based Passive Potential Sensors

Researchers at the University of Manitoba recently developed an RF-based passive sensor that enables monitoring half-cell potentials within concrete (Bhadra, Thomson and Bridges 2013). The sensor relies on the change of the resonant characteristics of an LC circuit to determine the corrosion potential. The embeddable sensor design comprises an inductive coil that is connected to a voltage dependent capacitor (varactor). Similarly to the Smart Pebble™ design, the sensor contains a pair of corrosion electrodes: a mild steel working electrode and a stainless steel reference electrode. Changes in the potential difference between the two electrodes alter the capacitance of the varactor leading to a change in the measured resonant frequency. While the sensor design provides a less inexpensive alternative for the ECI-1 wired system, the half-cell potential measurements remain sensitive to the variations in temperature and relative humidity. In addition, due to the sensitivity of the half-cell measurements on a number of factors, the absolute values measured might provide erroneous conclusions regarding the state of corrosion (Andrade, Alonso and Gulikers, et al. 2004).

2.5.2.4 Passive Threshold Corrosion Sensors

A novel class of passive sensors for early detection of corrosion was developed at the University of Texas at Austin (Simonen, et al. 2004, Dickerson, et al. 2006, Puryear 2007, Abu Yousef, et al. 2010). The sensor design employs two resonant LC circuits that are placed concentrically. The first circuit is connected in series to a sacrificial corroding wire and acts as a sensing circuit while the second circuit acts as a reference circuit. The sensing wire exhibits electrochemical properties similar to the reinforcing steel and it is exposed to the concrete environment. The wire acts as "switch" and once corrosion develops on the wire, the electric resistance of the sensing circuit increases and eventually reaches infinity as the wire fracture. As a result, the response of the sensing circuit disappears and only the response of the secondary reference circuit can be detected. Hence, the sensor acts as a threshold binary sensor that has two unique limit states (corrosion/ no corrosion). The cost of the prototype sensor was estimated to be in the order of few dollars (Wood and Neikirk 2009). Further details regarding the design, reliability, and limitations of the threshold corrosion sensor are provided in Section 3.2.1.

A similar sensor concept was proposed by Materer, Apblett, and Ley (2011). The sensor employs a sacrificial 99% iron wire to detect chloride ingress. The data communication and power transfer is conducted through a single low-frequency 125 kHz RFID tag. The tag is connected in series with the sacrificial wire. Thus, once the wire corrodes due to presence of chlorides, the sensor loses its signal and becomes unresponsive.

2.6 SUMMARY

The reliable detection of corrosion initiation within concrete structures is a complex engineering problem that requires innovative research and novel solutions. Detecting the presence of corrosion at early stages allows for corrective or preventive measures to be implemented rather than the costly and time-consuming repair and replacement projects. However, the state-of-practice relies on antiquated inspection methods that only enable the detection of severe internal delamination and cracking.

RF-based passive sensors have a great potential for enabling early detection of corrosion. However, the successful development of a sensor platform requires meeting a number of design criteria including low-cost, durable design, low impact on the structure, and a reliable output that is easy to interpret.

CHAPTER 3

Development of the Noncontact Corrosion Sensor Platform

3.1 OVERVIEW

A prototype passive sensor has been developed for the detection of corrosion initiation in reinforced concrete bridge decks. The sensor platform is envisioned to complement routine bridge inspections and enhance the quality of information gathered periodically over the service life of the bridge. The sensor is designed to be installed near the steel reinforcement before concrete placement and then interrogated during scheduled inspections. The sensors are scanned wirelessly using a mobile external reader that measures inductively coupled impedance. The embedded sensor acts as a point sensor that is triggered when a threshold level of corrosion damage has been exceeded. Figure 3-1 shows a schematic representation of the envisioned passive sensor platform. Unlike traditional corrosion monitoring techniques, the wireless sensor interrogations do not require removal of asphalt overlays and can detect corrosion at early stages mitigating the need for costly repairs. Furthermore, the innovative design provides a cost-effective, wireless and battery-free alternative for corrosion monitoring.

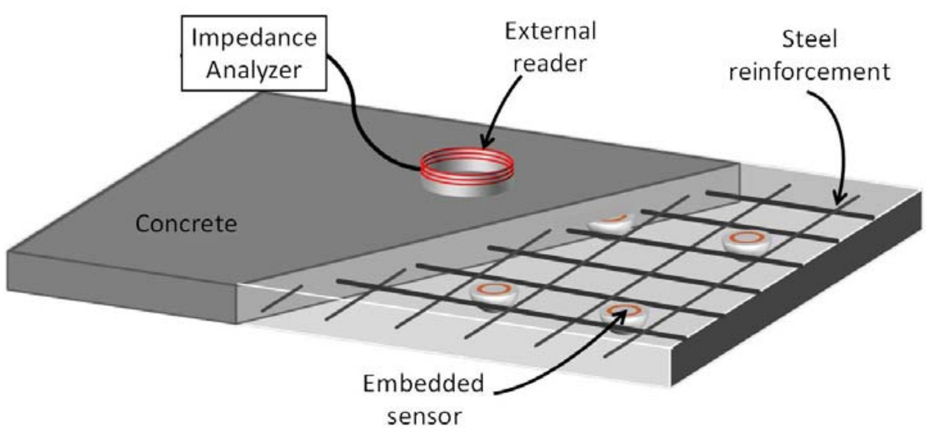

Figure 3-1: A schematic representation of the passive corrosion sensor platform

An earlier generation of the passive corrosion sensor was developed at UT Austin (Dickerson 2005, Andringa 2006, Wood and Neikirk 2009). The previous design used a sacrificial steel wire that was connected physically to the sensor circuit and was also exposed to the concrete medium. As a result, the sacrificial wire penetrated the protective housing enclosing the electric circuit components. Long-term exposure tests confirmed the ability of the passive threshold sensor to reliably detect corrosion activity within concrete. However, unintended corrosion of the sacrificial wire at the interface with the circuit housing was observed (Puryear 2007). The observed corrosion was the result of the formation of a concentration cell between the aerated exposed wire and the deaerated portions of the wire within the sensor housing. As a result, the penetration of the wire into the hermetic seal of the sensor circuit was expected to reduce the reliability of the sensor output and limit the durability of embedded sensors. Thus, a novel design that employs a contact-free interaction between the sacrificial corroding element and the circuit components was developed for the second-generation prototype sensor (Pasupathy, Munukutla, et al. 2009). The development of a new class of passive corrosion sensors, which addresses the vulnerability of the earlier design, is discussed in this Chapter.

The second-generation sensor relies on a sacrificial corroding element that is inductively coupled to the sensor circuit. Section 3.2 provides a brief description of the passive sensor platform and introduces the concept of the prototype Noncontact (NC) sensor. The construction details of the NC sensor are described in Section 3.3 and the sensitivity of the sensor response to the variation in the interrogation medium is examined in Section 3.4. The changes observed in the measured sensor response due to corrosion are described Section 3.5.

In order to provide a better understanding of the sensor behavior and assess design limitations, a SPICE circuit model of the NC sensor platform was developed. The model was employed to examine the sensitivity of the sensor response to variations in the main design parameters. In addition, an electromagnetic finite element model of the inductively coupled components was developed using ANSYS Maxwell® software

(ANSYS Inc. 2010). The details and major findings of the electric circuit model and finite element evaluation are summarized in Section 3.6 and Section 3.7, respectively.

3.2 PASSIVE SENSOR PLATFORM CONCEPT

The passive sensor platform relies on the wireless communication between two inductively coupled components, a resonant circuit and a reader coil. The resonant circuit is a resistor-inductor-capacitor (RLC) circuit that exhibits unique resonance properties. Figure 3-2 shows an equivalent circuit model of the resonant circuit. The reader powers and interrogates the resonant circuit through magnetic induction. The sensor platform relies on the frequency characteristics of the resonant circuit to obtain information about the conditions within the concrete.

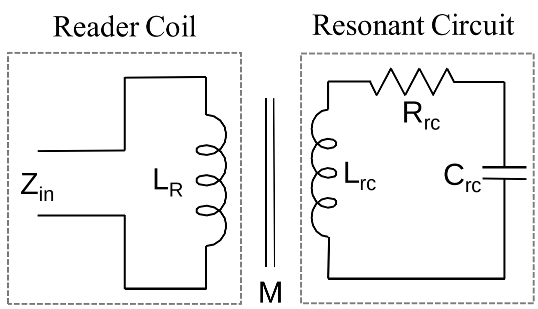

Figure 3-2: Circuit diagram of the resonant circuit

The frequency response of the resonant circuit is obtained by measuring the impedance at an external reader coil within a range of swept frequencies. The phase of impedance is typically used to identify the resonant parameters (Figure 3-3). The resonant frequency is identified by a minimum in the phase angle. For an RLC circuit, the resonant frequency (f_{rc}) depends solely on its inductance, L_{rc}, and capacitance, C_{rc} (Nilsson and Riedel 1996):

$$f_{rc} = \frac{1}{2 \cdot \pi} \sqrt{\frac{1}{L_{rc} \cdot C_{rc}}} \tag{3-1}$$

The difference between the baseline phase angle and the phase angle at the resonant frequency is defined as the phase dip. The measured phase dip is strongly dependent on the coupling, *M*, between the reader and the resonant circuit. Thus, the amplitude of the phase dip is sensitive to the read distance and the magnetic permeability of the medium separating the reader coil and the resonant circuit.

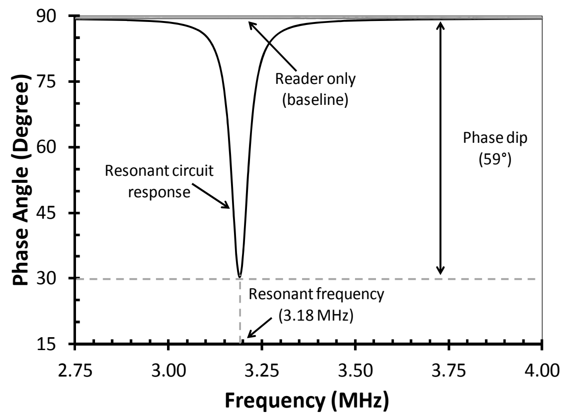

Figure 3-3: Phase response of a 3.18-MHz resonant circuit and the definition of response parameters.

The studies presented in this chapter were conducted using a 5-turn reader coil with a 4.0-in. diameter. The coil was assembled using 18-AWG enameled copper wire and connected to a 3.0-ft coaxial cable resulting in a self-resonant frequency of 6.0 MHz. The impedance response was acquired using a Solartron 1260A Impedance/Gain-Phase analyzer. The effect of the reader coil geometry and parameters on the measured impedance response of the NC sensor is briefly discussed in Section 3.3.4. In addition, Section 3.3.5 introduces the different interrogation techniques that can be used in practice to acquire the sensor response more rapidly.

3.2.1 First Generation Threshold Corrosion Sensor

The threshold corrosion sensor platform developed by Dickerson (2005) and Andringa (2006) consists of two passive resonant circuits (sensing and reference) arranged concentrically. Figure 3-4 shows the components of the first generation threshold corrosion sensor. The sensing circuit is connected to a steel sensing wire in series. Hence, the sacrificial wire acts as an electric switch. As the steel wire corrodes and fractures, the sensing circuit becomes an open circuit. The corroding wire is exposed to the same environmental conditions as the reinforcement within the concrete and is expected to corrode under the same conditions. The sensor circuit components are sealed in marine epoxy to prevent accidental damage during concrete placement and to ensure the durability of the sensor by preventing the corrosion of the circuit components.

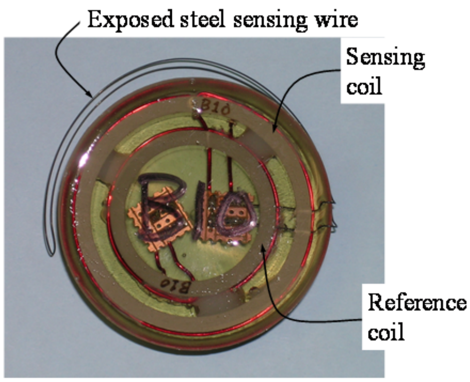

Figure 3-4: The first generation passive corrosion sensor (Dickerson 2005)

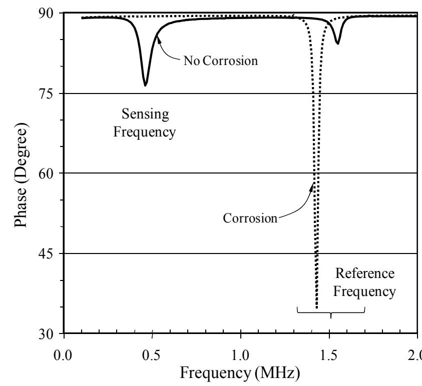

Figure 3-5: Phase response of a threshold sensor (Wood and Neikirk 2009)

The concentric sensor initially responds at two, distinct, resonant frequencies, corresponding to the sensing and reference circuits. Once the steel wire fractures due to corrosion, the frequency of the sensing circuit disappears as it becomes an open circuit (Figure 3-5). Therefore, the passive sensor can be idealized as a threshold sensor that changes its response once the level of corrosion damage is sufficient to break the sensing wire. Hence, two limit states can be identified when the sensor is interrogated: low probability of corrosion when two resonant frequencies are present and high probability of corrosion if only one frequency is present.

Accelerated long-term exposure tests of threshold sensors embedded in reinforced concrete slabs were conducted (Dickerson 2005, Puryear 2007). The test results showed that the sensors were successful in identifying the initiation of corrosion in the reinforcing steel (Wood and Neikirk 2009). However, corrosion products were observed within the epoxy housing of the embedded sensors (Figure 3-6). The physical connection between the wire and the sensor compromised the hermitic seal and provided a pathway for contaminants into the circuits. Although, this unexpected corrosion within the sensor components did not influence the response of the sensors, it could reduce the long-term durability of the sensors.

Figure 3-6: Presence of corrosion within sensor housing (Puryear 2007)

In addition, the interrogations during the exposure test indicated that the transition from the uncorroded state to the fully corroded state was gradual as the resistance of the wire increased to infinity. During transition, the concentric sensor frequency response was highly damped. As a result, the phase dip for some sensors became small and reached undetectable levels for a limited period of time (Puryear 2007).

3.2.2 Noncontact (NC) Corrosion Sensor

In order to prevent penetration of contaminants into the sensor body, a new configuration was proposed by Pasupathy (2009). The new design allows for a contact-free interaction between the corroding element and the sensor circuit. The NC corrosion sensor incorporates two components, a resonant RLC circuit and a sacrificial corroding element (Figure 3-7). The electrical components of the resonant circuit are hermetically sealed and protected from potential contaminants within the concrete. The corroding element is inductively coupled to both the resonant circuit and the external reader coil. The sacrificial corroding element is placed outside the sealed package and is subjected to the same environmental conditions as the surrounding concrete. To ensure accurate detection of corrosion in the adjacent reinforcement, the sacrificial element was selected to have electrochemical properties similar to the reinforcing bars.

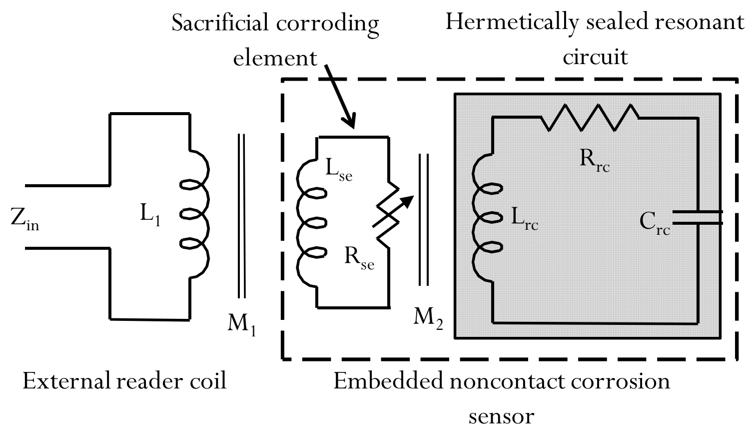

Figure 3-7: Circuit model of the NC corrosion sensor

The presence of the sacrificial element alters the frequency response of the sensor by shielding the magnetic fields between the reader and the resonant circuit. The effect appears as an increase in the measured resonant frequency and a reduction in the amplitude of the phase dip. Figure 3-8 illustrates the change in response due to the presence of a 0.001-in. thick steel washer directly over a 3.18-MHz resonant circuit. It can be seen that the resonant frequency increased from 3.18 MHz to 3.73 MHz and the phase dip decreased from nearly 60° to less than 5°. The degree to which the sacrificial element affects the resonant response depends on the mutual inductance between the corroding element and the resonant circuit. Hence, the geometry of the corroding element and the distance between the sacrificial element and the resonant circuit affect the characteristics of the initial uncorroded state of the NC sensor.

As corrosion develops in the sacrificial element, the resistance (R_{se}) increases and the magnetic coupling decreases gradually, which leads to a decrease in the resonant frequency of the corrosion sensor. When fully corroded, the sacrificial element becomes an open circuit and the phase response of the sensor reverts back to that of the resonant circuit. Hence, the NC sensor exhibits two limit states: an initial state where the sacrificial element is intact and a final state that exhibits the frequency characteristics of the resonant circuit only and is representative of a fully corroded sacrificial element.

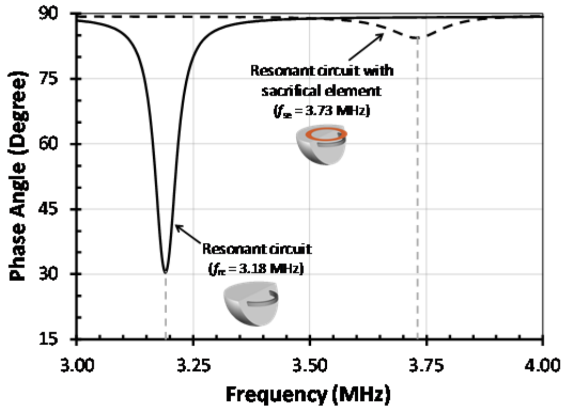

Figure 3-8: The change in phase response of a 3.18-MHz resonant circuit due to the presence of a steel washer

3.3 NC SENSOR COMPONENTS AND FABRICATION

The NC sensor consists of two inductively coupled components; a simple RLC resonant circuit and a sacrificial corroding element. Both components interact with the reader coil affecting the characteristics of the measured frequency response of the embedded NC sensor (Pasupathy, Munukutla, et al. 2009). Ideally, the electric components of the resonant circuit should remain protected and hermetically sealed throughout the service live of the embedded sensor. Thus, any changes in the measured frequency response should be induced only by the corrosion of the sacrificial element.

In the following paragraphs, the different components of the NC sensor are described and the fabrication details of the sensor prototype are summarized. A step-by-step description of the fabrication of an NC sensor is provided in Appendix A. In this section, the basis for the selection of each design parameter is briefly explained. Due to the developmental nature of this research, the sensors were fabricated by hand and the component selection was limited to the commercially available materials purchased from local suppliers. Hence, thorough and accurate parametric experimental studies could not be conducted to evaluate the sensitivity of the sensor response to each component. To this end, circuit and finite element models were developed to provide the basis for future developments and design assessments. The details of the models are described in Section 3.6 and Section 3.7.

3.3.1 RLC Resonant Circuit

The resonant circuit has three basic electric components: an inductor (L), a capacitor (C), and a parasitic resistance (R). The first two components are selected by design while the latter is a result of the inherent resistances of the circuit components and imperfect soldering of these components to the circuit board.

3.3.1.1 Resonant Circuit Inductor

The inductor for the resonant circuit can be idealized as a short solenoid coil. The inductance of the circuit coil and its coupling efficiency with the reader coil has a major impact on the measured phase response. The geometry of the inductor controls the value of its inductance, which can be calculated as follows (Grover 1946):

$$L = 0.002\pi^2 a\left(\frac{2a}{l}\right)N^2 K \tag{3-2}$$

where L is the inductance in μH, a is the radius of the inductor in cm, N is the number of turns, l is the length of the coil in cm, and K is Nagaoka's geometry correction factor.

Figure 3-9 is schematic representation illustrating of the resonant circuit components and the geometric parameters controlling the inductance value. A photograph of a typical resonant circuit is shown in Figure 3-10. Based on the findings of Dickerson (2005), the resonant circuit inductor was fabricated by winding five turns of 18-AWG enameled copper wire around a slice of PVC pipe. The inductor coil has a nominal diameter of 2.50 in. Based on Equation (3-2), the fabricated coil has a nominal self-inductance equal to 3.75 μH.

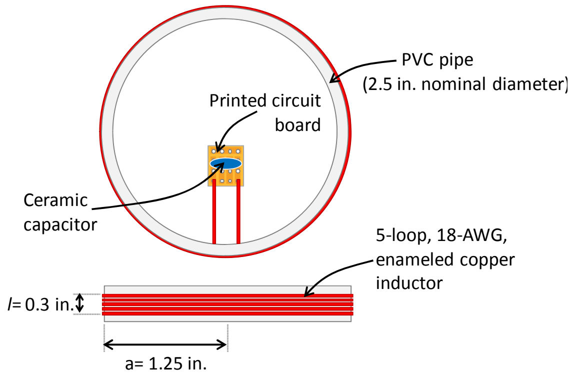

Figure 3-9: Schematic representation of the resonant circuit

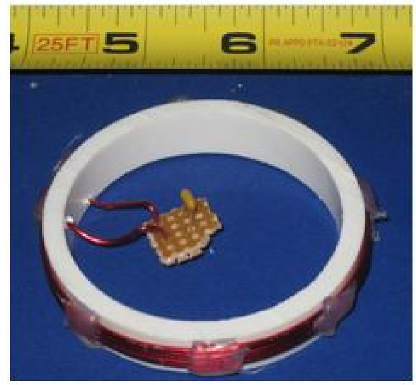

Figure 3-10: Photograph of the resonant circuit

3.3.1.2 Resonant Circuit Capacitor

As was shown in Equation 3-2, the phase response of a resonant circuit is dependent on the capacitance of the circuit. In addition, the quality of the capacitor influences the phase of the impedance and the stability of the sensor circuit to environmental variations. Dickerson (2005) conducted a detailed parametric evaluation using a wide range of commercially available capacitors. He concluded that that high-quality C0G or NP0 ceramic capacitors produce frequency signals that exhibit deeper phase dips. In addition, ceramic capacitors were the least sensitive to variations in temperature within the interrogation mediums.

Figure 3-11 shows the measured phase response of a single five-loop resonant circuit that was soldered to four different C0G capacitors. It can be seen that higher resonant frequencies were recorded for the sensors with lower capacitance values. However, no clear correlation was noted between the capacitance value and the measured phases dip values. The results confirmed that obtaining a strong signal from the resonant circuit is dependent on the selection of a high-quality capacitor. Thus, 820-pF C0G capacitors were selected for the design of the NC sensor circuits and were used in the fabrication of all the sensors used in this research.

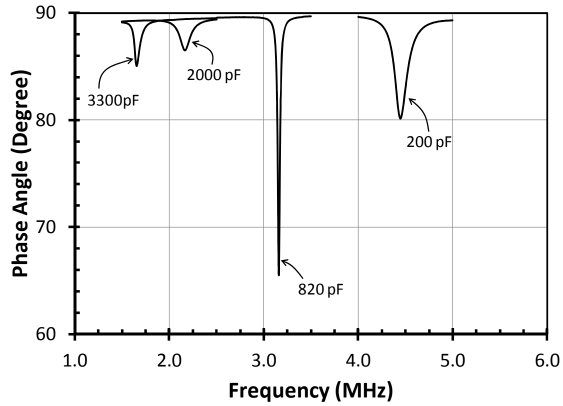

Figure 3-11: Phase response of a five-loop resonant circuit connected to 200-, 820-, 2000-, and 3300-pF ceramic capacitors

3.3.2 Sacrificial Element

The innovative design of the NC sensor enables the utilization of corrosion transducers fabricated from a variety of materials and morphologies. However, the selection of a suitable sacrificial corroding element is critical to the successful development of an embeddable NC corrosion sensor. To this end, the sacrificial element should possess the following three attributes:

- The sacrificial element should exhibit electrochemical properties that are similar to the low-carbon steels used for the manufacturing of deformed reinforcement. As a result, shifts in the response of the NC sensors embedded in concrete will be indicative of real active corrosion in the adjacent steel.
- The sacrificial element should be able to induce electromagnetic shielding on the magnetic fields forming between the reader and sensor coils. Consequently, the presence of the sacrificial element will alter and dampen the frequency response of the sensor. Corrosion accumulation on the sacrificial washer will gradually eliminate its ability to affect the phase response of the resonant circuit.

- The sacrificial element utilized should be inexpensive, commercially available, and can be easily mass-produced. This will minimize the final cost of the NC sensor and allow for the deployment of the corrosion sensor in typical concrete bridges.

3.3.2.1 Sacrificial Element Selection

Based on the stated attributes, two types of corroding sacrificial elements were initially investigated: steel washers and closed wire spirals. The washers are low-carbon, cold rolled steel spacers that are available commercially in numerous geometries and thicknesses (Figure 3-12). The spiral was fabricated manually using 18-AWG steel wire forming a 5-loop closed spiral (Figure 3-13). The spiral loop circuit is closed by soldering the wire ends using a silver-solder wire.

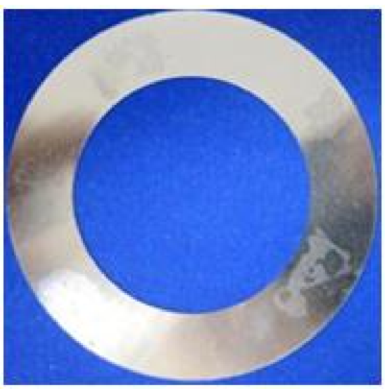

Figure 3-12: Photograph of a sacrificial steel washer

Figure 3-13: Photograph of a sacrificial 5-loop wire spiral

The experimental studies described in the following sections were conducted using a 3.18-MHz resonant circuit and utilizing the set-up and definitions described in Figure 3-14. Unless stated otherwise, the interrogations were conducted in air at a constant read distance of 1.5 in. and a separation distance of 0.1 in.

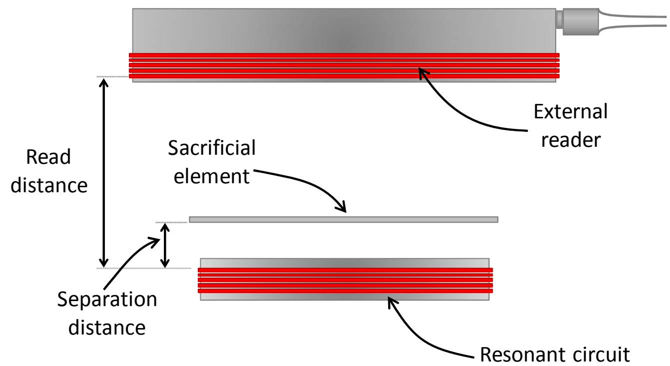

Figure 3-14: Experimental set-up and definitions of the parametric studies variables

It can been seen in Figure 3-15 that the washer provided more shielding of the resonant circuit than the spiral wire. Hence, the frequency shift between the uncorroded and corroded limits states was larger. This implies that the steel washer will provide more information regarding corrosion rates if analog data are extracted. In addition, the bimetallic junction at the solder between the ends of the wire spiral can promote accidental galvanic corrosion, which can jeopardize the reliability of the NC sensor.

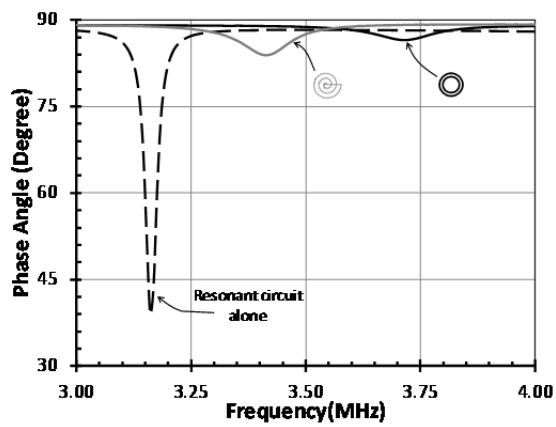

Figure 3-15: Phase response of the 3.18-MHz sensor and the change in response due to the presence of different sacrificial elements

Additionally, the results of an accelerated corrosion test have suggested irregular changes in the response of NC sensors fabricated with wire spirals (A. E. Abu Yousef, et al. 2011). Thus, the steel washers were selected as the sacrificial elements used in the fabrication of all the NC sensors discussed in this dissertation.

3.3.2.2 Sacrificial Element Geometry

The geometry of the sacrificial element has a major effect on the change of the measured frequency response. The degree of magnetic shielding is highly dependent on the dimensions of the sacrificial washer and its location relative to the resonant circuit and reader coil. The selection of an optimum geometric parameters is complicated and multi-variable. A high level of magnetic shielding is generally desirable as it provides a clear and easy means to interpret the distinction between the initial uncorroded and the final fully corroded states. However, if the coupling between the sacrificial element and the circuit becomes very high, the phase dip of the resonant circuit can become excessively damped, and the sensor becomes undetectable while in the uncorroded state.

Based on the results of initial parametric studies, the outer diameter of the sacrificial washer was found to have a major influence on the degree of magnetic coupling between the washer and the resonant circuit. Figure 3-16 shows the changes in the measured phase response of a 3.18-MHz resonant circuit due to the presence of identical washers having different outer diameters. It can be seen that the shielding of the resonant circuit signal was decreased as the diameter of the washer was reduced. The largest shift in the resonant frequency was observed when the diameter of the washer was equal to that of the resonant circuit. Similar conclusions were also reported by Pasupathy (2010).

The influence of the separation distance between the sensor and the corroding element was evaluated using a 2.75-in. diameter steel washer and multiple dielectric spacers. Figure 3-17 shows that separation distance has a direct effect on the inductive coupling: as the separation was reduced, higher resonant frequencies were measured. Furthermore, when the washer was cut through its width to simulate localized corrosion, the shielding effect was still observed at small separation distances. This is attributed to the disturbance of the magnetic fields that the remaining steel material imposes. This behavior diminishes rapidly as the separation distance increases.

The observed residual shielding imposed by the cut washer indicates that the shielding effect of the washer is affected two factors: the resistance of the sacrificial washer and the available metal area. However, the resonant frequency is more sensitive to changes in the resistance of the washer. Figure 3-17 shows that as the resistance of the washer increased from zero (point A) to infinity (point B), the resonant frequency shifted 90% of the available frequency range.

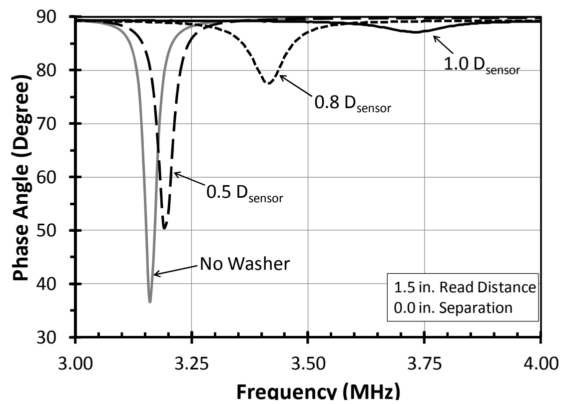

Figure 3-16: Effect of the diameter of the washer on the measured phase response

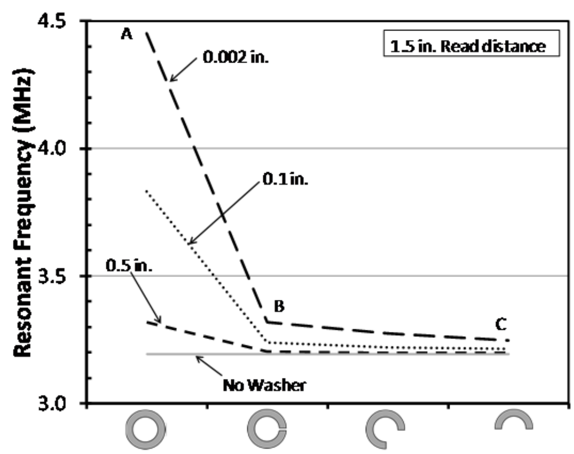

Figure 3-17: Measured resonant frequency for a noncontact sensor with a 0.002-in. thick washer placed at different separation distances.

3.3.3 Protective Housing of the NC Sensor

A major concern in the design of a reliable and durable corrosion sensor is the ability to shield the circuit components from the corroding contaminants surrounding the embedded sensor. Thus, a hermetic seal that engulfs the resonant circuit components and provides a moisture barrier is critical to the durability of the embedded sensor. Moisture presence can short the resonant circuit resulting in the loss of signal.

Chou (2010) suggested coating the resonant circuit components using a thin layer of SHEP-Poxy III® epoxy. The epoxy is typically used for pressure injection of cracks in concrete and as a chemical adhesive of post-insatlled anchors (Appendix B). According to the supplier, the epoxy has a thermal expansion factor similar to that of the concrete. Hence, the risk of cracking the hermetic seal due to temperature increase is reduced. The epoxy is applied by dipping the circuit components in the epoxy while it is curing. Then, the epoxy cover is allowed to cure and the dipping process is repeated again to ensure a full and intact coverage of the resonant circuit. Figure 3-12 shows a resonant circuit after the application of the epoxy cover. Severe exposure tests were conducted by Chou (2010) and demonstrated that the epoxy cover is water-tight and provide a reliable protection against water infiltration to the coil.

Figure 3-18: Resonant circuit covered with a layer of protective epoxy

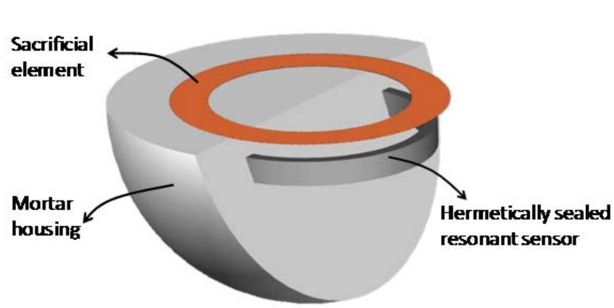

Figure 3-19: Fiber-reinforced mortar paste housing for the NC sensor

In order to protect the circuit components from accidental damage during construction and concrete placement, the sealed resonant circuit was embedded in fiber-reinforced mortar housing (Figure 3-19). The mortar housing provides physical protection to the sensor during construction and provides a convenient base to affix the sacrificial washer. Polypropylene fibers are used to reinforce the paste and control shrinkage cracking. The mortar mix properties were developed by Chou (2010) after a series of severe exposure tests. The outer diameter of the protective housing was set at 4.0 in. to prevent cracking during curing. The convex shape of the housing was selected to prevent trapping air below the sensor during the placement of concrete.

3.3.4 External Reader Coil

The external reader can be idealized as an LC circuit and its resonant properties affect the level of inductive coupling with the NC sensor. Hence, the characteristics of the measured phase response of an NC sensor are dependent on the type and geometry of the reader coil. The geometry of the reader coil controls the self-inductance of the reader while the capacitance of the LC circuit is mostly produced by the coaxial cable used to connect the reader coil to the phase analyzer. The reported inherent capacitance of the coaxial cable is 30.80 pF/ft.

In the absence of a coupled resonant circuit, the phase of impedance of a reader coil has three distinct baseline regions: (1) the inductive baseline, which is characterized by a 90° phase angle and occurs at frequencies below the self-resonant frequency of the reader; (2) the capacitive baseline, which is characterized by a -90° phase angle and occurs at frequencies above the self-resonant frequency of the reader; and (3) the resonant baseline, which corresponds self-resonant frequency of the reader coil and coincides with a phase angle equal to 0°. Figure 3-20 shows the different regions of phase response for a 5-loop 4.0-in. reader coil that is connected to a 3-ft coaxial cable.

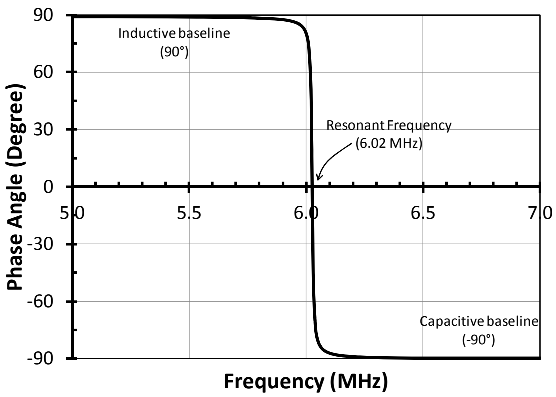

Figure 3-20: Phase response of a 5-loop 4.0-in. diameter external reader coil

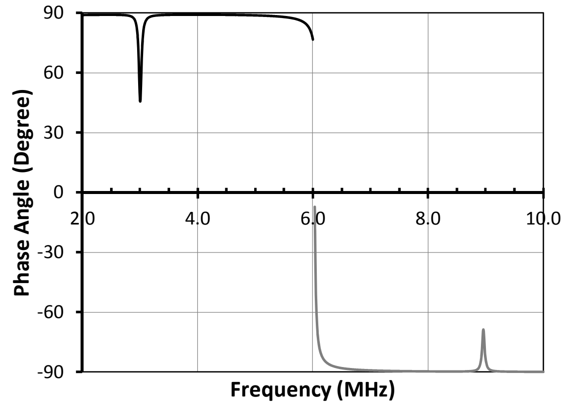

Figure 3-21: Phase responses of 3.0- and 9.0-MHz sensor circuits measured with a 5-loop, 4.0-in. diameter reader coil

The phase response of the NC sensor is expected to exhibit the strongest signal when the resonant frequency of the sensor is equal to the resonant frequency of the external reader coil. However, in this case the coupling between the reader and resonant circuit produces a phase response with a wide bandwidth. As a result, real changes in the sensor response due to the corrosion of the sacrificial washer are masked by the strong coupling. Thus, a reliable interpretation of the sensor output becomes very difficult.

In contrast, the capacitive baseline produces the weakest signal due to the low inductance of the reader capacitance. Pasupathy (2010) recommended that the resonant frequency of the NC sensors should be within the inductive region for a given reader coil. Figure 3-21 illustrates the difference in response between sensors that have resonant frequencies that are either within the inductive or capacitive baseline regions of 6.0 MHz reader coil. The resonant frequencies of the sensors were 3.0 MHz away from the resonant frequency of the reader coil, which minimizes the effect of mutual resonance. When measured at the same read distance, the inductively coupled sensor (3.0 MHz) had phase dip amplitude that was significantly higher than the sensor within the capacitive baseline (9.0 MHz).

In addition, Pasupathy (2010) conducted detailed analyses to study the effect of the reader coil geometry on the measured response of the sensor. He concluded that, if all other parameters remained constant, the optimum diameter for the external reader coil is equal to twice the distance between the centerlines of the reader coil and the resonant circuit inductor. Based on these findings, a 4.0-in. diameter coil was selected and used throughout this dissertation. This is due to the fact that the clear concrete cover used in the long-term exposure tests was 1.0 in. producing a center-to-center separation between the reader and sensor coils was approximately 1.75 in. While theoretically a 3.5-in. diameter reader could have resulted in a slightly better response, the widely available 4.0-in diameter concrete cylinders molds were used to build the reader coil, thus, reducing the fabrication costs.

Furthermore, a 5-loop arrangement was selected for the reader coil resulting in a nominal self-resonant frequency equals to 6.0 MHz. The number of loops mainly controls the self-resonant frequency of the reader coil. Hence, it was selected to ensure that a sufficient difference in the frequency range exists between the uncorroded frequency of the NC sensor (less than 4.0 MHz) and the resonant frequency of the reader.

Table 3-1 summarizes the different components and design parameters that are used to fabricate a typical NC sensor and the external reader coil

Table 3-1: Summary of the NC sensor platform properties

Resonant Circuit	
Inductor	5-loop, 2.5-in. diameter coil fabricated using 18-AWG enameled copper wire
Capacitor	820-pF, C0G, high-quality, ceramic capacitor
f_{rc}	approximately 3.18 MHz
External Reader	
Inductor	5-loop, 4.0-in. diameter coil fabricated using 18-AWG enameled copper wire
Cable	3-ft BNC RG-58C/U coaxial cable
f_{reader}	approximately 6.0 MHz
Sacrificial Washer	
Material	low-carbon , cold-rolled, AISI 1010 steel
Geometry	2.75-in. outer diameter with inner diameter of 2.0 in. or 1.75 in.
Separation Distance	0.10-0.25 in.

3.3.5 Sensor Interrogation Techniques

A number of interrogation techniques can be used to acquire information from the embedded inductively coupled passive sensors. The most commonly used method relies on monitoring the change of electric impedance at the ends of the reader coil. The presence of a resonant circuit within the magnetic field of the external coil induces a current in the sensor coil which appears as reflected impedance on the external reader input port. The degree of change in impedance is influenced by the self-resonant characteristics of the sensor circuit. In order to extract information regarding the state of the sensor circuit, an AC frequency sweep is conducted and the phase angle of the impedance at the reader coil input port at each AC frequency value is measured. In this research work, the impedance measurements were performed using the Solatron 1260A Impedance Gain-Phase Analyzer. This is a bulky and heavy piece of equipment which is not ideal for field measurements. It also requires 6 – 7 minutes to acquire the response of a single NC sensor. The large size and low speed of the reader electronics reduces portability and can hamper routine structural inspections for corrosion in bridge decks. In addition, the equipment needed to conduct accurate impedance measurements is expensive and requires AC power source.

A reflectometer-based reader was developed by Trivedi et al. (2012). The novel reader employs a National Instrument 5641R IF Transceiver platform.. The method evaluates the ratio between the signal reflected from the sensor coil and the input signal through the use of a 3-port directional coupler. The measurements are conducted through an AC frequency sweep. At the resonant frequency of the sensor, the reflected signal strength is at its maximum producing a dip in the frequency spectrum. The method requires only few seconds to acquire the sensor response. Thus, the reader facilitates fast interrogations during routine inspections and the electronics of the reflectometer-based reader is portable and can be used to conduct handheld interrogations.

3.4 SENSITIVITY OF NC SENSOR PHASE RESPONSE TO THE INTERROGATION MEDIUM

The concrete in a typical bridge deck is expected to undergo extreme fluctuations in the ambient temperature and moisture levels. Hence, the reliable and successful deployment of the NC sensors in the field requires the senor signal to be insensitive to ambient variations in the surrounding medium. In other words, any detectable shift in the measured frequency response of an embedded NC sensor should be the result of corrosion accumulation on the sacrificial washer. In addition, because bridge decks are designed differently and have different clear covers, the dependence of the acquired sensor response on the read distance needs to be examined.

The sensitivity of the amplitude of the phase dip and resonant frequency to the read distance and the interrogation medium is illustrated in Figure 3-22. A hermetically sealed, 3.18-MHz, resonant circuit was interrogated in air, water, and salt water. The measurements were taken at read distances of 0.5, 1.0, and 2.0 in. Then, the resonant circuit was cast in an 8.0-in. concrete cube with a nominal cover of 1.0 in (Figure 3-23). After curing, the resonant circuit was interrogated when the concrete was totally dry and completely saturated. As expected, the interrogation medium had minimal effect on the measured phase dip. This is due to the relatively small magnetic permeabilities of air, water, and concrete. However, the phase dip decreased dramatically as the read distance was increased. At large read distances, the phase dip becomes indistinguishable from the ambient noise and the resonant circuit becomes undetectable. Pasupathy (2010) provides a detailed discussion regarding the effect of the read distance, interrogation medium, and circuit components on the measured phase dip. Recent developments in reader technology have enabled sensor interrogations at read distances as large as 8.0 in. (Trivedi, et al. 2012). On the other hand, the resonant frequency of the NC sensor depends on the circuit components; hence, it is insensitive to the interrogation medium or the read distance (Figure 3-22).

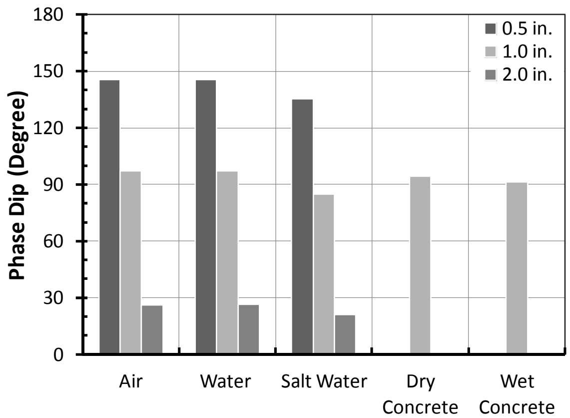

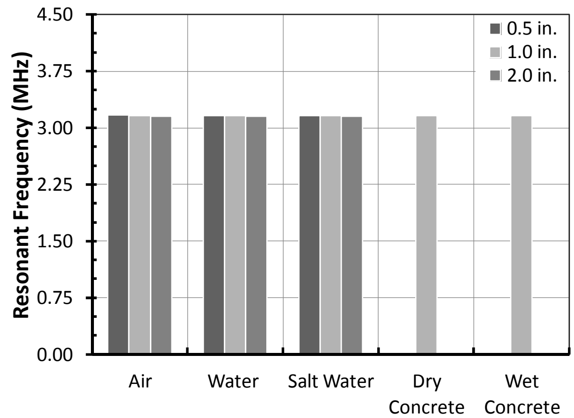

Figure 3-22: Measured phase dip (left) and resonant frequency (right) for a 3.16-MHz resonant circuit interrogated at different read distances and in different mediums.

The sensitivity of the sensor response to variations in temperature was evaluated using sensors embedded in 8-in. concrete cubes (Figure 3-23). The shift in response can be induced either by changes in the electric properties of the sacrificial element or the circuit components. Hence, two sensors were tested. The first had a 0.002-in. thick steel washer while the other was constructed without the sacrificial element.

Figure 3-23: NC sensors with and without sacrificial washer embedded in 8.0-in. cubes at a cover distance of 1.0 in.

The sensors were interrogated at two different concrete temperatures (100°F and 50°F). Figure 3-24 shows the measured response of the two sensors at the two different environments. For the sensor with a sacrificial washer, a reduction in resonant frequency of approximately 25 kHz was observed when the temperature increased to 100°F. However, the sensor with no sacrificial element experienced a frequency shift of only

5 kHz for the same temperature shift. The observed temperature related frequency shifts are negligible compared to the shift ensuing from changes due to the corrosion of the washer (shift from 3.70 to 3.18 MHz). The temperature induced shifts in frequency are the result of the small increase in the capacitance for both the sacrificial washer element and the resonant circuit due to temperature rise. Additionally, the phase dip amplitudes and the bandwidth values of the measured sensor responses do not change significantly due to temperature variations and the differences observed are within the noise margins of the interrogation equipment and set-up.

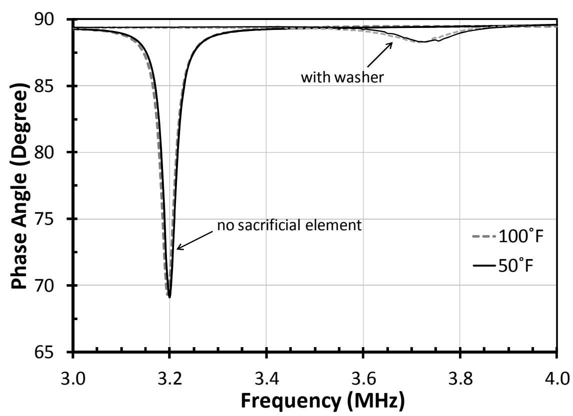

Figure 3-24: Change in phase response due to temperature for a resonant circuit with and without the sacrificial washer

3.5 Changes in Sensor Response Due to Corrosion of Sacrificial Washer

The NC sensor design employs a unique corrosion detection mechanism that relies on the increase in the apparent resistance of the sacrificial element. The reduction of the cross sectional area of the sacrificial element due to corrosion results in the resistance increase and alters the measured frequency response. As discussed in Section 3.2, the sensor response has two distinct limit states. The initial limit state corresponds to an uncorroded washer while the second limit state is indicative of a fully corroded sacrificial washer. Ideally, the measured response of the sensor at any point of time would be limited to one of the two limit states. However, corrosion of the sacrificial washer is a gradual process resulting in a transition phase between the two limit states.

In order to study the change in the frequency response due to corrosion build-up on the sacrificial washer, the change in frequency response of an NC sensor directly exposed to salt water exposure was examined. To this end, a sensor was fabricated using a 0.001-in. thick steel washer and was positioned inside a water tank. The sensor was submerged in 3.5% salt water solution for 3 days and then allowed to dry for 4 days. The sensor was interrogated and photographed at the end of each wet and dry period.

The change in frequency response due to the corrosion build up on the surface of the washer and photographs of the washer at different times are shown in Figure 3-25 and Figure 3-26, respectively. During the first 70 days of exposure, the phase response of the sensor remained unchanged and identical to the uncorroded state response. After the initial stability period, simultaneous changes in the resonant frequency, phase dip, and frequency bandwidth were observed, indicating the start of the transition period. The resonant frequency of the sensor decreased gradually and finally reverted back to the resonant circuit frequency (117 days in Figure 3-25). The phase dip initially decreased due to the increase of washer resistance. This was also accompanied by an increase in bandwidth indicating a larger system damping. At high corrosion levels, the phase dip increased dramatically reaching the original response of the resonant circuit alone.

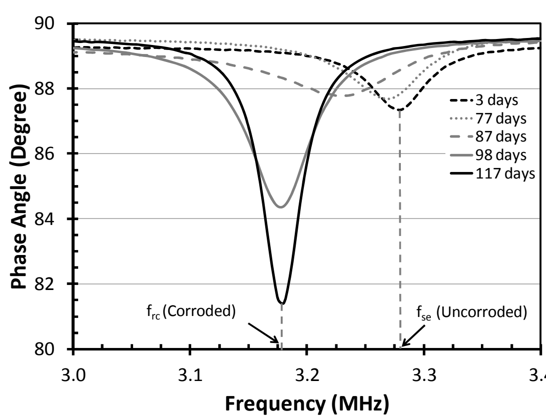

Figure 3-25: Measured phase response at 3, 77, 87, 98, and 117 days of exposure

4 days 53 days 88 days 102 days 158 days

Figure 3-26: Photographs of the corrosion accumulated on the sacrificial washer

Changes in measured resonant frequency with time are shown in Figure 3-27. It can be seen that the shift in frequency is gradual with three regions of response: uncorroded, transition, and corroded. In the uncorroded stage, the frequency remained constant and equal to the initial frequency. Then, the frequency decreased monotonically from the initial frequency (f_{se} = 3.28 MHz) to the final frequency (f_{rc} = 3.17 MHz). The resonant frequency remained constant thereafter. Slight fluctuations in the measured resonant frequencies were observed between consecutive wetting and drying periods. However, the fluctuations are minimal compared to the range of frequencies between the two limit states. A detailed discussion regarding the sensitivity of the NC sensor to variations in the surrounding environment is provided in Appendix C.

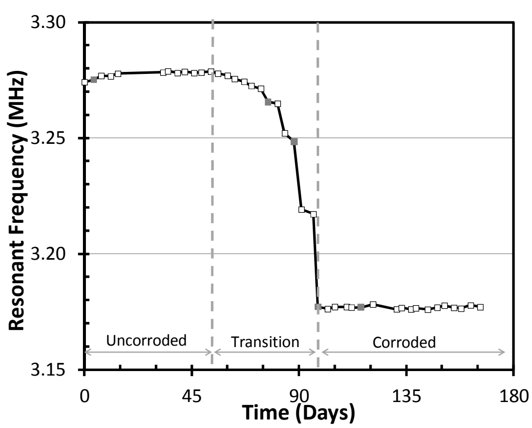

Figure 3-27: Measured resonant frequency of the sensor with time

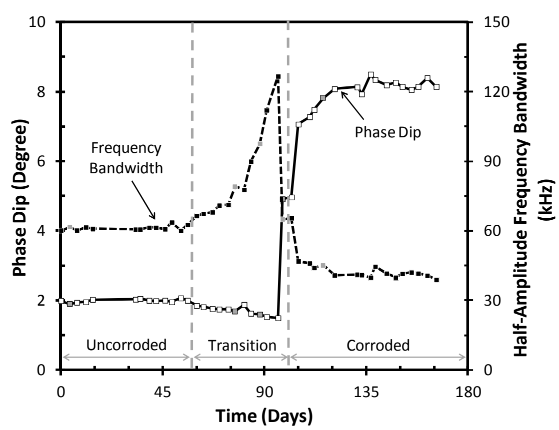

Figure 3-28: Measure phase dip and frequency bandwidth with time

The changes observed in the measured phase dip and the half-amplitude frequency bandwidth values with time are shown in Figure 3-28. The phase dip remained constant during the uncorroded stage and decreased slightly during transition (less than 0.5°). At the end of the transition stage, the phase dip value increased abruptly from 1.5° to 8° and become stable after that. The immediate increase in phase dip indicates that the resistance of the washer increased significantly due to corrosion and became very high, transforming the washer element into an open circuit. Similarly to the resonant frequency and phase dip, the frequency bandwidth was constant initially. However, the change in the measured bandwidth was not monotonic during the transition stage. The bandwidth values doubled gradually and decreased rapidly to a minimum after 117 days of exposure and remained constant in subsequent interrogations.

The results shown in Figure 3-27 and Figure 3-28 indicate that while the sensor reached the resonant frequency of the corroded state in approximately 98 days, the measured phase dip and frequency bandwidth values did not reach their corresponding stable corroded state values until 117 days of exposure. The monotonic nature of the shift in resonant frequency and the insensitivity of the resonant frequency to environmental variations and reading distance promote its use for indicating the state of the sensor.

3.6 SENSOR CIRCUIT MODEL

The initial parametric studies described in this chapter were limited by the commercial availability of the components used to fabricate the NC sensors. For example, the selection of the resonant circuit capacitor was limited by the quality of the commercial capacitors rather than its electric properties (Figure 3-11). In addition, the developmental nature of the parametric tests allowed only for testing discrete values for each circuit parameter. To this end, an electric circuit model was developed using a SPICE-based (Simulation Program with Integrated Circuit Emphasis) software (Sandler and Hymowitz 2006). Such simulation tools are used extensively by researchers and manufacturers of integrated circuits. SPICE models are the standard practice that is used to verify the circuit operation before mass-production (Sandler and Hymowitz 2006). Recently, circuit simulation suite providers have added features that enabled performing parametric evaluations and Monte Carlo analyses (National Instruments 2010). As a result, SPICE models became an integral part of the circuit development process as they provide insights into the entire spectrum of expected behavior of a circuit design prior to its manufacturing.

A circuit model was developed using National Instruments (NI) Multisim™ 11.0 suite. The model was used to evaluate the sensitivity of the frequency response of the NC sensor to variations in the design parameters. In addition, the model was used to simulate the measured changes in the sensor response due to the corrosion of the sacrificial washer. The NC sensor and the reader were modeled as RLC circuits. To incorporate the effects of the washer on the inductive coupling between the reader and the sensor, the washer element was idealized as an RL circuit. The mutual inductances between the reader-sensor, washer-sensor and reader-washer were defined using independent coupling factors. Figure 3-29 shows the circuit model used in the Multisim™ simulations. The frequency response was generated by sweeping different frequencies in the AC analysis module. The phase of the calculated impedance at the ends of the external reader inductor (L_r) was the primary analysis output.

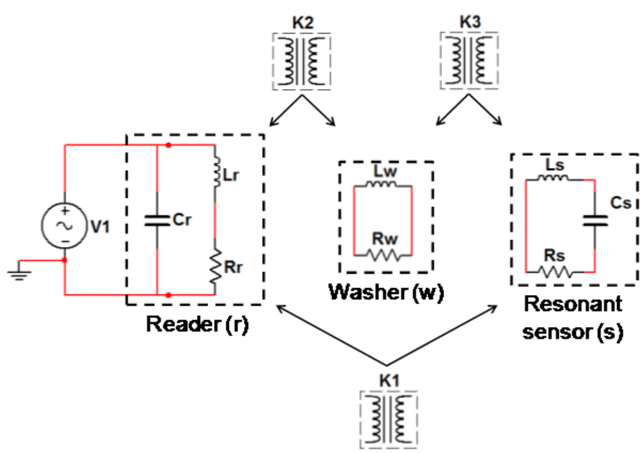

Figure 3-29: Circuit Model of the NC sensor platform

3.6.1 Calibration of the Model Components

The circuit values of the model parameters were selected to reflect the properties of the NC sensor used in the initial parametric studies. Hence, the numerical values were either calculated based on the geometry of the NC sensor prototype or were assigned based on the findings of Section 3.3. The phase responses in the corroded and uncorroded states for the NC sensor shown in Figure 3-8 were used to calibrate the circuit model. The parametric sensor had a 2.75-in. diameter sacrificial washer that was placed 0.25 in. away from the resonant circuit. The interrogations were conducted at a read distance of 1.5 in. The following sections explain the basis used to evaluate each of the model components.

3.6.1.1 External Reader Circuit

The reader coil parameters were calculated for a 5-turn coil with a 4.0-in. diameter made with 18-AWG enameled copper wire. The inductance of the reader (L_r) was calculated directly using Equation (3-2), which results in 6.95 μH. While the reader circuit does not include a built-up capacitance, the parasitic capacitance added by the 3-ft coaxial cable connecting the reader coil to the impedance analyzer was found to be substantial. Thus, a reader capacitance (C_r) of 100.3 pF was used and was assumed to include the influence of the coaxial cable and the parasitic capacitance of the reader coil and connectors. The reader coil resistance (R_r) was calculated based on the intrinsic material properties of enameled copper and the total length of the wire used to fabricate the coil (approximately 0.08 Ω).

Figure 3-30 compares the calculated phase response with the measured response. The response was generated by setting all the values of all the inductive coupling factors to zero ($k_1=k_2=k_3= 0$). It can be seen that the circuit model response closely mimics the measured response. Figure 3-30 (right) shows the comparison near the resonant frequency of the reader coil. The model accurately represented the measured value of the resonant frequency. Minimal deviations in the phase angle amplitudes (less than 2°) were observed in the measured response at frequencies less than 6.05 MHz and can be attributed to electromagnetic noise produced by the equipment.

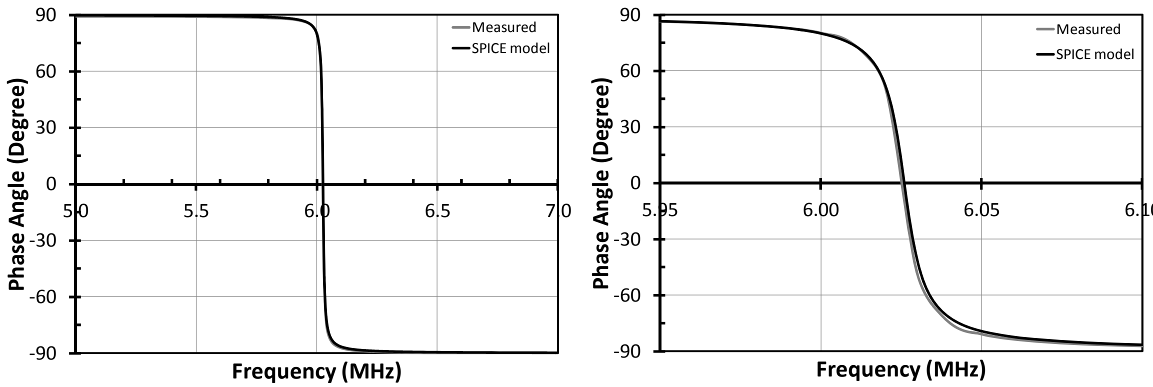

Figure 3-30: Comparison between the measured phase response of the external reader and the response calculated using the Multisim™ model (right is an enlarged plot of near resonance behavior)

3.6.1.2 Resonant Circuit of the NC Sensor

The circuit parameters of the resonant circuit were calculated for a 5-turn, 2.5 in. diameter coil fabricated using enameled copper wire. The inductance (L_s) was calculated using the coil geometry (3.08 μH). The value for the capacitance of the nominal resonant circuit (C_s) (820-pF) was selected to produce a corroded state frequency of approximately 3.18 MHz. The intrinsic resistance is expected to be relatively small and should include the influence of the wire and imperfect soldering. Hence, the resistance value was assumed to be 1.0 Ω.

The mutual inductance between the reader coil and the resonant circuit was evaluated in the SPICE circuit model by varying the coupling factor k_1. This value depends on the geometry and inductance of the reader and sensor coils, the interrogation medium, and the distance separating the two coils. Pasupathy (2010) concluded that the read distance has the strongest influence on the coupling factor where k_1 is inversely proportional to the cube of the separating distance.

A parametric analysis was conducted to evaluate the sensitivity of the response to the change in coupling. The frequency phase response of the reader-resonant circuit system was generated by setting the coupling factors corresponding to the sacrificial washer equal to zero (k_2=k_3= 0) and varying the value of k_1. Figure 3-31 shows the changes to the measured response due to the increase in the coupling factor. At k_1 equal to zero, the resonant circuit is assumed to be placed infinitely far from the reader coil and becomes undetectable. As the strength of coupling increase, the phase dip amplitude increases dramatically. However, as k_1 becomes greater than 0.6, the sensor response saturates reaching phase dip amplitudes of approximately 180º (Figure 3-32).

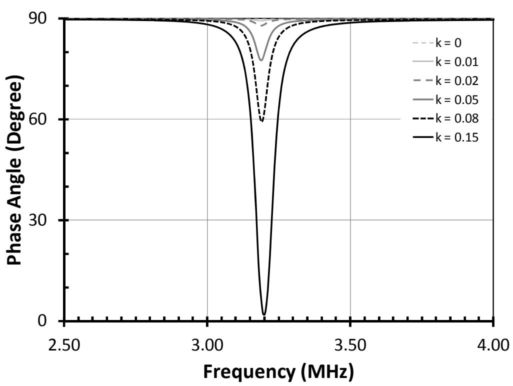

Figure 3-31: Simulated phase response curves for selected values of k_1

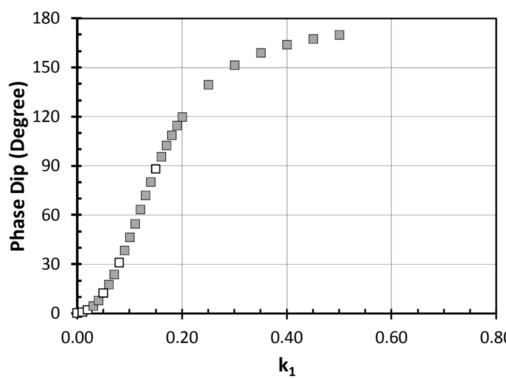

Figure 3-32: Change in phase dip amplitude due to k_1

For the parametric NC sensor under consideration, the coupling factor value was calculated using the Neumann formula (Pasupathy 2010, Andringa 2006). For a read distance of 1.50 in. and interrogations conducted in air, the calculated coupling factor was approximately equal to 0.10. Figure 3-33 compares the phase response obtained from the circuit model simulations with the measured response. It can be seen that for a coupling factor value of 0.10, the circuit model accurately approximated the resonant frequency of the circuit while underestimating the phase dip amplitude by more than 12°. Such difference in coupling estimates can be the result of numerous factors including inaccurate read distance measurements and errors in formula used to estimate the mutual inductance.

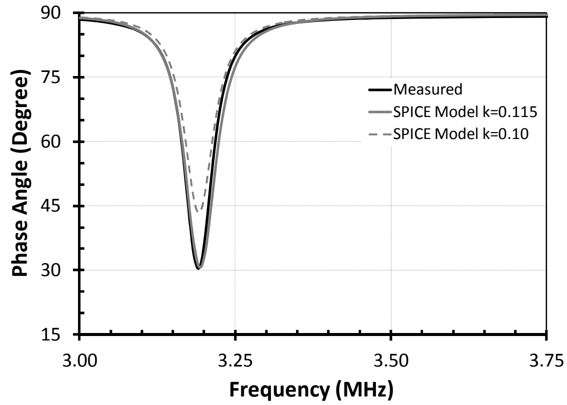

Figure 3-33: Comparison between the measured phase response of a 3.18-MHz resonant circuit and the response calculated using the Multisim™ circuit model

An optimization analysis was used obtain the value of the coupling factor that matches the measured phase response. The analysis indicated that a coupling factor of 0.115 produced an error in phase dip amplitude that is less than 0.5°. The resulting phase response estimated by Multisim™ was identical to the measured response; however, a 10 kHz shift in the resonant frequency of the NC circuit was still observed. The slight difference in frequencies can be attributed to the imprecise manufacturing of the ceramic capacitor (C_s) used to fabricate the resonant circuit.

3.6.1.3 Sacrificial Washer

The sacrificial washer was modeled as a simple RL circuit that is magnetically coupled to the inductors of the external reader and resonant circuit. The electric parameters were calculated for an intact AISI 1010 steel washer that is 0.001-in. thick and has outer and inner diameters of 2.75 and 2.00 in., respectively. The inductance of the sacrificial washer (L_w) was approximated by treating the washer as a single turn steel loop with a diameter equal to its average diameter. An inductance of 180 nH was calculated. Similarly, the resistance of the intact washer (R_w) was approximated for a single turn loop (0.17 Ω). However, the resistance of the sacrificial washer circuit was assumed to be variable and increase as corrosion developed on the washer surface.

The inductive coupling between the resonant circuit and the sacrificial washer (k_3) is an important parameter that affects the final design of the NC sensor prototype. This coupling is highly dependent on the separation distance between the two circuits and decreases rapidly as the separation distance increases. Figure 3-34 illustrates the effect of k_3 on the phase response of the sensor. At k_3 equal to zero, the simulated phase response is identical to the response of the NC sensor at the corroded state (f_{rc} =3.18 MHz). Hence, it is equivalent to the absence of the sacrificial washer. As the coupling factor increases, numerous changes in the measured response take place: (1) increase in the resonant frequency of the sensor, (2) reduction in the amplitude of the phase dip, and (3) increase in the half-amplitude bandwidth of the measured phase response.

It can be seen that for the design of a practical NC sensor, very large and very values of k_3 cannot be used. The small coupling produces a sensor with closely spaced limit states. Hence, the shifts in response due to environmental changes will become significant and the accurate interpretation of the state of the sensor can become impossible. In contrast, a relatively high level of inductive coupling between the sacrificial washer and the resonant circuit reduces the signal from the sensor and the embedded sensor becomes undetectable ($k_3 > 0.6$ in Figure 3-35).

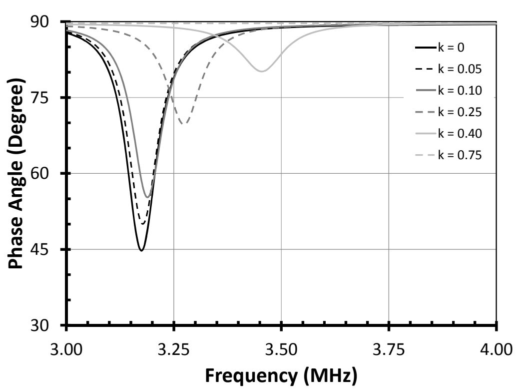

Figure 3-34: Simulated phase response curves for selected values of k_3

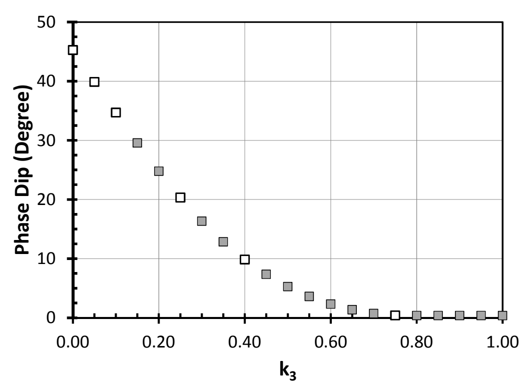

Figure 3-35: Change in phase dip amplitude due to k_3

For the calibration of the parametric NC sensor, the coupling factors controlling the mutual inductance between the washer and the reader circuit ($k_2 = 0.15$) and between the washer and the resonant circuit ($k_3 = 0.5$) were estimated using the Neuman formula (Andringa 2006). The values were calculated for a separation distance of 0.25 in. between the washer and the resonant circuit. Figure 3-36 compares the phase response obtained from the circuit model simulations with the measured response of the NC sensor. It can be seen that simulated response closely followed the measured response. However, minimal differences in the baseline curve and the resonant frequency were observed.

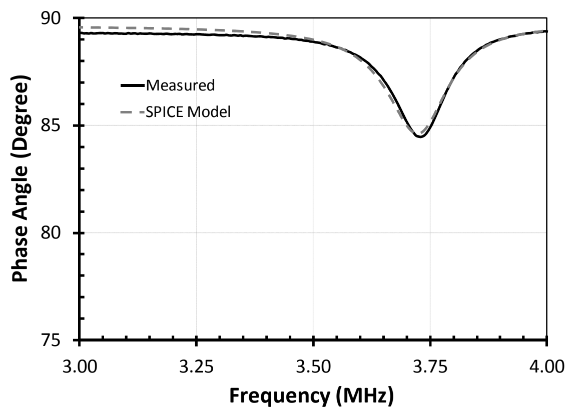

Figure 3-36: Comparison between the measured phase response of an NC sensor and the response calculated using the Multisim™ circuit model

The initial values for the electric components used in the NC sensor circuit model are summarized in Table 3-2.

Table 3-2: Electric components of the electric circuit model of the NC sensor

External Reader		Resonant Circuit		Sacrificial Washer	
L_r	6.95μH	L_s	3.08 μH	L_w	180 nH
C_r	100.3 pF	C_s	820 pF	C_w	-
R_r	0.08 Ω	R_c	1.0 Ω	R_w	0.17 Ω
k_1	0.115	k_2	0.15	k_3	0.5

3.6.2 Simulation of Corrosion Accumulation

The corrosion of the sacrificial washer causes significant changes of a number of parameters used to model the electric components in the SPICE model. Theoretically, the electric components of the reader coil and resonant circuit, along with the mutual conductance of the two elements, remain constant as corrosion develops on the sacrificial washer. Thus, corrosion induced changes are only expected to affect the electrical components of the sacrificial washer and mainly increase the resistance of the washer (R_w). Reduction in the inductance of the washer (L_w) also occurs due to corrosion. This reduction is expected to affect the values of the coupling factors (k_2 and k_3). Thus, the effect of corrosion on the inductance is a multi-variable phenomenon that cannot be evaluated using the circuit models developed. The finite element model described in Section 3.7 will be used to evaluate this phenomenon.

The effect of increasing only the resistance of the washer (R_w) on the frequency response is shown in the simulation results presented in Figure 3-37. It can be seen that the model successfully captures the trends observed experimentally for NC sensors with corroding washers. The resonant frequency decreased gradually and eventually reached the frequency of the resonant circuit (3.18 MHz). Furthermore, the simulations show analogous patterns of change in the phase dip and bandwidth. The DC resistance (0.18 Ω) of the uncorroded washer was used as a starting value for R_w. The results also indicate that an increase in the washer resistance of over three orders of magnitude is needed to alter the sensor response from the uncorroded state to the corroded state (≈ 1 kΩ).

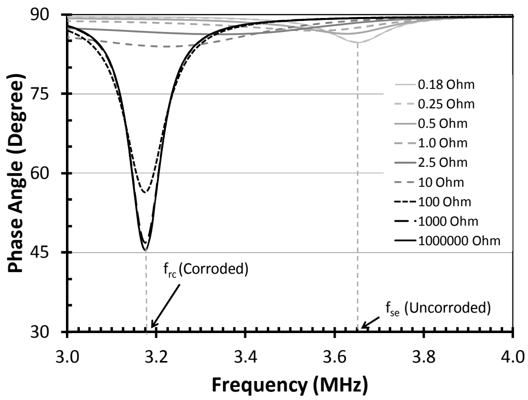

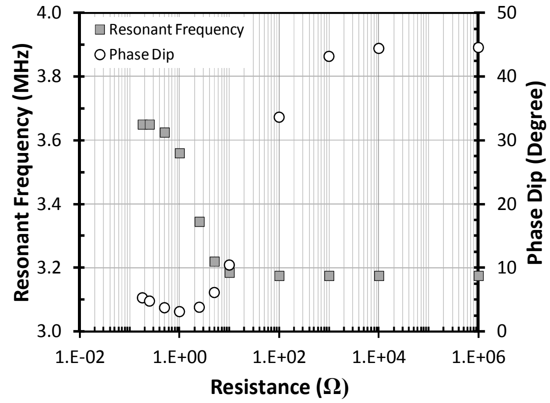

Figure 3-37: Simulated frequency response results for different washer resistance (R_w) values

Figure 3-38: Resonant frequencies and phase dip amplitudes obtained from simulation for different R_w values

Figure 3-38 plots the resonant frequencies and phase dip amplitudes extracted from the simulations using different R_w values. The patterns follow the same trends observed in the results of the accelerated corrosion test (Section 3.5). The resonant frequency remained constant for resistance values less than 0.25 Ω and shifted gradually to the corroded state, which was reached when the resistance of the washer was equal to approximately 10 Ω. The resonant frequency remained constant for all resistance values higher than 100 Ω.

The phase dip amplitudes decreased initially and reached a minimum of 3.1°. The minimum phase dip amplitude value is critical for the development of a reliable external reader. By optimizing the signal to noise ratio for an external reader, the detectability of an NC sensor with a known minimum signal strength (phase dip) can be ensured. The subsequent increase in the resistance of the washer dramatically increased the phase dip which reached amplitude of 43° at R_w equal to 1000 Ω. However, the rate of phase dip increase became modest for higher washer resistance values. The phase dip amplitude only increased by 1.4°, even though the resistance of the sacrificial washer increased by three orders of magnitude (from 1000 to 10^6 Ω).

The circuit model can also be used to evaluate the state of the sacrificial washer of an NC sensor embedded in concrete. Figure 3-39 is a spectrograph of the measured frequency responses of an NC sensor exposed to accelerated corrosion testing while Figure 3-40 shows the simulated change in the response of the NC sensor model due to resistance increase. It can be seen that the model reflected the same trends of the measured response. Unlike the discrete nature of the measured data, the model results were smooth and the transition region was continuous and easily distinguishable. In field applications, the characteristics of the frequency response measured for an embedded NC sensor can be used to approximate the resistance of the washer at the time of the reading. Thus, the model can be used to provide an indication of the state of the washer and the rate of corrosion activity.

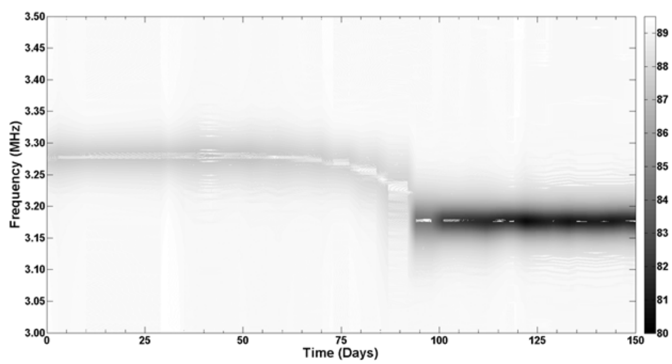

Figure 3-39: A spectrogram of the measured response of NC sensor exposed to accelerated corrosion exposure

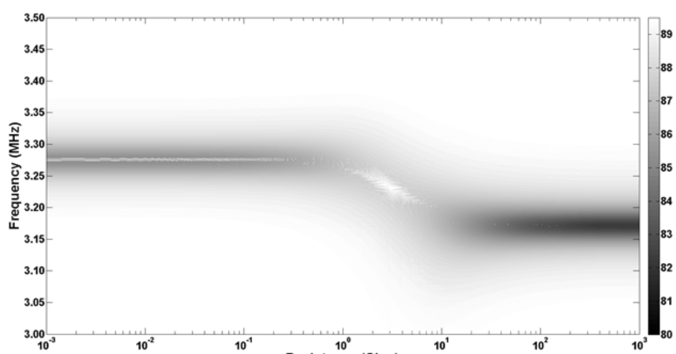

Figure 3-40: A spectrogram showing the changes in the simulated response of the NC sensor due to the increase of the resistance of the sacrificial washer

3.7 FINITE ELEMENT MODEL

The circuit model of the NC sensor provides a powerful tool that enables evaluating the effect of the different circuit parameters on the measured response of the NC sensor. The model can be used to examine the general trends that control the design of the NC sensor and understand the changes in measured response of an embedded sensor. In addition, the model can be used to determine the optimum component values, such that the response of the sensor is reliable and easy to detect. However, the extracted component values cannot be directly translated into physical parameters. In addition, the values of the electrical inductance of the external reader (L_r), sacrificial washer (L_w), and resonant circuit (L_s) can only be approximated. Furthermore, the inductive coupling coefficients of the three-circuit system cannot be accurately evaluated without calibrating the model using measured phase response data. The calibration process can be tedious and highly dependent on the accuracy of the calibration measurements. In order to address the limitations of the circuit model, a low-frequency electromagnetic finite element model was developed. The FE model is used mainly to evaluate the inductive coupling characteristics of the NC sensor platform.

Electromagnetic finite element (FE) assessments have been used extensively for the design of transformers and electric motors (ANSYS Inc. 2010). Recently, researchers have employed FE simulations for the design and optimization of inductively coupled coils (Felic, Ng and Skafidas 2013, Birdsell, Park and Allen 2004, Ota, et al. 2012, Marschner, et al. 2008, Engel and Rohe 2006). The work reported was primarily directed toward improving the signal strength between coupled coils and extending the range of wireless power transfer. Hence, the FE model of NC sensor will allow for conducting parametric studies that can lead to a better sensor design. The FE model allows each component of the NC sensor to be evaluated thoroughly and provides unlimited flexibility in the selection of component parameters. This is important, because the initial development of the NC sensor relied primarily on commercially available components and predefined dimensions (capacitors, sacrificial elements types and geometries, and coils).

3.7.1 Description of the Finite Element Model

The NC sensor model was developed using the ANSYS Low-Frequency Electromagnetic suite (ANSYS Inc. 2010). This commercial suite allows for dynamic interaction between the finite element model representing the inductive components and a circuit model containing the remaining electric circuit components. Thus, any modifications made in the FE model directly affect the characteristics and the behavior of the whole circuit.

Figure 3-41 shows a schematic of the electric circuit model used to study the NC sensor. The initial values of resistance and capacitance for the three circuits are modeled in the electric circuit and were based on the initial design parameters listed in Table 3-2. However, the values of the inductance and coupling coefficients were evaluated in an external inductance sub-circuit. The inductance sub-circuit was solved using the finite element method. Hence, the electric circuit and the inductance sub-circuit are dynamically linked and are mutually dependent. The electric circuit model was developed using ANSYS Simplorer® software (ANSYS Inc. 2012) and the model was used to perform the AC frequency sweep analyses.

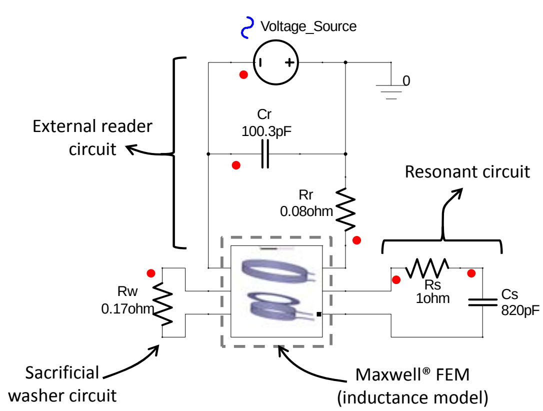

Figure 3-41: Schematic circuit model of the NC sensor including the link to the inductance FE model

The inductive coils of the reader and the resonant circuit along with the sacrificial element were all modeled using ANSYS Maxwell®. This high-performance FE software employs Maxwell's equations to solve electromagnetic field problems within a finite region (ANSYS Inc. 2010).

The geometry of the coils representing the reader and resonant circuit inductors was based on the initial NC sensor design described in Table 3-1. Hence, the reader and resonant circuit inductors were modeled as 5-loop enameled copper wire spirals with a constant pitch of 0.06 in. and nominal diameters of 4.0- and 2.5-in., respectively. The sacrificial washer was modeled as a toroid generated by rotating a 0.5-in. wide and 0.01-in. deep rectangle around the Z-axis. Hence, the ensuing shape was a 0.01-in thick steel washer with external and internal diameters of 2.75 and 1.75 in., respectively. The separation distance between the sacrificial washer and the resonant circuit was set at 0.2 in. and a read distance of 1.0 in. was selected for the analysis. The three model components were concentrically aligned.

The size of the analysis region is critical to the accuracy of the FE analysis. If the region modeled is too small, the stronger magnetic fields generated by the coils will be interrupted, which can affect the final results. On the other hand, if the region modeled is too large, the results will be better. But the computation time is increased dramatically. Based on the recommendations of the software developers, the analysis region was defined as a 6x5x5 in. cube with its centroid coinciding with the center of the topmost loop of the reader coil. In order to provide an electrical link that connects the FE model to the output of the Simplorer® circuit model, the reader and resonant circuit coil wires were extended to reach the edge of the analysis region. The electric linkage to the sacrificial washer circuit was formed by creating an internal boundary surface at the intersection between the washer volume and the YZ-plane. Figure 3-42 and Figure 3-43 provide a three-dimensional, side and top views of the geometry of the finite element model indicating the relative size of the analysis region and the position of the different components.

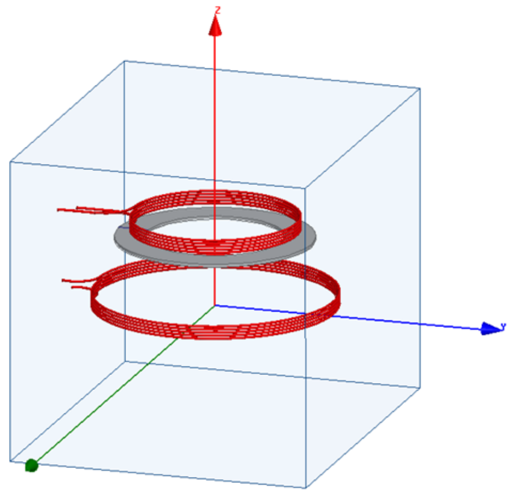

Figure 3-42: 3D view of the Maxwell® finite element model showing the reader and resonant circuit coils, and the sacrificial washer

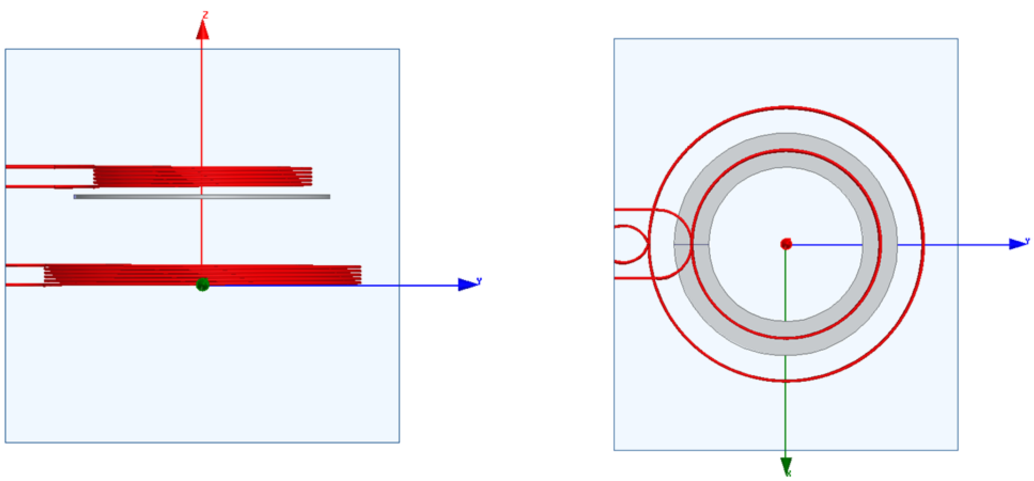

Figure 3-43: Side and top views of the Maxwell® finite element model showing the reader and resonant circuit coils, and the sacrificial washer

The electromagnetic material properties were selected from the ANSYS Maxwell® material database. The inductor coils were defined as enameled copper wire and the sacrificial washer was assigned the electromagnetic properties of low-carbon steel. The interrogation medium (analysis region) was selected to be air, which is expected exhibit an electrochemical behavior that is identical to a concrete medium.

Maxwell® contains an adaptive meshing algorithm that refines the FE mesh automatically to optimize the performance and accuracy of results. The algorithm performs either a skin depth-based or a length-based seeding and refines each model accordingly. The skin-depth meshing limits the size of each tetrahedral element that is located on an exterior surface of a component to the skin depth of the component material at a predefined AC frequency. Hence, both inductors and the sacrificial washer in the NC sensor model were meshed on skin-depth basis with an AC frequency of 3.0 MHz. The analysis medium was meshed using the length-based algorithm with the maximum edge size of 0.25 in. Figure 3-44 shows a view of the finite element mesh of the XZ plane. The mesh at the surface of the washer and the reader coil are also shown.

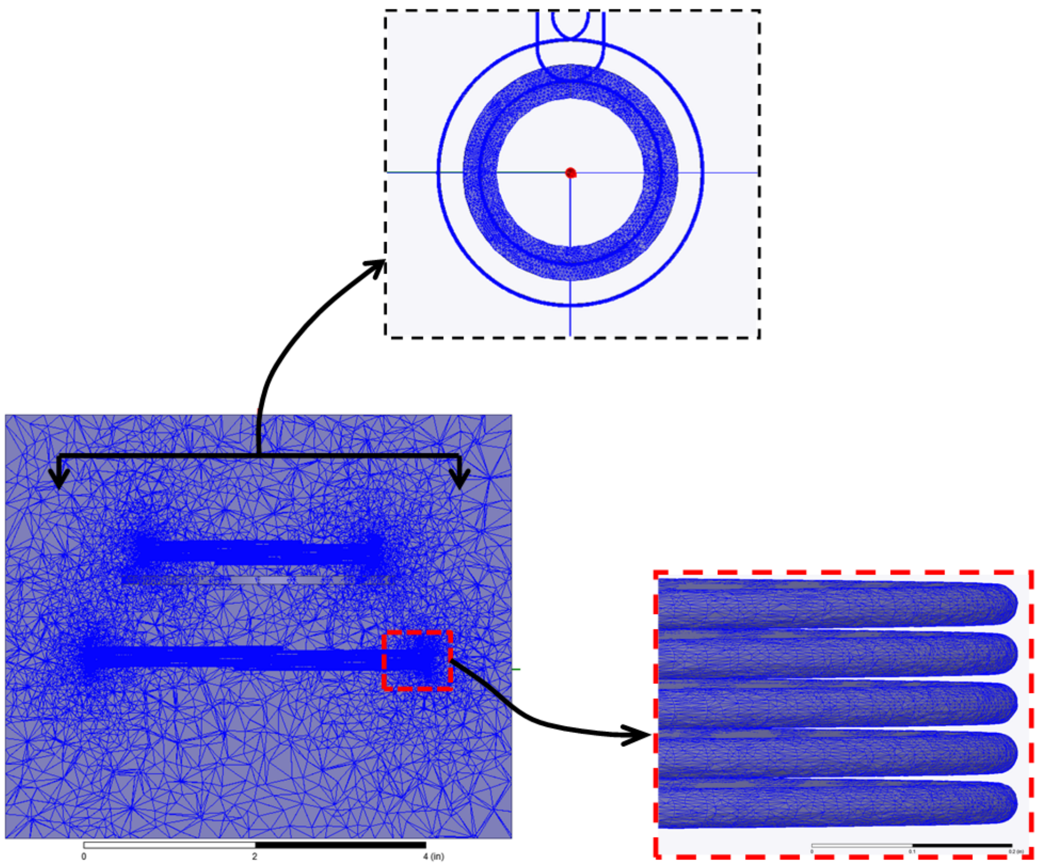

Figure 3-44: Finite element mesh of a cross-section along the XZ plane

3.7.2 Finite Element Model Results

The results of the FE model can be used to better understand the shielding effect imposed by the sacrificial washer. Figure 3-45 shows the distribution of the magnetic field magnitude in the XZ plane with and without the presence of the sacrificial washer. The analysis was conducted at an AC frequency of 3.15 MHz (the resonant frequency of the resonant circuit). It can be seen that the presence of the washer altered the field distribution and reduced the interaction between the two coils. Due to its proximity to the resonant circuit, the sacrificial washer had a higher impact on the fields surrounding the resonant circuit compared with the reader coil. The contour plot indicates that the presence of the washer forced the interaction between the two coils to be limited to the region within the internal diameter of the washer. Furthermore, the field intensity indicates that a region with extremely weak magnetic fields formed immediately below the bottom surface of the washer.

Similar observations can be seen in the vector plots of the magnetic field shown in Figure 3-46. The figure demonstrates that the presence of the metal washer altered the uniformity of the generated magnetic field. Furthermore, the washer forced the inductive coupling to shift around the washer surface.

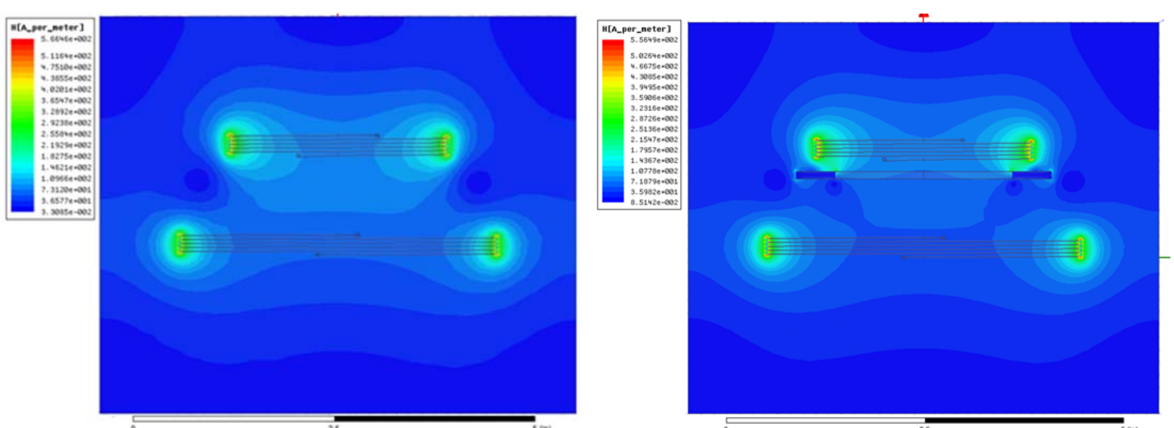

Figure 3-45: Magnitude of the magnetic fields for the NC sensor without (left) and with (right) the sacrificial washer

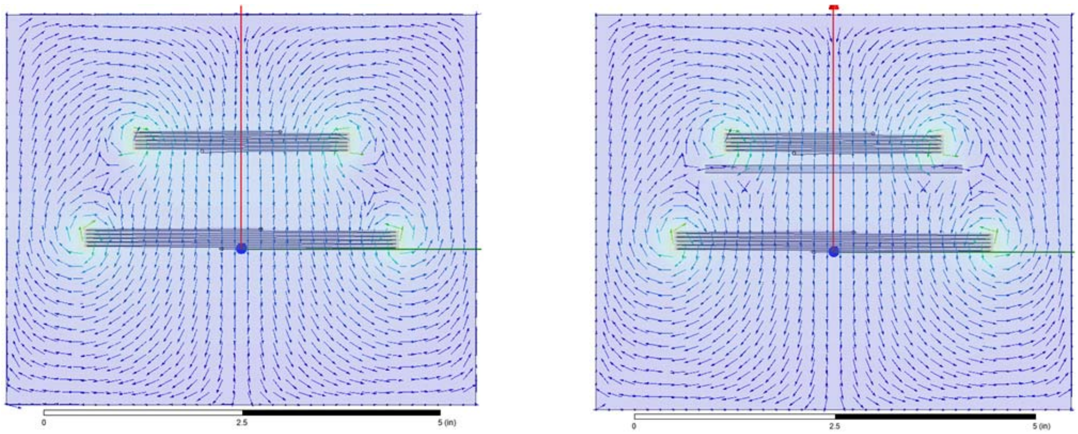

Figure 3-46: Vector plot of the magnetic fields for the NC sensor without (left) with (right) the sacrificial washer

The FE model described above provides a powerful tool that enables the optimization of the NC sensor. While the initial experimental studies provided insight regarding the general trends, the dependency on commercially available components limited the range of variables that could be tested. To this end, the coupled circuit and FE models were used in two parametric studies to examine the effect of the washer geometry on the phase response of the NC sensors.

First, the effect of the washer diameter on the response of the senor was examined. The thickness and width of the sacrificial washer were kept constant while the inner diameter was increased. Figure 3-47 shows plan views of the FE models for two different washer diameters.

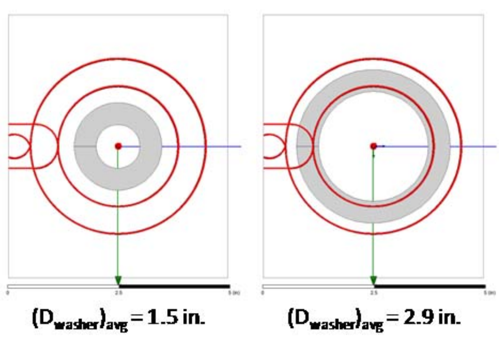

Figure 3-47: Top views of the FE models used to measure the response due to the presence of a 1.5-in (left) and 2.9-in. average diameter washers

Figure 3-48 plots the resonant frequencies and phase dip amplitudes extracted from the calculated phase response from the FE model. The coupling between the washer and the resonant circuit was highest when the diameter of the washer (D_{washer}) was approximately equal to the diameter of the coil in the resonant circuit (D_{rc}). This coupling translates into a larger shift in the resonant frequency when the sacrificial element is present and deeper phase dip. For washers with an average diameter less than 0.8 D_{rc} or greater than 1.25 D_{rc}, the change in frequency response due to the presence of the washer is minimal (frequency shift of less than 5%) and a phase dip less than 2°.

These results indicate that a sacrificial washer with an average diameter equal to that of the resonant circuit will cause the greatest shift in measured response, which gives the sensor two limit states that are well separated and can be easily distinguished. However, the results presented are only applicable for a read distance of 1.0 in and a separation distance of 0.2 in. between the washer and the resonant circuit. While, a washer with an average diameter of D_{rc} is favorable for these conditions, at greater read distances a washer of this size can reduce the phase dip drastically, which severely limits sensor detection. Thus, the FE model should be used to examine the optimum washer diameter for the expected read range.

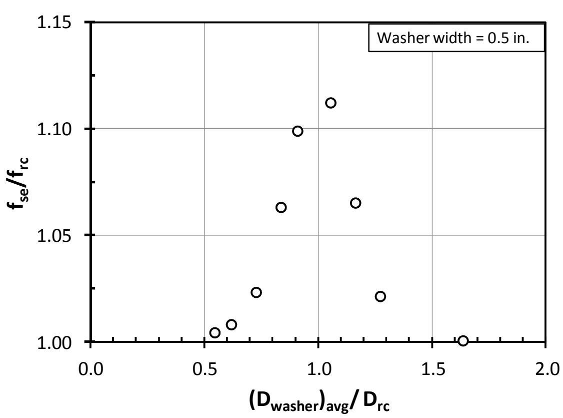

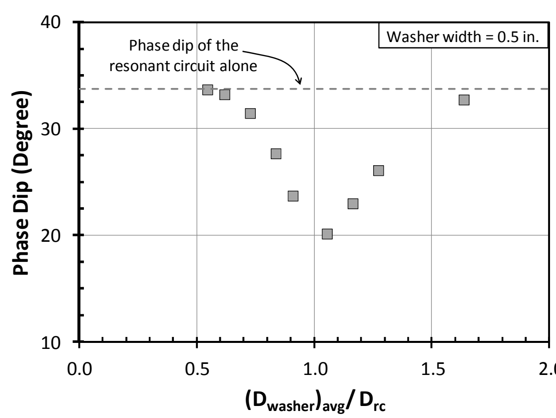

Figure 3-48: Sensitivity of resonant frequency (left) and phase dip amplitudes (right) of the NC sensor to the change in the average diameter of the sacrificial washer

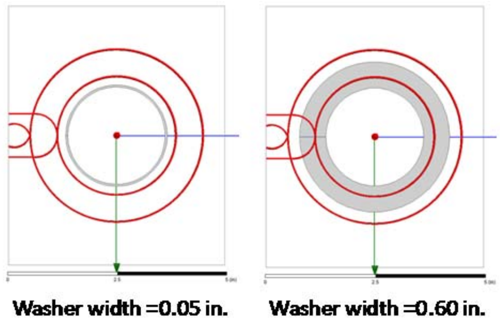

Figure 3-49: Plan views of the FE models used to measure the response due to the presence of 0.05-in (left) and 0.6-in. wide washers

The effect of the washer width on the response of the senor was also examined. The inner diameter of the washer was kept constant at 2 in. while the outer diameter was increased. Figure 3-49 shows plan views of the FE models for the cases of 0.05 and 0.60-in. wide washers. The results of the parametric analyses (Figure 3-50) indicate that increasing the washer width increases the shielding, which translates to higher resonant frequencies and lower phase depths. The shielding effect was minimal for washer widths below 0.1 in. In addition, the shielding effect seems to plateau at washer widths larger than 0.9 in. due to constant magnetic field leaking through the center void of the washer.

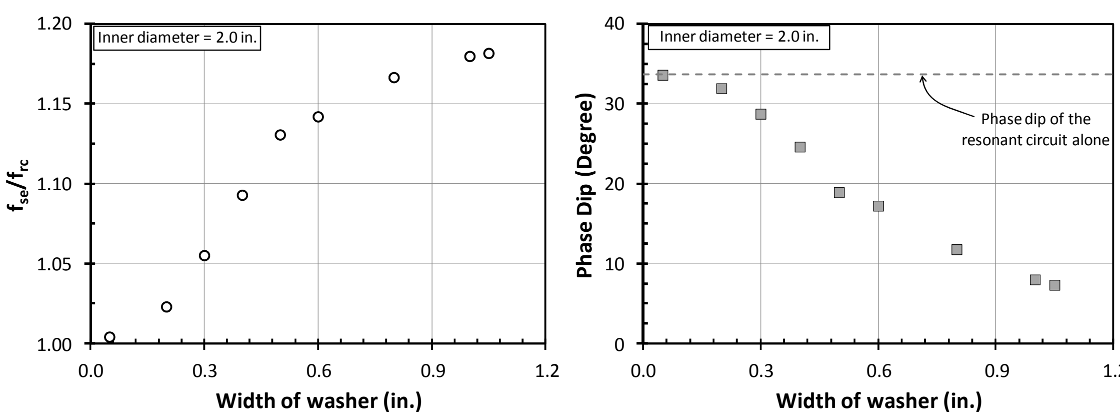

Figure 3-50: Sensitivity of resonant frequency and phase dip amplitudes of the NC sensor to the change in the width of the sacrificial washer

3.8 SUMMARY

A novel NC sensor design was developed at UT Austin. The sensor relies on the contact-free magnetic interaction between a resonant circuit and a sacrificial corroding element. The corrosion is interrogated in a wireless manner using the inductive coupling between the embedded sensor and a mobile external reader. The sensor exhibits two limit states that correspond to either an intact sacrificial element or a fully corroded one. The sensor response is represented by measuring the impedance of an AC frequency sweep across the reader inductor. It was concluded that while the phase response provides a wealth of information regarding the senor state, the measured resonant frequency provides a reliable and robust parameter that is insensitive to both the environmental variations and the read distance. In addition, the sensor response was found to be insensitive to variations in the surrounding medium and the ambient temperature. Hence, any detectable shifts in the sensor response are expected to be the result of corrosion accumulation on the sacrificial element.

The basis for selecting the different design components of the NC sensor was discussed in this chapter and an initial senor prototype was developed. However, the initial development was limited by the commercial availability of the different sensor components. To this end, an electric circuit and electromagnetic finite element models were developed. The models were used to evaluate the changes in the sensor response due to changes in the circuit parameters and better understand the mechanisms leading to the signal shift. Furthermore, the initial analytical results indicate that the finite element model provides a powerful developmental tool that can be used to optimize the performance of the NC sensor. The model can also be used to evaluate sacrificial elements of different morphologies and geometries. It also can be used to assess the feasibility of integrating multiple sacrificial elements in a single sensor for a multi-threshold sensor design.

CHAPTER 4
Electrochemical Evaluation of the Sacrificial Corroding Element

4.1 OVERVIEW

Corrosion of reinforcing steel in concrete is an electrochemical process that is highly dependent on the chemical composition of the steel and the oxidizing conditions within the concrete medium. Numerous factors can affect the oxidizing conditions in concrete, including temperature variations, moisture fluctuations, and the chloride content levels. The reliability of the embedded Non-Contact (NC) sensor relies primarily on the selection of sacrificial corroding elements that exhibit electrochemical properties and corrosion tendencies similar to those of the adjacent reinforcement. Consequently, the response of the sacrificial element to changes in the conditions within concrete will mimic the response of the reinforcing bars. If the response of the sacrificial corroding element does not mimic the response of the adjacent reinforcement, the sensor readings will range from misleading to meaningless.

The sacrificial washers used to fabricate the NC sensor are made from sheets of cold-rolled AISI 1010 steels. Thus, the washers have a chemical composition and metallurgical arrangement that is different from reinforcing steel. As a result, the two steels cannot be assumed to have similar electrochemical properties. To this end, an electrochemical investigation examining the corrosion characteristics of washer and rebar samples was conducted. The linear polarization resistance and potentiodynamic polarization techniques were used to evaluate the corrosion response of samples immersed in different mediums. The mediums were selected to replicate electrochemical conditions expected within reinforced concrete members.

Section 4.2 contains a review of the electrochemical aspects of corrosion in reinforced concrete and a description of the methods employed to evaluate the corrosion characteristics of the sacrificial element. The experimental program is described in Section 4.3 and the investigation results are discussed in Section 4.4.

4.2 Electrochemical Aspects of Corrosion Within RC Structures

The electrochemical nature of corrosion implies that in order for the chemical reactions to take place, a transfer of electrons is needed. Consequently, the corrosion of embedded reinforcement consists of four partial processes that occur simultaneously on the surface of the rebar: the anodic process where the iron metal oxidizes losing electrons and forming free ions (Equation 4-1), the cathodic process where the electrons are consumed by oxygen reduction and forming rust (Equation 4-2), the flow of the iron ions through the concrete pore solution from the anodic regions to the cathode, and finally, the circuit is completed by the transport of the electrons released at the anode to the cathodic region through the metal (Figure 4-1).

$$\boldsymbol{Fe \longrightarrow Fe^{+2} + 2\,e^{-}} \qquad \textit{Equation 4-1}$$

$$\boldsymbol{2\,H_2O + O_2 + 4\,e^{-} \longrightarrow 4\,OH^{-}} \qquad \textit{Equation 4-2}$$

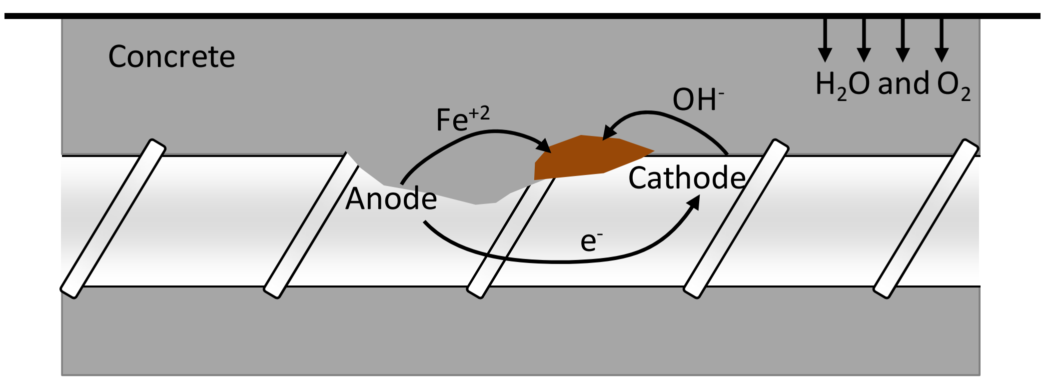

Figure 4-1: Schematic representation of the corrosion process of steel in concrete

4.2.1 Corrosion Thermodynamics

A principal concept of corrosion thermodynamics states that materials always seek the lowest energy state. Active metals are thermodynamically unstable and tend to form oxides that are more stable for each specific medium (Jones 1996). In reinforcement corrosion, the free iron ions combine with the hydroxyl ions produced at the cathodic reaction or the available oxygen to form rust. The type of rust species formed depends on the pH levels of the concrete medium and the concentrations of oxygen and hydrogen. Figure 4-2 shows the Pourbaix diagram of iron and indicates the areas where each rust species is thermodynamically stable. The dashed lines, a and b, show the potentials at which hydrogen and oxygen evolve, respectively. For a concrete with a pH value of 13.5, it can be seen that Fe_2O_3 and Fe_3O_4 oxides form creating the passive protective layer over a wide range of potentials. Changes in the concrete pH due to carbonation or the increase of chloride levels can alter the thermodynamic balance and shift the system into an area in the diagram where corrosion becomes active.

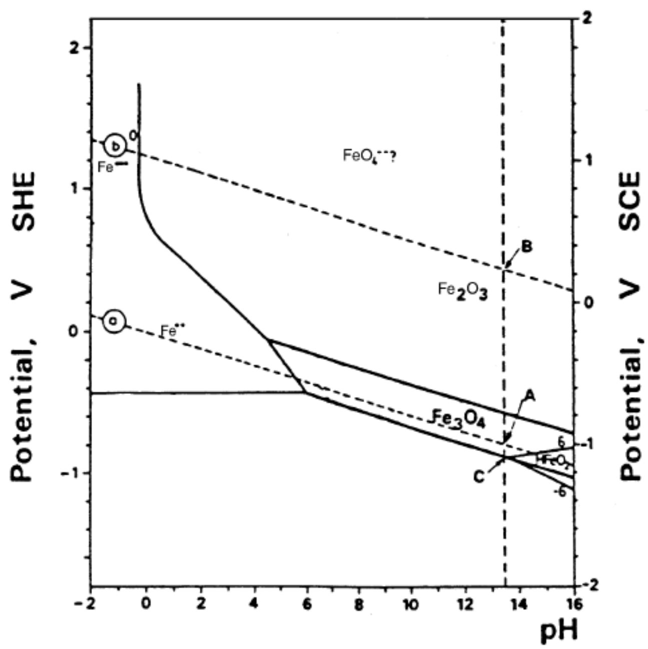

Figure 4-2: Pourbaix diagram of iron in an aqueous solution (ACI 222R 2010)

The potential of an electrochemical reaction indicates the ease of electron transfer from the metal to the surrounding medium and, hence, electrochemical potential is a function of the metal/medium interface. In electrochemical studies, the absolute value of the potential cannot be measured easily; hence, the reaction potential is typically measured with respect to some reference electrode. Saturated Calomel Electrode (SCE) is typically used in laboratory applications.

4.2.2 Corrosion Kinetics

The anodic and cathodic reactions are half-cell reactions that occur at their respective equilibrium potentials. In the absence of passivity, the relationship between the change in the half-cell equilibrium potential and the ensuing current is described by the Butler-Volmer equation (Jones 1996). The current produced in an electrochemical cell is exponentially related to the potential change, as follows;

$$i = i_0 \left(e^{2.3 \frac{\eta}{\beta_a}} - e^{-2.3 \frac{\eta}{\beta_c}} \right)$$ ***Equation 4-3***

where,

i = current density

i_0= exchange current density between products and reactants at equilibrium.

η = overpotential defined as the difference between the applied potential, E, and the equilibrium potential, E_0.

β_a and β_c = Anodic and cathodic Tafel constants or the slope of the each leg in the Evans diagram.

Figure 4-3 shows the Butler-Volmer relationship and its parameters for a single half-cell reaction.

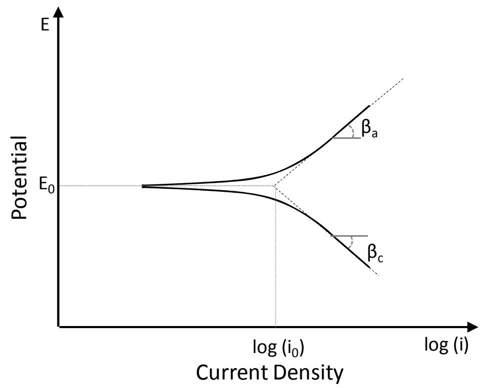

Figure 4-3: Schematic plot of the Butler-Volmer Equation.

When the anode and cathode are connected, an electrochemical cell is formed and current flows through the cell. As a result, the oxidation and reduction reactions deviate from their equilibrium potentials towards a common corrosion potential, E_{corr}. The mixed system exhibits corrosion potentials, E_{corr}, and current density, i_{corr}, that represent the corrosion activity of the electrochemical cell. Figure 4-4 shows the how the anodic and cathodic equilibrium conditions change when corrosion is active. It can be seen that when corrosion occurs and current flows between the anodic and cathodic areas, the potential of the anode increases in the noble direction and the potential of the cathode decreases into more negative value. The shift in electrochemical potential due to the passage of current is defined as polarization. This phenomenon is commonly called the mixed potential theory and it is only applicable in ideal conditions where there is no passivity or external factors limiting the ion concentrations (Bertolini et al. 2004).

Changes in the environmental conditions surrounding the metal can alter the equilibrium conditions for the anodic reaction, cathodic reactions, or both. As a result, the corrosion potential and current density of the mixed reaction change accordingly. Figure 4-5 shows the effect of different oxidation conditions on the corrosion kinetics. For example, an increase in the electrolyte temperature can move the anodic reaction to lower potentials and move the equilibrium state from point a to point c leading to higher corrosion rates and more active potentials.

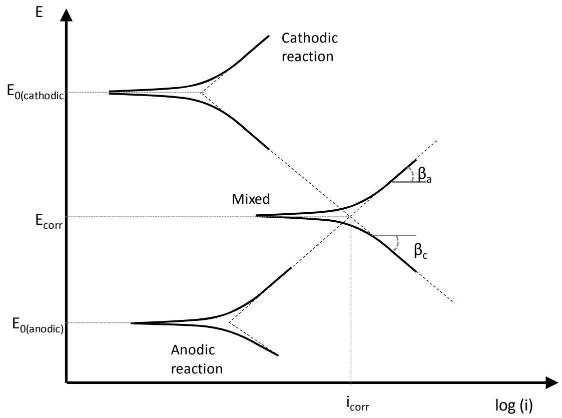

Figure 4-4: Schematic illustrating the mixed potential theory

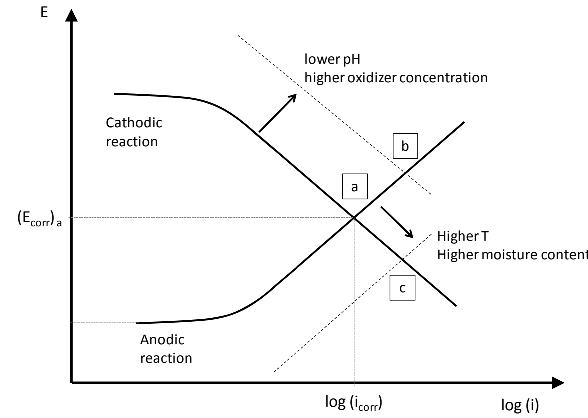

Figure 4-5: Schematic illustrating the effect of the changes in medium conditions on mixed potential theory reactions

4.2.3 Electrochemical Evaluation Techniques

Electrochemical test methods are used extensively to understand and study numerous corrosion phenomena (Thompson and Payer 1998). The techniques are used to evaluate different material alternatives, determine the parameters controlling a specific corrosion process, or monitor the effectiveness of a corrosion control system. The tests are quick and are inexpensive to conduct. The tests are particularly useful in examining the corrosion behavior of a sample over a wide range of oxidizing conditions within a single environment. Furthermore, some electrochemical tests can be used to provide real-time measurements of the instantaneous corrosion rates and can be used monitor the conditions of structures that are in-service.

In order to examine the electrochemical properties of the sacrificial steel washer and reinforcing steel, linear polarization resistance (LPR) and potentiodynamic tests were conducted. Both tests are typically used to compare the performance of different materials and their susceptibility to corrosion in certain environments. Both tests are performed by polarizing the examined specimen in the anodic and cathodic directions.

This is achieved by applying a sufficient electric current to change the equilibrium corrosion potential. The potential is changed in a stepped manner using a high impedance potentiostat while the current is continuously monitored. A reference electrode is used to assess the change in corrosion potential of the working electrode (specimen). The electric current is applied through a counter electrode (graphite rods). The three electrodes are placed in an electrochemical cell that contains a conductive electrolyte representing the environment under consideration (Figure 4-6).

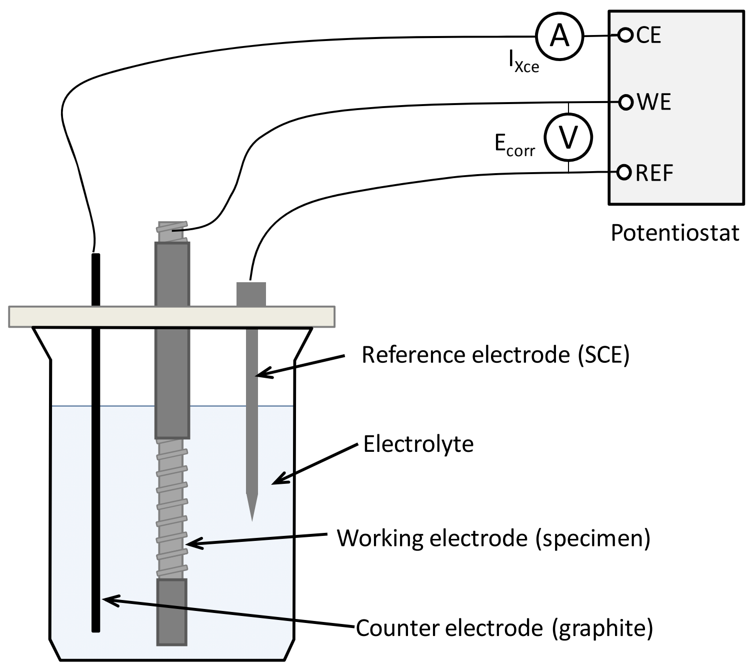

Figure 4-6: Schematic of the electrochemical cell and test set-up

4.2.3.1 Cyclic Potentiodynamic Test

The cyclic potentiodynamic test evaluates the corrosion behavior of a metal under a wide range of oxidizing conditions. In addition to the equilibrium corrosion rate (i_{corr}) and half-cell potential (E_{corr}), the test can indicate regions of passivity and the critical potential where the breakdown of the passive film takes place and pitting corrosion occurs (E_{pit}). The test is also used to obtain the anodic and cathodic Tafel slopes of a metal.

The potentiodynamic test is conducted using high impedance Potentiostat that increases the reference potential monotonically while monitoring the current needed to maintain the instantaneous equilibrium. The scan starts in the cathodic region ($E < E_{corr}$) and the potential is increased monotonically in the anodic direction. The scan is started at a potential that is 100 mV more negative than the equilibrium corrosion potential. The upper scan limit is selected based on the pH value of the electrolyte solution and using the Pourbaix diagram of the alloy under consideration (Figure 4-2). For example, for a steel sample immersed in a solution with a pH of 13.50 (dashed line in Figure 4-2), an upper potential limit of 225 mV vs. SCE is selected to prevent oxygen evolution in the electrochemical cell (point B). When the potentiodynamic scan reaches the upper limit, the scan direction is reversed to examine the degree of pitting that has taken place during the test and the potential for repassivation. Due to the high polarization levels, the potentiodynamic test is considered to be destructive and is limited to laboratory experiments (Thompson and Payer 1998).

The polarization scan rate can adversely affect the quality of the results obtained from the potentiodynamic test. It was observed that faster scan rates produce higher currents for the same potentials leading to incorrect corrosion rate estimates (Thompson and Payer 1998). It is desirable to select a scan rate that can reflect the steady state conditions within concrete. However, slow scans can take months to conduct and the electrochemical cell can change significantly during that time and become unrepresentative of the original test conditions. Poursaee (2010) examined the effect of scan rate on the polarization of reinforced concrete members and suggested a scan rate of 0.167 mV/sec. The same rate is suggested by the ASTM G5 standard.

Figure 4-7 shows a polarization curve of a reinforcing bar specimen indicating the parameters that can be extracted from the test. The equilibrium corrosion potential (E_{corr}) is identified as the potential where the applied current is a minimum (E_{corr} = -641 mV). The equilibrium corrosion density can be extracted using the Tafel extrapolation methods (i_{corr} = 1.01µA/cm^2). The sample shown exhibits a region of passivity where an increase in potential does not require additional applied current (-400mV < E < -100mV). In this region, the Butler-Volmer relationship is not applicable. At potentials higher than E_{pit} (-100 mV), the passive layer breaks down and pitting commences starting the transpassive region of the curve. After the potentiodynamic scan reaches the upper potential limit (E_{max} = 200 mV for electrolyte with a pH=13.75), the scan direction is reversed to examine the degree of pitting that has taken place during the test. If the reversed scan resulted in a hysteresis, pitting is assumed to have occurred and the size of the hysteresis loop is often related to the amount of pitting(Tait 1994) (Kujur and Bhattacharjee 2011). For example, the passive layer is assumed to be broken and pitting has taken place in Figure 4-7 because the currents measured during the reversed scan were higher than the original direct scan. However, if the reversal currents were smaller than the original currents, the passive layer is assumed to be stable and pitting was halted. Repassivation is assumed to take place if the reverse scan intersected the polarization curve within the anodic region.

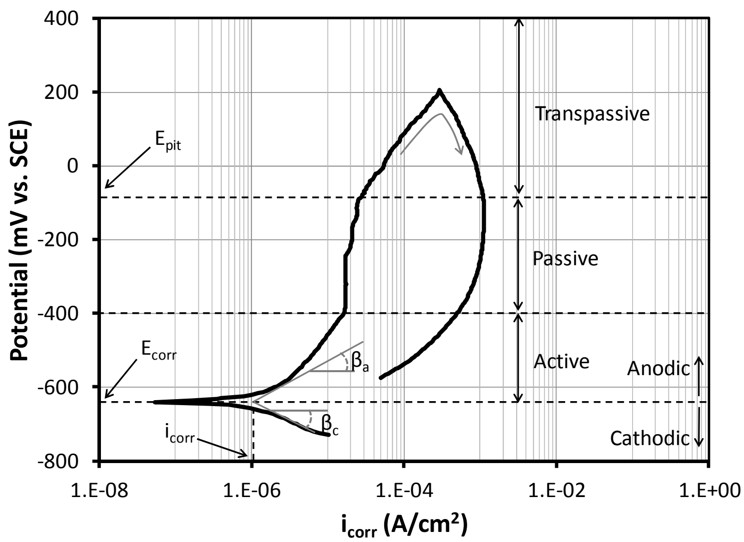

Figure 4-7: Polarization curve of a reinforcing bar sample showing the electrochemical parameters

4.2.3.2 Linear Polarization Resistance Test

The LPR technique is a non-destructive test that measures the corrosion rate and corrosion potential within an electrochemical system. The technique allows for a direct and simple comparison of the corrosion rates of different metals exposed to the same corrosive conditions. The corrosion rates obtained using the LPR test are instantaneous and only reflect corrosion behavior at the state of equilibrium. Hence, changes in the corrosion behavior due to variations in the metal ion concentrations, oxygen content, chloride levels or moisture levels cannot be examined directly using the LPR method.

The LPR method utilizes the approximate linearity in the polarization behavior at potentials near the equilibrium state (Stern and Geary 1957). The linear proportionality between the potential and the polarizing current is approximate and only applicable within 10-30 mV of the equilibrium corrosion potential. The ratio between the change in the overvoltage and the change in current within the linear portion is defined as the polarization resistance, R_p (Figure 4-8). The corrosion current is inversely proportional to the polarization resistance and can be calculated using the Stern-Geary relationship,

$$R_p = \left[\frac{\Delta E}{\Delta I_{app}}\right]_{\Delta E \to 0} = \frac{\beta_a \beta_c}{2.3\, i_{corr}(\beta_a + \beta_c)} \qquad \textbf{\textit{Equation 4-4}}$$

where,

β_a and β_a are the anodic and cathodic Tafel slopes given in volts per decade of current,

i_{corr} is the corrosion current density in A/m^2,

and R_p is the polarization resistance with units of Ω m^2.

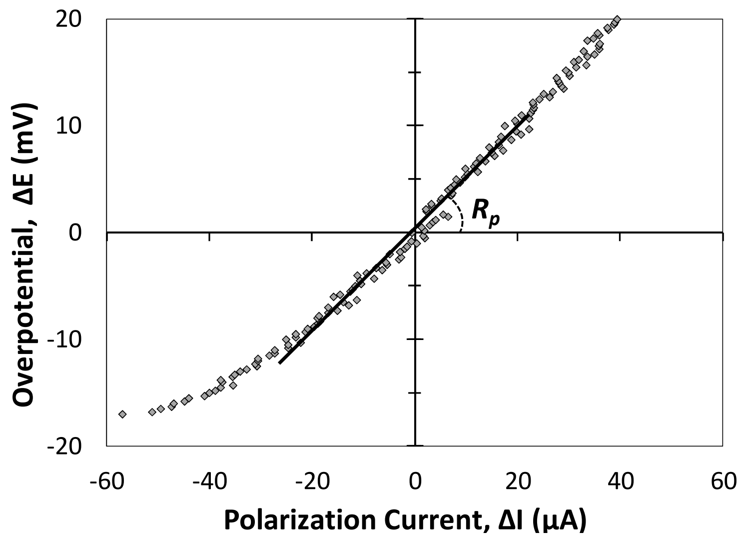

Figure 4-8: Typical linear polarization resistance plot

4.3 EXPERIMENTAL PROGRAM

While the sacrificial washers and the reinforcing bars are manufactured using low-carbon steels, their chemical composition and metallurgical structure are not the same. A chemical composition analysis of rebar and washer specimens was conducted by Chicago Spectro Service Laboratory, Inc. The samples were examined in accordance with ASTM E1019 and ASTM E415 and the results of the chemical composition analysis are summarized in Table 4-1. The results indicate that the reinforcing steel contains higher percentages of nickel, chromium, and copper. Those alloys tend to improve the corrosion resistance of low-carbon steels (Foroulis and Uhlig 1964; Jones 1996). Furthermore, the metallurgical properties and the crystalline structures are different for the cold-rolled washers and the hot-rolled rebar. Hence, the corrosion tendencies for the sacrificial washers and the rebar cannot be assumed identical and need to be examined.

Table 4-1: Chemical composition of the reinforcing bar and the sacrificial washer (%)

Element	C	Mn	P	S	Si	Ni	Cr	Mo	Cu	Va	Al	Fe
Reinforcing Bar	0.29	0.71	0.026	0.028	0.14	0.13	0.20	0.06	0.33	0.024	-	Bal.
Washer	0.12	0.31	0.01	0.01	0.01	0.04	0.02	0.01	0.04	-	0.031	Bal.

4.3.1 Specimen Preparation

Reinforcing bar sections and sacrificial washer specimens were evaluated using the linear polarization resistance and the cyclic polarization techniques (Figure 4-9). The steel reinforcement specimens were 12-in. long sections cut from a #4 deformed rebar. In order to eliminate the boundary effects and to ensure a uniform corrosion behavior, the ends of the rebar samples were coated with epoxy resin producing an exposed length of 4 in. (Figure 4-10). Furthermore, the top of the rebar section was left exposed for the electrical connection.

The sacrificial washers used in the fabrication of the NC sensors are produced from low-carbon, cold-rolled AISI 1010 steel. The washers used in this evaluation had a 1.75-in. inner diameter and a 2.75-in. outer diameter. The samples were partially epoxied to prevent any extraneous effects resulting from polarizing the electric connection (Figure 4-10). The epoxy resin was applied to half the surface area of the washer resulting in an exposed surface area of approximately 9.5 cm^2.

Mammoliti et al. (1996) demonstrated that the surface condition of the steel rebar specimens used in laboratory corrosion tests can affect the results tremendously. The study showed that metallographically polishing or mechanically grinding the rebar specimens led to higher corrosion resistance that is not representative of embedded reinforcement. Hence, the samples used in this evaluation were tested in their as-received condition. However, the samples were degreased by light immersion in acetone followed by immersion in distilled water to improve the reproducibility of the measurements.

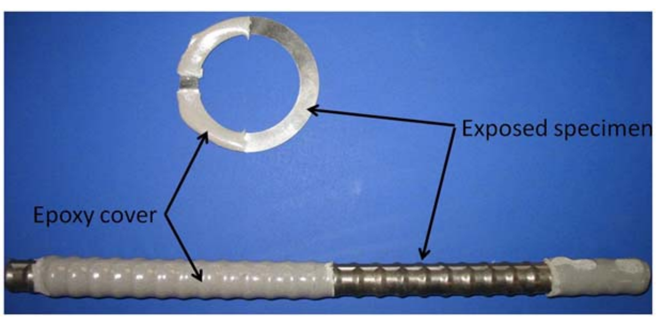

Figure 4-9: Reinforcing bar and sacrificial washer specimens

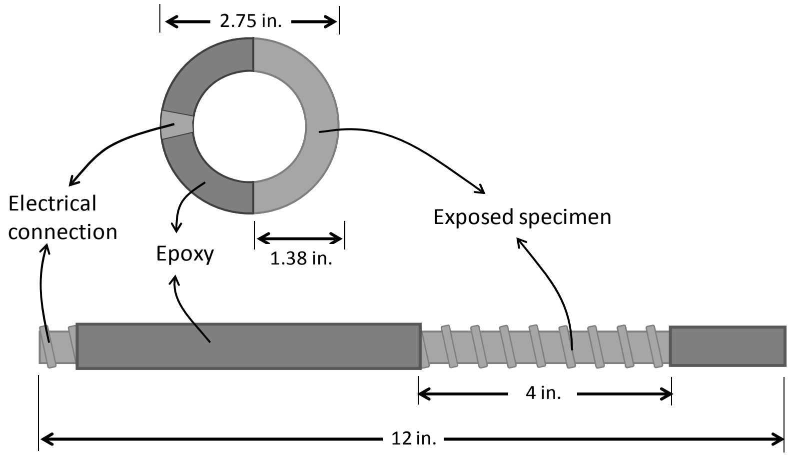

Figure 4-10: Schematic showing the dimensions of the reinforcing bar and sacrificial washer specimens

4.3.2 Electrochemical Cell and Equipment

The electrochemical cell used in this investigation was illustrated in Figure 4-6 and the cell components can be seen in Figure 4-11. The three-electrode cell consists of a 2.5-L cylindrical beaker with a 0.25-in. thick acrylic cover. The acrylic cover was not air tight and was only used to provide fittings that hold the electrodes in place. A gel-filled saturated calomel electrode (SCE) was used as the reference electrode. The stability of the SCE electrode was checked regularly by measuring the voltage difference between the electrode and a second reference electrode that was stored throughout the duration of the experiments.

Two 0.25-in. diameter and 10-in. long graphite rods were used as the counter electrodes. The rods were positioned on either side of the working electrode allowing for a uniform current distribution over the exposed surface area of the rebar or washer. The size of the rods was selected to ensure that the counter electrode was large enough to allow for sufficient current to flow and drive the electric potential of the rebar or washer to the desired maximum scan limit.

The cell electrodes were connected to an EG&G Model 273A Potentiostat through a control cell. The data were acquired using a TRI-Star data acquisition system. The measurements were conducted at a scan rate of 0.167 mV/sec and the post-measurement calculations and data interpretation were executed through EG &G Model 342 software. The electrochemical evaluation tests were conducted at the laboratories of the Department of Mechanical Engineering.

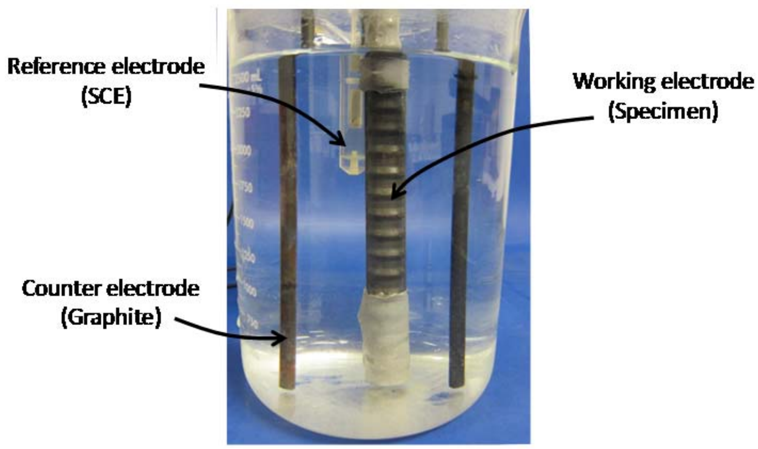

Figure 4-11: Electrochemical cell used for the tests

4.3.3 Test Environments and Electrolyte Solutions

The significance and accuracy of the information and conclusions obtained from any electrochemical evaluation depend on the ability to mimic the conditions in real life applications. Due to the high electric resistance of concrete, conducting the electrochemical evaluations on samples embedded in concrete is unreliable, costly, and highly variable. To this end, simulated pore solutions that have chemical compositions similar to that of the concrete have been used extensively in the literature to evaluate corrosion behavior of embedded reinforcing steel. In this study, five solutions were used to assess the corrosion tendencies of the washer and rebar samples. The solutions were prepared using deionized water and reagents ingredients. The selected environments are discussed in the following paragraphs.

4.3.3.1 Simulated Concrete Pore Solution

Portland cement concrete pore solution consists mainly of saturated calcium hydroxide ($Ca(OH)_2$). Numerous studies of rebar corrosion used saturated $Ca(OH)_2$ alone to simulate the concrete medium (Gonzalez et al. 2007; Blanco, Bautista, and Takenouti 2006). However, recent studies have shown that the addition of sodium hydroxide (NaOH) and potassium chloride (KOH) to the electrolyte better represents the actual concrete medium (Hansson 1984; Goni and Andrade 1990; Lianfang and Sagues 1999; Poursaee and Hansson 2007; Poursaee and Hansson 2009; Poursaee 2010). The addition of those elements increases the pH levels to approximately 13.3 and improves the stability of the passive film structure. Furthermore, by adjusting the concentrations of the NaOH and KOH, different concrete mixtures can be simulated. The composition of the simulated concrete pore solution used in this test series (Table 4-2) was based on the pore solution extracted from Type I cement paste samples with w/c=0.42 (Poursaee 2010). The pore solution had a pH of 13.26, hence, the upper limit of anodic polarization was set as 250 mV vs. SCE.

Table 4-2: Chemical composition of the simulated concrete pore solution

Solution	$Ca(OH)_2$	NaOH	KOH	$CaSO_4$	pH
Simulated Concrete Pore Solution	Sat.	0.1 M	0.3 M	0.002 M	13.26

Based on the results of Raman Spectroscopy analysis and continuous half-cell monitoring, Pourasee and Hanson (2007) recommended a curing period of at least 7 days for reinforcing bars in simulated concrete pore solution. In order to ensure the formation of a stable and strong passive film, the samples were cured in the pore solution for at least three weeks before being tested. During the three-week curing period, the corrosion cells were checked regularly for their electrolyte levels and replenished with distilled water to keep the concentrations constant.

4.3.3.2 Simulated Carbonated Concrete Solution

Corrosion of steel reinforcement in concrete structures is typically the result of chloride contamination. However, carbonation of the concrete can also induce corrosion damage within concrete. Carbonation occurs due to the infiltration of CO_2 and moisture into the concrete and the ensuing consumption of $Ca(OH)_2$ to produce carbonate and bicarbonate. The transformation leads to a reduction of the pH levels (from 13.5 to approximately 9.0) resulting in the formation of a weak and unstable passive layer (Bertolini et al. 2004; Broomfield 2007).

The carbonation process is slow and hard to test in reinforced concrete specimens. Hence, simulated carbonated concrete solution is often used in literature to assess the corrosion behavior within carbonated concrete (Moreno et al. 2004; Huet et al. 2005). The composition of the simulated carbonated concrete solution used in this study is described in Table 4-3. The solution contains high levels of carbonate and bicarbonate. Using the simulated carbonated concrete solution, Moreno et al. (2004) has reported the formation of an extensive breakdown of the passive film on the surface of the steel reinforcement due the low pH levels.

Table 4-3: Chemical composition of the simulated carbonated concrete pore solution

Solution	$NaHCO_3$	$NaCO_3$	pH
Simulated Carbonated Concrete Pore Solution	0.3 M	0.1 M	9.01

In order to mimic the conditions leading to the carbonation induced corrosion damage of in-service reinforced concrete structures, the specimens were initially cured in the simulated concrete pore solution for three weeks. Thus, the specimens were allowed to form a stable protective passive film. Then, the specimens were immersed in the carbonated concrete solution for a week to allow ample time for the breakdown of the passive film.

4.3.3.3 Deionized and Salt Water Solutions

The NC sensor design allows the use of sacrificial elements of different thicknesses which in turn allows the detection of multiple levels of corrosion damage. However, the effect of the additional cold-working used to produce thinner washers was found to affect the corrosion behavior of low-carbon steels (Furolouis 1964). Hence, washers of different thicknesses were evaluated in deionized (DI) water, 1% salt water, and 3% salt water electrolyte solutions. While performing electrochemical evaluations in salt water is not representative of the behavior within concrete, it allows for a direct comparison of washers exposed to different levels of cold-working. These solutions also eliminate any additional variables that might be raised by the formation of passive films. For comparison, steel rebar samples were also tested in the salt water solutions.

4.3.3.4 Cement Mortar

Reinforcing steel and sacrificial washer samples were embedded in mortar and examined using the potentiodynamic test (Figure 4-12). The dimensions of the mortar samples are shown in Figure 4-13. Both specimens were partially epoxied to prevent non-uniform behavior near the mortar boundaries. The mortar was mixed using Type I Portland cement with a w/c of 0.45. The steel rebar samples were cast in a 3.0-in. diameter cylinder and had a uniform clear cover of approximately 1.2 in. The washer samples were embedded in 2.4 x 2.4 x 3.0 in. mortar cubes. The dimensions of the washer mortar samples were selected to obtain the same clear cover distance from the edge of the mortar to the surface of the washer. The samples were wet cured for 28 days and then left to dry at room temperature. The samples were later immersed in 3% salt water solution for one week before being tested.

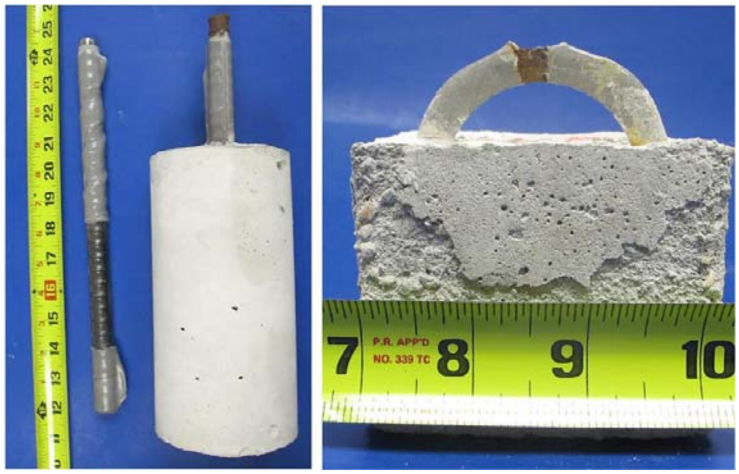

Figure 4-12: Steel rebar (left) and sacrificial washer (right) specimens embedded in mortar.

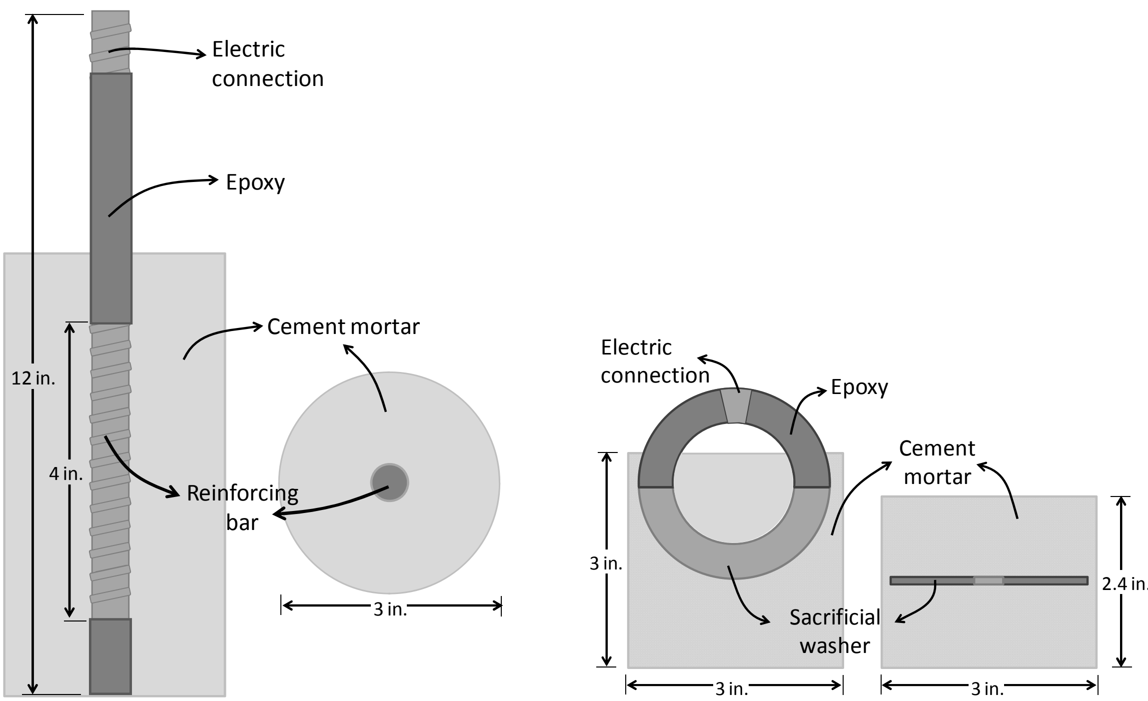

Figure 4-13: Cross-sections and plan views of the steel rebar (left) and sacrificial washer (right) specimens embedded in mortar.

4.3.3.5 *Specimens Extracted from the Long-Term Exposure Test*

A long-term experimental program was conducted to evaluate the reliability of the NC sensor and examine its ability to detect corrosion in reinforced concrete structures. The details of the long-term tests are presented in Chapter 6. The sensors were embedded in reinforced concrete slab sections and were continuously exposed to salt water or tap water solutions for 19 months. At the end of the exposure period, the slabs were autopsied and the condition of the sensors and the adjacent rebar was documented (Chapter 7). Some of the sensors were embedded in regions that had limited exposure to chlorides. As a result, their sacrificial elements remained intact throughout the test period.

Four intact sacrificial washers and the adjacent reinforcing bar sections were extracted from the slabs to evaluate their electrochemical behavior. The samples can be divided into two groups. The first group includes specimens extracted from slabs that experienced cyclic exposure to tap water (T). While the rebar samples had the same dimensions, the washers were either 0.001-in. or 0.002-in. thick and were labeled T1 and T2, respectively. The sacrificial washers of sensors T1-7 and T2-7 were used in the electrochemical evaluation tests. The average chloride content of concrete powder samples extracted 2 in. away from the sacrificial washers evaluated ranged between 55 and 97 ppm. These values are significantly lower than the suggested critical chloride content of 500 ppm (ACI 222R 2010).

The second group of samples experienced exposure to 3.5% NaCl solution (S), hence, had a higher risk of corrosion. The sacrificial washers of sensors S1-8 and S2-7 and the adjacent reinforcing bar sections were used in this series of tests. The concrete powder samples collected in the vicinity of the salt water specimens had chloride contents of 704 and 1507 ppm for the S1-8 and S2-7 specimens, respectively.

The samples were epoxied and degreased as described in Section 4.3.1. Concrete pieces collected from the region surrounding the selected washers were immersed in deionized water for 21 days. The filtered solution had a pH of 13.37 and was used as the electrolyte in the electrochemical cells.

This set of specimens provides the most accurate representation of the conditions within reinforced concrete structures. Both the sacrificial washers and the reinforcing bar samples developed a stable passive film structure in concrete and remained unaltered for a long period of time.

Table 4-4 summarizes the curing details and the exposure of the specimens for each test environment.

Table 4-4: Summary of the curing conditions and test electrolytes used for each test environment

Solution	Curing	Chloride Addition	Test Electrolyte
Concrete Pore Solution	Three weeks in the concrete pore solution	3% NaCl added one day before testing	Concrete pore solution with or without NaCl
Long-term Concrete Pore Solution	Three months in the concrete pore solution	3% NaCl added one day before testing	Concrete pore solution with or without NaCl
Carbonated Concrete Solution	Three weeks in the concrete pore solution followed by one week in the carbonated concrete solution	0.2% NaCl added one day before testing	Carbonated Concrete pore solution with or without NaCl
Salt Water Solution	No Curing	NaCl added one hour before testing.	Deionized water or salt water
Cement Mortar	Wet curing for 28 days and then drying at room temperature.	Immersed in 3% NaCl solution one week before testing	3% NaCl solution
Specimens Extracted from the Long-Term Tests	Embedded in concrete and exposed to tap water for 19 months	No added chlorides	Filtered pore solution extracted from the concrete surrounding the specimens
	Embedded in concrete and exposed to salt water for 19 months		

4.4 Results and Discussion

4.4.1 Simulated Concrete Pore Water Solution

In order to examine the formation of the passive film, two steel rebar samples and two washers were placed in the concrete pore solution. Half-cell potentials (E_{corr}) and the corrosion currents (i_{corr}) for the four samples were measured daily using the LPR technique over a period of 20 days and are shown in Figure 4-14 and Figure 4-15, respectively. As expected, the rebar samples initially exhibited high corrosion potentials and corrosion current densities, but both parameters decreased gradually and stabilized after 96 hours (4 days) of exposure indicating the formation of the passive layer. On the other hand, the measured potential and current density values of the washer samples were comparatively small initially and increased gradually to a stable value. This unexpected behavior can be the result of the presence of oil deposits on the surface of the washer at the time of immersion. The oil is applied on the washers by the manufacturers to facilitate packaging. The oil layer acts as a barrier that inhibits the transfer of ions resulting in small measured corrosion potentials and currents. However, the oil layer dissolves in the pore solution allowing the formation of the passive film. Once the passive state is reached, the measured half-cell potentials of the washer samples were slightly more active than rebar samples.

In order to examine the effect of chlorides on the passivity of both steels, chlorides were added to one rebar and one washer sample in the form of 3% NaCl by weight at day 14 (hour 331). The corrosion potentials of the rebar and washer samples exposed to chloride increased dramatically reaching a potential of -530 mV after only one day of chloride addition and remained stable afterwards. The corrosion currents followed the same pattern after the addition of chlorides. However, the final corrosion current of the washer sample was 1.75 times higher than that of the rebar sample.

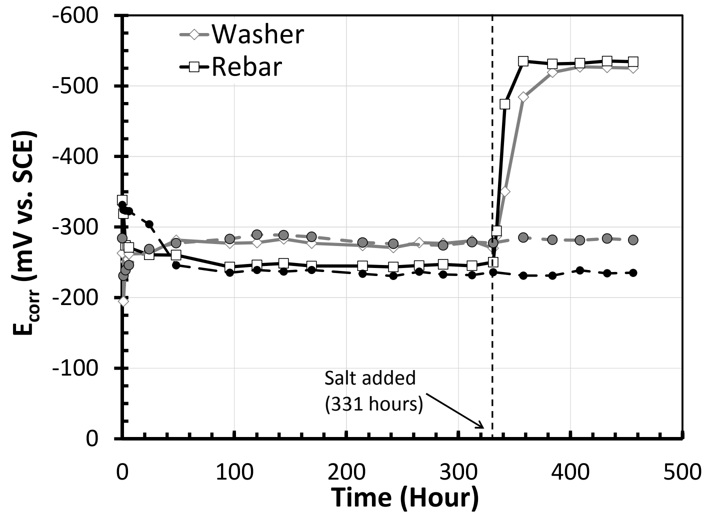

Figure 4-14: Measured half-cell potentials of the steel rebar and washer samples immersed in simulated concrete pore solution

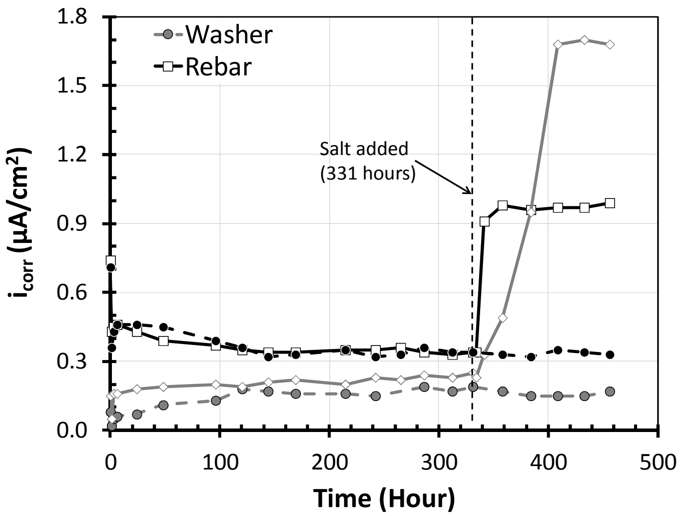

Figure 4-15: Measured corrosion current densities of the steel rebar and washer samples immersed in the simulated concrete pore solution

Two groups of rebar and washer specimens that were immersed in the simulated concrete pore solution for 21 days were used for the cyclic potentiodynamic testing. The first group was examined without the addition of chlorides. However, the second group was tested in a chloride contaminated simulated concrete pore electrolyte. The chlorides (3% NaCl by weight) were added 24 hours before conducting the test.

Figure 4-16 shows the cyclic polarization curves for the rebar and washer samples immersed in the simulated concrete pore solution and the chloride contaminated solution. The samples immersed in the pore solution had corrosion potentials of about -250 mV and the shape of the polarization curve did not indicate a breakdown of the passive layer. This was confirmed by the shape of the reversed scan portion of the curve. The rebar and washer samples exposed to chloride contamination exhibited significantly higher corrosion rates and more negative corrosion potentials indicating a higher tendency for corrosion activity. In addition, a region of passivity was observed at potentials between -400 mV and -190 mV. At higher potentials, the samples reached the transpassive region where pitting occurs. The breakdown of the passive layer was confirmed by the reversed scan. The washer samples exhibited higher corrosion currents along the whole scan range in both solutions. This indicates that regardless of the changes in oxidizing conditions, the washers tend to corrode at a higher rate than the surrounding reinforcing steel.

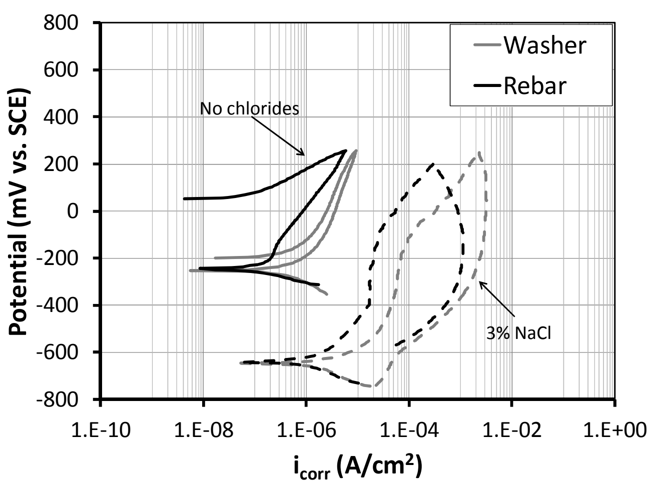

Figure 4-16: Cyclic polarization curves of steel rebar and washer specimens immersed in simulated concrete pore solution and chloride contaminated pore solution

In order to ensure the formation of a stable and intact passive film on the specimens, a third group of samples was immersed in a simulated concrete pore solution and kept undisturbed for three months. After curing, the samples were evaluated using the potentiodynamic polarization test. The samples were either tested in an uncontaminated pore solution or a concrete pore solution containing 3% NaCl by weight.

Figure 4-17 shows the cyclic polarization curves for the sample series after being cured for an extended period of time. It can be seen that the washer samples had higher corrosion rates and potentials compared to the steel rebar sections throughout the scan range, hence, the corrosion trends remained the same regardless of the curing period. However, evidence of stronger and more stable passive films was observed. The corrosion rates were significantly lower than the samples with three-week curing and the corrosion potentials were more noble. Furthermore, the reversed scans of the samples polarized in a chloride containing electrolyte indicated that the passive film remained intact for the rebar sample. In contrast, repassivation was observed in the washer sample at potential equal to -10 mV indicating that the passive film was not totally destroyed.

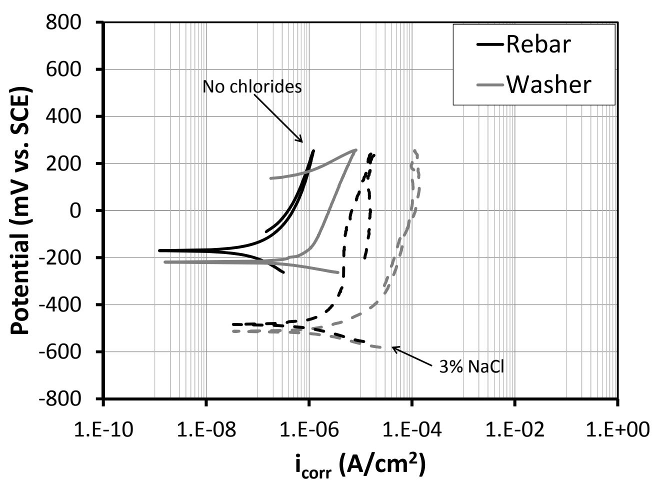

Figure 4-17: Cyclic polarization curves of steel rebar and washer specimens cured in simulated concrete pore solution and chloride contaminated pore solution for 3 months

4.4.2 Simulated Carbonated Concrete Solution

Figure 4-18 shows the cyclic polarization curves of a rebar and washer specimens immersed in simulated carbonated concrete solution. Both specimens had equilibrium corrosion potentials of approximately -200 mV. The curves indicate the presence of passive layers in both specimens which remain stable throughout the test. Similarly to the findings for the specimens immersed in the simulated concrete pore solution, the measured corrosion current density of the sacrificial washer was higher than the steel rebar. However, the corrosion rates of the specimens immersed in the simulated carbonated concrete solution were significantly higher than the specimens placed in the chloride-free concrete pore solution (Figure 4-16). This difference in the corrosion rates suggests that weaker passive layers have formed in the carbonated specimens.

The effect of chlorides on the corrosion behavior of specimens immersed in the low pH medium was also examined by adding 0.2% NaCl to the simulated carbonated concrete solution. The polarization curves had remarkably high corrosion currents that were two orders of magnitude higher than the chloride-free carbonated samples and approximately five times higher than the chloride contaminated pore solution samples. Hence, the passive film formed in the simulated carbonated concrete solution is weak, unstable, and breaks down easily under external polarization.

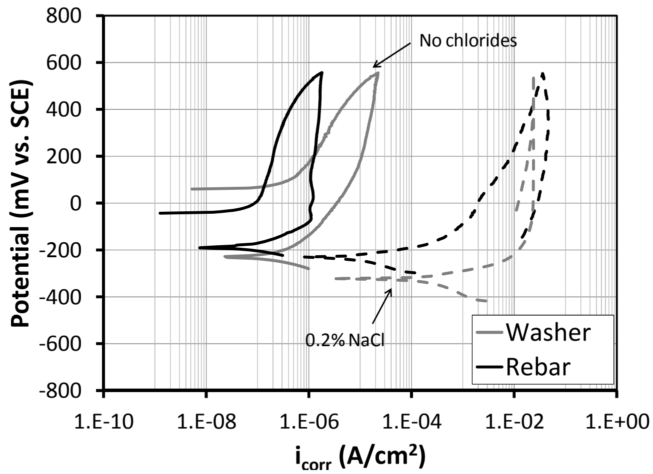

Figure 4-18: Cyclic polarization curves of steel rebar and washer specimens immersed in simulated carbonated concrete solution

4.4.3 Deionized and Salt Water Solutions

LPR tests were conducted using three corroding solutions: deionized (DI) water, 1% salt water, and 3% salt water solutions. The nondestructive nature of the test allowed each specimen to be tested in each solution without affecting the accuracy of the results. Figure 4-19 summarizes the measured corrosion potentials for each specimen in the three solutions. As expected, the corrosion potentials for all the specimens increased as the chloride ion concentrations increased. For each solution, the corrosion potential values of the rebar and washer samples were relatively close and within the experimental scatter.

The measured corrosion currents the LPR specimens in each of the three corrosive solutions are summarized in Figure 4-20. The lack of free ions in the DI electrolyte limited the corrosion activity and resulted in corrosion rates close to zero for all the samples examined. As the chloride content in the electrolyte increased, the measured corrosion rate for each specimen increased. Generally, the washers exhibited corrosion rates significantly higher than the rebar samples.

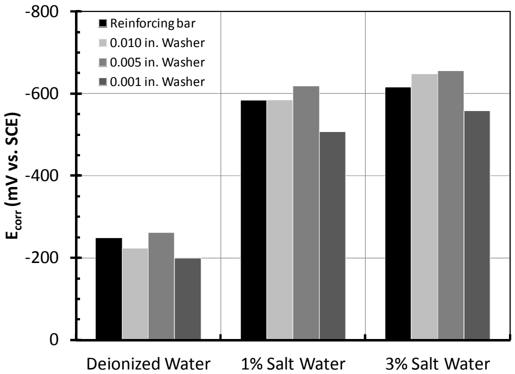

Figure 4-19: Corrosion potentials for the rebar and washer samples immersed in salt water solutions

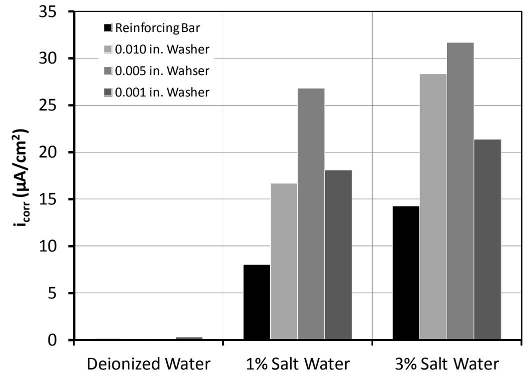

Figure 4-20: Corrosion current densities for the rebar and washer samples immersed in salt water solutions

Based on the LPR test results, it can be concluded that the sacrificial washers and the steel reinforcement have the same tendency to corrode under salt water exposure; however, the washers will corrode at higher rates. On average, the corrosion rates of the sacrificial washers were two times higher than the rebar samples.

The polarization curves for the washer and rebar specimens were obtained using the potentiodynamic test (Figure 4-21). The tests were conducted using a 3% salt water solution as an electrolyte. Unlike the samples examined using the simulated concrete pore solution, the corrosion potentials for the washer samples and the rebar are close in value. This is due to the fact that the chromium and nickel alloys improve the corrosion resistance of the rebar samples by forming stronger and more stable passive films. In this test series, the samples were directly immersed in salt water with no formation of a passive film and as a result the corrosion response of the washer and rebar samples was similar. As expected, both curves exhibited an active corrosion behavior with no passivity or transpassive regions. The washer sample suffered severe corrosion damage and at a potential of 100 mV vs. SCE, the washer broke and a loss of current was observed and is identified by the horizontal line in the polarization curve. The measured corrosion potentials and current densities were close to the values obtained using the LPR technique.

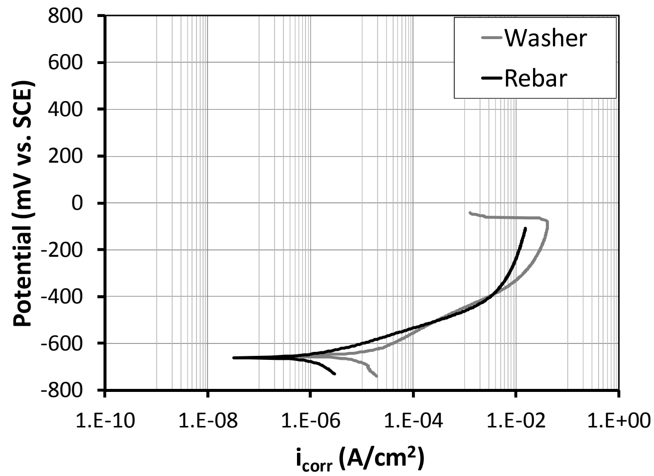

Figure 4-21: Potentiodynamic polarization curves for the rebar and washer samples

4.4.4 Specimens Embedded in Mortar

Three steel rebars and two washer specimens embedded in mortar were tested using the potentiodynamic test. Figure 4-22 shows the polarization curves of all the specimens embedded in mortar. The washer specimens experienced corrosion rates that are two orders of magnitude higher than the rebar samples. Furthermore, the half-cell potentials of the washer specimens were much higher (-550 mV) than the rebar samples (-250 mV). The findings suggest that the washers embedded in mortar will corrode faster and at a higher rate than the surrounding rebar. Furthermore, the polarization curves suggest that the rebar specimens had a small region of passivity extending between -200 and -100 mV vs. SCE. On the other hand, the washer specimens show no sign of passivity and had corrosion potentials that suggest a higher corrosion tendency.

The curves can also be used to examine the variability of the test method. The replicate samples were cast at the same time using the same mortar mix; however differences in response can still be observed. This is an inherent disadvantage of using the electrochemical evaluation techniques on samples directly embedded in concrete or mortar. The potentiodynamic test is sensitive to the local differences in the metal surface which is expected within a concrete medium.

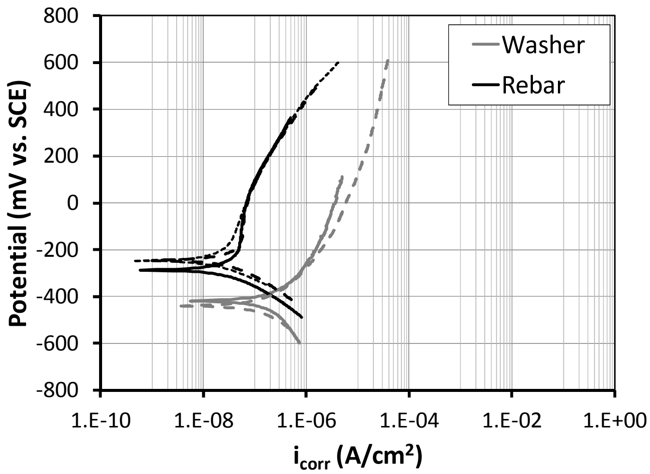

Figure 4-22: Cyclic polarization curves of steel rebar and washer specimens embedded in mortar and immersed in 3% NaCl electrolyte

4.4.5 Specimens Extracted from the Long-Term Exposure Test

The polarization curves for the tap water specimens are shown in Figure 4-23. The rebar samples had corrosion potentials of approximately -290 mV vs. SCE and the curves of both samples were identical. The washer samples had more negative potentials and corrosion rates higher throughout the scan range. The thickness of the washer did not influence the measured response and the polarization curves of the T1-7 and T2-7 washers were very similar.

Figure 4-24 shows the polarization curves of the S1 and S2 samples. The rebar samples had corrosion potentials at around -600 mV vs. SCE and pitting potentials at approximately 35 mV vs. SCE. Both samples showed identical trends and their reverse scans indicated a breakdown in the passive films beyond pitting. The washer samples followed the same trends observed in the rebar samples. However, the washers exhibited consistently higher corrosion rates and more active potentials. In addition, the thicker washer had a notably higher corrosion rates compared to the thinner S1-8 washer. This can be attributed to the higher chloride content measured in the concrete surrounding sensor S2-7 (1507 ppm) compared to the concrete near S1-8 (704 ppm). This also explains the higher corrosion currents and more active potentials observed in the samples extracted from the beams exposed to salt water exposed beams when compared to the tap water samples.

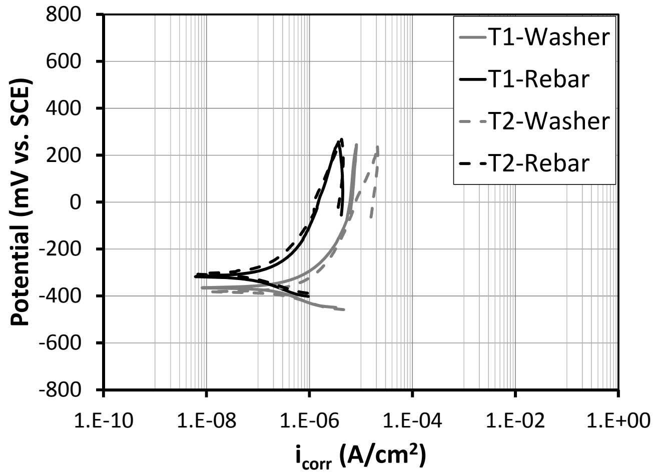

Figure 4-23: Cyclic polarization curves of steel rebar and washer specimens extracted from reinforced concrete beams exposed to cyclic exposure of tap water

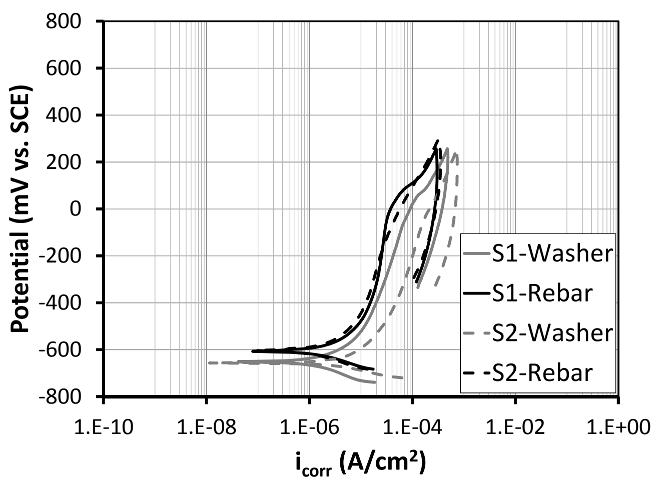

Figure 4-24: Cyclic polarization curves of steel rebar and washer specimens extracted from reinforced concrete beams exposed to cyclic exposure of 3.5% salt water solution

4.5 SUMMARY

Table 4-5 lists the measured half-cell potential (E_{corr}), equilibrium corrosion density (i_{corr}), and the pitting potential for the specimens tested. The polarization results indicate that regardless of the medium investigated, the washers will behave in a pattern similar to the surrounding rebar. Furthermore, the sacrificial washers exhibit higher corrosion rates and more active corrosion potentials over a wide range of oxidation levels compared to the reinforcing steel, thus, allowing for an early detection of rebar corrosion. Hence, the selection of AISI 1010 sacrificial washers in the fabrication of the NC sensor is recommended for reliable corrosion detection.

In addition, the experimental results have shown that the additional cold-working processes needed to produce thinner sacrificial washers did not adversely affect their corrosion response. The study also demonstrated the detrimental role carbonation plays on the passive film structure.

The experimental program developed in this study can be used to assess the mass loss of the rebar at the moment when the NC sensor shifts to its corroded state. This can be done by first examining the chemical composition of the concrete medium where the sensor is embedded. Then, using the potentiodynamic polarization examination data, the ratio between the corrosion rate of the washer and the corrosion rate of the adjacent rebar can be evaluated and used to calculate the expected mass loss in the adjacent rebar. Furthermore, the test protocol used herein can be used to select suitable sacrificial elements for new types of steels or specific concrete environments.

Table 4-5: Measured corrosion potential (E_{corr}), corrosion density (i_{corr}), and the pitting potential (E_{pit}) for the rebar and washer samples in the electrolytes investigated

Solution	Chlorides	E_{corr} (mV vs. SCE)		i_{corr} ($\mu A/cm^2$)		E_{pit} (mV vs. SCE)	
		Rebar	**Washer**	**Rebar**	**Washer**	**Rebar**	**Washer**
Concrete Pore Solution	No Cl^-	-244	-252	0.09	0.14	*	*
	3% NaCl	-641	-647	1.21	1.38	-102	-114
Long-term Concrete Pore Solution	No Cl^-	-170	-219	0.04	0.22	*	*
	3% NaCl	-484	-509	0.85	1.13	-51	-120
Carbonated Concrete Solution	No Cl^-	-191	-228	0.80	1.30	*	*
	0.2% NaCl	-230	-322	49.0	120.3	**	**
Salt Water Solution	3% NaCl	-660	-655	13.53	24.53	**	**
Cement Mortar	3% NaCl	-247	-505	0.01	1.76	*	*
Specimens Extracted from the Long-Term Tests	Tap water specimens	-317	-365	0.01	0.14	**	**
		-308	-382	0.06	0.22	**	**
	Salt water specimens	-607	-656	1.14	1.68	46	7
		-603	-654	1.65	1.79	-2	-31

* The passive layer remained intact within the scan range

** The reverse scan indicated a breakdown in the passive layer, but pitting was not observed.

CHAPTER 5

Preliminary Investigation of the Reliability of the Noncontact Sensor

5.1 OVERVIEW

The change in the measured response of the noncontact (NC) sensors due to the corrosion of the sacrificial washer was examined in Chapter 3. Furthermore, an electrochemical evaluation of the corrosion characteristics of the sacrificial washers was conducted using a number of representative simulated pore solutions in Chapter 4. However, an evaluation of the ability of the NC sensors to detect the initiation of corrosion activity within concrete members is needed to confirm the reliability of the sensor. To this end, an accelerated corrosion test was initiated using small-scale specimens. Four NC sensors were embedded in two reinforced concrete prisms and interrogated periodically over a period of fourteen months. The measured sensor readings were also used to assess the sensitivity of the sensor to changes in the environmental conditions, such as temperature, moisture content, and chloride levels. Furthermore, traditional electrochemical corrosion monitoring measurements, half-cell and linear polarization, were taken and compared with the sensor output.

Section 5.2 provides a description of the concrete specimens and construction details. The experimental set-up and the design of the experiment are detailed in Section 5.3. The results obtained from the sensor interrogations and the electrochemical evaluation techniques are presented in Section 5.4 and Section 5.5, respectively. A physical autopsy was conducted at the end of the exposure test and the corrosion damage in the steel reinforcement and the state of the sensors were documented and are summarized in Section 5.6. Finally, the reliability of the sensor output and the conclusions from the electrochemical methods are examined and compared with the autopsy results in Section 5.7.

5.2 Specimen Construction

Two identical reinforced concrete prisms were cast with two NC passive sensors embedded in each. The prisms were 18 in. long, 7 in. wide and 6 in. deep (Figure 5-1). The relatively small size of the prisms was selected to permit the specimens to be stored in environmental chambers. Each prism was divided into three regions (A, B and C) of equal lengths, and the sensors were embedded in the center of regions A and B. Hence, one sensor was placed at midspan and the second was 6.0 in. away from the centerline of the prism.

A single layer of two #3 reinforcing bars was used as longitudinal reinforcement with 1.0 in. top clear cover. To ensure a microcell corrosion activity, the reinforcing bars were electrically isolated and were positioned in place by extending the ends of each bar through the sides of the formwork (Figure 5-2). The exposed ends of the reinforcing bars were cut after the concrete hardened and the sides of the prisms were covered with black epoxy paint and a layer of shrink tape. The electrical connection needed for the electrochemical measurements was achieved by soldering an 18-AWG copper wire to one end of each reinforcing bar 1.0 in. from the end of the prism in region C. The solder area was thoroughly dried and then covered using heat shrink tape to prevent unintended bimetallic corrosion. Throughout this chapter the reinforcing bars in each prism are designated “rebar 1” and “rebar 2” to facilitate comparisons.

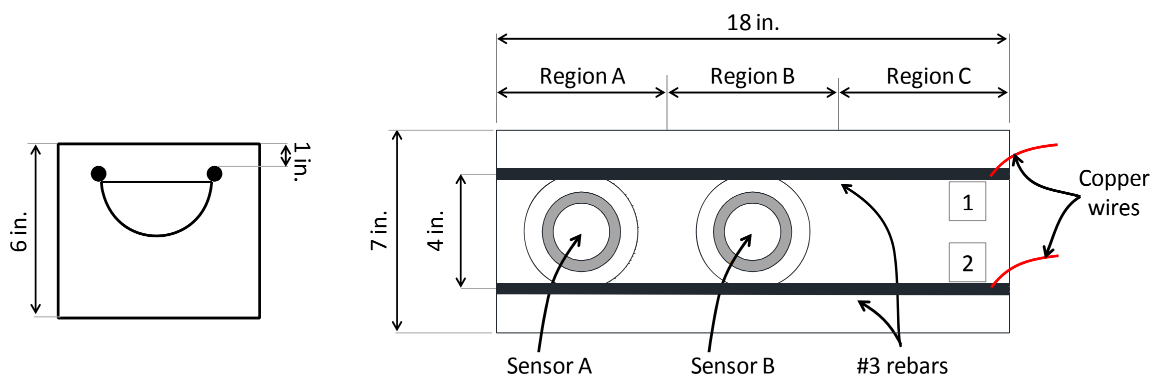

Figure 5-1: Cross-section and plan view of the concrete prisms

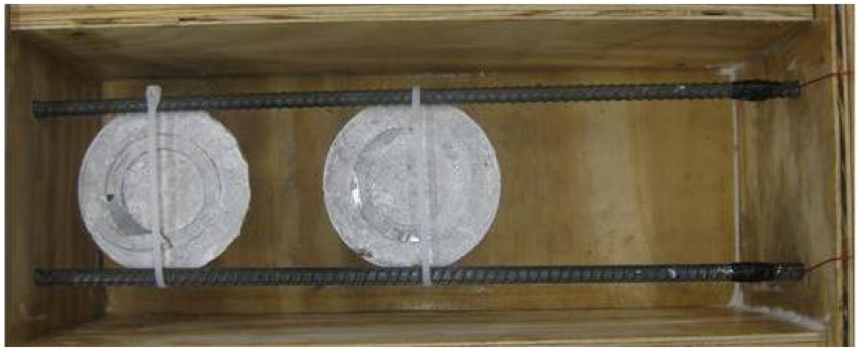

Figure 5-2: Photograph of a reinforced concrete prism before concrete placement

The embedded sensors were fabricated with low-carbon, cold-rolled AISI 1010 steel washers. The washers were 0.001-in. thick with a 2.0-in. inner diameter and a 2.75-in. outer diameter. The chemical composition of the steel reinforcement and washers are summarized in Table 4-1. The sensors were positioned vertically such that the sacrificial corroding washer was at the level of the bottom fiber of the reinforcing bars (Figure 5-1). The sensors were secured in place using plastic zip ties which were wrapped around the cement housing and attached the sensors to the longitudinal rebars. In order to prevent accidental movement or rotation of the NC sensors, the top surface of the cement housing was pulled firmly against the bottom surface of the reinforcement.

The specimens were cast on May 4, 2010 at Ferguson Structural Engineering Laboratory. QUIKRETE® commercial concrete mix was used to cast the prisms and the compressive strength of the mixture at 28 days was 3800 psi. To limit movement of the sensors, the specimens were internally compacted using a 0.5-in. diameter rod and externally using a concrete vibrator. Figure 5-3 shows the casting of the concrete prisms. The prisms were covered using plastic sheets and were left to cure for 28 days. Initial sensor interrogations indicated that the NC sensors were intact and remained in place during the placement of concrete.

Figure 5-3: Concrete placement in the accelerated corrosion prisms

5.3 DESIGN OF EXPERIMENT

5.3.1 Experimental Set-up

The main objective of this preliminary evaluation was to assess the reliability of the prototype NC sensors and evaluate the sensor response at different levels of chloride exposure. To this end, one of the reinforced concrete prisms was exposed to a salt water solution (prism SW), while the second prism was exposed to tap water (prism TW). The salt water solution contained 3.5% NaCl by weight and was expected to initiate corrosion faster than tap water.

Because the corrosion rate is higher when oxygen is present(Hansson 1984), the solution was dripped onto the top surface of the prisms. Essentially, this creates a splash zone on the surface of each test prism. The solution was dripped over the center of the prism (region B). However, due to the relatively small size of the prisms, the corroding solution spread over the entire top surface of the prisms. Figure 5-4 is a schematic illustration of the exposure test set-up. A cycle of 3 days wet and 4 days dry was used. The containers that held the solution were refilled regularly during the wet periods to maintain a continuous exposure. The solution that was not absorbed by the prisms was collected and recycled. New solutions were prepared once a month. An average of 15 gallons of the solution was dripped onto the surface of each prism during a typical wet period.

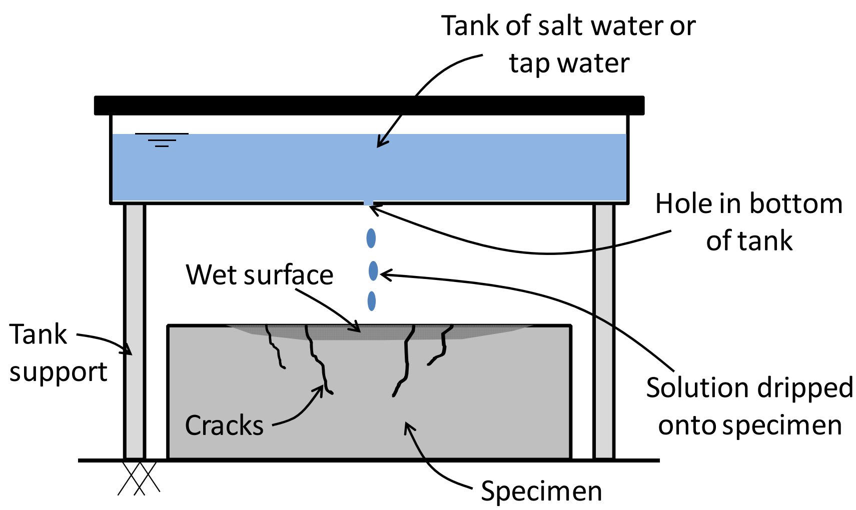

Figure 5-4: Schematic of the accelerated corrosion test set-up

. The prisms were stored in an unheated building and experienced temperature fluctuations of more than 74°F during the test. The prisms were exposed to the moisture cycles between July 2010 and September 2011 (423 days of exposure). However, the exposure and testing of prism SW was stopped in April 2011 (284 days of exposure) after threshold levels of corrosion were detected in both sensors. In the period between October 2010 and February 2011, the prisms were stored in an environmental chamber that was set at a controlled temperature of 95°F during the dry periods. The higher drying temperatures dried the concrete faster and were expected to increase the rate of chlorides diffusion into the concrete.

Prior to starting the exposure test, the prisms were cracked in flexure using a three-point loading setup. The load was increased until the maximum crack width reached 0.03 in. Due to the relatively large size of the NC sensors compared to the size of the concrete prisms, the cracks were concentrated over the embedded sensors and extended across the width of the top surface of both prisms (Figure 5-5). In prism SW, the widest cracks ranged between 0.01 and 0.03 in. The cracks in prism TW were larger over Sensor A (0.03 in.) compared with the cracks near Sensor B (0.008 in.).

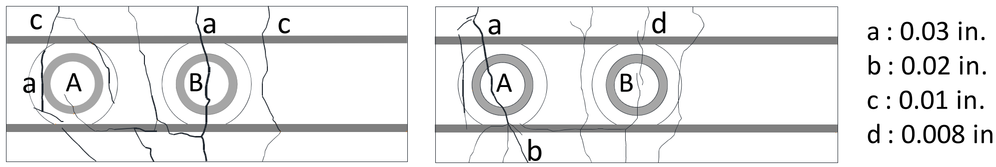

Specimen SW　　Specimen TW

Figure 5-5: Crack maps for prisms SW and TW

5.3.2 Nondestructive Testing

The sensors were interrogated after each wet and dry period using a five-turn reader coil with a 4.0-in. diameter. The coil was assembled using an 18-AWG copper wire and had a self-resonant frequency of 6.0 MHz. The impedance response was acquired using a Solartron 1260A Impedance/Gain-Phase Analyzer. The reader coil was placed directly on the concrete surface resulting in a read distance of approximately 1.2 in.

Assessments of the corrosion risk and activity of the steel reinforcement in the prisms were conducted using traditional electrochemical corrosion evaluation techniques. The half-cell potentials were measured on a biweekly basis using a Saturated Calomel Electrode (SCE) and a high-impedance voltmeter. The measurements were conducted in accordance with ASTM C876 (2009), which also provides potential thresholds for evaluating the corrosion risk. The measurements were taken at four points along the length of each reinforcing bar with two measurement points selected to coincide with the centers of the embedded sensors. Figure 5-6 illustrates the location of the half-cell measurements within the test prisms.

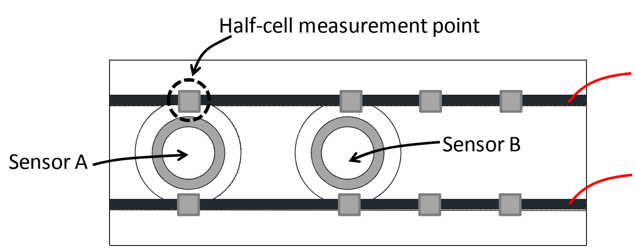

Figure 5-6: Locations of half-cell measurement points

In addition, linear polarization resistance (LPR) measurements were also used to measure the corrosion rates of the reinforcement. The data were collected using a GECOR 8™ corrosion rate system with copper/copper sulfate reference and auxiliary electrodes and a stainless steel guard ring. The corrosion current densities were measured for the two reinforcing bars in each prism. The GECOR 8™ equipment has a 7.0-in. diameter sensing probe and the measured corrosion currents are limited to the rebar sections directly below the sensing probe. Figure 5-7 shows the locations where the GECOR™ sensing probe was placed to obtain the LPR measurements. It can be seen that the probe was centered on the rebar section under consideration and parts of the measuring probe extended beyond the edge of the prism. To prevent erroneous readings, a wet unreinforced concrete surface was positioned next to the prism during the measurements, as recommended by the manufacturer.

The LPR readings were taken only in March and August 2011. Four sets of corrosion current measurements were collected during March 2011 (273 to 284 days). The measurements were collected after two sets of consecutive wet and dry periods. Only prism TW was evaluated in August 2011 (403-406 days), and two sets of readings were collected after consecutive wet and dry periods of a single cycle. The average recorded concrete surface temperature and relative humidity values during the LPR measurements are listed in Table 5-1.

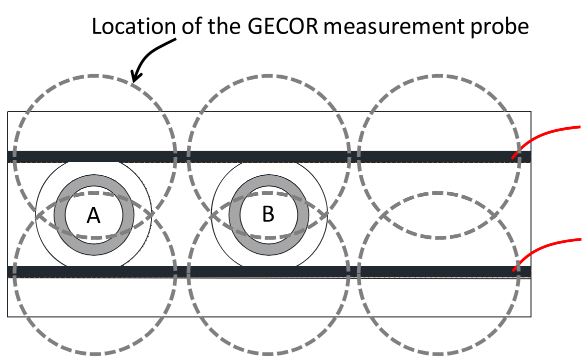

Figure 5-7: Locations of the LPR measurement points

Table 5-1: Average concrete surface temperature and relative humidity during LPR measurement periods

Interrogation Period	Average Temperature (°F)	Average Relative Humidity (%)
March 2011	71	54
August 2011	93	51

5.3.3 Post-Experiment Destructive Testing and Autopsy

At the end of the exposure period, concrete powder samples were collected and analyzed to obtain the acid-soluble chloride content levels within each prism in accordance with ASTM C1152/ C1152M (2004). The powder samples were collected by drilling vertically from the top surface using a 0.25-in. diameter drill hammer. The sampling locations were selected to avoid damaging the embedded sensors or the reinforcing bars and only powder collected at depths between 1.00 and 1.25 in. was retained. The samples were analyzed by Tourney Consulting Group and the results were reported in parts per million (ppm).

Then, the prisms were autopsied to examine the extent of corrosion damage in the reinforcement and the condition of the sacrificial washers. The top concrete cover was removed using an impact hammer with a 0.50-in. diameter drilling rod. A chisel was then used to remove the remaining concrete minimizing the possibility of causing accidental damage to the reinforcing bars or passive sensors.

Finally, mass loss measurements were conducted using the reinforcing bars removed from the prisms. Three 4.0-in. sections were cut from each reinforcing bar. Two sections were adjacent to the embedded sensors and the third section was cut from the middle of region C. The measurements were performed in accordance with ASTM G1 (2003), and the corrosion product removal was performed using the chemical procedure C.3.5.

Figure 5-8 plots the timeline of the accelerated corrosion test and highlights the main events associated with the test. Figure 5-9 shows the monitoring activities conducted in a typical cycle during the exposure period of the accelerated corrosion test.

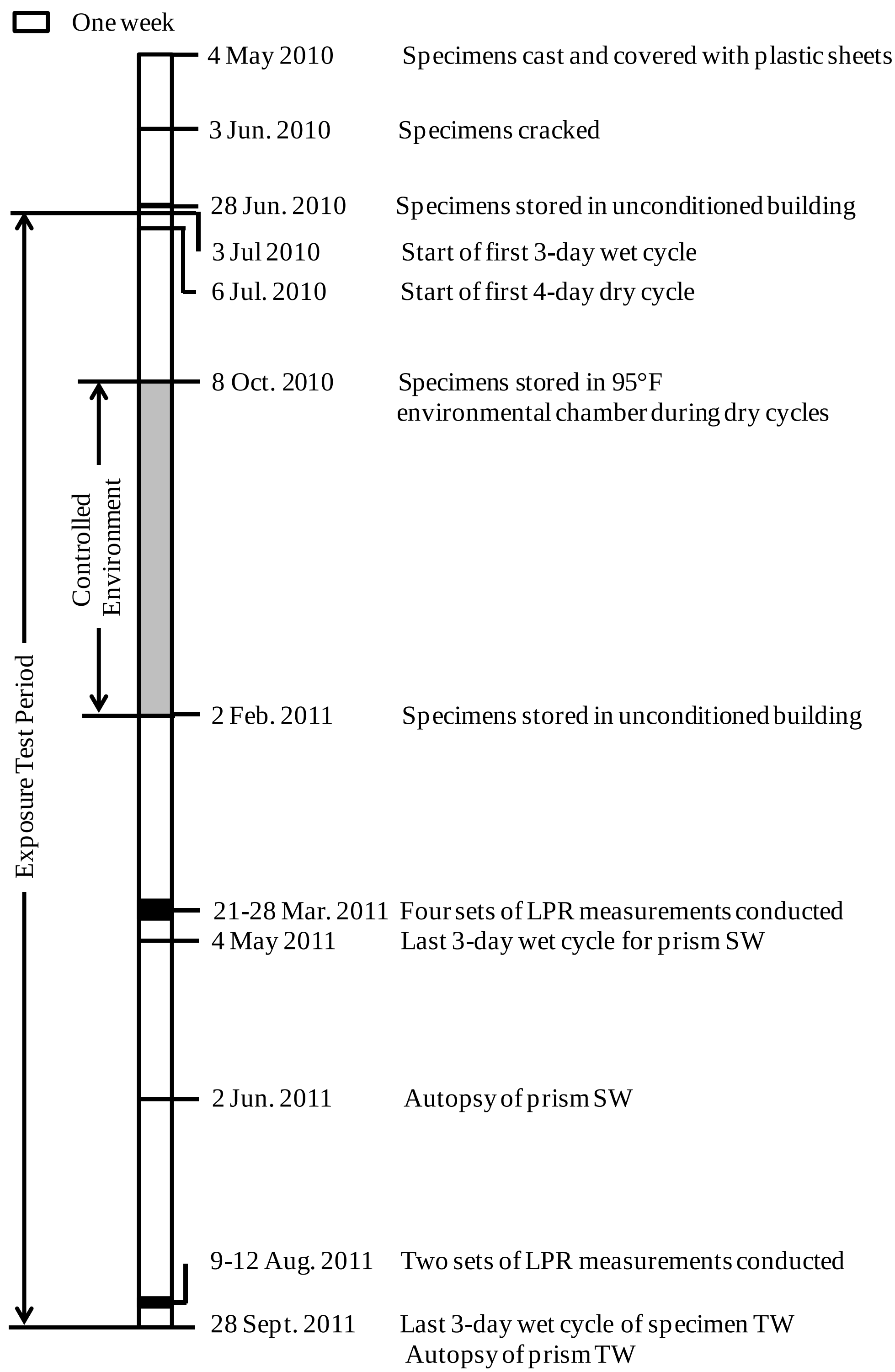

Figure 5-8: Timeline of accelerated corrosion tests for prisms

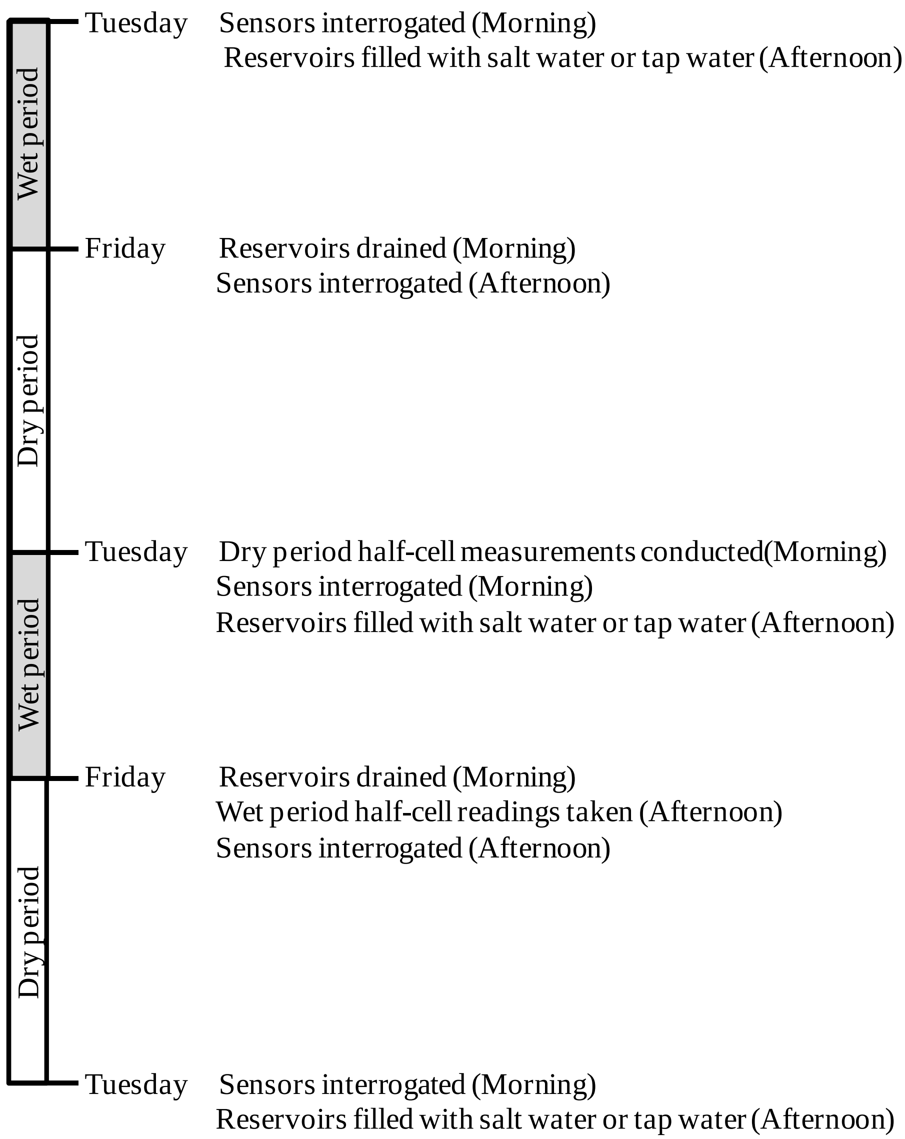

Figure 5-9: Typical timing of the measurements conducted in a two-week period

5.4 MEASURED RESPONSE OF THE NC SENSORS

The frequency response of the NC sensors embedded in the concrete prisms was acquired regularly. The phase of impedance data were used to determine the state of the sensors. Changes in the measured resonant frequency, phase dip, and bandwidth were indicative of corrosion activity in the sacrificial washer.

Figure 5-10 through Figure 5-13 show selected phase response curves of sensors SW-A, SW-B, TW-A, and TW-B, respectively. It can be seen that sensors SW-A, SW-B, and TW-A shifted to the corroded state before the end of the exposure test. While the time needed to start transitioning from the uncorroded state and reach the corroded state varied for the three sensors, the patterns were very similar and match the observations discussed in Chapter 3. During the transition to the final corroded state numerous changes to the measured phase response take place simultaneously:

a) Monotonic reduction in the resonant frequency
b) Initial dampening of the phase dip followed by an steep increase once the sensor reaches the corroded resonant frequency (f_{rc}).
c) Increase in the bandwidth reaching a maximum when the phase dip is at a minimum followed by a reduction to a minimum once the sensor reaches the corroded resonant frequency (f_{rc})

The final phase dip for sensor SW-B (284 days) was notably smaller than the final phase dips for sensors SW-A and TW-A. This is due to the termination of the exposure test in prism SW soon after sensor B shifted to the corroded resonant frequency. If more time had been allowed, it is anticipated that the phase dip would have continued to increase and reach values similar to the other two corroded sensors.

Sensor TW-B remained in the uncorroded state throughout the exposure period. The phase response readings shown in Figure 5-13 had slight variations in resonant frequency and phase dip. The variations can be attributed to variations in temperature, and moisture content within the concrete medium. However, the changes in response are minimal compared to the available range of possible frequency readings. Hence, the response of an embedded sensor can be easily interpreted and the distinction between the signals of different states can be done easily.

As was discussed earlier, the shift in resonant frequency due to corrosion of the sacrificial washer is monotonic and easy to interpret. Hence, the shift in the resonant frequency of each sensor over the period of the experiment is used to evaluate the sensitivity of the NC sensor response to the chloride exposure. Figure 5-14 and Figure

5-15 show the change in the measured resonant frequencies with time for the sensors embedded in prisms SW and TW, respectively. The frequency shift is expressed as a percentage of the available dynamic frequency range (f_{se} - f_{rc}).

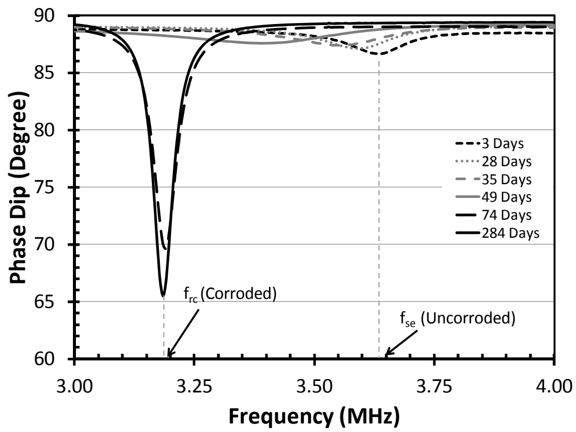

Figure 5-10: Measured phase response of sensor SW-A at 3, 28, 35, 49, 74, and 284 days of exposure

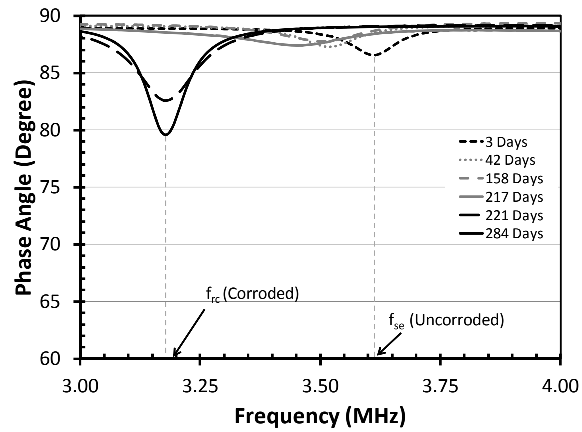

Figure 5-11: Measured phase response of sensor SW-B at 3, 42, 158, 217, 221, and 284 days of exposure

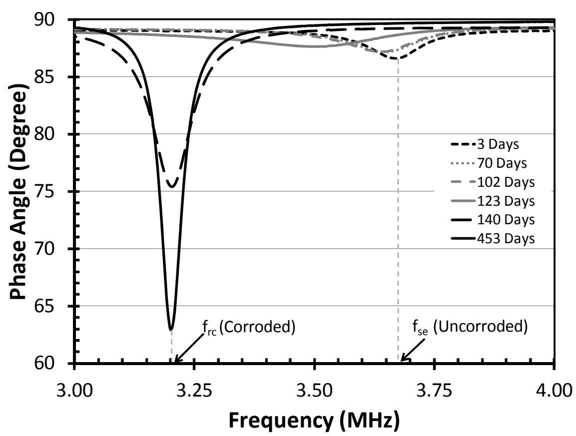

Figure 5-12: Measured phase response of sensor TW-A at 3, 70, 102, 123, 140, and 453 days of exposure

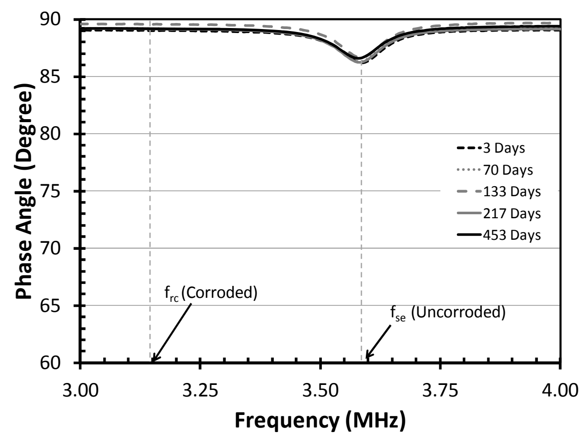

Figure 5-13: Measured phase response of sensor TW-B at 3, 70, 133, 217, and 453 days of exposure

Both of the sensors embedded in prism SW shifted to the corroded state indicating the onset of corrosion. The resonant frequency of sensor SW-A started the transition to the corroded state after only 3 weeks of exposure. The resonant frequency of SW-A shifted gradually and monotonically reaching the fully corroded frequency on day 70. In contrast, the resonant frequency of sensor SW-B drifted initially to one-fifth the available frequency range and remained relatively constant between days 30 and 160. Then the frequency shifted slightly to 40% of the range and remained constant for 60 days. Finally, the sensor frequency dropped abruptly to the corroded state and remained constant afterwards. This unpredicted response could have been the result of the repassivation phenomenon observed by other researchers (Yuan et al. 2009, 2010). It is hypothesized that the initial corrosion products created a dense layer that blocked the supply of chloride ions to the anode region, hence, halting the corrosion process. This is typically observed in regions where localized corrosion occurs which is expected in the vicinity of cracks. A detailed evaluation of the effect of crack sizes and their location on the transition response is provided in Chapter 8. In addition, improvements to the NC sensor design are proposed in Section 8.5 to mitigate the repassivation phenomenon.

Only sensor A shifted to the corroded frequency in prism TW (Figure 5-15). The measured response of sensor TW-A was similar to sensor SW-A. The initial shift in the resonant frequency of sensor TW-A was noted in day 70 and the sensor gradually transitioned to the corroded state in day 137.

As discussed previously, sensor TW-B remained at the uncorroded state throughout the exposure test period indicating a low risk of corrosion in the surrounding reinforcement steel. The maximum measured shift in the resonant frequency of sensor TW-B was less than 3.5% of the available dynamic range. The standard deviation of the acquired resonant frequencies was 3.01 kHz which results in a coefficient of variation less than 0.1%.

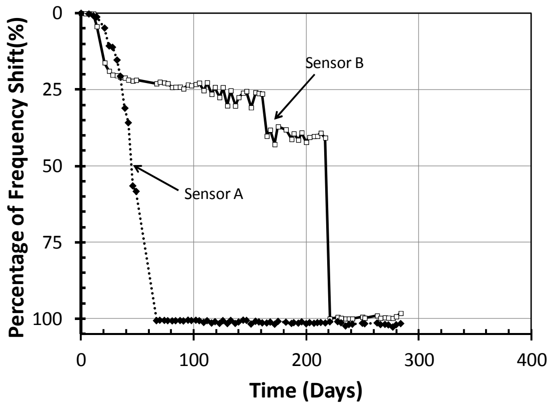

Figure 5-14: Measured shift in resonant frequency for the sensors in prism SW

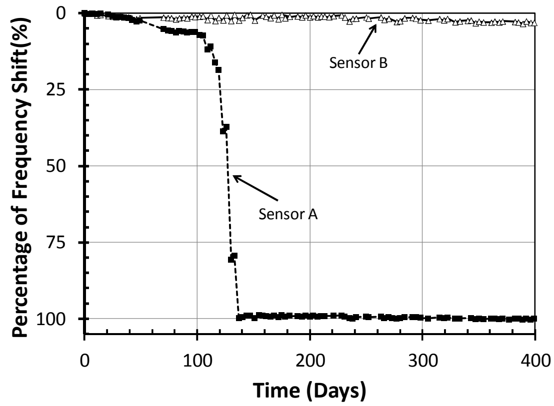

Figure 5-15: Measured shift in resonant frequency for the sensors in prism TW

Figure 5-16 summarizes the times needed by each sensor to shift from the uncorroded state and the corresponding transition times. It can be seen that the sensors in prism SW started the shift to the corroded state after less than one month of exposure. In addition, sensors SW-A and TW-A were located under cracks of the same size and in the same region of the corresponding prisms. However, sensor SW-A reached the corroded state faster which confirms that corrosion initiated faster in the prism under the more severe chloride exposure. Furthermore, the transition of time sensor SW-A was also faster than TW-A which suggests that the rate of corrosion was higher in the prism exposed to the salt water solution.

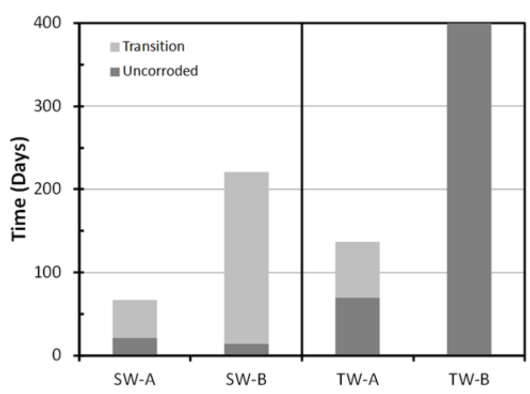

Figure 5-16: Number of days spent in the uncorroded state and transition for the NC sensors in prisms SW and TW

5.5 ELECTROCHEMICAL EVALUATION RESULTS

Electrochemical evaluation techniques were employed to assess the corrosion risk within the concrete prisms. The conclusions obtained from the results of these traditional techniques are compared to signals obtained from the embedded NC sensors in Section 5.7. In addition, the results of the electrochemical evaluations are also used to assess the sensitivity and reliability of the half-cell and the LPR methods.

5.5.1 Half-Cell Potentials

The half-cell potentials were measured every other cycle at the end of consecutive wet and dry periods. Figure 5-17 shows the average of the measured half-cell potentials along reinforcing bars 1 and 2 at sensor locations for both prisms. The measured potentials in prism SW indicated high risks of corrosion immediately after the first wet cycle. On the other hand, low to moderate corrosion risk potentials were typically measured in prism TW. Due to the small separation distance between the sensors (6.0 in.), the average potentials measured in the vicinity of sensors A and B were close in value and generally followed the same trends in both prisms. It is important to note that the half-cell potentials were sensitive to the moisture content levels. Fluctuations greater than 180 mV were observed in consecutive readings at the same locations between wet and dry periods.

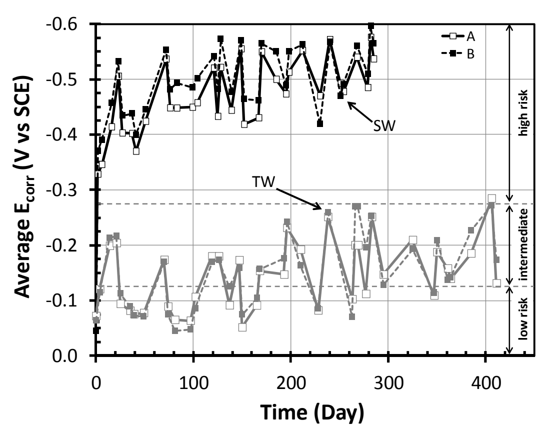

Figure 5-17: Measured variations of half-cell potentials with time

Figure 5-18 shows half-cell potential profiles along the length of the steel reinforcement. The profiles are shown for the days when the maximum and minimum potential averages were recorded during the last 100 days of exposure. The more negative potentials were associated with readings conducted after the wet cycles while the more noble potentials were associated with dry period measurements. It can be seen that for both prisms, i.e. regardless of the level of chloride exposure, the difference between the maximum and the minimum potential profiles is about 180 mV. The figure highlights the wide range of half-cell potential values that can be measured in a concrete medium with variable moisture levels. Furthermore, the plotted profiles suggest that the risk of corrosion is the same along the length of the reinforcing bar with limited variability.

The frequency distributions of the half-cell potential readings for prisms SW and TW are shown in Figure 5-19 and Figure 5-20, respectively. The readings collected during the exposure test were distributed in 25-mV bins. It can be seen that readings in prism SW were mostly higher than -300 mV vs. SCE. In addition, the SW readings had two major peaks at -475 and -575 mV vs. SCE that correspond to typical values measured after the dry and wet periods, respectively. The mode of the TW potential measurements was concentrated at -125 mV vs. SCE and all the measured potentials were equal or less than -300 mV vs. SCE.

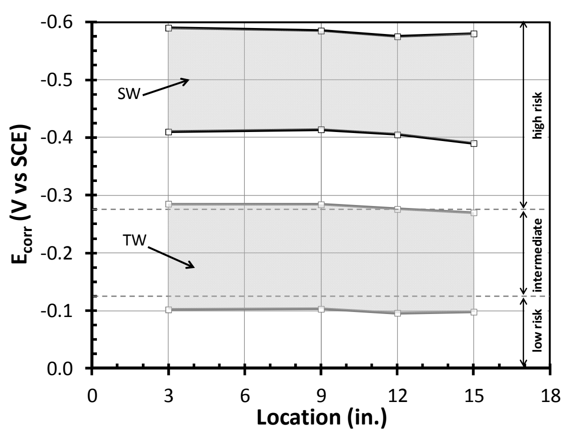

Figure 5-18: Maximum and minimum measured half-cell potentials along the length of reinforcing bar 1 in both prisms in the last 100 days of exposure

The cumulative distributions of the readings frequency for prisms SW and TW are also shown. It can be seen that all of the readings in the SW prism were indicative of a severe corrosion risk and the readings had a median half-cell potential of -479 mV vs. SCE. In contrast, fewer than 3% of the readings obtained in prism TW were indicative of a high corrosion risk. The median half-cell potential in TW was -132 mV vs. SCE, which is slightly higher than the threshold potential separating potentials of low and intermediate corrosion risk (-125 mV vs. SCE). It can also be seen that approximately 25% of the recorded potentials in prism TW were indicative of a low corrosion risk and most of the readings were within the intermediate corrosion risk band.

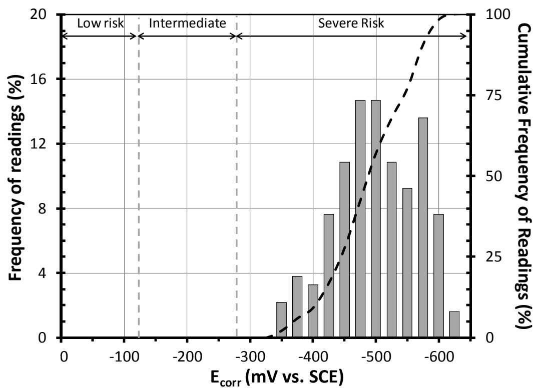

Figure 5-19: Frequency distribution and cumulative distribution of the half-cell potential data collected in prism SW

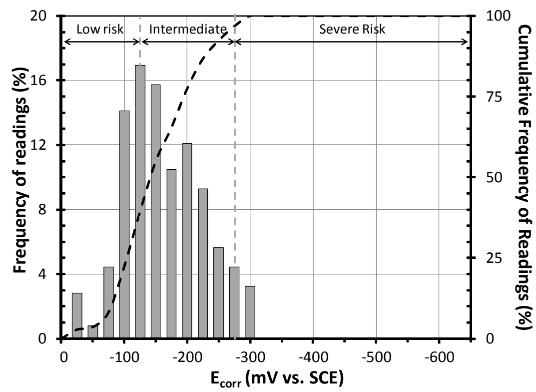

Figure 5-20: Frequency distribution and cumulative distribution of the half-cell potential data collected in prism TW

5.5.2 Linear Polarization Resistance

Corrosion rates were obtained using the linear polarization (LPR) method. The GECOR 8™ equipment was used to acquire the corrosion currents (i_{corr}) after two wet/dry cycles in March 2011 and one wet/dry cycle in August 2011. Figure 5-21 shows the measured corrosion currents for prism SW. It can be seen that the values vary considerably based on the measurement location. Furthermore, the LPR method was sensitive to fluctuations in moisture content between wet and dry periods. However, it can be concluded that corrosion is active in reinforcing bar 2 near midspan of the prism (region B) and that limited corrosion activity is taking place in reinforcing bar 2 near sensor A. The readings from bar 1 were very sensitive to the moisture content of the concrete. Readings take immediately after a wet cycle exceeded the readings taken after the dry periods by a factor of 2.5.

The corrosion currents acquired for prism TW are shown in Figure 5-22. The initial measurements (March 2011) indicated a very low corrosion activity within the prism with relatively small variability between the wet and dry period readings. However, the LPR measurements performed before the autopsy (406-410 days) showed an increase in corrosion activity to moderate levels and the variability of the current densities due to the change in moisture levels was also observed.

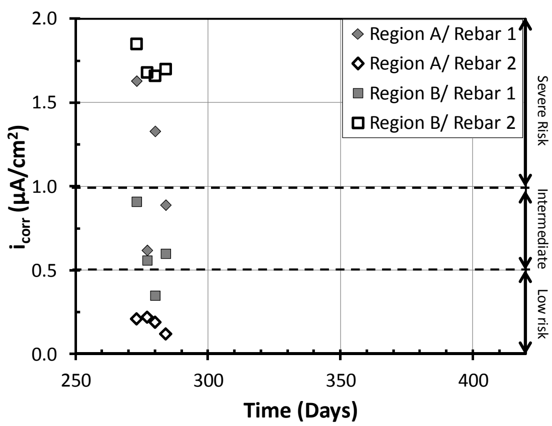

Figure 5-21: Localized corrosion current densities measured along the two reinforcing bars in prism SW

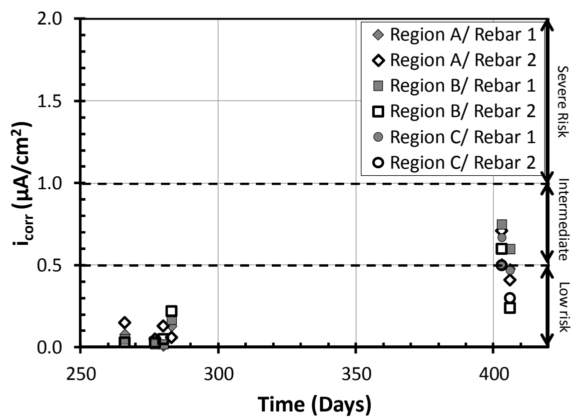

Figure 5-22: Localized corrosion current densities measured along the two reinforcing bars in prism TW

5.6 RESULTS FROM POST-EXPERIMENT AUTOPSY AND DESTRUCTIVE TESTING

5.6.1 Acid-Soluble Chloride Ion Concentrations

Prior to physical autopsy, concrete powder samples were collected and analyzed to obtain the chloride ion concentrations. Eleven concrete powder samples were collected from prism SW and 5 samples were extracted from prism TW. Table 5-2 lists the measured chloride content concentrations for all the samples extracted from both prisms. The location of each sample is measured from the edge of the prism in region A. Figure

5-23 is a sketch illustrating the location of the extracted powder samples in prism SW relative to the location of the reinforcement, embedded sensors, and flexural cracks. All the samples from prism SW had high levels of chloride ion concentrations, which exceeded the critical chloride threshold suggested by ACI 222R (2010) to cause a break down in the passive layer and initiate corrosion within concrete members. Furthermore, it can be seen that the samples taken from the vicinity of cracks had chloride ion levels that were on average two times larger than those measured in the samples extracted away from the cracks.

Table 5-2: Measured acid-soluble chloride content from prisms SW and TW

Prism	Sample ID	Location, (in.)	Chloride Content, (ppm)
SW	1	1.25	6517
	2	0.75	3300
	3	5.25	3023
	4	5.25	3554
	5	7.00	5411
	6	6.50	6950
	7	7.25	2718
	8	11.25	5590
	9	11.50	5541
	10	11.25	4950
	11	15.25	2300
TW	1	1.00	320
	2	5.75	128
	3	6.75	142
	4	9.89	179
	5	12.85	89

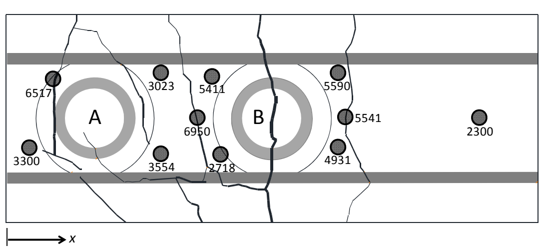

Figure 5-23: Location of the chloride content samples and measured acid-soluble chloride content in prism SW

The profiles of the average chloride contents are shown in Figure 5-24 for both prisms. For prism SW, the profile was created by averaging adjacent samples. As expected, the chloride contents for the prism exposed to salt water are very high and were on average seven times the critical chloride threshold (500 ppm) expected to initiate corrosion (ACI 222R, 2010). The minimum chloride levels in prism SW were recorded in region C due to the absence of cracks in that area. Hence, chloride ions were inhibited by the concrete barrier and diffused at a much slower rate. As expected, the measured levels in prism TW were lower than the critical chloride threshold level indicating a low risk of corrosion.

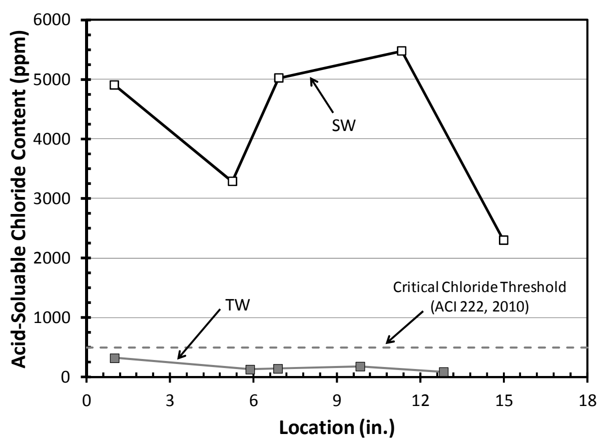

Figure 5-24: Profile of the average acid-soluble chloride ion content along the length of both prisms

5.6.2 Observations from Physical Autopsy

The final autopsy confirmed that the passive sensors were successful in detecting the onset of corrosion in the adjacent reinforcing bars. Figure 5-25 is a sketch illustrating the observed state of the reinforcement and the sacrificial element of the embedded sensors in prism SW. Photographs of the reinforcing bar sections and the sacrificial washers are shown in Table 5-3. Both reinforcing bars exhibited evidence of microcell corrosion where localized anodes formed in the immediate vicinity of the cracks. The washer in sensor SW-B was corroded at sections located directly under the flexural crack, while the remaining steel was undamaged. In contrast, the washer in sensor SW-A was entirely corroded without any trace of the original metal. These observations suggest that when the washers are embedded in concrete, localized corrosion is initiated in areas of high chloride concentrations (near cracks). Then, the corrosion damage spreads to consume the entire washer.

The autopsy results of prism TW are shown in Figure 5-26 and photographs documenting the observed state of the reinforcement and washers are shown in Table 5-4. Localized corrosion anodes formed on the reinforcing bar near sensor TW-A. The washer in Sensor TW-A was partially corroded and the corrosion damage was concentrated under a crack. No corrosion was noticed around sensor TW-B and its sacrificial washer was intact with no evidence of corrosion initiation.

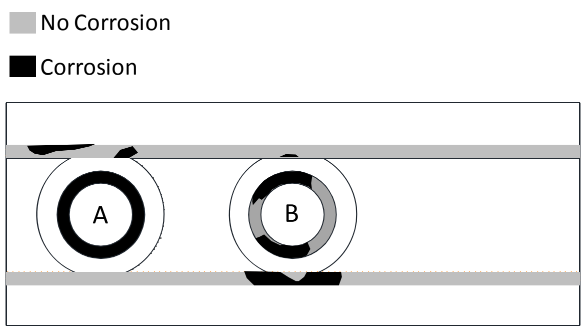

Figure 5-25: Observed corrosion damage in the reinforcing steel and sacrificial washers at the time of autopsy of prism SW

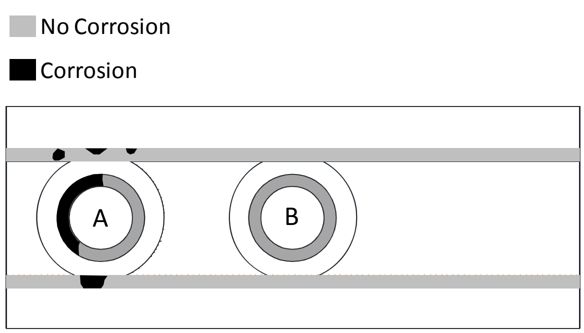

Figure 5-26: Observed corrosion damage in the reinforcing steel and sacrificial washers at the time of autopsy of prism TW

Table 5-3: Photographs of the steel reinforcement and sacrificial washers of prism SW after autopsy

	Region A	Region B	Region C
Reinforcing bar 1			
Reinforcing bar 2			
Sacrificial washer			No embedded sensor

Table 5-4: Photographs of the steel reinforcement and sacrificial washers of prism SW after autopsy

	Region A	Region B	Region C
Reinforcing bar 1			
Reinforcing bar 2			
Sacrificial washer			No embedded sensor

5.6.3 Mass Loss Results

The mass loss measurements were conducted on 4.0-in. rebar sections. Three rebar sections were cut from each reinforcing bar so that the centerline of the sections coincided with the centerline of the three regions within the prisms. Figure 5-27 summarizes the mass loss results for both prisms. As expected, higher levels of mass loss occurred in prism SW than prism TW. Furthermore, the results suggest a localized corrosion behavior where a single anode formed along each rebar. For example, rebar SW-1 developed an anode within region A where the losses reached 2.5%. However, sections B and C of rebar SW-1 experienced negligible losses. The local anode formed in region B for rebar SW-2. Both reinforcing bars in prism TW developed localized anodes in region A, which translated into mass losses of approximately 1%. Very low levels of mass loss were observed in region C within the two prisms due to the lack of cracks in that region. Low mass loss percentages (less than 0.3%) were measured in sections where no corrosion was visually observed after autopsy. These could be the result of mass loss in the native steel due to the harsh chemical cleaning required for mass loss measurements(ASTM G1 2003).

The levels of mass loss measured at the end of the exposure test were quite modest. The losses and patterns of observed corrosion damage are indicative of an early stage of corrosion. In practice, the repair schemes for concrete members with such low levels of damage are usually simple and relatively inexpensive(Emmons 1993). For example, surface sealers or surface replacement can be used to limit any further moisture ingress, hence, halting the corrosion process within concrete(ACI 222R 2010).

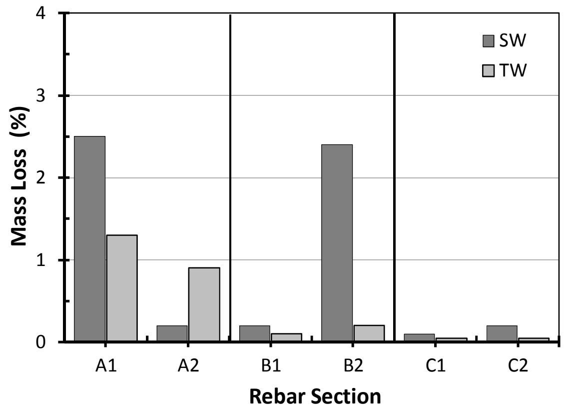

Figure 5-27: Mass loss results for rebar sections extracted from prisms SW and TW

5.7 DISCUSSION OF TEST RESULTS

5.7.1 Comparison of Sensor Response Observed Condition of Reinforcing Bars

All the signals obtained from the embedded NC sensors were reliable and correctly described the state of the adjacent reinforcing bars. The autopsy results confirmed the ability of the sensor to detect corrosion initiation within concrete members. The choice of relatively thin washers allowed the early detection of corrosion activity. The mass loss in the sections of the reinforcing bars that experienced corrosion ranged between 0.9% and 2.5%. Higher thresholds of corrosion damage can be detected if thicker sacrificial elements are used (Abu Yosef, et al. 2012).

The sensor interrogation results suggest that the time needed for the NC sensor to start transitioning and reach the corroded state is highly dependent on the size of the adjacent cracks. Figure 5-28 plots the time needed by each of the embedded sensors to reach the corroded state as a function of the size of the largest adjacent crack. Given that all the sensors were fabricated using identical sacrificial washers, it can be confirmed that for sensors embedded in the same prism, wider cracks lead to a faster switch in the signal of the NC sensors. In addition, for sensors positioned under cracks of the same size (0.03 in.), the sensor experiencing more severe chloride exposure reached the corroded state faster.

Figure 5-29 plots the measured mass loss at each of the rebar sections adjacent to the embedded NC sensors against the time the sensor needed to reach the corroded state. It can be seen that higher corrosion levels were observed in the prism exposed to salt water. Notably, while more time was needed to switch the signal of sensor SW-B to the corroded state compared with sensor SW-A, the measured losses in both regions were close in value. Generally, the losses in beam TW were lower than the SW samples.

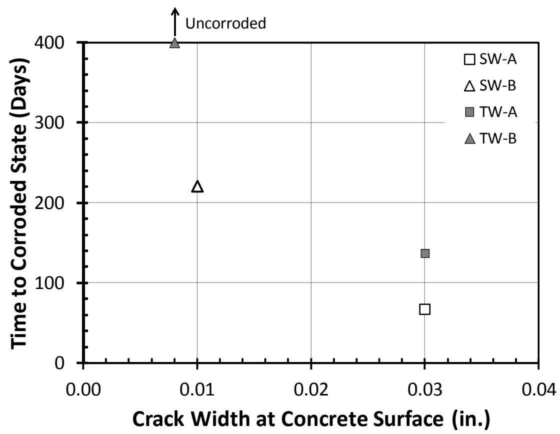

Figure 5-28: Time each sensor needed to reach the corroded state compared the width of the largest flexural crack in the vicinity of the sensor

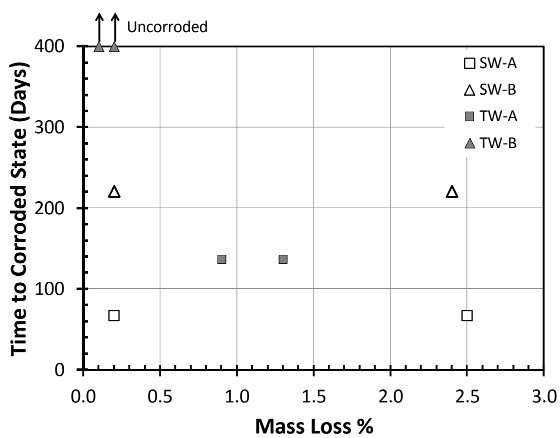

Figure 5-29: Time to reach the corroded state against measured mass losses at adjacent rebar sections

5.7.2 Reliability of the Linear Polarization Resistance (LPR) Method

The results presented in Section 5.5.2 indicated the ability of the LPR technique to detect regions of localized corrosion. In sections where the measured current densities were higher than the threshold current value suggested by the manufacturer for severe corrosion, corrosion damage was observed in the rebar. On the other hand, sections where the currents were consistently low exhibited a passive corrosion behavior and limited corrosion damage. As with the half-cell method, the LPR technique was very sensitive to temperature and moisture level variations.

5.7.3 Reliability of the Half-Cell Method

The results of the half-cell measurements confirmed the reliability of the electrochemical technique and demonstrated its ability to distinguish between the levels of chloride exposure in each prism. The potentials measured in the prism exposed to salt water solution were always more negative than the threshold indicating a high risk of corrosion as suggested by ASTM C876(2009). In contrast, the recorded potentials in the prism exposed to tap water were on average indicative of a moderate corrosion risk.

However, the readings in both prisms were very sensitive to the moisture level. Readings taken after the wet periods were on average 100-150 mV more negative than the half-cell potentials recorded after the dry periods. Such behavior is expected because the method relies primarily on the ease of ion transfer within the concrete medium(Jones 1996). However, such large variation in potential values can lead to the wrong conclusions regarding the corrosion activity in field applications. This is more important in practice where a single set of half-cell measurements is typically use to evaluate the corrosion risk without an a priori knowledge of the moisture levels in the structure.

In addition, the measured half-cell potentials in a single day were generally uniform along the length and width of each prism. The maximum observed difference in the measured potential values were on average less than 50 mV. Hence, the half-cell results were not spatially sensitive enough to identify the observed regions of localized corrosion. For example, the half-cell potentials measured at the middle of regions A and C (12 in. apart) of prism SW were identical in value and suggested a high risk of corrosion, however, the autopsy showed that the rebar sections in region C were passive and did not experience any corrosion damage.

Figure 5-30 plots the correlation between the half-cell potentials and the simultaneous corrosion current densities measured using the GECOR™ equipment in the prisms. It can be seen that the readings with more negative potentials had higher corrosion rates. Furthermore, there is a clear separation between the data recorded in prism SW and those from TW. However, the results demonstrate the poor correlation between the results obtained using the two methods. Figure 5-30 also includes the threshold values at which severe corrosion risk is assumed to be taking place based on the guidelines and recommendations used in practice. It can be seen that the methods provide conflicting information in 40% of the readings. The data points in the lower left corner belong to the measurements where the half-cell method indicated a high risk of corrosion while the corrosion rate was actually quite small.

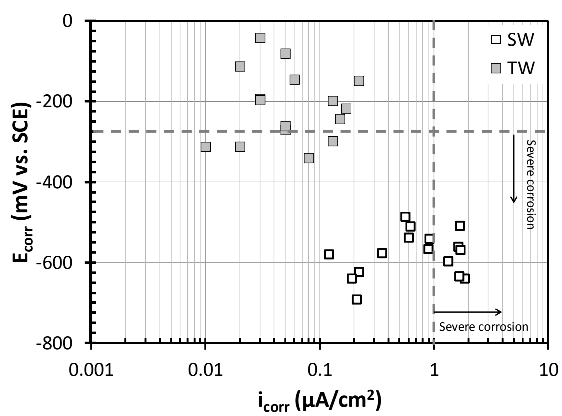

Figure 5-30: Correlation between the half-cell potentials and LPR corrosion current densities measured using GECOR™ in prisms SW and TW

5.8 SUMMARY

Four NC sensors were embedded in two reinforced concrete prisms. The prisms were exposed to two different levels of chloride exposure. The sensor reliability was assessed based on the measured frequency response. Electrochemical evaluation techniques were also used to assess the risk of corrosion within the prisms and their results were used to evaluate the performance of the NC sensors. Table 5-5 and Table 5-6 summarize the results and conclusions from the different corrosion assessment methods for each section of reinforcing bar. The maximum and minimum recorded half-cell potentials during the last 100 days of exposure are tabulated. The linear polarization densities listed only include the values measured prior to the physical autopsy. The autopsy findings and mass loss results for the reinforcing bars in both prisms are also reported.

The embedded NC sensors successfully detected corrosion initiation in both test prisms. Corrosion was observed on the surface of at least one adjacent reinforcing bar for the three passive sensors that detected corrosion. No corrosion was observed on the adjacent reinforcing bars for the one NC sensor that indicated corrosion was not present. Furthermore, unlike the electrochemical techniques, the response of the passive sensors was insensitive to environmental variations. Once the corroded frequency was reached, the resonant frequency of each sensor remained constant in all subsequent interrogations. Hence, the passive sensor platform provides an economical, reliable and nondestructive alternative for corrosion detection within concrete structures.

After removing the concrete cover, localized corrosion was observed on the surface of the reinforcing bars in the immediate vicinity of the cracks. The formation of localized anodes is typically observed in members with early stages of corrosion damage and is expected for cases of microcell corrosion. As a result, the level of corrosion damage varied along the length of each reinforcing bar. The amount of corrosion also varied between the two reinforcing bars embedded in the same prism.

The results of this preliminary investigation emphasized the sensitivity of the sensor output to the presence and size of cracks in the vicinity of the sensor. However, due to the relatively small size of the prisms, the effect of the crack location and distribution on the reliability of the sensor could not be examined. A detailed examination of the effect of cracks on the sensor response is presented in Chapter 8.

The unpredictable behavior of sensor SW-B where the sensor response stabilized in transition can affect ability to interrogate the sensor using rapid acquisition techniques and can lead to misinterpretation of the sensor signal. However, this unpredictable response was not observed in any other test and can be the result of local and unique electrochemical conditions that caused temporary repassivation of the steel washer. In addition, an alteration to the sensor design which employs diffusion layers to uniformly distribute the chlorides over the surface of the washer was found to eliminate the issue. A detailed discussion of the diffusion layer concept is found in Chapter 8.

Table 5-5: Summary of results from all the techniques used to monitor corrosion in prism SW.

Prism	SW					
Region	A		B		C	
Reinforcing bar	1	2	1	2	1	2
Passive Sensor	Corrosion		Corrosion		-	
Half-Cell (mV vs. SCE)	-596 to -420		-585 to -429		-580 to -390	
	Severe Corrosion	Severe Corrosion	Severe Corrosion	Severe Corrosion	Severe Corrosion	Severe Corrosion
Linear Polarization (µA/cm^2)	0.62 to 1.68	0.12 – 0.21	0.35 to 0.91	1.68 to 1.85	-	-
	Inconclusive	Low Corrosion	Inconclusive	Severe Corrosion	-	-
Chloride Content (ppm)	4100		5253		2300	
	Corrosion	Corrosion	Corrosion	Corrosion	Corrosion	Corrosion
Mass Loss (%)	2.5	0.2	0.2	2.4	0.1	0.2
Physical Autopsy	Corrosion	No Corrosion	No Corrosion	Corrosion	No Corrosion	No Corrosion

Table 5-6: Summary of results from all the techniques used to monitor corrosion in prism TW.

Prism	TW					
Region	A		B		C	
Reinforcing bar	1	2	1	2	1	2
Passive Sensor	Corrosion		No Corrosion		-	
Half-Cell (mV vs. SCE)	-285 to -102		-284 to -103		-276 to -96	
	Low to Intermediate Corrosion	Low to Intermediate Corrosion	Low to Intermediate Corrosion	Low to Intermediate Corrosion	Low to Intermediate Corrosion	Low to Intermediate Corrosion
Linear Polarization ($\mu A/cm^2$)	0.50 to 0.51	0.41 to 0.71	0.60 to 0.75	0.24 to 0.60	0.50 to 0.67	0.30 to 0.50
	Low to Intermediate Corrosion	Low to Intermediate Corrosion	Low to Intermediate Corrosion	Low to Intermediate Corrosion	Low to Intermediate Corrosion	Low to Intermediate Corrosion
Chloride Content (ppm)	300		161		89	
	No Corrosion	No Corrosion	No Corrosion	No Corrosion	No Corrosion	No Corrosion
Mass Loss (%)	1.3	0.9	0.1	0.2	0.0	0.0
Physical Autopsy	Corrosion	Corrosion	No Corrosion	No Corrosion	No Corrosion	No Corrosion

CHAPTER 6

Design of Long-Term Tests of Noncontact Corrosion Sensor

6.1 OVERVIEW

The results of the preliminary investigation, discussed in Chapter 5, demonstrated the reliability of the noncontact (NC) corrosion sensor. The embedded sensors successfully detected the onset of corrosion in the reinforced concrete prisms. The sensors' output was reliable and insensitive to fluctuations in temperature and moisture content. However, the small size of the prisms did not allow for assessing the spatial coverage of the embedded sensors or the sensitivity of the sensors to different exposure levels. Furthermore, all sensors embedded in the prisms were located directly underneath cracks providing a direct access to salt water, hence, the influence of the crack location on the sensor response needed to be examined. To this end, NC sensors were embedded in larger scale reinforced concrete specimens that were designed to represent sections of a bridge deck. The specimens were continuously exposed to wet and dry cycles of either a salt water solution or tap water for more than 19 months.

The construction details of the large-scale specimens and the design of the long-term experiments are described in Section 6.2 and Section 6.3, respectively. Chapter 7 includes an analysis of the response of the embedded NC sensors and compares the sensors output to conclusions drawn from the half-cell readings, linear polarization measurements, and observations from the physical autopsy.

6.2 SPECIMEN CONSTRUCTION

Four identical reinforced concrete slab specimens were constructed for the long-term tests. The dimensions and reinforcement of the specimens were selected to reflect a typical bridge deck design. The slabs were 11.5-ft long, 12-in. wide and 8-in. deep and each slab had two layers of reinforcing steel. A cross-section illustrating the arrangement of the steel reinforcement is shown in Figure 6-1. The top layer of steel reinforcement consisted of two #5 longitudinal bars that were supported on four transverse 0.75-in. diameter PVC pipes. To minimize the time to initiation of corrosion, both the sensors and the top reinforcement layer had a nominal clear cover of only 1.0 in. The electrical connection needed for the electrochemical measurements was set by soldering an 18-AWG enameled copper wire to the end of each top reinforcing bar. The solder region was thoroughly dried and covered using heat shrink tape to prevent galvanic corrosion (Figure 6-2). The bottom steel layer was used to prevent cracking and accidental damage during lifting and consisted of three #3 longitudinal and ten #3 transverse bars that were evenly spaced. The two steel layers were kept electrically isolated to prevent macrocell corrosion.

The sensors were secured using two #3 transverse bars spanning between the top two longitudinal bars (Figure 6-3). A plastic zip tie was also used to prevent the sensor from tilting during concrete placement. In order to prevent bimetallic corrosion, the transverse support rebars were dipped in black epoxy paint. Furthermore, shrink tape was used at the points of intersection with the main longitudinal reinforcement. In order to ensure early detection of corrosion, the sensors were positioned so that the sacrificial washer was at the level of the top surface of the longitudinal reinforcement.

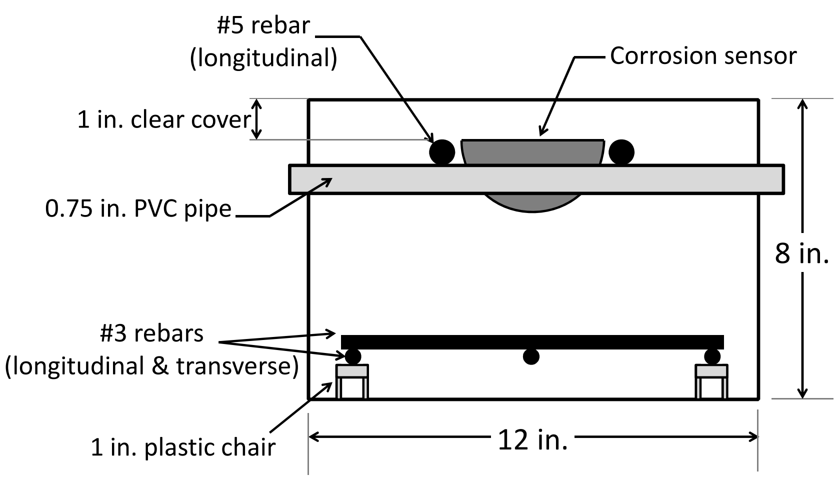

Figure 6-1: Cross-section of the reinforced concrete slab specimen

Figure 6-2: Electrical connection for electrochemical measurements

Figure 6-3: NC corrosion sensor attached to the top reinforcement layer

Figure 6-4 shows the layout of the sensors and the steel reinforcement in the four slabs prior to the concrete placement. It can be seen that in addition to the NC corrosion sensors, passive conductivity sensors were also embedded in the specimens (Kim 2013).

The slabs were cast on June 19th 2011 using a 0.42 w/c concrete mix with 0.75 in. maximum aggregate size and a 28-day compressive strength of 3920 psi. The specimens were covered with plastic sheets and allowed to cure for three weeks. At the end of the curing period, the forms were removed and the sensors were interrogated. The initial readings indicated that all the embedded sensors were intact and survived concrete placement.

Figure 6-4: Layout of the NC corrosion sensors, passive conductivity sensors, and steel reinforcement

6.3 DESIGN OF EXPERIMENT

Two main issues were evaluated in this study: (1) the threshold level of corrosion damage in the embedded reinforcement that will cause the sensor to respond in the corroded state and (2) the effect of the chloride concentration on the sensor behavior. The first issue was evaluated using two groups of sensors that are identical except for the thickness of the sacrificial element (0.001 or 0.002-in. thick washers). All sensors embedded in a given slab were fabricated with the same washer thickness. The slabs were divided also into two groups: the first was exposed to a high chloride concentration using 3.5% salt-water solution, while the second group was exposed to tap water. Table 6-1 lists the experimental parameters and the nomenclature adopted.

Table 6-1: The experimental parameters and the nomenclature

		Corroding Solution	
		3.5% Salt Water	Tap Water
Washer Thickness	0.001 in.	S1	T2
	0.002 in.	S2	T2

6.3.1 Experimental Set-up

After curing for 28 days, the slabs were placed on reaction beams and were subjected to sustained end point loads. Intermediate supports were placed at the middle section of the slab creating a region of constant negative moment (Figure 6-5). As the post-tension rods were loaded, cracks started to form on the top surface of the slab. The load was locked when the average crack width reached 0.020 in.

Puryear (2007) employed the test set-up described above to evaluate the performance of the initial passive corrosion sensor prototype in concrete. In order to promote the corrosion process, Puryear placed salt water reservoirs over the constant moment region during the wet periods. Due to the direct exposure to chlorides, it was expected that the highest corrosion damage will take place within the constant moment region. However, the autopsy results indicated that corrosion was more active in the regions just outside the reservoirs. This is due to the continuous availability of moisture and oxygen in the transition regions. Based on these observations, the set-up was adjusted and the chloride exposure was achieved by dripping the corroding solution over the constant moment region. Consequently, the constant moment region simulates a splash zone and corrosion is accelerated due to the continuous availability of oxygen. To this end, the plastic containers were mounted above each beam. Eight dripping holes were drilled at a uniform spacing over the constant moment zone using a 0.1-in. diameter drill bit. The solution containers were refilled regularly to maintain continuous dripping during the wet periods. On average, a total of 60 gallons of the corroding solution were dripped on each slab during a wet period.

The slabs were stored in an unheated building and experienced temperature fluctuations of more than 70 °F during the test period. The slabs were exposed to moisture cycles between July 19, 2011 and January 28, 2013 (560 days). Initially, an exposure cycle of 3 days wet and 4 days dry was used. However, the dry period was increased to 11 days starting February 2012 to allow the concrete in the splash zone to dry completely, which promotes faster corrosion development. Beginning in December 2012, infrared heaters were positioned over the slabs during the dry periods to dry the concrete more rapidly. The 36-in. long heaters maintained a constant surface temperature of 105° F within the constant moment region and the corrosion rates increased dramatically.

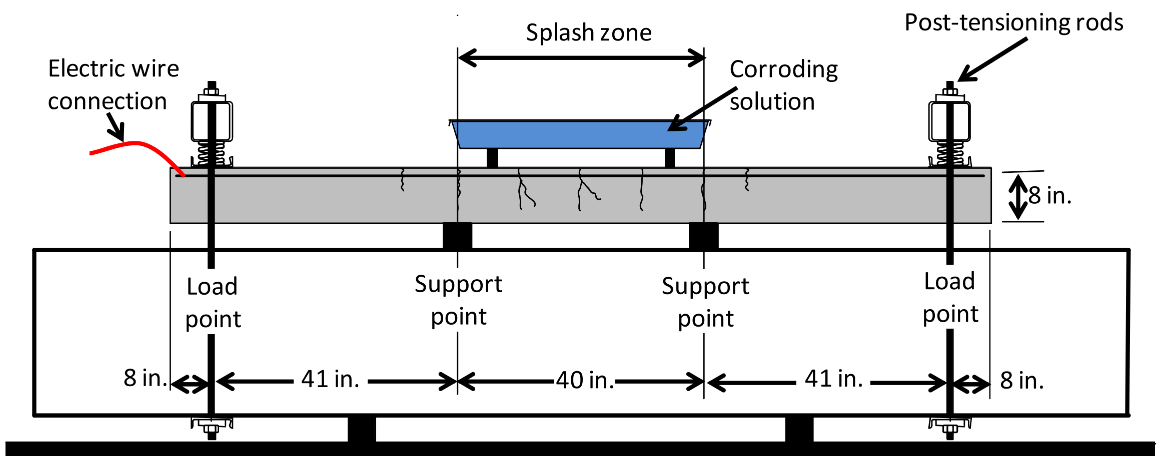

Figure 6-5: Long-term test set-up

6.3.2 Layout of Sensors

Eight corrosion sensors were distributed along the length of each slab as shown in Figure 6-6. However, the corroding solution was dripped only in the midsection of the specimens. As a result, the sensors were exposed to different level of chlorides. Sensors 1 and 8 were positioned sufficiently far from the splash zone that the surrounding concrete was anticipated to remain dry throughout the test period and no exposure to chlorides. Hence, the risk of corrosion was low and the sensors were not expected to show any indications of corrosion. Sensors 3, 4, 5, and 6 were directly exposed to the corroding solution and exhibit the highest levels of corrosion risk. However, the corrosion risk was still variable in this region, because the risk depends on the location and size of adjacent cracks. Finally, sensors 2 and 7 were located in the transition zone, where chlorides need to migrate through the concrete to initiate corrosion at the location of the sensor.

In addition, five passive conductivity sensors were embedded in each specimen (Figure 6-4). The conductivity sensor prototype was developed at UT Austin to measure the changes in the conductivity of the concrete medium due to the presence of chlorides and moisture. The large scale of the long-term test specimens and the variability of the exposure conditions allowed for assessing the reliability of the conductivity sensor. Details regarding the development of the passive conductivity sensor and the observations from the long-term tests can be found in Kim(2013).

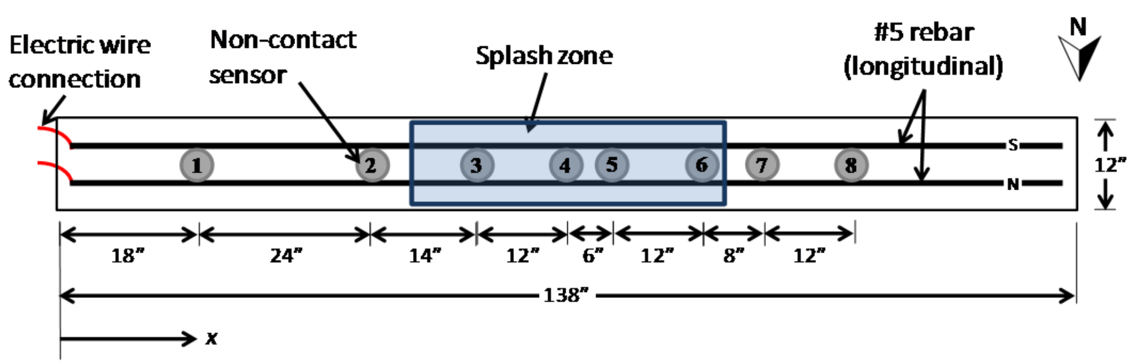

Figure 6-6: Slab layout and the distribution of the embedded corrosion sensors

6.3.3 Nondestructive Testing

The sensors were interrogated after each wet and dry period using a five-turn reader coil with a 4-in. diameter. The coil was assembled using an 18-AWG copper wire that was connected to a 3-ft coaxial cable resulting in a self-resonant frequency of 6 MHz. The reader coil was placed directly on the concrete surface resulting in a read distance of approximately 1.25 in. For the first ten months of testing, the interrogations were conducted by measuring the impedance response using a Solartron 1260A Impedance/Gain-Phase Analyzer. Each impedance measurements took approximately 7 minutes required bulky equipment. To address those issues, a bench-scale reader was developed by Travidi et al. (2012) that employed an RF instrumentation module of a National Instruments PXI system to measure the strength of the reflected signal at the reader coil. The reflectometer technique allowed for rapid interrogation and reduced the measurement time to less than 10 seconds. The reflectometer reader was used for interrogating the sensors starting June 2012. Travidi et al. (2012) demonstrated that the reflectometer method provides an accurate measurement of the resonant frequency of the embedded sensors. However, information regarding the phase angle and the pseudo quality factor cannot be extracted from the measured data using the reflectometer method. Hence, the impedance analyzer was used to measure the response of a sensor whenever the reflectometer interrogations indicated a noticeable shift in the resonant frequency.

Electrochemical corrosion monitoring techniques were also used to assess the corrosion risk within the slab specimens. Half-cell potentials were measured using a saturated calomel electrode (SCE).The measurements were conducted and interpreted in accordance with ASTM C876(2009). In order to capture the differences among the three exposure regions, the measurements were collected at 13 points along the length of each reinforcing bar (Figure 6-7). The temperature of the concrete surface was recorded immediately before the half-cell readings were measured. The half-cell measurements were conducted at the end of the wet and dry periods on a biweekly basis for the first 10 months of exposure. The measurements were taken after the first wet and dry period of each month after the first year.

The linear polarization resistance technique was used to measure the corrosion rates of the steel reinforcement. Data were collected using a GECOR 8™ corrosion rate system with copper/copper sulfate reference and auxiliary electrodes and a stainless steel guard ring. The corrosion current densities were measured at 13 points along the length of each reinforcing bar (Figure 6-7). In order to prevent excessive polarization of the reinforcing bars, consecutive measurements on the same rebar were separated by a thirty-minute waiting period. In order to evaluate the consistency of the linear polarization readings, the readings were repeated at seven randomly selected points, which were taken an average 3 to 4 hours after the first measurement. Because the linear polarization equipment was not available continuously, a total of fourteen set of readings were collected throughout the exposure period. The measurements were taken in August 2011, April 2012, August 2012, November 2012, and January 2013. In order to assess the effect of moisture on the measured current densities, readings were taken during consecutive wet and dry periods.

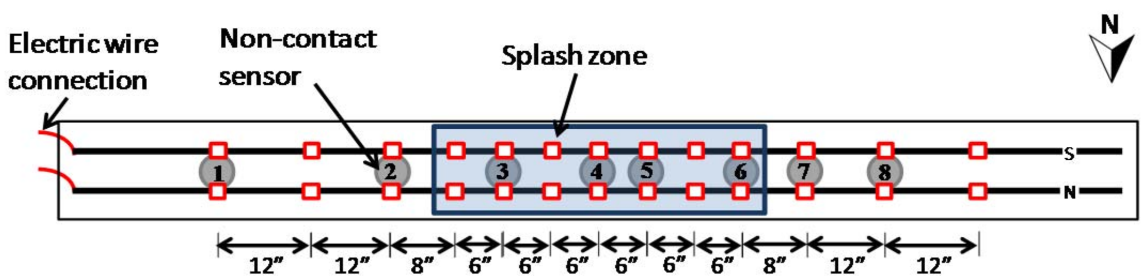

Figure 6-7: Half-cell and linear polarization measurement points

6.3.4 Post-Experiment Autopsy and Destructive Testing

At the end of the exposure period, the slabs were cleaned with tap water and the distribution of the cracks over the top surface of each slab was mapped. The size and location of each crack were documented and the crack maps for each of the slabs is shown in Figure 6-8 through Figure 6-11.

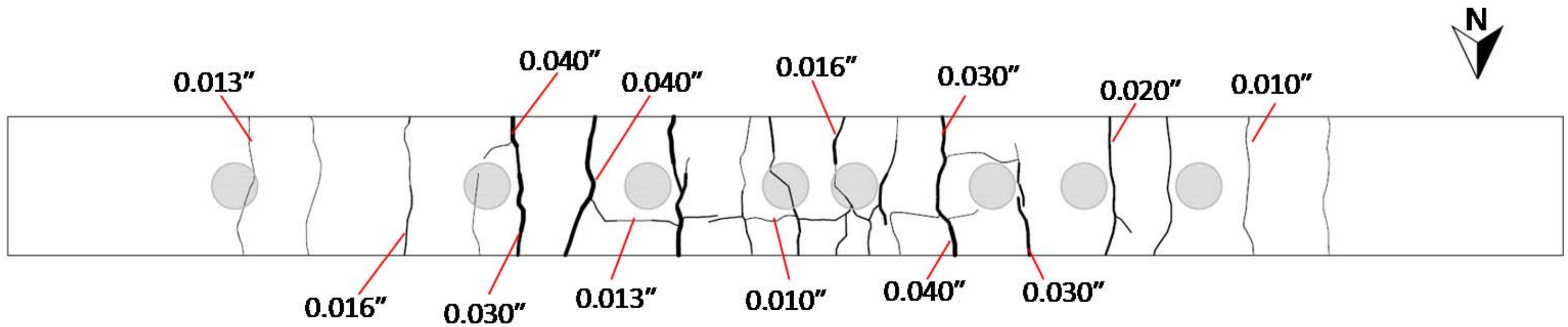

Figure 6-8: Crack map of slab S1

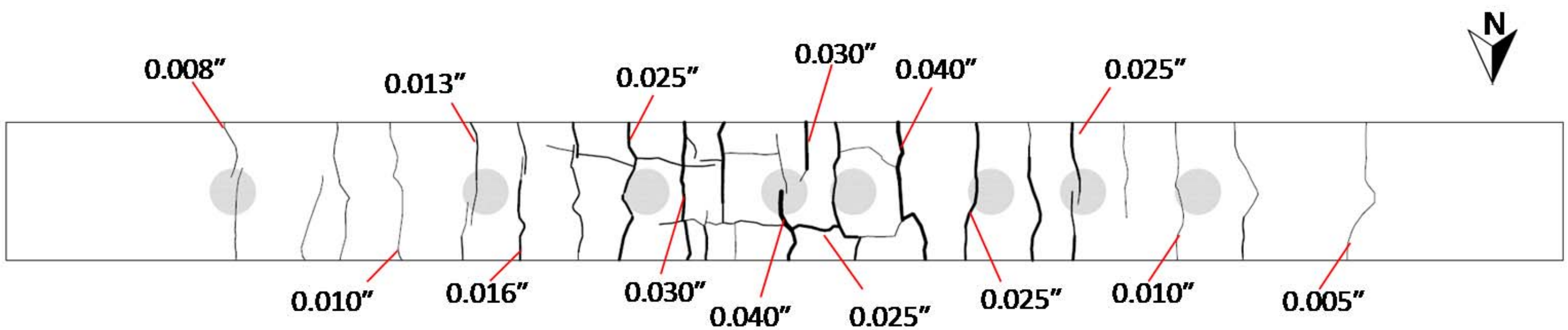

Figure 6-9: Crack map of slab S2

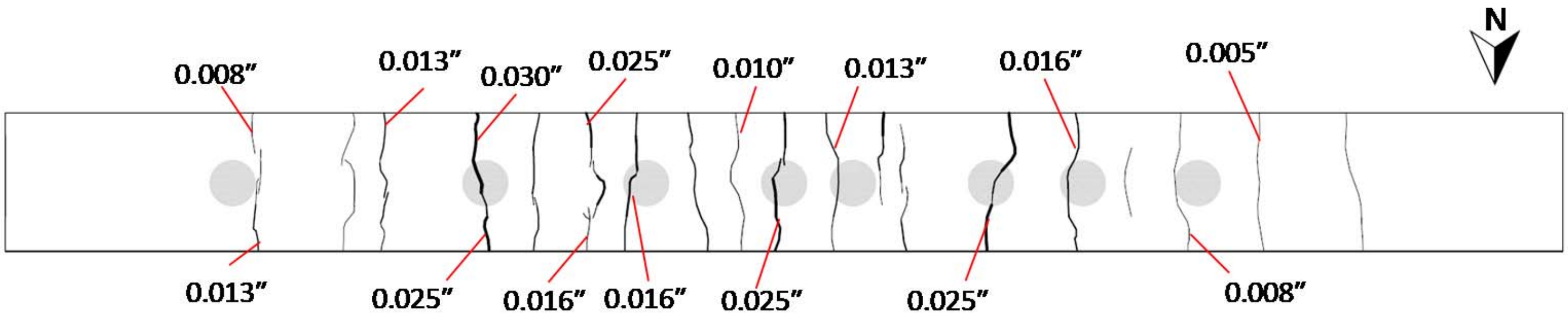

Figure 6-10: Crack map of slab T1

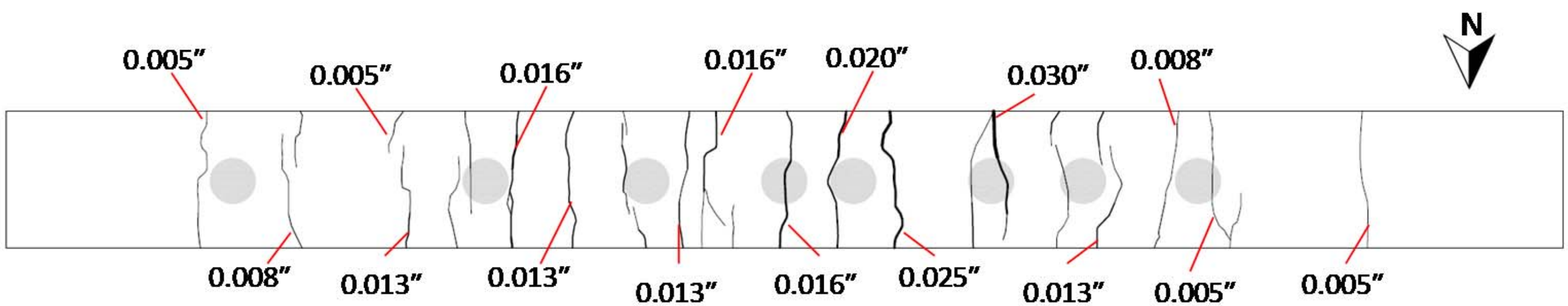

Figure 6-11: Crack map of slab T2

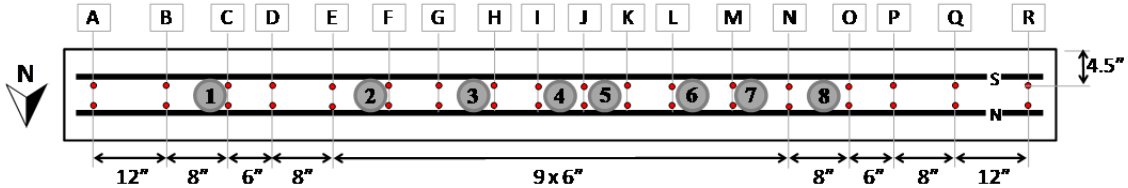

Figure 6-12: Locations of the concrete powder samples

Concrete powder samples were collected at 18 locations along the length of each specimen to determine the chloride concentration profiles (Figure 6-12). Each concrete powder sample consisted of a mixture of the dust collected from two adjacent holes. The samples were extracted by drilling vertically from the top surface of the concrete using a 0.5-in. diameter rotary impact drill (Figure 6-13). The concrete powder was taken starting from a depth of 1 in., the clear cover of the reinforcement steel. The samples were sent to Tourney Consulting Group in Kalamazoo, Michigan for analysis. The chloride ion concentrations were determined using the acid-soluble titration method in accordance with ASTM C1152/ C1152M (2004) and were reported in parts per million (ppm).

Figure 6-13: Chloride sample extraction with hammer drill

The physical autopsy of the slabs was performed to determine the extent of corrosion in the reinforcement and the condition of the sensors in February 2013. The concrete cover was mostly removed using an EDCO scarifier (Figure 6-14). In order to minimize accidental damage of the reinforcing bars or passive sensors, a chisel was used to chip the remaining concrete cover (Figure 6-15). Then, the condition of the NC corrosion sensors and the surrounding reinforcement steel was documented and photographed.

In order to evaluate the reliability of the NC sensors and the accuracy of the corrosion rate results, mass loss measurements were conducted using sections of the reinforcing steel removed from the slabs. The measurements were performed in accordance with ASTM G1(2003) and the chemical procedure C.3.5 was selected for the removal of the corrosion product. Thirteen 4.0-in. sections were cut from each reinforcing bar. The sections were selected so that their centers corresponded to the points where half-cell and linear polarization measurements were conducted (Figure 6-7). As a result, the mass loss was measured for the two sections of reinforcing bars adjacent to each embedded sensor.

Figure 6-14: Concrete cover removal using the scarifier

Figure 6-15: Concrete cover chipping using a chisel

Figure 6-16 plots the timeline of the long-term exposure test and highlights the main events associated with the test.

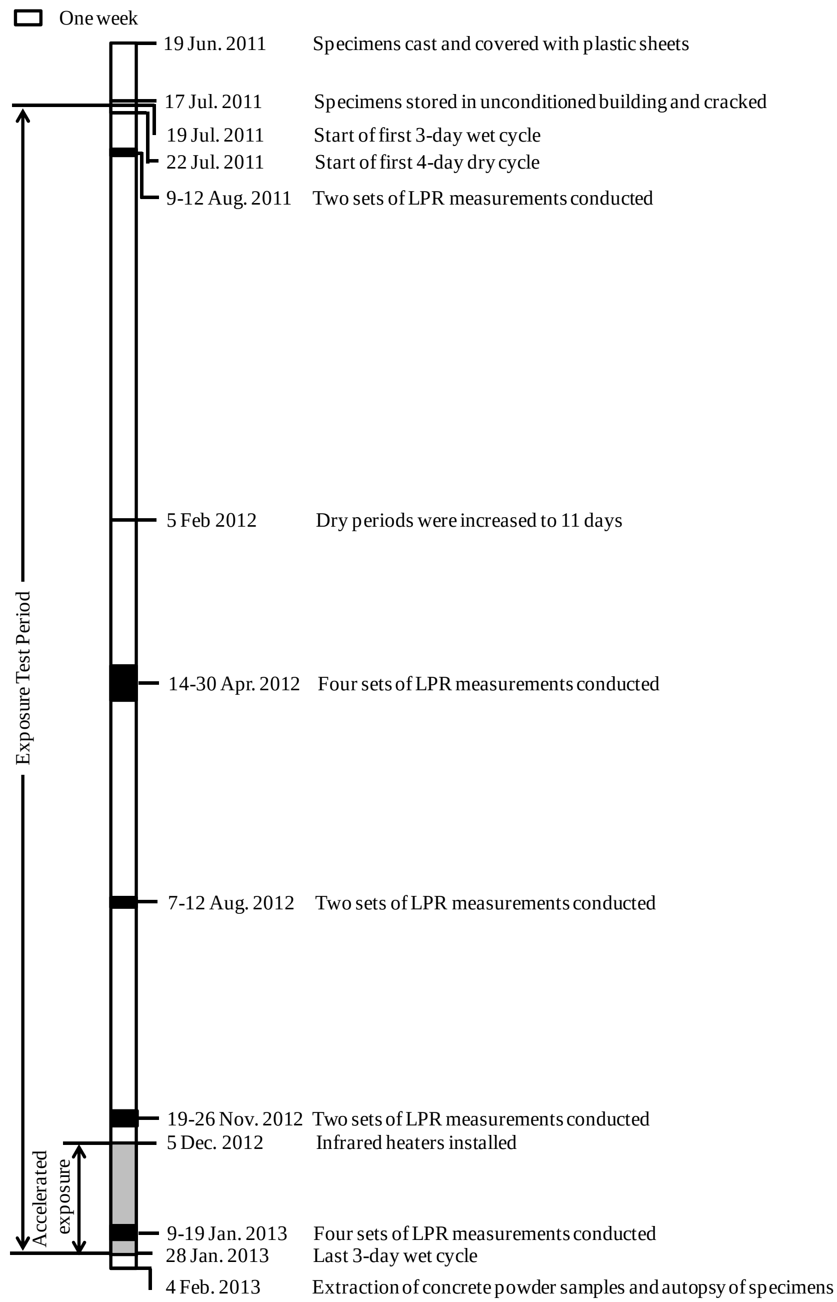

Figure 6-16: Timeline of accelerated corrosion tests for reinforced concrete slabs

CHAPTER 7

Analysis of Response of Noncontact Corrosion Sensors

7.1 OVERVIEW

The long-term exposure tests were initiated in July 2011 to evaluate the reliability of the noncontact (NC) passive sensors. The design of the experiment and the details of the specimens were discussed in Chapter 6. The response of the embedded NC corrosion sensors during the test is summarized in Section 7.2 and the measured response of each sensor is presented in Appendix D. Section 7.3 presents the results of the electrochemical evaluation techniques employed throughout the exposure period and Section 7.4 includes a summary of the physical autopsy findings and highlights the observed corrosion damage after the conclusion of the exposure test. An assessment of the reliability of the NC sensor in detecting the initiation of corrosion in the steel reinforcement is provided in Section 7.5. The latter section also includes a comparison between the response of the sensors and the conclusions drawn from electrochemical corrosion evaluation techniques. In Section 7.5.1, the results of the mass loss measurements are used to determine the corrosion damage associated with the shift in sensor response. Finally, the reliability of the linear polarization technique is evaluated using the mass loss data in Section 7.5.2.

7.2 MEASURED RESPONSE OF THE NC SENSORS

The impedance response of the embedded sensors was acquired regularly during the test period. The measured phase of impedance was used to assess the state of the sensor at the time of interrogation. Figure 7-1 shows the change in the measured phase response for sensor S2-6 due to the corrosion of the sacrificial washer. Initially, the resonant frequency, phase dip and bandwidth remained constant and identical to the response acquired on day 7. After 315 days of exposure to salt water, the resonant frequency started decreasing gradually, indicating the onset of the transition period. The shift in frequency was accompanied by a reduction in phase dip and a widening of the bandwidth. Finally, the resonant frequency of the sensor reached the resonant frequency of the corroded state (f_{rc}) after 533 days. The behavior shown in Figure 7-1 was typical for all the sensors that shifted to the corroded state during the test, however, the time needed to initiate transition and reach the final frequency varied.

On the other hand, the sensors that remained in their uncorroded state exhibited limited variation in the measured phase response throughout the exposure test. Figure 7-2 shows the phase response of sensor S2-1 acquired at different times during the test. It can be seen that there are only minor differences between the readings acquired at the beginning and at the end of the test. Slight shifts in the resonant frequency and phase dip were observed and can be attributed to numerous factors including variations in temperature and the moisture content, and reader coil deterioration.

The maximum recorded deviation in the measured resonant frequency of the sensors that remained in the uncorroded state was less than 5% of the range of available frequencies between the uncorroded state frequency (f_{se}) and the corroded state frequency (f_{rc}). Further details regarding the variation in the sensor response due to the environmental conditions are provided in Appendix C.

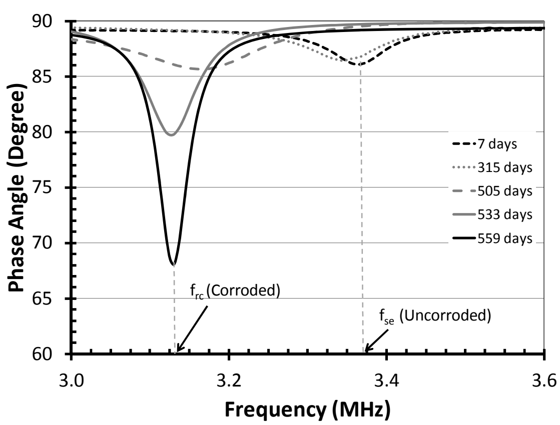

Figure 7-1: Measured phase response of sensor S2-6 at 7, 315, 505, 533, and 559 days of exposure

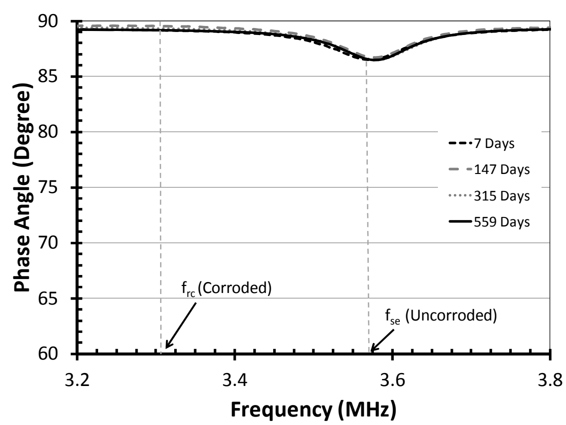

Figure 7-2: Measured phase response of sensor S2-1 at 7, 147, 315, and 559 days of exposure

The shift of the sensor response to the corroded state is associated with changes in the resonant frequency, phase dip, and bandwidth (Figure 7-1). As discussed in Chapter 3, the change in the resonant frequency due to the corrosion of the sacrificial element is monotonic and irreversible. Furthermore, the resonant frequency of an embedded sensor is relatively insensitive to the changes in the environmental conditions and can be measured easily using the fast Reflectometer interrogation technique. Hence, the measured resonant frequency was used to identify the state of the embedded sensor. In this Chapter, the frequency shift is expressed as a percentage of the available dynamic frequency range ($f_{se} - f_{rc}$). Hence, the corroded (f_{rc}) and uncorroded (f_{se}) limit states are equivalent to 0% and 100%, respectively.

The changes in the measured resonant frequencies of each of the sensors embedded in slabs S1 and S2 over the exposure test period are shown in Figure 7-3 and Figure 7-4, respectively. In slab S1, three sensors shifted to the corroded state and two were in transition when the exposure test was stopped in January 2013. Sensors S1-2 and S1-3 switched to the corroded frequency in less than 100 days of exposure. The transition period for sensors S1-2 and S1-3 was short and lasted less than three weeks. No changes in the frequency response were measured in any of the S1 slab sensors for the following 300 days. The resonant frequency of sensor S1-4 started transitioning after 380 days of exposure and reached the corroded state in less than 14 days. Sensors S1-6 and S1-7 started the shift from the initial frequency after the installation of the infrared heaters and were in the transition region at the end of the experiment. Sensor S1-5 was the only sensor located in the high exposure or transition regions that remained in its uncorroded state. However, signs of corrosion damage on the sacrificial washer of sensor S1-5 were observed during the physical autopsy.

In slab S2, all the sensors embedded in the splash zone shifted to the corroded state. However, the sensors in the dry and moist zones remained in the uncorroded state throughout the test period. Sensor S2-4 was located under a large crack (0.04 in.) and shifted to the corroded state in less than 100 days. Sensors S2-3 and S2-6 started their transition to the corroded state after 370 days of exposure. The transition time of sensor

S2-6 was approximately twice as long as the transition time of sensors S2-3 and S2-4. Finally, sensor S2-5 transitioned from the uncorroded state at day 475 and reached the corroded state after two months in transition.

The time needed to reach the corroded state and the time in transition for each of the corroded sensors in slabs S1 and S2 are shown in Figure 7-5. It can be seen that the sensors started the transition to the corroded state either within the first 100 days of exposure or after 350 days. Both time periods correspond to the summer months where higher ambient temperatures were present and an elevated corrosion activity is expected within the concrete slabs. The results indicate that there is a wide variability in the time needed to shift from the uncorroded state between the sensors embedded in a single slab. This is due to the fact that the time needed to start the transition period is highly dependent on the location of the sensor and the size of adjacent cracks.

The transition times for the sensors embedded in slab S1 were faster when compared with the sensors with the sensors having thicker washers in slab S2. The transition times in slab S1 ranged between 14 and 24 days (average 18 days) while the average transition time for the sensors in slab S2 was approximately 65 days and ranged between 45 and 110 days. Longer transition times for thicker washers were also observed in parametric studies evaluating the corrosion rates of washers with different thicknesses exposed to uniform corrosion damage (Abu Yosef, et al. 2012).

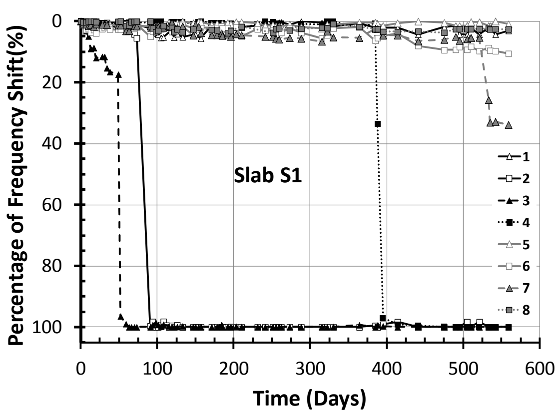

Figure 7-3: Measured shift in resonant frequency for the sensors in slab S1

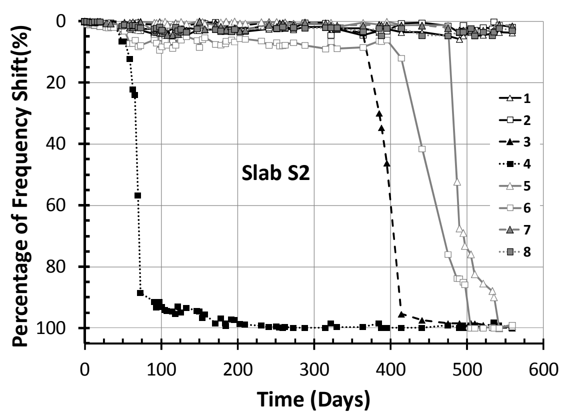

Figure 7-4: Measured shift in resonant frequency for the sensors in slab S2

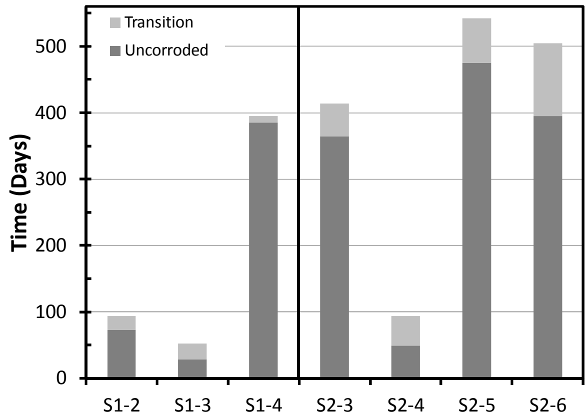

Figure 7-5: Number of days spent in the uncorroded state and transition for the corroded sensors in slabs S1 and S2

All the sensors embedded in the slabs exposed to tap water remained uncorroded throughout the exposure period. Figure 7-6 and Figure 7-7 show the shift in the resonant frequency of each of the sensors in slabs T1 and T2, respectively. Slight deviations from the initial resonant frequency were observed in almost all of the sixteen sensors embedded in T1 and T2. However, the observed deviation was always less than 5% of the available dynamic range. Furthermore, the phase response plots did not indicate any other signs of transition from the uncorroded state. The deviation can be the result of numerous factors, including temperature and moisture fluctuations and errors in the extraction of the resonant frequency from the phase response Andringa (2006).

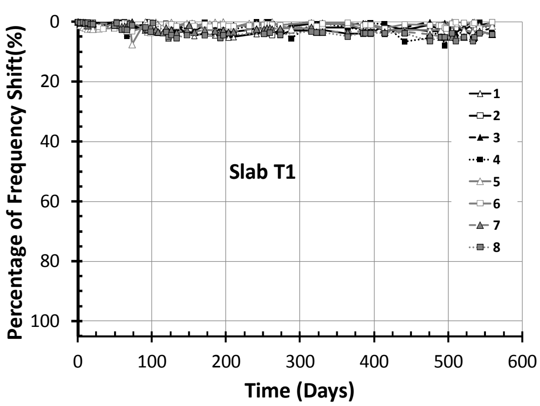

Figure 7-6: Measured shift in resonant frequency for the sensors in slab T1

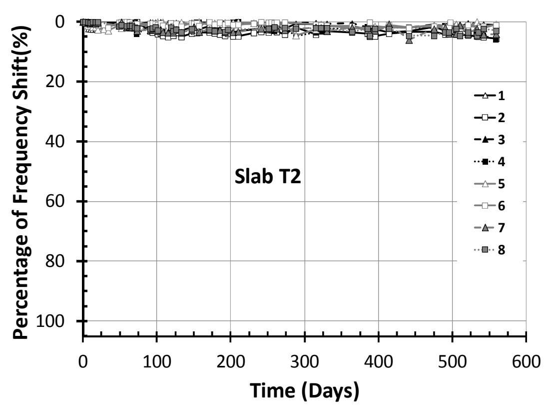

Figure 7-7: Measured shift in resonant frequency for the sensors in slab T2

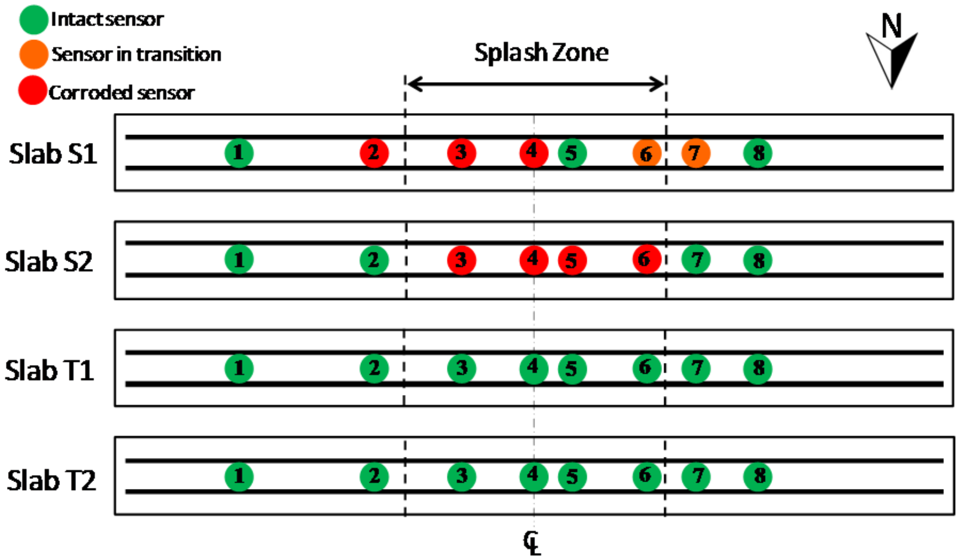

Figure 7-8: Detected state of the NC sensors at the end of the exposure test

The layout of the NC sensors and the state of each sensor at the end of the exposure period is shown in Figure 7-8. In slab S1, three of the four sensors within the splash zone indicated corrosion activity and the two sensors in the moist zone also indicated corrosion damage. S1-6 and S1-7 started the transition to the corroded state during the accelerated exposure period and remained in transition when the exposure test was stopped. On the other hand, only the sensors within the splash zone in slab S2 shifted to the corroded state during the test period. As expected, none of the sensors embedded in the dry regions or the sensors embedded within the slabs exposed to the low-chloride exposure (slabs T1 and T2) had any measureable signs of corrosion initiation within their sacrificial washers.

7.3 Electrochemical Evaluation Results

Electrochemical corrosion monitoring techniques were employed to assess the corrosion risk within the reinforced concrete slabs. Half-cell potentials and linear polarization resistance (LPR) measurements were conducted during the exposure test. In the following sections, the results obtained are used to demonstrate the reliability of both methods and their sensitivity to the surrounding environmental conditions. The LPR results discussed were acquired in April 2012, August 2012, November 2012, and January 2013. The average recorded values of the concrete surface temperature and relative humidity during the four interrogation periods are listed in Table 7-1.

Table 7-1: Average concrete surface temperature and relative humidity during LPR measurement periods

Interrogation Period	Average Temperature (°F)	Average Relative Humidity (%)
April 2012	74	60
August 2012	95	53
November 2012	43	55
January 2013*	105 (dry period) 42 (wet period)	42

* Infrared heaters were used during drying periods only.

7.3.1 Half-Cell Potentials

Half-cell potentials were measured using a saturated calomel electrode (SCE) on the surface of the concrete at 13 points along the length of each reinforcing bar. Figure 7-9 shows the variations in the half-cell potentials measured at two locations along the north rebar in slab S1. The first point is located within the splash zone and at the centerline of sensor S1-4. The measured potentials within the splash zone indicated a high risk of corrosion immediately after the initial wetting cycle using salt water. The potentials jumped drastically from the initial reading (-93 mV vs. SCE) and continued to fluctuate at potentials more negative than -400 mV vs. SCE throughout the test period. The potentials measured after the wet cycles were more negative due to the availability of moisture and chloride ions. The fluctuations in the measured potentials between consecutive wet and dry period measurements were as high as 200 mV during the summer months and approximately 80 mV during the winter months. The consecutive readings were usually only four days apart. After the installation of the infrared heaters and the start of the accelerated exposure conditions on day 505, the measured potentials were slightly more negative than usual during the wet cycles and more nobel after the dry cycles.

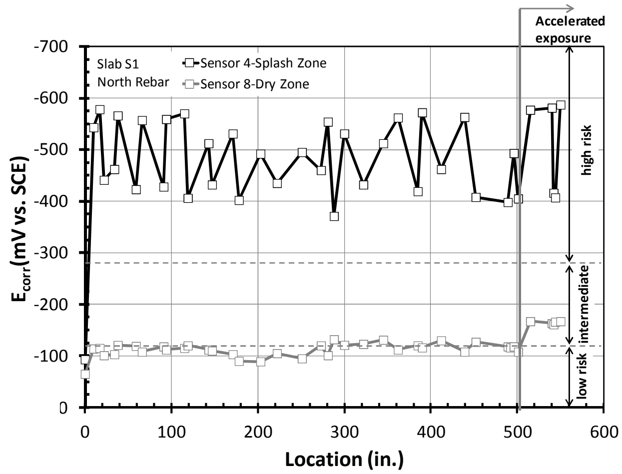

Figure 7-9: Half-cell potentials measured at sensors 4 and 8 along the north rebar in slab S1

Figure 7-9 also shows the half-cell potentials recorded at a point located in the dry zone and at the centerline of senor S1-8. The dry zone readings indicated a low risk of corrosion damage throughout the test period. The readings fluctuated between the wet and dry periods. However, the degree of cycle variation (25 mV) was considerably less than that observed in the splash zone readings. Noticeably, the potentials decreased by 50 mV immediately after the infrared heaters were used to accelerate the exposure conditions.

The half-cell potentials measured along the north reinforcing bar in slab S1 after wet and dry periods are shown in Figure 7-10 and Figure 7-11, respectively. It can be seen that the half-cell potentials indicated high corrosion risk within the splash zone. The potentials gradually drop to potential values that are indicative of intermediate and low corrosion risk at the dry sections of the slab. This pattern was captured in all the readings, regardless of the moisture level or the ambient environmental conditions. However, fluctuations in potentials, as high as 200 mV, can be observed between wet and dry periods in the readings taken within the splash zone. The variation level decreases dramatically for the readings taken within the dry zones where the average variation was less than 30 mV.

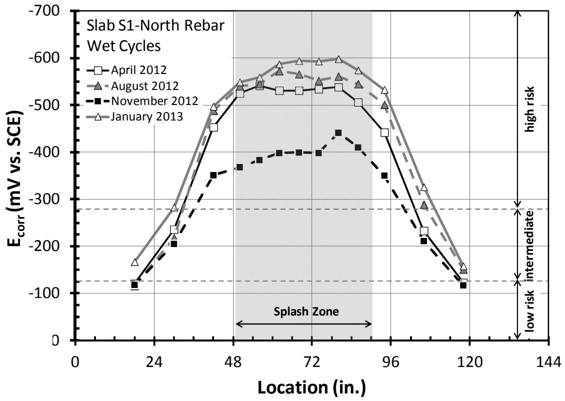

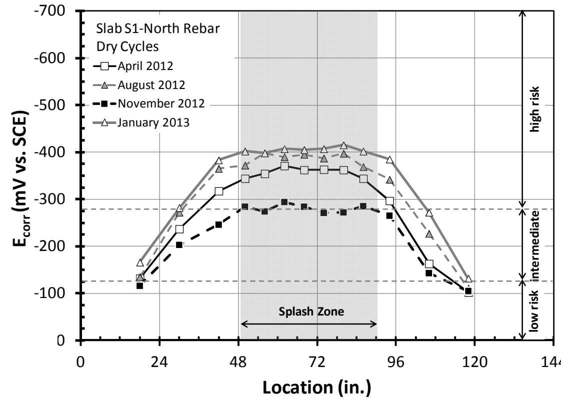

Figure 7-10: Measured half-cell potentials along the length of the north rebar in slab S1 after selected wet periods

Figure 7-11: Measured half-cell potentials along the length of the north rebar in slab S1 after selected dry periods

The temperature of the concrete surface had a clear influence on the recorded potentials. For the wet measurements, the highest potentials were recorded in January 2013 after the installation of the infrared heaters. The potentials were more than 180 mV lower for the readings acquired two months earlier (November 2012) where the concrete temperature was 62 ºF lower. Furthermore, it can be seen that higher potentials were recorded in the dry regions when the temperature at the time of the reading was higher. These results demonstrate the dependency of the half-cell technique on the moisture conditions, temperature and relative humidity.

The half-cell potential profiles recorded after the wet periods along the length of the north rebar in slab T1 are shown in Figure 7-12. The profiles followed the same trends observed in the S1 slab with the splash zone exhibiting more negative potentials compared to the dry zones. However, the measured potentials within T1 were indicative of intermediate and low corrosion risks with potentials between -25 and -250 mV vs. SCE. Furthermore, the temperature had a direct influence on the measured potential with more active potentials corresponding to higher ambient temperatures. The maximum variation in the measured potential at any point was less than 70 mV for the four data sets presented.

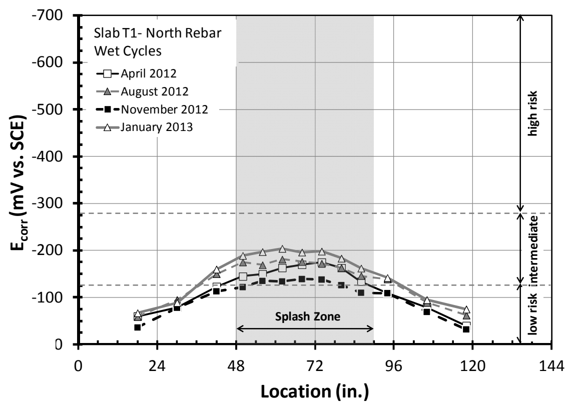

Figure 7-12: Measured half-cell potentials along the length of the north rebar in slab T1 after selected wet periods

A statistical analysis was performed for half-cell potential readings obtained from the slabs exposed to salt water (S1 and S2). A total of 1456 readings collected during the exposure test were placed into 25-mV bins and the data were divided according to their location along the slab. The frequency distributions of the readings recorded at the splash, moist, and dry zones are shown in Figure 7-13. It can be seen that the mode of the readings from the dry region was at -100 mV vs. SCE, which is slightly lower than the suggested upper limit for a low corrosion risk. In contrast, most of the readings within the splash exposure zones exceeded -275 mV vs. SCE and peaks were observed at -450 and -575 mV vs. SCE. The two peaks correspond to the typical values recorded after dry and wet periods, respectively. The splash zone distribution does not include the data collected prior to the start of the exposure tests. The initial readings had average potentials of approximately -125 mV vs. SCE. The moist zone readings exhibited less pronounced peaks and the readings were spread more uniformly along the entire range of possible potentials. Generally, most of the readings acquired at the splash or moist zones indicated a high probability of severe corrosion risk. While, the dry readings were typically within the low and intermediate corrosion risk limits.

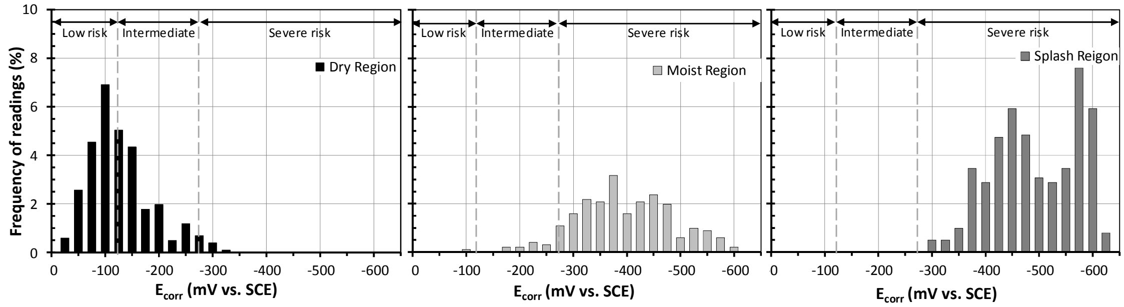

Figure 7-13: Frequency distributions of the half-cell potential data collected in slabs S1 and S2 in the dry, moist, and splash regions

In addition, the cumulative frequency distributions for the three regions are shown in Figure 7-14. The shape of the cumulative distribution for the dry region indicates a relatively uniform distribution with a median half-cell potential of -149 mV vs. SCE. The calculated average potential of the dry region readings was -153 mV vs. SCE. As expected, the curve of the splash region had generally the highest recorded potentials while the lowest values were recorded at the dry region. The median half-cell potentials at the moist and splash regions were -369 and -456 mV vs. SCE, respectively.

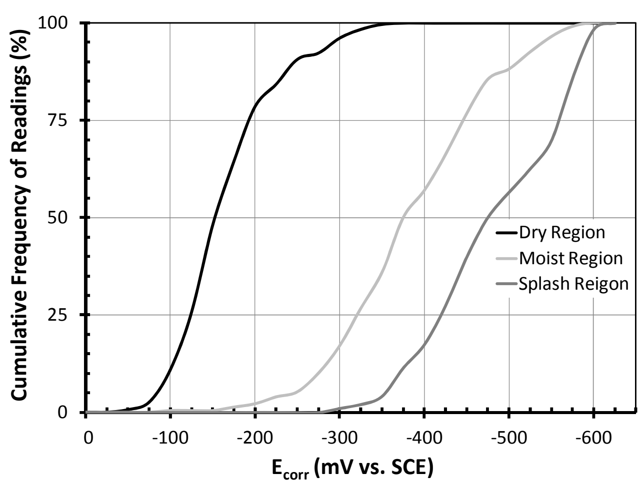

Figure 7-14: Cumulative frequency distribution curves of the half-cell potential data collected in slabs S1 and S2

7.3.2 Linear Polarization Resistance

The corrosion rates of the steel reinforcement were measured using the LPR technique. The data were collected sporadically using the GECOR 8™. A total of fourteen sets of readings were acquired throughout the exposure test. The measurements were taken in August 2011, April 2012, August 2012, November 2012, and January 2013. In all cases, readings were taken following consecutive wet and dry periods.

The measured corrosion current densities at three points along the north rebar in slab S1 are shown in Figure 7-15. The measurement points are located at the centerlines of sensors 4, 7, and 8. As a result, each point is located within a different exposure zone. The corrosion currents measured in the splash zone were typically the highest compared with the moist and dry zones. Furthermore, the measured currents in the splash and moist zones were always greater than 1μA/cm^2, the threshold value at which severe corrosion activity is assumed to be taking place (Broomfield 2007). Noticeably, the current densities recorded after only two cycles of exposure (day 17) suggested severe corrosion activity within the splash zone. While such conclusions are expected in regions with high chloride exposure, it is unreasonable to believe that a breakdown of the passive layer occurred and that active corrosion was taking place after only two weeks of exposure. Furthermore, the measured current densities near sensor 4 were very sensitive to the moisture levels and varied as much as 200% between successive wet and dry periods. The higher current densities were typically recorded after the wet periods due to the availability of moisture and chlorides, which enable the easy transfer of ions between the active corrosion electrodes. The corrosion currents recoded at day 550 were taken during the accelerated exposure period and were twice as high as the currents recorded before the installation of the infrared heaters. Again, the limited availability of moisture after the dry periods led to lower apparent corrosion currents.

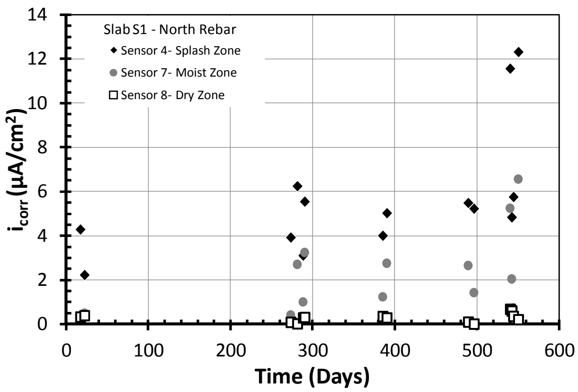

Figure 7-15: Corrosion current densities measured at sensors 4, 7, and 8 along the north rebar of slab S1

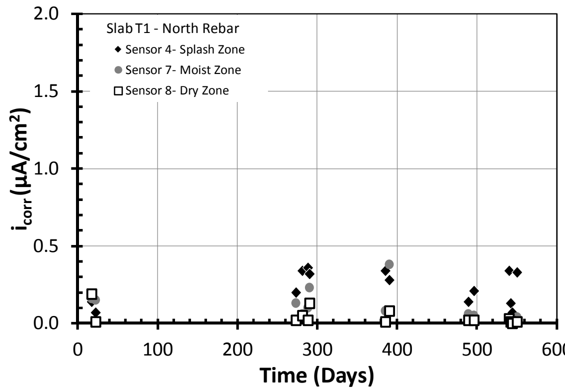

Figure 7-16: Corrosion current densities measured at sensors 4, 7, and 8 along the north rebar of slab T1

On the other hand, the corrosion currents measured at the dry zone were quite low and indicative of a passive corrosion activity. As expected, the variability between the measurements taken after consecutive wet and dry periods was limited due to the lack of moisture transfer in the dry zone. The measured dry zone currents increased slightly during the accelerated corrosion period but the currents remained below the threshold for an elevated corrosion risk. The corrosion currents recorded at the moist zone (Sensor 7) indicated active corrosion conditions. However, the initial readings (day 17) and the dry period measurements taken during the first year of exposure indicated remarkably low corrosion currents. For readings taken in the same time period, the corrosion currents in the moist zone were generally between those recorded for the dry and splash zones. During the accelerated exposure period, the corrosion currents at the moist zone were twice as high as the readings taken 60 days earlier.

Figure 7-16 shows the recorded corrosion current densities along the north rebar in slab T1 at the centerline of sensors T1-4, T1-7, and T1-8. While, the three measurement points were located at three different regions of exposure, the corrosion currents were generally small and relatively close in value. Nonetheless, the splash zone currents were slightly higher than the moist zone readings and the lowest values were recorded in the dry zone. Remarkably, all the measured currents were below the active corrosion threshold of 1µA/cm^2. The variability of the recorded corrosion currents due to changes in moisture content and ambient temperature was small and within the error margin expected for the GECOR™ equipment.

The measured current densities along the north rebar in slab S1 after the wet and dry periods are plotted in Figure 7-17 and Figure 7-18, respectively. The recorded current densities were generally higher within the splash and moist sections of the slab and the values in the two sections were always higher than the threshold for severe corrosion. The corrosion currents were very sensitive to the moisture content and ambient temperature. It can be seen that the measured corrosion rates varied by more than 400% between the November 2012 and the January 2013 readings. The latter readings were conducted during the accelerated exposure period where concrete temperatures were kept at 105°F. On the other hand, corrosion currents measured at the dry sections of the S1 slab were extremely small and were not affected by temperature variations, suggesting that the steel rebar is passive in this region.

Furthermore, the sensitivity of the linear polarization method to the moisture content is clearly demonstrated by the stark difference in the measured current densities between the wet and dry periods of a single cycle. For example, the measurements obtained after the dry period in January 2013 were on average five times smaller than the readings obtained after the wet period. However, the values recorded after the dry periods were still indicative of a severe corrosion activity.

Figure 7-19 shows the profiles of the measured corrosion currents along the length of the north rebar in slab T1. It can be seen that the currents were significantly smaller than those recorded in slab S1 (Figure 7-17). The recorded values in slab T1 were indicative of a passive corrosion activity with slightly active corrosion within the splash zone. In general, the measurements conducted after the dry cycles were smaller than the wet cycle values and followed the same trends seen in Figure 7-19.

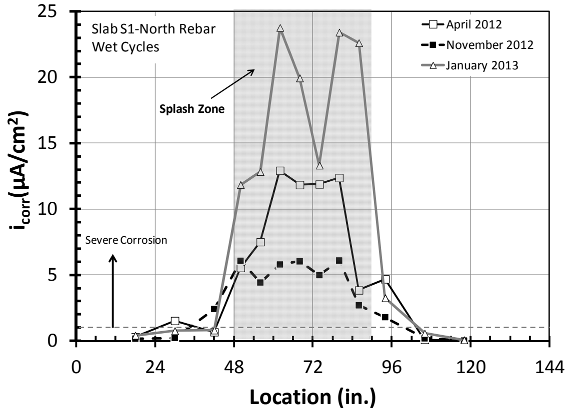

Figure 7-17: Localized corrosion currents measured along the length of the north rebar of slab S1 after selected wet periods

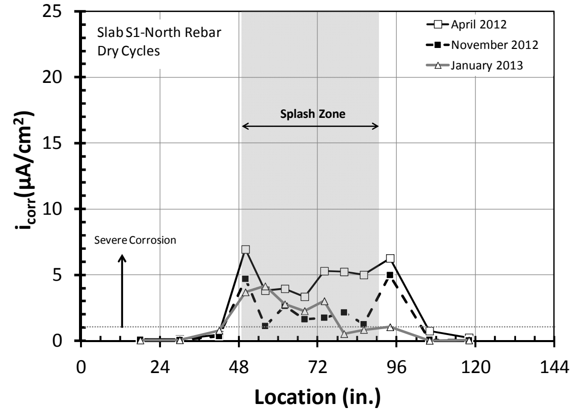

Figure 7-18: Localized corrosion currents measured along the length of the north rebar of slab S1 after selected dry periods

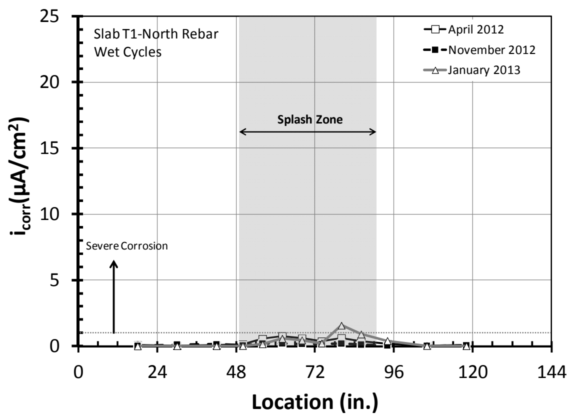

Figure 7-19: Localized corrosion currents measured along the length of the north rebar of slab T1 after selected wet periods

Figure 7-20 shows the frequency distribution of the recorded LPR data for the salt water slabs (S1 and S2). The statistical analysis was performed on 728 data points distributed in 0.5-µA/cm^2 bins. The distribution of the data in the dry region shows a strong peak with a small bandwidth at corrosion currents below the threshold for severe corrosion. On the other hand, the data recorded at the moist and splash regions were distributed over a wide range of current densities with notable skews toward higher corrosion currents. The highest peaks for the data in the moist and splash regions were observed at 1.00 and 1.25 µA/cm^2, respectively.

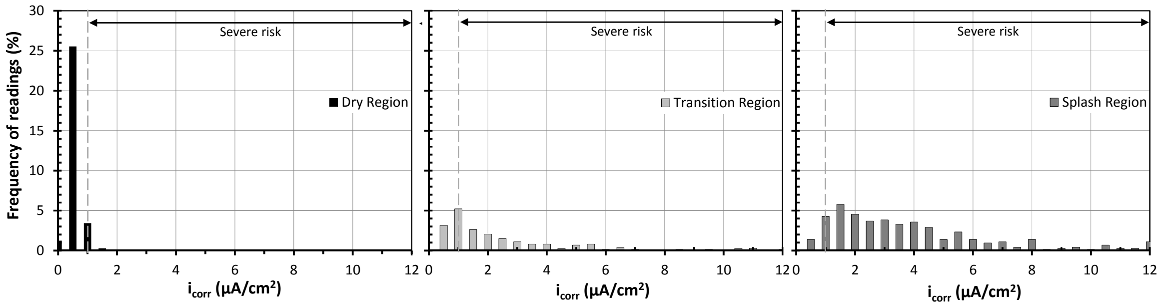

Figure 7-20: Frequency distribution of the LPR data collected in slabs S1 and S2

Similar observations regarding the distribution of the current density data can be seen in the cumulative frequency curves shown in Figure 7-21. The LPR data collected within the dry region had a comparatively narrow distribution. The median current density of the dry region data was equal to 0.16 µA/cm^2 and 98.2% of the recorded currents were equal or less than the threshold for severe corrosion (1.0 µA/cm^2). On the other hand, the cumulative frequency distribution curve of the data collected in the splash zone indicated a broad distribution with the median current density of 3.02 µA/cm^2. Similarly, the distribution of the data collected in the moist region was wide with a median equal to 1.39 µA/cm^2. Most of the LPR data recorded within the moist and splash zones were greater than the threshold suggested for severe corrosion activity.

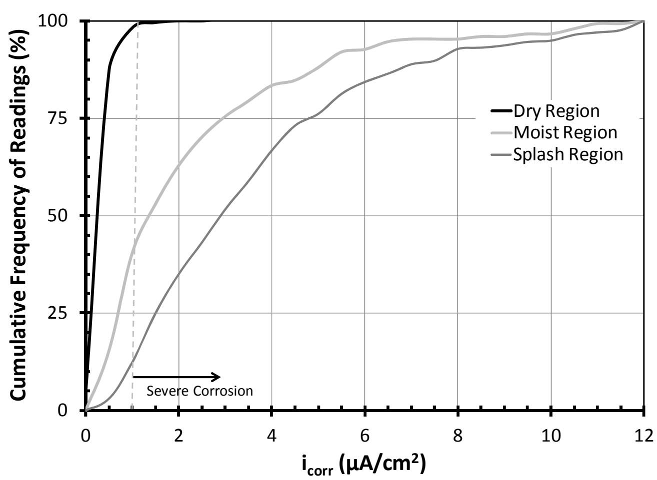

Figure 7-21: Cumulative frequency distribution curves of the LPR data collected in slabs S1 and S2

7.4 RESULTS FROM POST-EXPERIMENT AUTOPSY AND DESTRUCTIVE TESTS

7.4.1 Acid-Soluble Chloride Ion Concentrations

The chloride level profiles are shown in Figure 7-22 for the four slabs. As expected, the measured acid-soluble chloride content for both slabs exposed to salt water (S1 and S2) is high and on average it is five times higher than the critical chloride content of 500 ppm reported in ACI 222R (Protection of Metals in Concrete Against Corrosion 2010), which is considered to be the threshold for initiation of corrosion within reinforced concrete members. The chloride content at the dry regions in the slabs S1 and S2 was below the 500 ppm threshold, except for the west side of slab S1 where the chloride levels remained high at locations only two feet away from the eastern slab edge (location < 24 in.). In contrast, the measured chloride content levels along the length of the slabs exposed to tap water (T1 and T2) were extremely low and below the threshold level, thus, indicating a low risk of corrosion.

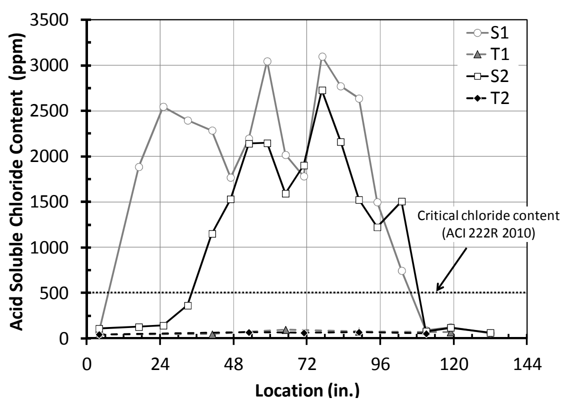

Figure 7-22: Acid-soluble chloride ion concentration profiles for the four slabs

7.4.2 Observations from Physical Autopsy

In February 2013, the physical autopsy of the four slabs was performed to determine the extent of corrosion on the reinforcement and the condition of the sacrificial washer for each embedded sensor. The condition of the corrosion sensors and the surrounding reinforcing bars was documented and photographed. Figure 7-23 and Figure 7-24 show the state of sensors S2-1 and S2-4 and the adjacent reinforcing bars after the autopsy. It can be seen that the state of corrosion in the reinforcement steel was captured by the two NC sensors. The sacrificial washer of sensor S2-1 remained intact and exhibited no evidence of corrosion initiation. On the other hand, the sacrificial washer of sensor S2-4 was entirely corroded without any trace of the original metal.

Figure 7-25 is a schematic representation of the observations from the physical autopsy and illustrates the location and range of observed corrosion on the reinforcement and the state of the NC sensors after the physical autopsy. Due to the electrical isolation of each reinforcing bar, the corrosion pattern observed was suggestive of microcell corrosion, where multiple anodes formed separately along the length of each reinforcing bar. In slabs S1 and S2, the corrosion damage was concentrated within the splash zone and the corrosion damage decreased towards the ends of the specimens. The autopsy findings suggest that corrosion initiated under the wider cracks or at the locations of the rebar ties, and then spread along the surrounding steel. Slab S2 exhibited the highest levels of corrosion damage. The middle sections of both rebars in slab S2 exhibited uniform levels of corrosion. The reinforcement in slabs T1 and T2 exhibited numerous locations where local anodes and local pitting had initiated, but did not spread. Figure 7-26 shows the extent of corrosion on 4.0-in. sections of the north reinforcing bars at the midspan of each slab (near sensor 4).

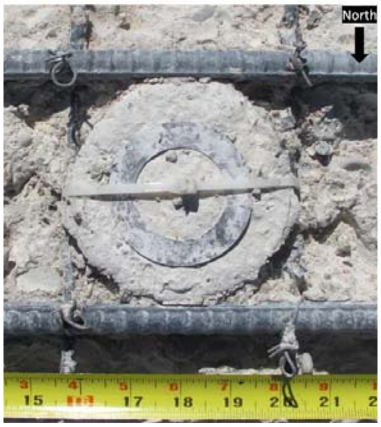

Figure 7-23: Sensor S2-1 and the surrounding reinforcement after the autopsy

Figure 7-24: Sensor S2-4 and the surrounding reinforcement after the autopsy

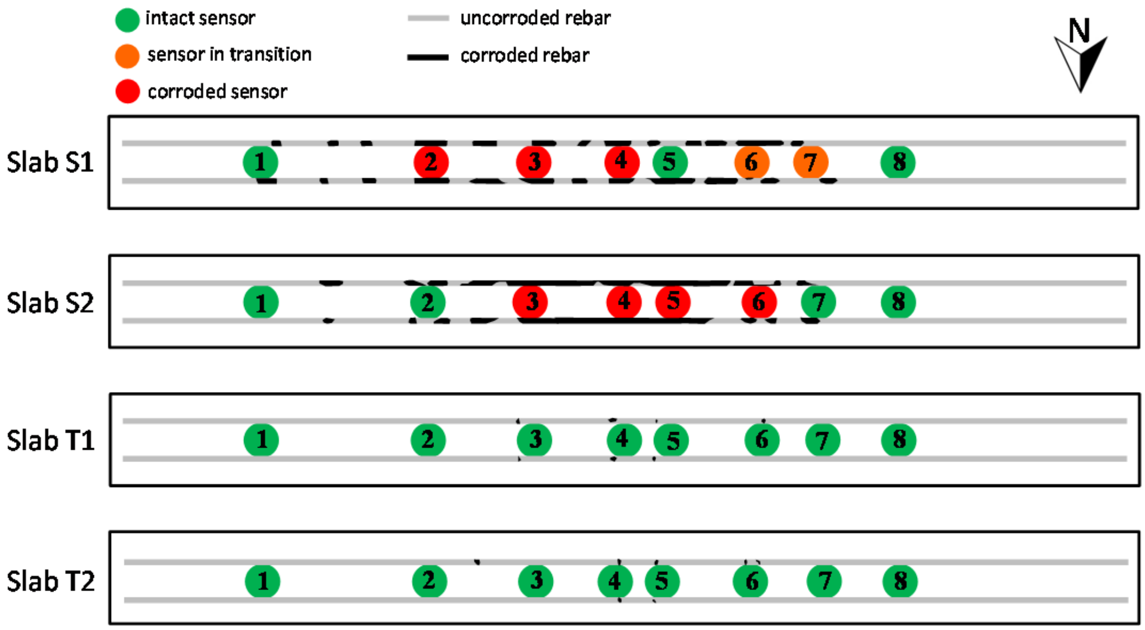

Figure 7-25: Observed corrosion damage in the reinforcing bars and the state of the NC corrosion sensors at the time of the autopsy

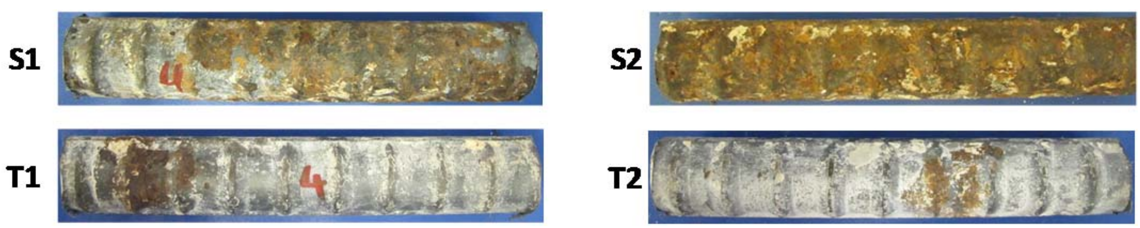

Figure 7-26: Photographs of observed corrosion on 4.0-in. sections from the north rebar at midspan of each slab (adjacent to sensor 4)

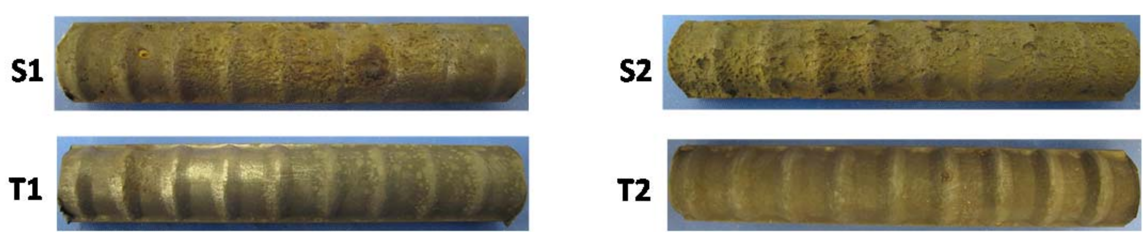

Figure 7-27: Photographs of 4.0-in. sections from the north rebar at midspan of each slab following mass loss measurements (adjacent to sensor 4)

7.4.3 Mass Loss Results

The reinforcing bars were extracted from the slabs and were cut into 4.0-in. long sections to measure the mass loss. The centerline of the rebar sections coincided with centerlines of the embedded NC and conductivity sensors. The mass loss measurements were performed in accordance with ASTM G1 (2003). Figure 7-27 shows the condition of the rebar sections shown in Figure 7-26 after the mass loss evaluation. The measured mass losses of the S1-4N, S2-4N, T1-4N and T2-4N rebar sections are 3.57%, 5.70%, 0.26%, and 0.27%, respectively. It can be seen that a notable reduction in the cross sectional area took place in both S1-4N and S2-4N. The reduction in the cross section was distributed over the whole length of these reinforcing bar sections. In contrast, the damage in the T1 and T2 rebar sections was limited to minor pits, which were localized, and the location of the observed pits corresponded to the location of the flexural cracks in each slab.

Figure 7-28 and Figure 7-29 show the measured mass loss of the rebar sections along the length of slabs S1 and S2, respectively. It can be seen that the highest losses were observed in the middle sections of each slab, which were directly exposed to salt water. The measured mass loss towards the ends of the slab was minimal and close to zero except for the south rebar of slab S1 where a mass loss of about 1.2% was recorded only 18 in. away from the end of the slab. The maximum mass loss measured in both slabs did not exceed 6% and the losses within the splash zone ranged between 1.5% and 5.7%. These levels are below the mass loss levels expected to induce cracking and delamination in reinforced concrete members. Al-Shiek et al. (2003) reported that a mass loss of approximately 8% is needed to initiate longitudinal cracking for concrete members with a ratio of clear cover to rebar diameter greater than 1.5 (the ratio was 1.6 for the slab specimens). However, due to the lack of transverse reinforcement in the test specimens, corrosion-induced longitudinal cracks were observed in slabs S1 and S2.

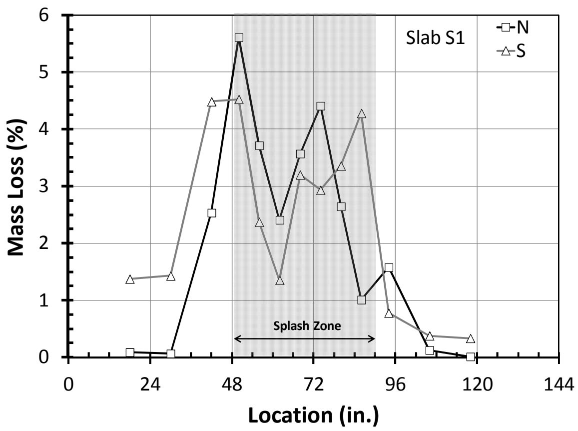

Figure 7-28: Mass loss profiles for the north (N) and south (S) reinforcing bars in slab S1

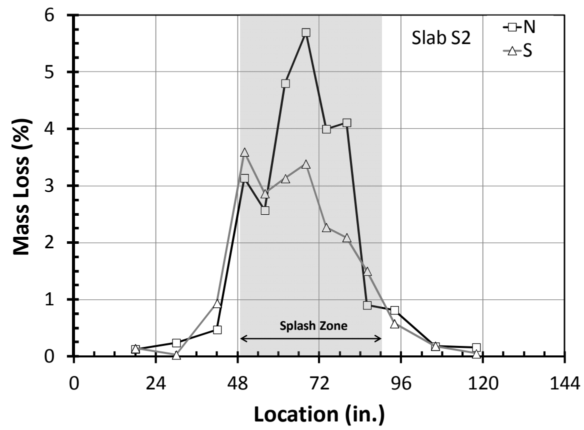

Figure 7-29: Mass loss profiles for the north (N) and south (S) reinforcing bars in slab S2

The mass loss levels measured in the test specimens are considered to be within the levels of corrosion damage that can be repaired using relatively inexpensive techniques(Emmons 1993). Emmons (1993) suggested the application of surface sealers or concrete cover replacement as the adequate actions for the repair of reinforced concrete members with mass loss levels less than 5%.

The mass loss distributions over the length of slabs S1 and S2 demonstrate the stochastic nature of the corrosion process. While, the two longitudinal reinforcing bars in each slab were exposed to the same nominal exposure conditions and chloride concentrations, the variability in the measured mass loss at each point along the length of the north and south rebars is considerable. For example, the mass losses observed in the north rebar in slab S2 are significantly higher than the south rebar. Furthermore, while the rebar sections taken from the north rebar in slab S1 had relatively little corrosion damage between 18 and 30 in., the sections from the south rebar had corrosion losses of approximately 1.3%.

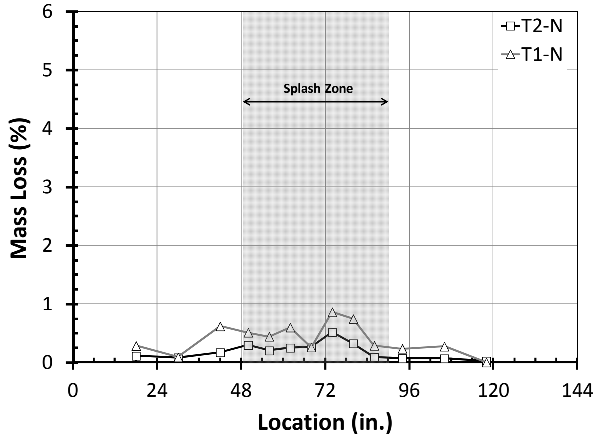

Figure 7-30: Mass loss profiles for the north (N) rebar in slabs T1 and T2

As expected, the measured mass losses in the concrete slabs exposed to tap water (T1 and T2) were considerably lower than the losses measured in slabs S1 and S2. Figure 7-30 shows the mass loss profiles for the sections of the north rebars in slabs T1 and T2. The measured mass losses were generally less than 1%. The losses observed outside the splash zone were modest and can be attributed to the errors associated with the inadvertent losses in the uncorroded metal due to the aggressive cleaning process used for mass loss measurements(ASTM G1 2003). Generally, the middle section of each slab had slightly higher levels of mass loss and the losses dropped to approximately zero towards the ends of each slab. The mass losses in the sections cut from the south reinforcing bars exhibited similar trends. Levels of corrosion damage for all reinforcement steel are reported in Appendix D.

Figure 7-31 through Figure 7-38 provide a classification of the observed corrosion damage along the length of the north and south reinforcing bars of slabs S1, S2, T1, and T2 respectively. The relative location and the final state of the embedded NC sensors are also shown. The observed state of the reinforcement was classified using five groups: passive, pitting, light, moderate, and high.

The classification of damage level was based on the mass losses measured along the length of each rebar. For rebar sections where the mass loss was not evaluated, the classification was based on visual assessment and direct comparison to similar sections where mass loss was measured. Locations on the reinforcing bar with localized pits that were limited to the top of the bar and experienced mass losses less than 0.5% were classified as pitting regions. Sections with mass loss levels between 0.5% and 2.0% were classified as having light corrosion damage, while sections with losses greater than 4.0% were classified as having high level of corrosion damage.

The microcell nature of the observed corrosion activity is evident from the classification plots. The results indicate the formation of multiple, localized and concentrated anodes along the length of each rebar. Clear differences in the corrosion activity between adjacent steel sections were also observed at numerous locations. However, the middle region of the reinforcing bars in slab S2 exhibited uniform and consistent corrosion damage for lengths longer than 2 ft. It can be concluded that the regions of uniform corrosion damage were initiated by a number of localized anodes that spread and connected forming an area of uniform corrosion damage. Although slabs S1 and S2 were nominally identical and experienced the same cycles of salt water exposure, the corrosion damage observed in slab S2 was more severe than slab S1.

As was discussed previously, the corrosion damage within the slabs exposed to tap water was limited to a number of localized pits that were concentrated mainly under the splash zone (Figure 7-35 through Figure 7-38). The pits were limited in size and were generally less than 1.0-in. long. In addition, the location of the pits coincided with the location of the transverse flexural cracks.

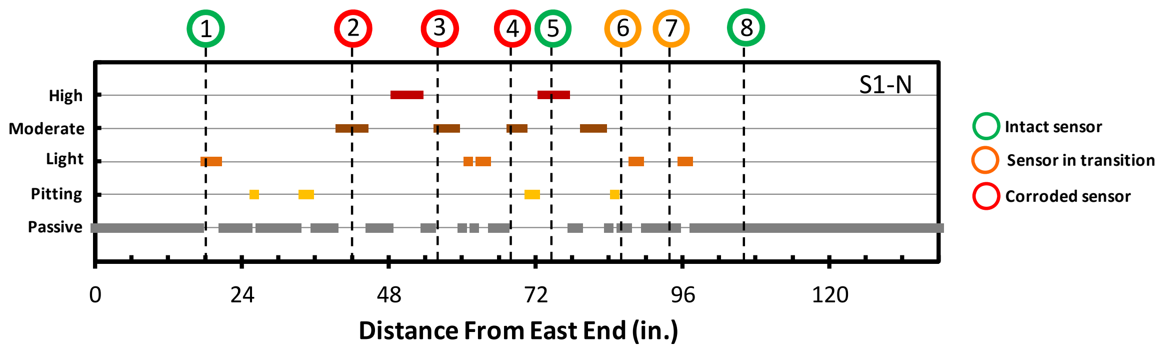

Figure 7-31: Corrosion damage classification along the north reinforcing bar in slab S1

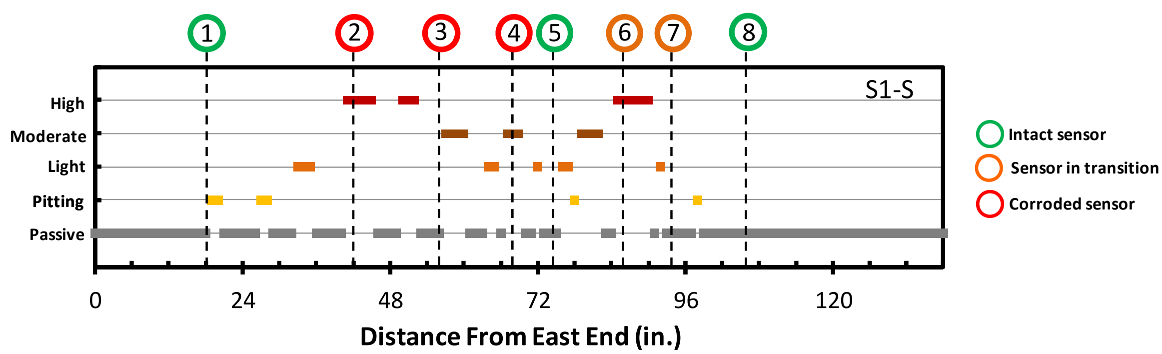

Figure 7-32: Corrosion damage classification along the south reinforcing bar in slab S1

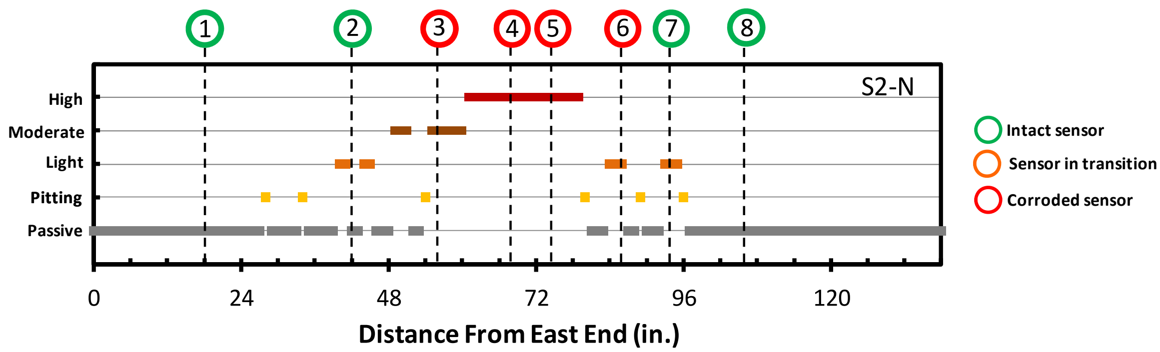

Figure 7-33: Corrosion damage classification along the north reinforcing bar in slab S2

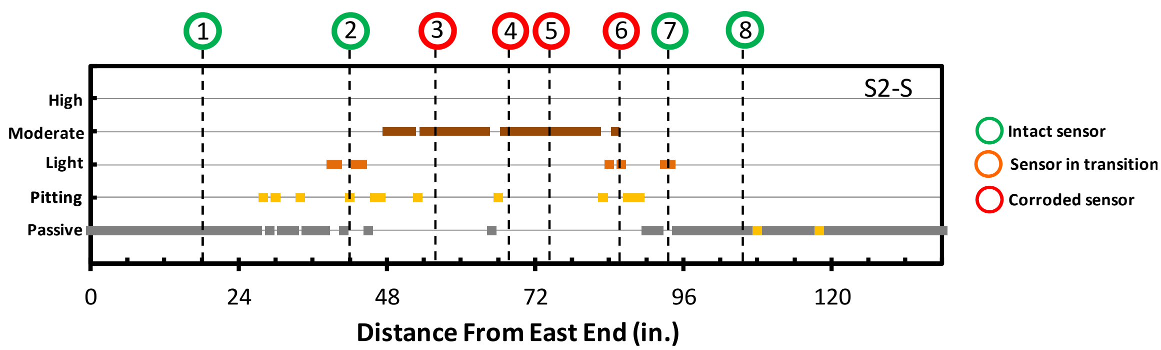

Figure 7-34: Corrosion damage classification along the south reinforcing bar in slab S2

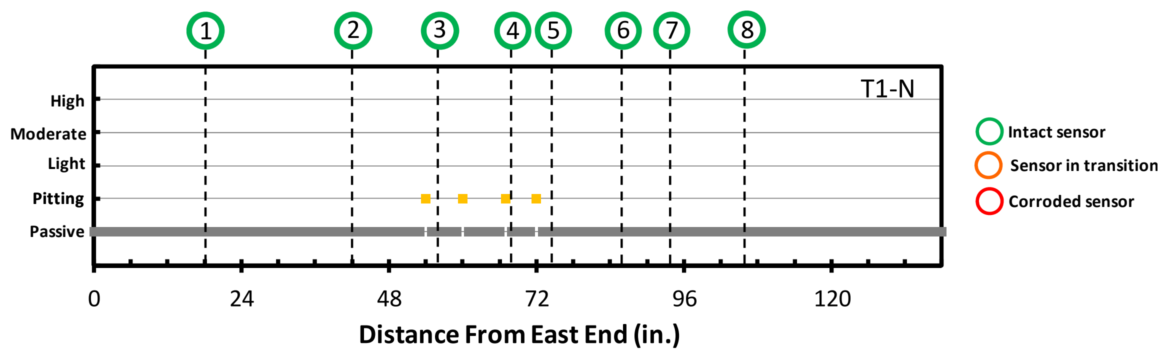

Figure 7-35: Corrosion damage classification along the north reinforcing bar in slab T1

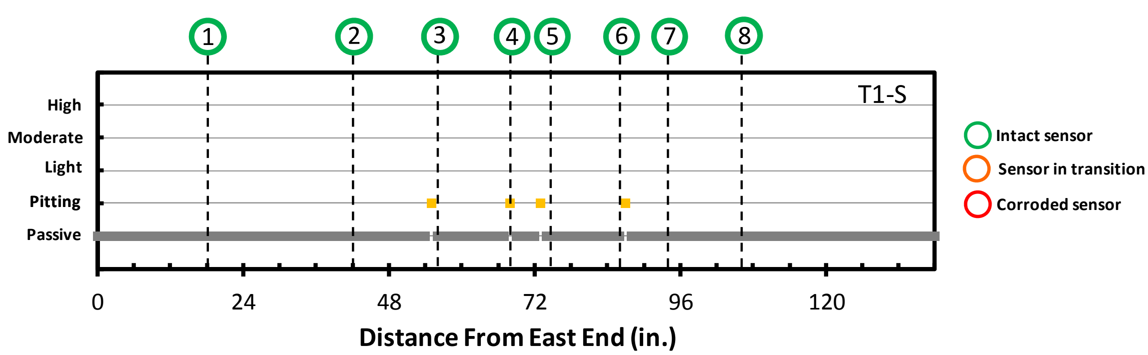

Figure 7-36: Corrosion damage classification along the south reinforcing bar in slab T1

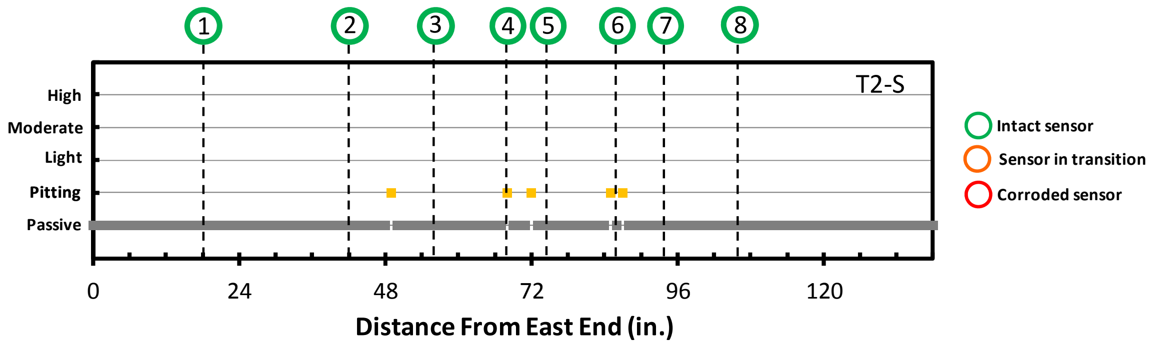

Figure 7-37: Corrosion damage classification along the north reinforcing bar in slab T2

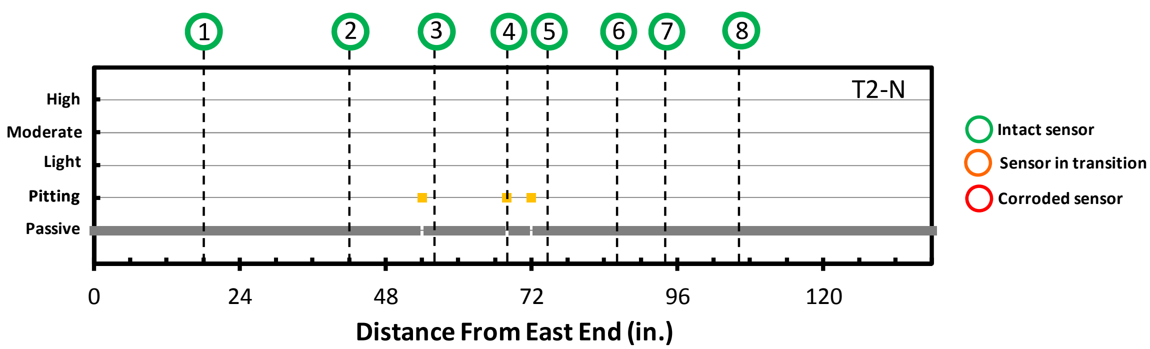

Figure 7-38: Corrosion damage classification along the south reinforcing bar in slab T2

7.5 DISCUSSION OF LONG-TERM EXPOSURE TEST RESULTS

The ability of the NC sensor to detect corrosion initiation in the adjacent reinforcing steel successfully is critical for successful deployment of the passive sensor technology. The results of the long-term exposure test are used to evaluate the reliability of the NC corrosion sensors (Section 7.5.1). Furthermore, the reliability of the LPR technique is examined in Section 7.5.2.

7.5.1 Comparison of Sensor Response with Post-Experiment Rebar Condition

There are two types of errors that can limit the reliability of a corrosion detection system. The first is a false positive which is associated with sensor signals indicating corrosion in the adjacent rebar when corrosion did not occur. The second is a false negative signal, which describes a condition where the sensor fails to detect corrosion in the adjacent steel. Table 7-2 summarizes the responses from all the NC sensors, and the condition of the adjacent reinforcement, from all four slabs. At the end of the long-term exposure test, sensors S1-6 and S1-7 had shifted more than 10% of the dynamic range from the initial frequency. Therefore, these sensor readings were interpreted to correspond to the onset of corrosion.

Table 7-2: Response of the NC sensors by reliability category

		Observed state of the reinforcement	
		No Corrosion	Corrosion
Readings from the NC Sensors	Corrosion	0 (False Positive)	9
	No Corrosion	23	1 (False Negative)

As evident from Figure 7-31 through Figure 7-38, none of the NC sensors exhibited a false positive signal. Corrosion damage was observed in at least one of the sections of reinforcing bar adjacent to all the sensors for which the resonant frequency shifted.

In contrast, the frequency of sensor S1-5 did not shift, while corrosion was observed in the adjacent reinforcement. This was the only case where a false negative signal was observed. The sensor remained in its uncorroded resonant frequency throughout the long-term exposure test, but the autopsy identified corrosion damage with appreciable mass loss (higher than 2%) in the adjacent reinforcement. At the time of the autopsy, corrosion product was observed on the sacrificial washer in sensor S1-5; however, the sacrificial washer in sensor S1-5 was inadvertently damaged during the autopsy of slab S1. Therefore, the photographic evidence of the condition of the washer is inconclusive (Figure 7-39). However, Figure 7-40 shows the corrosion product from the washer of S1-5 that remained on the cement housing for this sensor. Hence, while S1-5 did not shift to the corroded state during the test, the sacrificial washer was corroding at the time that the test concluded. It is anticipated that the sensor would have indicated the corrosion activity if the exposure period had been longer. This unexpected sensor response could be the result of the unique crack pattern surrounding sensor S1-5. As shown in Figure 6-8, 0.016-in. wide flexural cracks were present over the steel reinforcement adjacent to sensor S1-5, but these cracks did not continue above the sacrificial washer of the sensor (Figure 7-41).

The results from sensor S1-5 demonstrate the sensitivity of the sensor readings to the location and size of cracks. The presence of cracks over a sensor will promote higher corrosion rates and cause an earlier shift to the corroded state. Figure 7-42 plots the time needed by the sensors in the splash and moist zones in slabs S1 and S2 to reach the corroded state against the largest crack size in the vicinity of each sensor. In general, faster transitions to the corroded state were observed where large cracks crossed the sensor.

Figure 7-39: Observed corrosion and damage due to physical autopsy of the sacrificial washer in sensor S1-5

Figure 7-40: Observed corrosion product on the surface of the cement housing of sensor S1-5

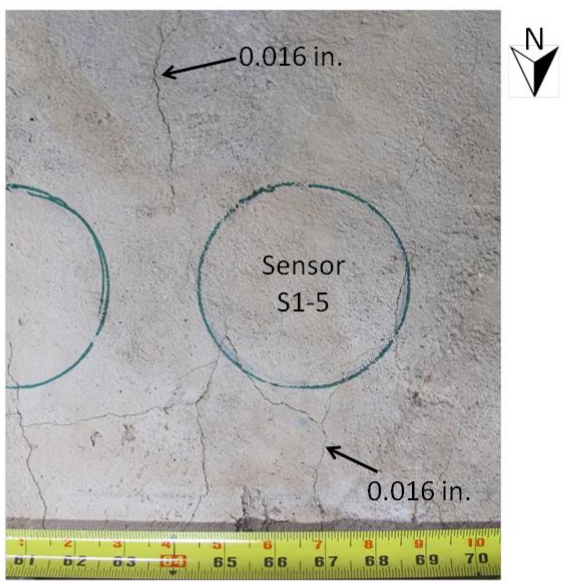

Figure 7-41: Surface cracks in the vicinity of sensor S1-5

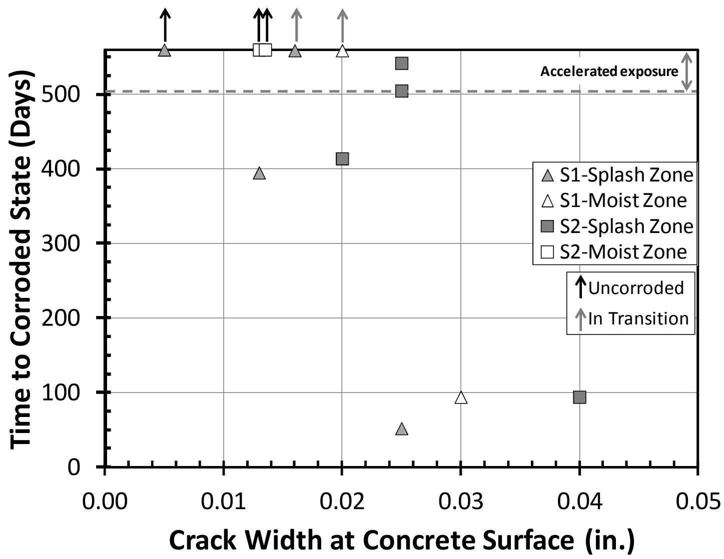

Figure 7-42: Sensitivity of time to corrosion of the embedded NC sensors to crack width

In addition, the effect of the thickness of the sacrificial washer on the time needed to indicate corrosion initiation can also be demonstrated using the data in Figure 7-42. When positioned under cracks of the same size, the sensors with thicker washers required longer times to reach the corroded response. Three NC sensors were located under 0.025-in. wide cracks, the sensor fabricated with the 0.001-in. thick washer shifted to the corroded state after only 50 days, while the S2 sensors needed more than 500 days to corrode. Similarly, for the sensors that shifted to the corroded state after approximately 100 and 400 days, larger cracks were present above the sensors.

The chloride content evaluation is used extensively in practice as a destructive method that provides direct indication regarding the level of corrosion damage within concrete. Due to the diffusive nature of chloride ingress, higher chloride content is indicative of more active corrosion. Figure 7-43 plots the time each sensor in slabs S1 and S2 needed to indicate corrosion against the average measured acid-soluble chloride content in the vicinity of the sensor. It should be noted that these chloride content levels were measured at the end of the experiment and as a result cannot be correlated to the critical chloride threshold expected to initiate corrosion.

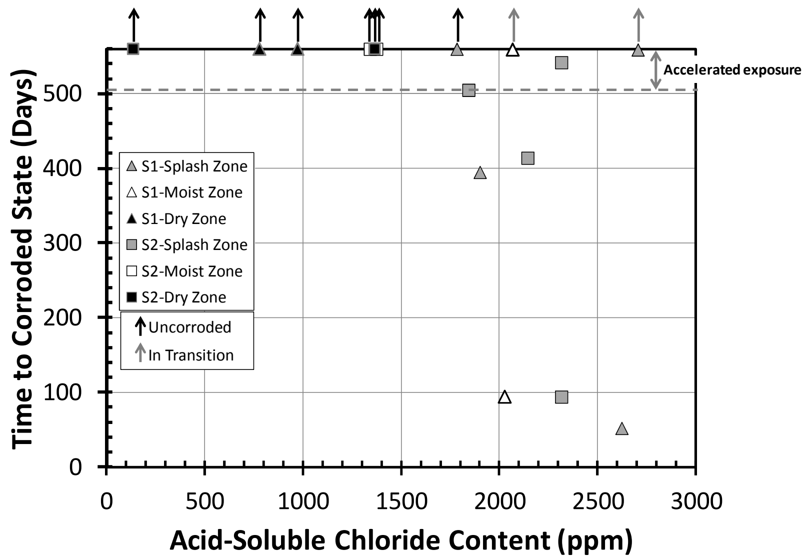

Figure 7-43: Sensitivity of time to corrosion of the embedded NC sensors to acid-soluble chloride content level

In general, it can be seen that sensors with higher chloride content levels reached the corroded state faster. Furthermore, all the sensors with chloride content levels below 1800 ppm remained uncorroded throughout the test. While the NC sensors surrounded by concrete powders with chloride levels higher than 1800 ppm had either corroded or were in transition to the corroded state. A direct correlation between the thickness of the sacrificial washer and the chloride content level measured can also be seen in Figure 7-43. The S2 sensors that reached the corroded state at the same time an S1sensor (100 and 400 days) had higher chloride content concentrations.

The damage categorization plots for slabs S1 and S2 (Figure 7-31 through Figure 7-34) imply a correlation between the amount of reinforcement mass loss and the thickness of the sacrificial washers. The mass losses measured in the rebar sections adjacent to the sensors fabricated with the 0.002-in. thick washers (slab S2) were generally higher than 2%. On the other hand, the S1 sensors indicated corrosion initiation at mass loss levels merely higher than 1%.

The measured mass loss at each of the sections surrounding an NC sensor is plotted against the time at which the sensor reached the corroded state in Figure 7-44.

Only the sensors embedded in slabs S1 and S2 were included in the figure. For the sensors that shifted to the corroded state before the accelerated exposure conditions were applied, higher mass losses were recorded near the sensors that signaled the corrosion activity earlier. The figure also demonstrates the stochastic nature of reinforced concrete corrosion where identical rebars exposed to the same conditions experienced remarkably different degrees of mass loss.

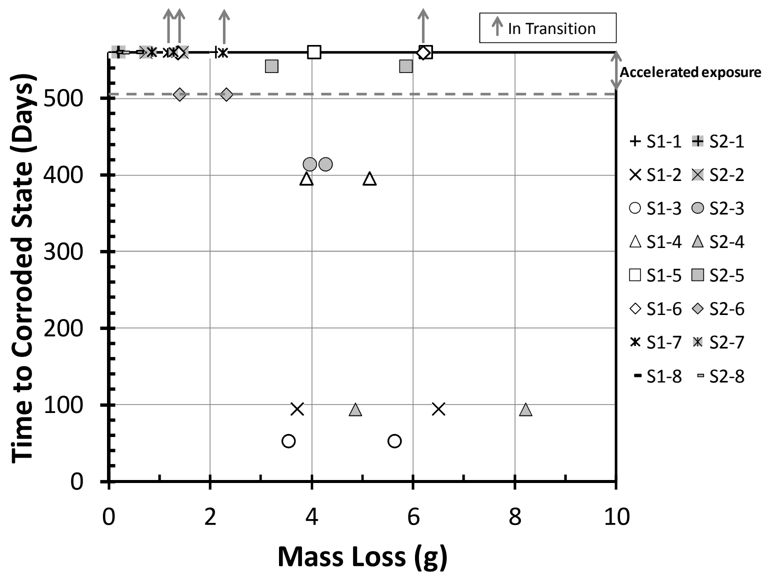

Figure 7-44: Sensitivity of time to corrosion of the NC sensors embedded in slabs S1 and S2 to mass loss

7.5.2 Reliability of the Half-Cell Method

The half-cell technique has been used in the concrete industry for decades to assess the risk of corrosion activity within concrete members. As was discussed in Section 7.3.1, the results of the exposure test confirmed the ability the half-cell method to distinguish between regions of different levels of chloride exposure reliably. At sections where the measured potentials exceeded the threshold potential identifying high corrosion risk, corrosion damage was observed on the surface of the reinforcing bars after the autopsy. In contrast, no corrosion was observed in the slab regions where nobel potentials were typically recorded. However, the sensitivity of the half-cell potentials to the changes in the environmental conditions was demonstrated using the readings acquired during the long-term exposure test. The simplicity of the half-cell measurement technique and its ability to characterize the state of corrosion activity qualitatively within concrete made it the method the most frequently used in the field. However, the method cannot be used to indicate the severity or extent of corrosion damage. This was confirmed by the results in Figure 7-9 where the measured potentials indicated severe corrosion after only one week of exposure.

Comparisons between the acid-soluble chloride content measured before the physical autopsy and the average half-cell potentials measured at sensor locations along the length of slabs S1 and S2 are shown in Figure 7-45. The corrosion potentials plotted represent the average recorded half-cell potentials over the total period of the exposure test. It can be seen that there is a good correlation between the measured potentials and the final chloride content. Higher corrosion potentials corresponded to sections of the slab where the measured chloride content was high. The data seemed to follow a power function with an R^2 value of 0.88. Notably, the measured corrosion potentials became relatively constant and insensitive to the additional increase in chloride ions for sections with chloride content levels higher than 1600 ppm.

In addition, Figure 7-45 shows the threshold value at which the half-cell method suggests that corrosion is active and the critical chloride content at which the passive layer is assumed to be damaged. It can be seen that the half-cell potentials were able to correctly identify regions where the high levels of chlorides were present and exhibit high corrosion risk. Only 9.6% of the half-cell measurement locations (4 locations) indicated a high risk of corrosion while the measured chloride ion concentrations were below the critical threshold levels.

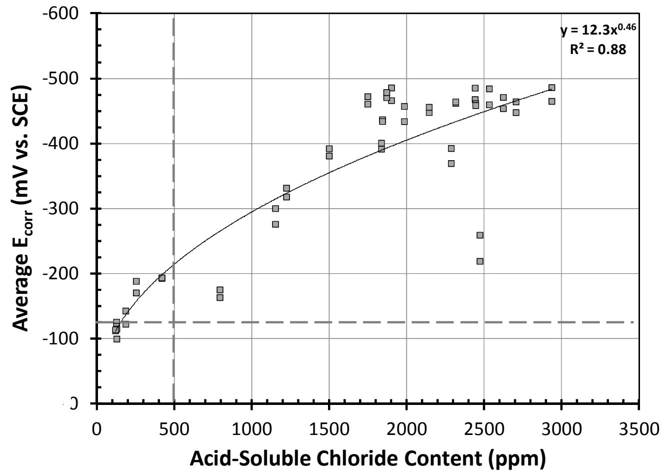

Figure 7-45: A comparison of average half-cell potentials and acid-soluble chloride content in slabs S1 and S2

Figure 7-46 is a plot of all the half-cell potential data points and the corresponding corrosion rates measured at the same time using the LPR technique in slabs S1 and S2. Figure 7-46 also shows the threshold values at which the corrosion risk is considered to be severe by the half-cell and LPR techniques (-275 mV and 1 μA/cm^2, respectively). While most of the data showed a correct agreement between the two methods, more than one fifth of the half-cell readings would have led to incorrect conclusions if used alone. In 13.9% of the readings, the half-cell potentials indicated a high probability of corrosion while the corrosion currents were modest. In addition, 7.2% of the half-cell readings were indicative of moderate to low corrosion risk while the corrosion currents were severe. These observations stress the need for complementing half-cell measurements with other corrosion assessment techniques.

The observed negative Tafel slope indicates that the corrosion activity in slabs S1 and S2 was under anodic control (Jones 1996). However, the large scatter in the data indicates that the correlation between the two techniques is poor. Similar findings were reported by Feliu et al. (1996), Huang et al. (1996), Pourasee and Hansson (2009), and Otieno et al. (2010).

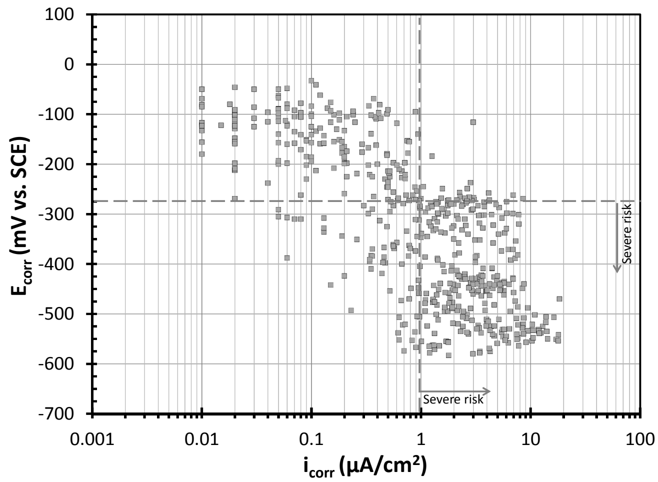

Figure 7-46: Comparison of half-cell potentials and LPR corrosion current densities for the reinforcement in slabs S1 and S2

7.5.3 Reliability of the Linear Polarization Resistance (LPR) Method

The LPR technique is widely used in practice to assess the extent of corrosion within reinforced concrete members. The method measures the local instantaneous corrosion current density of an embedded rebar section. The current densities can then be used to calculate the mass loss in the monitored section using Faraday's Law (Broomfield 2007). In practice, the instantaneous LPR data obtained during a single set of measurements are conservatively assumed to be constant throughout the service life of the structure. However, electrochemical corrosion evaluation methods can be unreliable and cannot be assumed constant because they depend on the environmental conditions in the surrounding concrete (Bertolini et al. 2004; Millard et al. 2001). Grantham and Broomfield (1997) reported average variability in the calculated reinforcement mass loss using the LPR data of 400% between readings acquired during the winter season and those collected during the summer for a corrosion distressed structure.

The results presented in Section 7.3.2 demonstrated the sensitivity of the LPR method to the variations in ambient temperature and moisture content in the concrete medium. However, the results also demonstrate the ability of the LPR method to correctly detect regions in the slabs where corrosion is active. Furthermore, the method had stable and consistent readings showing low corrosion current densities in the areas with passive reinforcement. While the ability of the LPR technique to locate areas with active corrosion is advantageous, similar conclusions can be extracted from half-cell potential investigations. The latter method is less expansive and can be conducted faster (Hansson 1984). The attraction to employ the LPR method in practice stems from the ability to convert the results into mass loss information which in turn can be used to perform service life estimates for the structure or member under consideration. In the following paragraphs, the accuracy of the mass loss estimated based on the LPR readings obtained during the long-term exposure test is investigated.

Throughout the test period (560 days), fourteen sets of linear polarization readings were collected. The readings were concentrated within five time periods (Section 7.3.2). Due to the variability of the consecutive LPR readings, the average current densities of each interrogation period were used to calculate the corrosion loss in that period. As a result, the average values include the effect of the higher currents measured after the wet periods and the lower currents measured after the dry periods. Figure 7-47 shows the average current densities and the corresponding time periods that were used to calculate the mass loss in the steel section extracted from the north rebar near sensor S1-4.

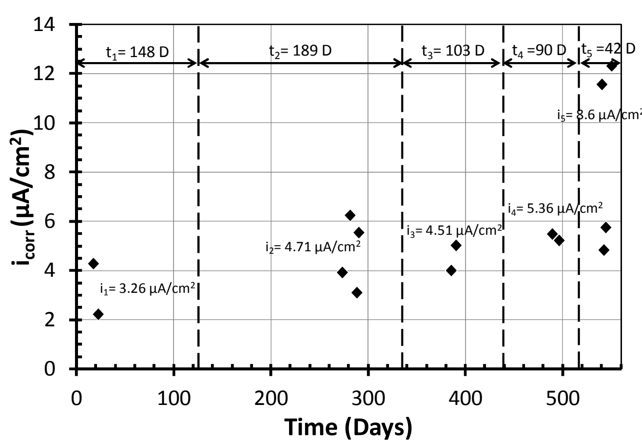

Figure 7-47: Average LPR current densities for each interrogation period and the associated time period for the north rebar section of sensor S1-4

The corrosion current densities were converted into section mass loss using Faraday's law as follows:

$$m = \sum \frac{M\, I_n\, t_n}{z\, F} \qquad \textbf{\textit{Equation 7-1}}$$

where,

m = mass of steel consumed in the corrosion reaction in grams

M = atomic weight of steel in grams (56 g)

I_n = corrosion current in Amperes

t_n = duration of the corrosion activity in seconds

z = ionic charge (2 for steel metal dissolution)

F = Faraday constant (96500 A.s).

Figure 7-48 shows the correlation between the actual mass loss in the reinforcing bars and the mass loss calculated using the LPR data for rebar sections extracted from slabs S1 and S2. The sections were classified based on their location within the slab. Figure 7-49 is an enlarged view of Figure 7-48 to show the losses calculated gravimetrically for the sections in the dry zone. The results indicate that there is a correlation between the loss estimated using the LPR data and the actual mass loss. As was discussed earlier, the LPR accurately indicated the regions where corrosion was active and where measureable mass loss was expected. However, the accuracy of the calculated mass loss values was very limited. Most of the sections examined (67%) lay within 50%-200% of the actual mass loss values. Similar ranges of variability were reported by other researchers (Bertolini, et al. 2004). Furthermore, the calculated mass loss underestimated the actual loss in 11% of the sections studied by more than half.

The mass loss calculations were also conducted on the steel sections extracted from the slabs exposed to tap water (Figure 7-50). The results showed the same level of variability observed in slabs S1 and S2.

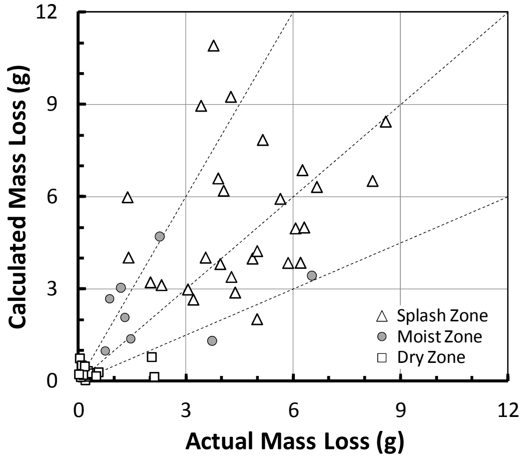

Figure 7-48: Measured mass loss in reinforcing bar sections from slabs S1 and S2 compared with mass loss estimates using the LPR data

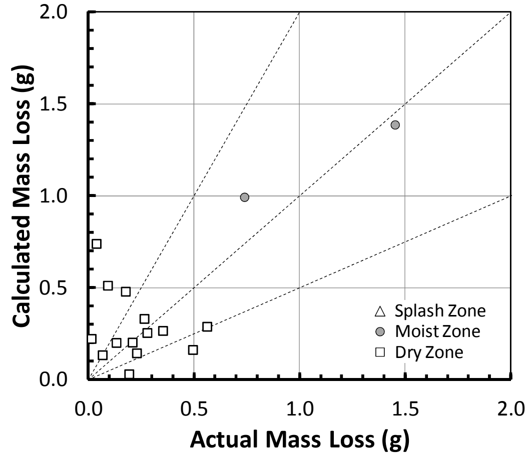

Figure 7-49: Measured mass loss in reinforcing bar sections from slabs S1 and S2 compared with mass loss estimates using the LPR data

It is important to note that the mass loss values obtained in this study were based on fourteen readings accounting for numerous variations in the environmental conditions throughout the test period. However, a single LPR measurement is typically used in practice to assess the mass loss and evaluate the remaining service life of structures under investigation. Hence, the accuracy of the LPR assessments used in practice is expected to be less than the findings shown here.

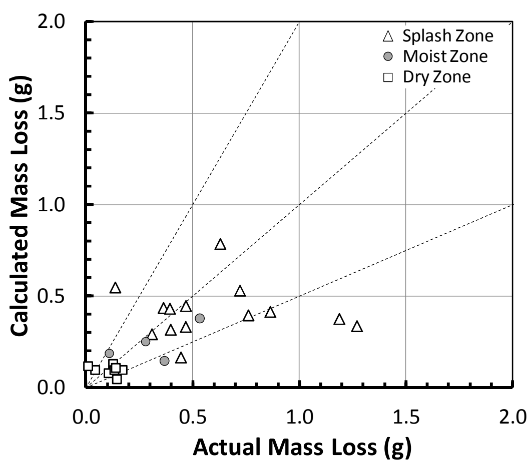

Figure 7-50: Measured mass loss in reinforcing bar sections from slabs T1 and T2 compared with mass loss estimates using the LPR data

7.6 SUMMARY

A set of 32 NC corrosion sensors were embedded in four reinforced concrete specimens resembling sections of bridge decks. The sensors were fabricated using sacrificial washers of different thicknesses and the specimens were exposed to different levels of chloride exposure. The response of the sensors was used to assess their reliability at detecting corrosion initiation in the steel reinforcement. In addition, electrochemical evaluation techniques were used to assess the corrosion activity within the concrete slabs.

The NC sensor successfully detected the corrosion damage within the concrete slabs. The reliability of the sensors was assessed with respect to the observed condition of the reinforcement. Nine of the embedded sensors switched to the corroded state and corrosion was present in the adjacent rebar sections. Furthermore, negligible to no corrosion damage was observed in the vicinity of the sensors that remained in the uncorroded state. However, only one sensor exhibited a false negative signal, which was attributed to the unique distribution of cracks surrounding that sensor.

In addition, the sensor readings exhibited limited variability throughout the duration of the exposure test. The measured frequency response of the NC sensors was only affected by the corrosion of the sacrificial washer. Throughout the exposure test period, the embedded sensors experienced variations in temperature as high as 65°F, fluctuations in moisture availability, and chloride levels; however, the measured resonant frequencies of the NC sensors were remained stable and insensitive to the environmental conditions.

The thickness of the sacrificial element was found to affect the threshold amount of corrosion damage detected by the NC sensors. The measured mass losses in the rebar sections surrounding the NC sensors fabricated using the thicker washers were generally higher and more severe. Furthermore, the 0.002-in. sensors required longer times to reach the corroded state when compared to the 0.001-in. sensors that were embedded underneath cracks of similar widths. In addition, the chloride content needed to cause a sensor transition was higher for the thicker washers.

Half-cell and LPR techniques were used during the exposure test to assess the corrosion risk. Although, variations in the measured potentials due to temperature and moisture levels were observed, the half-cell method correctly identified the regions under higher exposure to chlorides. However, the half-cell method indicated severe corrosion damage immediately after the initial exposure to chlorides and showed limited correlation with the corrosion activity or corrosion rates. Hence, it can be concluded that the half-cell technique is useful in identifying regions of high corrosion risk. However, it is critical to complement half-cell investigations with other destructive or nondestructive assessments.

The LPR measurements were sensitive to the variations in the physicochemical conditions of the embedded reinforcement including the electrochemical state of the rebar and the ionic conductivity of the concrete medium. Hence, the measured values were affected by the changes in the ambient temperatures and moisture levels. The LPR data reflected the instantaneous and localized rates of corrosion under set condition. Variations in the medium were found to cause to cause the readings to vary by as much as 400% between consecutive readings. Mass loss estimations using Faraday's Law were performed to assess the reliability of the LPR method. The calculated mass losses had significantly large scatter and had a limited correlation with the corrosion losses measured gravimetrically.

CHAPTER 8

Additional Sensor Design Considerations

8.1 OVERVIEW

The sensing transducer in the noncontact (NC) sensor prototype provides the potential for versatile and adaptable sensor deployment. By simply changing the nature of the contact-free transducer, Kim (2013) developed a passive wireless conductivity sensor that monitors the change in the conductivity of the concrete medium due to moisture and chloride ingress. So far, the work presented in this dissertation concentrated on the development of a binary state sensor for detecting corrosion. Through the use of a single sacrificial washer as the transducer, the NC sensor design has basically two limit states with an intermediate transition period. Such binary output is easy to interpret and can generally provide an adequate level of information regarding the state of corrosion within concrete. However, the current NC sensor design is a single-use sensor. Once the response of the sensor reaches the corroded limit state, no additional information regarding the rate, level, or extent of corrosion damage can be extracted from the embedded sensor response. To this end, an adjustment in the sensing layer of the NC sensor that enables the detection of ternary or even quaternary corrosion threshold states was investigated. The ability of the NC sensor to detect different levels of corrosion damage is demonstrated in Section 8.2 and the multi-threshold NC sensor designs are introduced in Section 8.3.

In Chapter 5, localized corrosion was found to affect the behavior of the NC sensor during its transition to the corroded state. In order to mitigate the undesirable effects of localized corrosion, a simple and inexpensive solution was developed. The solution relies on employing a diffusion layer to distribute the chlorides uniformly. Details regarding the localized corrosion and the diffusion layer concept are discussed in Section 8.4.

8.2 DETECTION OF DIFFERENT CORROSION DAMAGE THRESHOLD LEVELS

The flexibility of the NC sensor design allows the sensor platform to be utilized for detecting different levels of corrosion damage. Thus, bridge owners and maintenance personnel have the freedom to identify and select the critical corrosion damage level that meets their infrastructure management plans. While early detection can allow for inexpensive repairs, some bridge owners are more concerned about avoiding excessive delaminations and concrete spalling. By simply adjusting the physical or material properties of the sacrificial element, the NC sensor can be used to either provide an early warning of chloride ingress or to identify regions of severe corrosion accumulation. In other words, the NC sensor can be customized to meet the needs of the owner.

For sacrificial washers, increasing the thickness increases the level of corrosion damage that occurs before the sensor trigers. The parametric studies in Section 3.3 demonstrated that the thickness of the sacrificial washers have marginal effect on the initial shielding and frequency shift of the NC sensor. However, the thickness of the washer was expected to have a direct influence on the threshold corrosion level. To evaluate the effect of the washer thickness on time needed to detect corrosion, five steel washers with nominally identical geometries and different thicknesses (0.001, 0.002, 0.004, 0.005 and 0.010 in.) were affixed in a plastic tank and exposed to 2-day wet and 5-day dry cycles using a 3.5% salt water solution. The washers had an outer diameter of 2.75 in. and 1.75 in. inner diameter. The sensors were interrogated using one 3.20 MHz resonant circuit, which was moved from washer to washer, while maintaining a constant separation distance of 0.2 in. As a result, the final corroded state resonant frequencies were equal for all the washers examined ($f_{\text{final}} = f_{\text{rc}}$ =3.20 MHz). Furthermore, because the washers had identical inner and outer diameters, the initial frequencies were also the same ($f_{\text{initial}} = f_{\text{se}}$= 3.72 MHz). Hence, the use of a single resonant circuit ensured that the transition region between the uncorroded and corroded states for each washer could be compared directly. Figure 8-1 illustrates the experimental set-up used to evaluate the effect of the washer thickness during a dry period interrogation.

The sensor interrogations were conducted at the end of each wet and dry period. The salt water tank was thoroughly dried at the end of the wet periods before the impedance measurements. Figure 8-2 shows the change in the measured phase response for the 0.004-in. washer due to corrosion accumulation. Initially, the resonant frequency, phase dip and bandwidth remained constant and identical to the response acquired at day 7. After 56 days of continuous exposure, the resonant frequency started decreasing gradually; hence, indicating the onset of the transition period. The shift in frequency was accompanied by a reduction in phase dip and a widening of the bandwidth. Finally, the resonant frequency reached the corroded frequency (f_{rc}) after 75 days. The behavior shown in Figure 8-2 was observed in all the washers examined, however, the times needed to initiate transition and reach the final frequency were different for each washer thickness.

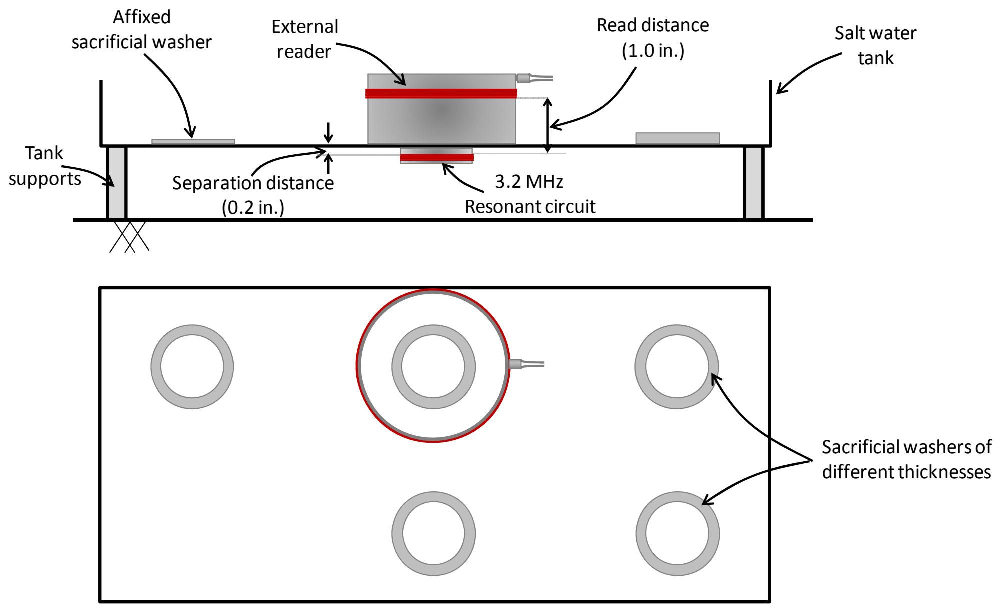

Figure 8-1: Elevation and plan views of the experimental set-up used to evaluate the effect of the washer thickness

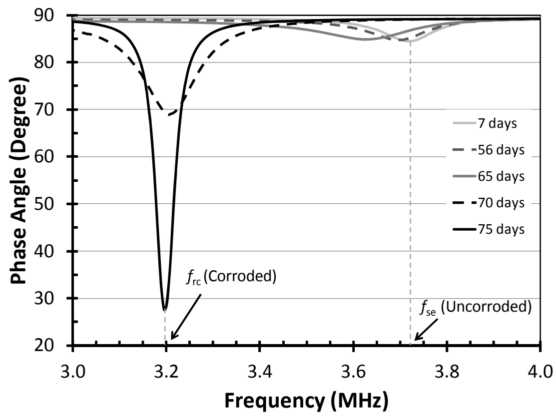

Figure 8-2: Measured phase response of the 0.004-in. thick washer at 7, 56, 65, 70, and 75 days of exposure

The change in the resonant frequency with time for the 0.001 and 0.004 in. washers is shown in Figure 8-3. The frequency of each washer shifted monotonically from the initial to the final resonant frequency (3.72 MHz and 3.20 MHz, respectively). Both curves show three regions of response: an initial stage where the resonant frequency remains constant (uncorroded), a transition period where the frequency decreases monotonically (transition), and the corroded stage where the frequency remains constant and equal to the resonant circuit frequency. It can be seen that the uncorroded stage was longer for the 0.004-in. washer than the 0.001-in. washer. Furthermore, the transition for the 0.004-in. washer was more gradual and took a longer period of time. Given that the chloride exposure level was identical for all the washers examined, the time axis in Figure 8-3 is proportional to the corrosion damage threshold that would be observed in adjacent reinforcement. Therefore, a higher level of corrosion damage will be detected near the sensor fabricated with the 0.004-in. thick washer.

Figure 8-4 summarizes the test results and shows the times needed to start the resonant frequency transition from the uncorroded stage and the times needed to reach the corroded stage for all the washers. It can be seen that the time needed to start the transition increases proportionally with the washer thickness. In addition, the time spent in the transition stage is longer for thicker washers.

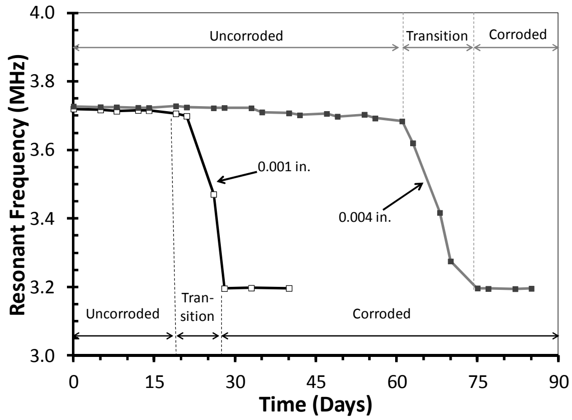

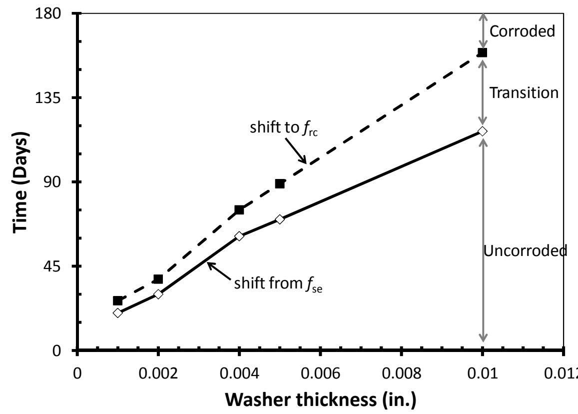

Figure 8-3: Change of resonant frequency with time for the 0.001-in. and 0.004-in. thick washers

Figure 8-4: Time needed to start transition and reach the corroded stage for different sacrificial washers

The results can also help clarify the effect of corrosion build-up on the measured sensor response. The washer shielding is an electromagnetic phenomenon that requires a finite material thickness for current flow (skin depth). The skin depth for low-carbon AISI 1010 steel at 3.2 MHz is approximately $2x10^{-4}$ in. Hence, the washer resistance to current remains equal to its initial value as long as the thickness of the uncorroded steel is greater than the skin depth. Once the thickness of the uncorroded material is less than the skin depth, the resistance of the washer increases gradually. Finally, the resistance reaches infinity indicating that no path for current flow can be realized. Therefore, initial measurements during the uncorroded stage remain constant for a time period proportional to the washer thickness. The increase in the transition period for thick washers can be attributed to the formation of a dense layer of corrosion products that hinders the diffusion of moisture and chlorides into the uncorroded material.

The results also demonstrate the flexibility of the NC sensor design. The novel design gives the owner the freedom to select the degree of acceptable damage. If detecting the onset of corrosion is the goal of the monitoring plan, a thin washer can be used as a sacrificial element. Furthermore, detection of different corrosion damage levels can be achieved easily by fabricating an assembly of NC sensors composed of a series of closely spaced resonant circuits with a unique washer attached to each circuit. The threshold corrosion damage can be varied by using washers of different thicknesses or materials. Similarly, NC sensors made with identical washers can be arranged in a stepped manner, such that the embedment depth increased, to monitor the progression of the chloride front into the concrete medium.

8.3 MULTI-THRESHOLD NC SENSOR

The NC sensor prototype discussed in the previous chapters of this dissertation employs a single transducer to detect corrosion. Hence, each embedded sensor is a single point sensor that is only capable of detecting one level of corrosion damage within the concrete medium. Once the NC sensor response shifts to the final corroded state, the embedded sensor becomes obsolete and does not provide any additional information regarding the corrosion activity. However, the contact-free interaction between the sensing layer and the resonant circuit permits the potential utilization of multiple sacrificial elements within a single sensor to detect different levels of corrosion damage. Hence, by simply adjusting the sacrificial elements, the NC sensor can be upgraded from a simple binary threshold sensor into a multi-threshold sensor capable of detecting a spectrum of corrosion damage levels. The upgrade in the scope of the NC sensor can be achieved by introducing additional sacrificial layers of different geometries, materials, separation distances, and/or types.

The following paragraphs describe three examples of potential multi-threshold NC sensor designs. Due to the developmental nature of this research, all the initial designs were limited by the commercially available dimensions and sizes of the sacrificial washers.

8.3.1 Preliminary Multi-Threshold Sensor Design

The initial multi-threshold NC sensor design incorporated three geometrically different sacrificial washers that were arranged concentrically (Figure 8-5). The sensing layer comprised an inner washer (0.75-in. outer diameter and 0.002-in. thick), an intermediate washer (1.50-in. outer diameter and 0.004-in. thick), and an outer sacrificial washer (2.75-in. outer diameter and 0.006-in. thick). The width of the washers was not selected by the research team but rather limited by the commercially available washer sizes. The resonant circuit used for the fabrication of the NC sensor was a 2.5-in. diameter coil with a resonant frequency of 3.15 MHz.

With this configuration, the inner washer was expected to corrode first and induce a small change in the resonant frequency of the multi-threshold sensor. This is due to the lower inductive coupling expected between the 2.5-in. diameter resonant circuit and the smaller diameter washers (Chapter 3). In contrast, the 2.75-in. diameter washer was expected to corrode last and induce the largest shift in the measured resonant frequency. Therefore, the selected sensor assembly ensured that the shift in the measured resonant frequency was higher for larger corrosion damage thresholds.

Prior to fabrication of the multi-threshold NC sensor, the resonant frequencies of the four possible limit states were measured in air (Table 8-1). The percentage in the frequency shift due to the corrosion of each washer is also shown. As expected, the corrosion of the larger washers resulted in larger shifts in the measured resonant frequency.

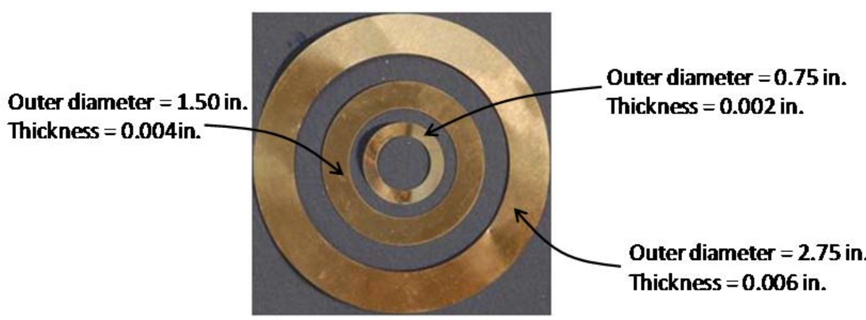

Figure 8-5: Sensing layer of the concentric multi-threshold NC sensor

Table 8-1: Resonant frequencies of the four possible limit states of the concentric multi-threshold NC sensor measured in air

Sacrificial Layer Arrangement			Resonant Frequency (MHz)	Shift in Resonant Frequency (%)
2.75-in. Washer	1.50-in. Washer	0.75-in. Washer		
P	P	P	3.315	0.00
P	P	-	3.309	3.7
P	-	-	3.280	21.5
-	-	-	3.152	100

P: Washer present   - : Washer removed

The concentric multi-threshold sensor was fabricated in a similar manner as the binary NC sensor (Appendix A). The addition of the two inner washers was the only extra step for the construction process. The sensor was positioned inside a plastic water tank and exposed to 3.5% salt water. During the exposure testing, the tank was filled with salt water for one day and drained for two days. The multi-threshold NC sensor was interrogated at the end of each wet and dry period.

Because the exposure to chlorides was uniform and equal for the three washers, the increase in the time needed to fully corrode a sacrificial washer is indicative of a higher level of corrosion damage. The change in the measured resonant frequency with time is shown in Figure 8-6. The frequency dropped in a stepped manner with four distinct plateaus corresponding to the expected four limit states. Initially, the resonant frequency response was stable for almost 14 days. During this period, corrosion developed uniformly over the exposed sacrificial washers. Then, the frequency dropped slightly from 3.31 to 3.30 MHz indicating that the 0.002-in. washer became fully corroded. The small change in frequency was expected due to the limited coupling between the sensor circuit and the inner washer. The frequency remained constant for the next 30 days and then gradually dropped to a new plateau at 3.28 MHz. The later frequency shift was due to the consumption of the 0.004-in. washer. Finally, the sensor frequency dropped monotonically and reached the final fully corroded limit state in day 78 where the measured frequency was equal to the resonant frequency of the circuit resonant and remained constant afterwards.

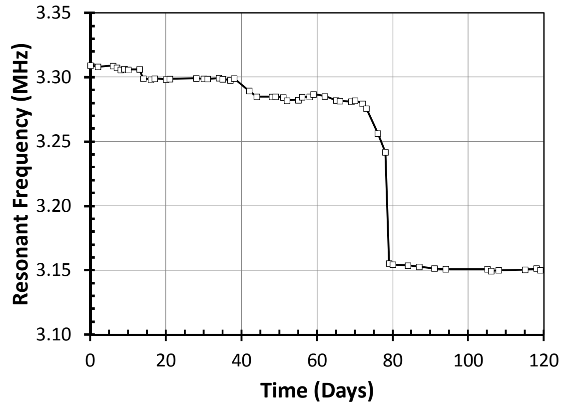

Figure 8-6: Shift in resonant frequency with time for the concentric multi-threshold NC sensor

Figure 8-7 shows the washers before the exposure and at the end of the test. The exposure test results were comparable to the findings reported in Section 8.2. The thicker washers exhibited longer plateaus and longer transition periods. For example, the time periods where a constant resonant frequency was measured increased from 14 days for the 0.002-in. thick washer to 70 days for the 0.006 washer.

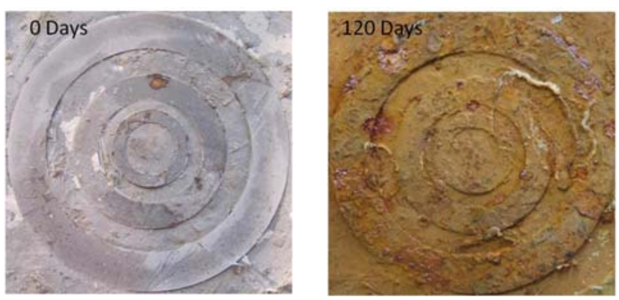

Figure 8-7: Sensing layer of the concentric NC sensor before (0 days) and after (120 days) the exposure test

The observed response demonstrated the potential for successful development of a multi-threshold detection using a single NC sensor. However, the shift in the resonant frequency due to the corrosion of the smallest washer was limited and fell within the range of frequency shifts attributed to variations in ambient temperature and the surrounding environmental conditions (5 to 8% frequency shift). This limitation can restrict the useful deployment of the multi-threshold sensor prototype. Hence, an optimized design that ensures relatively equal inductive coupling coefficients between the resonant circuit and all the sacrificial elements employed is desirable. Such optimization can be achieved using the finite element modeling technique discussed in Section 3.7 and the conclusions of the NC sensor development studies. Two optimized multi-threshold NC sensor designs were developed and investigated using accelerated corrosion testing. The description and test results of the two sensors are summarized in the Section 8.3.2.

8.3.2 Optimization Options of the Multi-Threshold NC Sensor

The main shortcoming of the concentric multi-threshold NC sensor design was the weak coupling between the resonant circuit and the inner washers. To this end, two optimized multi-threshold NC sensor prototypes were constructed. The first design takes advantage of the significant increase in the inductive coupling between any two coaxial coils as the separation distance between the two decreases. Hence, by adjusting the separation distances between the resonant circuit and three geometrically different washers, the difference in the mutual coupling coefficients can be reduced. Based on the initial parametric studies, it is expected that the washer with an outside diameter that is approximately equal to the diameter of the resonant circuit coil exhibit the highest inherent coupling. So, this washer should be placed the furthest from the resonant circuit.

The stepped NC sensor was constructed using three geometrically different washers. The outer washer was 0.001-in. thick and had an outer diameter of 2.75 in. The smallest washer was 1.275 in. in diameter and 0.003-in. thick. The intermediate washer was 0.002-in. thick with an outer diameter equal to 2.125 in. The stepped NC sensor was fabricated by placing the smallest washer at the same level as the resonant circuit coil. The remaining two washers were placed concentrically in a stepped manner with a constant step height of 0.20 in. Figure 8-8 and Figure 8-9 show a photograph and a schematic illustrating the stepped NC sensor design, respectively.

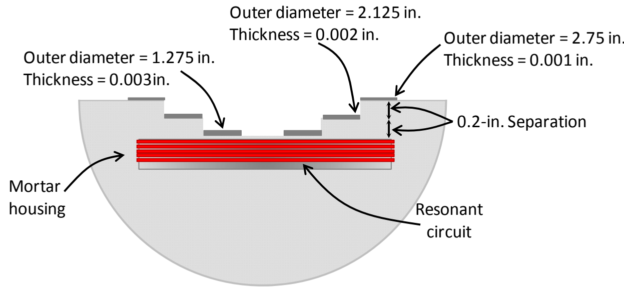

Figure 8-8: Photograph of the stepped NC sensor design

Figure 8-9: Schematic illustrating the components of the stepped NC sensor

In reinforced concrete structures, the chloride front ingress is ideally uniform. Hence, the topmost sacrificial washer is expected to be exposed to higher chloride levels and start corroding first. As the chlorides front penetrates into the concrete, the second corrosion threshold is reached by corroding the intermediate sacrificial washer. The final corroded state is reached once the innermost washer corrodes. Hence, the stepped NC sensor design can also be used for monitoring the rate of chlorides diffusion within concrete. This can be achieved by simply using washers of similar thicknesses and monitoring the times needed for each threshold state to be reached. However, the initial design employed washers of different thicknesses to ensure a stepped drop in the measured resonant frequencies in the salt water submersion tests.

The second optimized multi-threshold sensor design relies on the observed reduction in the inductive coupling between coils that are not coaxial. As the lateral eccentricity between two coils increase, the mutual coupling is expected to decrease rapidly (Dickerson 2005). Hence, it is possible that the eccentric placement of the sacrificial washers can adjust the different magnetic coupling coefficients resulting in distinguishable and sufficiently-spaced threshold steps. Three washers were used to assemble the eccentric NC sensor. The outer diameters of the sacrificial washers were 3.25, 2.125, and 1.375 in. and the washers were 0.001-, 0.002-, and 0.003-in. thick, respectively.

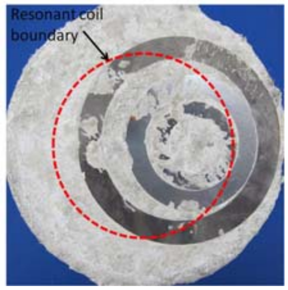

Figure 8-10: Photograph of the eccentric NC sensor design

After a number of initial placement options were examined, the eccentric arrangement shown in Figure 8-10 was selected. In this design, the edge of the washer with the smallest outer diameter was placed exactly above the resonant circuit boundary, which increased its shielding effect on the coil. The other two washers were placed eccentrically on the outside of the sensor boundary. The design ensured that the washers were not physically in touch as such contact can allow the inductively induced current to flow between the different washers jeopardizing its ability for multi-threshold detection.

Impedance response measurements were conducted prior to the fabrication of the new multi-threshold prototypes. Figure 8-11shows the percentage change in resonant frequency as the washers were removed successively. The data for the initial concentric prototype are also included for comparison. It can be seen that the optimized sensor designs are strongly coupled with the three sacrificial elements providing a definite and significant drops in frequency corresponding to each corrosion damage threshold.

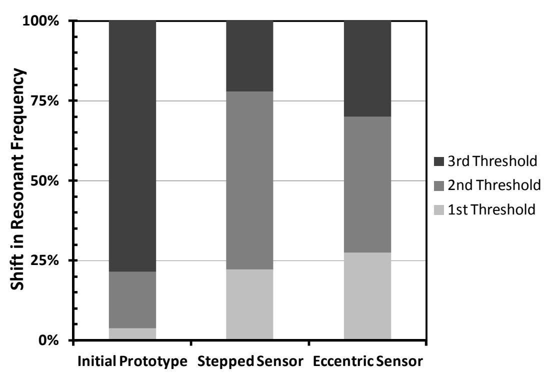

Figure 8-11: Percentage change in the resonant frequency for each corrosion threshold of the multi-threshold sensor prototypes.

The optimized NC sensors were fabricated and were affixed in a plastic tank. The sensors were exposed to 2-day wet and 5-day dry exposure cycles and were interrogated occasionally. Figure 8-12 shows the change in the measured resonant frequency of the stepped NC sensor with time. The transition from the initial uncorroded state to the final fully corroded state includes a distinct and relatively uniform stepped profile with four plateau regions. Initially, the resonant frequency of the stepped sensor remained stable at the uncorroded resonant frequency (f_{se} = 3.30 MHz) for 51 days. During this period, uniform corrosion build up was observed on the surface of the three sacrificial washers. Then, the resonant frequency transitioned gradually into an intermediate frequency (approximately 3.26 MHz) indicating that the thinnest washer has fully corroded. The initial transition took place within 25 days. The response remained unchanged for only 20 days before the resonant frequency started shifting to the third threshold state at a frequency of 3.19 MHz. Again, the response plateaued for almost 50 days before transitioning to the final fully corroded resonant frequency (f_{rc} = 3.140 MHz) after a total 214 days of salt water exposure. The response remained constant in later interrogations indicating that all the sacrificial washers were fully corroded.

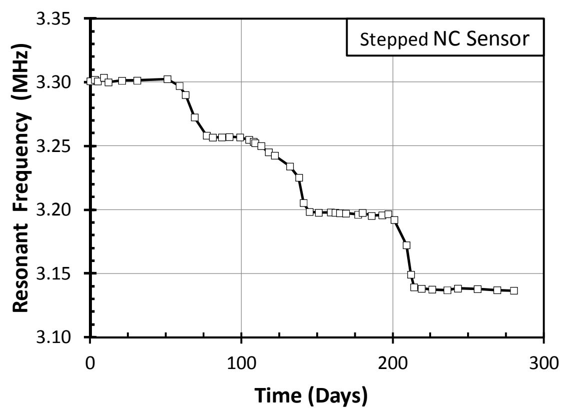

Figure 8-12: Measured resonant frequency with time for the stepped multi-threshold NC sensor

The accelerated corrosion test results indicate that the change in the response of the stepped NC sensor is ideal for multi-threshold corrosion monitoring. The four threshold limit states are easily distinguishable and the separation between any two consecutive drops in resonant frequency is substantial and approximately equal. Hence, the interpretation of the state of an embedded sensor at the time of interrogation can be easily done as the level of corrosion damage exceeded can be identified directly from the resonant frequency. The relatively large shifts in resonant frequencies between successive threshold levels (48, 54, and 61 kHz, respectively) are on average ten times higher than the accidental drifts in frequency which are produced by fluctuations in temperature and moisture levels (Appendix C). Based on these observations, it can be concluded that the stepped NC sensor design provides a promising and practical alternative for multi-threshold corrosion detection applications.

The change in the resonant frequency of the eccentric NC sensor over time is shown in Figure 8-13. The response of the eccentric sensor remained initially stable for 100 days with minimal drift in the initial resonant frequency (3.29 MHz). The resonant frequency shifted slightly to the second threshold state at 3.275 MHz (approximately 8% of the dynamic range) and remained constant for 46 days. Then the sensor decreased gradually to 3.23 MHz (36% of the dynamic range) reaching the third threshold level and indicating that the intermediate washer was fully corroded. With one sacrificial washer remaining uncorroded, the resonant frequency of the eccentric NC sensor remained unchanged for more than 110 days. While the salt washer exposure was continuous and all the sacrificial washers were under the same conditions, the thickest sacrificial washer did not indicate any physical signs of corrosion initiation. The surface of the 0.003-in. thick washer remained in its original shape with no signs of corrosion build-up. Figure 8-14 shows the eccentric NC sensor after 265 days of chloride exposure. Hence, the exposure test was stopped at day 280. To simulate corrosion of the thick washer, the sacrificial washer was cut and the resonant frequency of the circuit was found to be approximately 3.13 MHz.

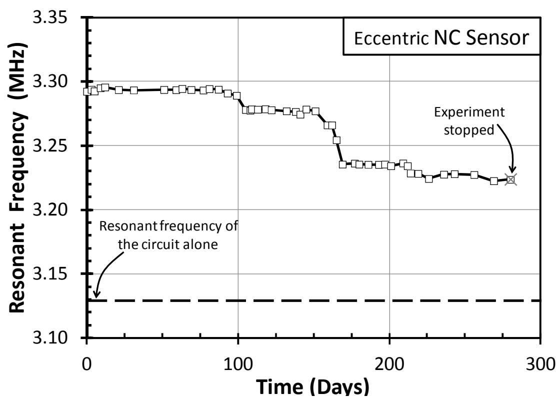

Figure 8-13: Measured resonant frequency with time for the eccentric NC sensor

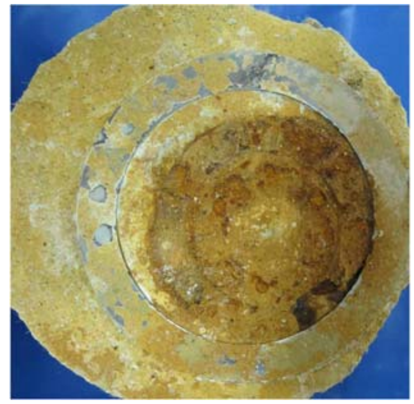

Figure 8-14: Photograph of the eccentric NC sensor at the end of exposure test

The unexpectedly higher corrosion resistance of the 3.25-in. diameter sacrificial washer can be either an anomaly in production or it can be the result of a change in the chemical composition of the steel used to manufacture this specific washer dimension. None of the sacrificial washers used to fabricate any of the sensors examined throughout this dissertation exhibited such a considerable level of corrosion resistance. Hence, future developments should include material chemical composition analyses and electrochemical evaluations similar to those described in Chapter 4 for all the sacrificial washer types being used in sensor fabrication.

While the experimental evaluation was terminated before the final corroded limit state was reached, the profile of the measured change in the resonant frequency of the eccentric NC sensor is suitable for the multi-threshold use. The observed differences between the resonant frequencies of the uncorroded state and the threshold states corresponding to the corrosion of the two smaller washers are significant. However, the initial frequency drop was approximately 15 kHz which is on average only 2.5 times higher than the temperature induced frequency drifts. Hence, an adjustment to the design of the eccentric NC sensor is needed to slightly increase the coupling with the smallest sacrificial washer. This can be simply achieved by increasing the width of the smallest washer.

8.4 INFLUENCE OF LOCALIZED CORROSION ON NC SENSOR RESPONSE

The autopsy results of the exposure test conducted on reinforced concrete prisms have shown that the response of the corrosion sensor can be affected by localized corrosion (Section 5.4). It was observed that the transition to the corroded state of one of the sensors was halted temporarily before reaching the fully corroded state. This unexpected behavior can be the result of the formation of a dense layer of corrosion products in the crack region that subsequently blocked the supply of chloride ions to the active anode and halted the corrosion process. The slower corrosion rate can also be the result of local and unique electrochemical conditions that led to the repassivation of the steel near the cracked region. Although the unexpected behavior did not affect the ability of the sensor to detect the corrosion activity reliably, it can lead to misinterpreting the response of the sensors embedded in the field. In addition, this unusual behavior will jeopardize the potential for utilizing the NC sensor for multi-threshold applications and can impede the development of a reliable rapid interrogation technique.

In an attempt to replicate the observed effect of the localized corrosion damage, an accelerated exposure test was conducted. Two identical NC sensors were fabricated using 0.001-in. thick sacrificial washers. In order to induce localized corrosion, the washer surface of one sensor was partially covered with marine epoxy, thereby, restricting the chloride exposure to the epoxy-free regions. To simulate the crack, a 0.04-in. thick plastic shim was taped to the surface of the washer prior to covering the sensor with epoxy. After the epoxy set, the adhesive tape was removed creating the simulated crack region that is prone to corrosion damage. In order to simulate the conditions observed in the prisms test, the size of the simulated crack was selected to match the crack size above sensor SW-B which exhibited the unexpected behavior. For comparison, the second NC sensor was left without the epoxy layer allowing for a uniform corrosion development.

Figure 8-15: Uniform corrosion sensor

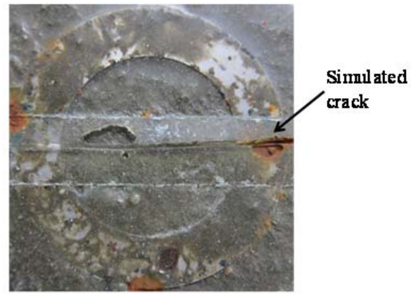

Figure 8-16: Localized corrosion sensor with a simulated 0.04 in. crack

The two sensors were attached to a plastic water tank and exposed to alternating 2-day wet and 5-day dry cycles of a 3.5% salt water exposure. The sensors were interrogated regularly. Figure 8-15 shows the evidence of uniform corrosion activity on the surface of the sacrificial element that was not covered by epoxy. In contrast, Figure 8-16 shows the corrosion forming on the surface of the washer with the simulated 0.04-in. wide crack. It can be seen that the corrosion build up was restricted to the epoxy-free region and areas of the washer where air bubbles had formed during the setting of epoxy. However, the sensor response is expected to be only affected by the corrosion occurring in the simulated crack region where the whole width of the sacrificial washer is actively corroding.

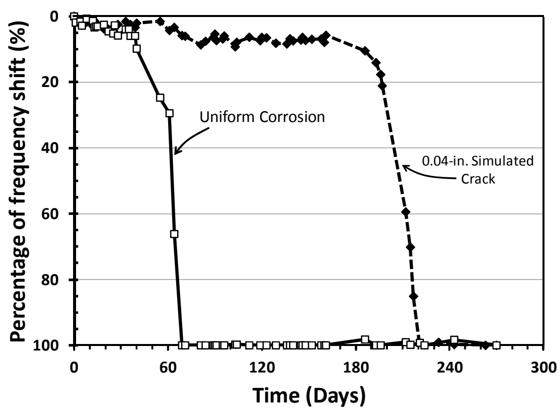

Figure 8-17: The change in the resonant frequencies of the uniform corrosion sensor and the 0.04 in. simulated crack sensor.

Figure 8-17 shows the percentage change in the resonant frequencies of both sensors. The uniform corrosion sensor started transitioning after 30 days of exposure and the resonant frequency decreased monotonically reaching the corroded state in day 70. On the other hand, the resonant frequency of the 0.04-in. simulated crack sensor remained constant for 55 days and then dropped to 8% of the dynamic range. Then the sensor response remained constant for additional 75 days before finally transitioning monotonically to the resonant frequency of the corroded state in day 220.

The results of the exposure test show the same patterns observed in the long-term accelerated corrosion tests of the reinforced concrete prisms. When the corrosion activity on the sacrificial washer was localized due to the presence of cracks, the transition of the sensor response to the corroded state was slower than the sensors exposed to uniform corrosion. Furthermore, the localized corrosion caused the resonant frequency of the NC sensor to remain temporarily constant at an intermediate frequency after an initial shift from the uncorroded state.

While the undesirable behavior during transition was not observed in any of the NC sensors embedded in the reinforced concrete slabs (Chapter 7), there is still a good possibility that the unusual transition to the corroded state can occur in future field deployments. It should be noted that any significant shift in the resonant frequency from the uncorroded limit state can still be used to identify the status of corrosion activity within concrete. Hence, the current NC sensor design can still be used as a binary state point sensor. However, a simple and inexpensive alteration to the NC sensor design was found to mitigate the problem of localized corrosion and eliminate the potential of an embedded sensor exhibiting the undesirable behavior during its shift to the corroded state. Section 8.5 introduces the concept of the diffusion layer and discusses the results of a long-term accelerated corrosion test that demonstrate the benefits of the design modification.

8.5 DIFFUSION LAYER CONCEPT

A diffusion layer is envisioned to be placed directly over the exposed sacrificial washer during the NC sensor fabrication. The layer used should be a water-absorbing medium that enables the dispersion of chlorides from the regions of high concentrations near cracks to the rest of the sacrificial washer. Thereby, the addition of the diffusion layer ensures a more uniform distribution of chlorides over the surface of the sacrificial washer mitigating the localized corrosion problem. Figure 8-18 is a schematic illustrating the concept of the diffusion layer.

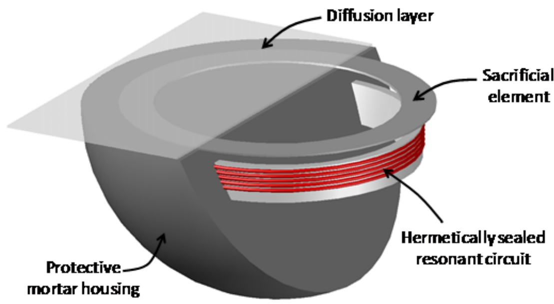

Figure 8-18: Schematic view of the diffusion layer concept

An experimental study was conducted to examine the effect of localized corrosion exposure on the response of embedded sensors. The study examined the sensitivity of the response of the NC sensor to the location and size of cracks. Furthermore, the feasibility of the diffusion layer concept and its ability to resolve the localized corrosion problem was evaluated. To this end, NC corrosion sensors were embedded in reinforced concrete specimens. The specimens were 8.0-in. long, 8.0-in. wide, and 5.0-in. deep concrete blocks that were reinforced with two #3 steel rebars. The steel reinforcement was used to facilitate stabilizing the embedded sensor during concrete placement and allow for validating the reliability of the original and modified NC sensors. The simulated cracks were created artificially by temporarily placing a thin steel shim at the desired crack location before concrete placement. The shims were removed after the concrete had hardened creating the desired crack that has a width approximately equal to the thickness of the shim.

Three variables examined experimentally in this test were: (1) crack size, (2) crack location relative to the embedded NC sensor, and (3) the presence of diffusion layers. In order to simulate the results of the long-term exposure testing, crack sizes of 0.01 and 0.04 in. were selected. Furthermore, the artificial cracks were either located at the center of the sacrificial washer (C), the edge of the sacrificial washer (M), or at the edge of the NC sensor (E) (Figure 8-19). Paper- or polyester-based fabrics were selected to act as potential diffusion layers. The diffusion layers were wrapped around the fabricated sensor and covered the surface of the sacrificial washer and the cement housing of the sensor. Two layers of either the paper or polyester fabric were used for each embedded sensor to add a redundancy against breakage during the placement of the concrete. Figure 8-20 and Figure 8-21 show specimens with a paper and polyester diffusion layers before concrete placement, respectively. Table 8-2 summarizes the experimental matrix of the reinforced concrete prism specimens used in this study.

The specimens were cast on August 12th 2011 using QUIKRETE® concrete mix. The compressive strength of the mixture at 28 days was 3300 psi. To prevent accidental movements of the embedded NC sensors, the specimens were compacted using a 0.5-in. diameter rod. The blocks were moist cured for 21 days before the forms were removed. Initial sensor interrogations indicated that the NC sensors were intact and remained in place during the placement of concrete.

The specimens were exposed repetitively to salt water solution that was dripped directly over the simulated crack for two days and then the specimens were allowed to dry for five days. The exposure cycles started on September 10th 2011 and stopped on June 28th 2013. The sensor interrogations were performed regularly using the Reflectometer technique. The test was initially conducted in an air conditioned room where the ambient air temperature ranged between 70° and 80° F. After 215 days of exposure, none of the sensors had indicated corrosion initiation. The specimens were then moved into an unheated and unairconditioned building and experienced temperature fluctuations of more than 70°F with a maximum recorded temperature of 113°F.

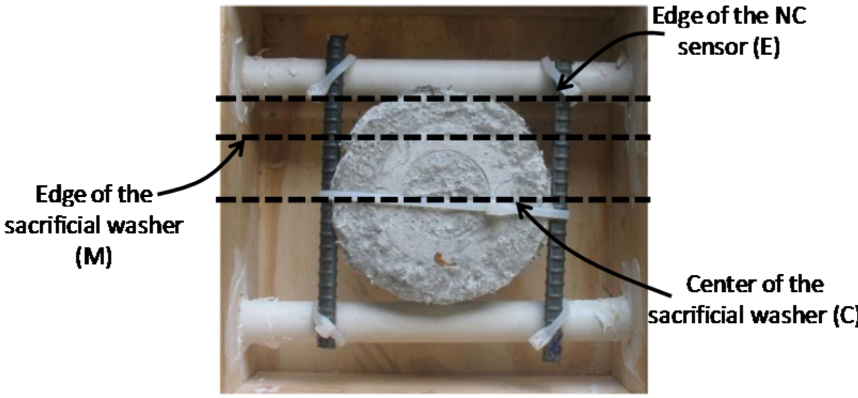

Figure 8-19: Photograph of the NC sensor specimen indicating the locations of the simulated cracks

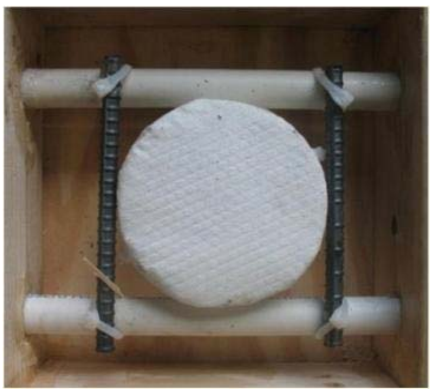

Figure 8-20: NC sensor with a paper-based diffusion layer

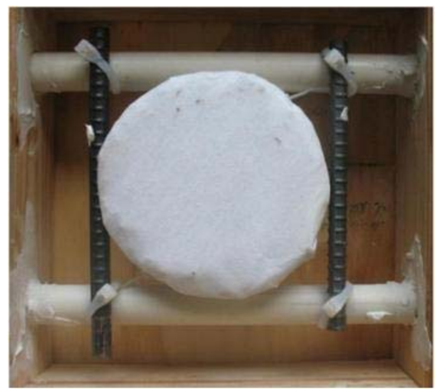

Figure 8-21: NC sensor with a polyester-based diffusion layer

Table 8-2: Experimental matrix and nomenclature of the concrete specimens used in the localized corrosion and diffusion layers study

		Diffusion Layer		
Crack Location	**Crack Size**	**None**	**Paper**	**Polyester**
Center of the wahser	**0.04 in.**	NoC-4	PC-4	PolC-4
	0.01 in.	NoC-1	-	-
Edge of the washer	**0.04 in.**	NoM-4	PM-4	PolM-4
	0.01 in.	NoM-1	-	-
Edge of the NC sensor	**0.04 in.**	NoE-4	PE-4	PolE-4
	0.01 in.	NoE-1	-	-

Once the signal of an embedded NC sensor switched to the corroded state, the concrete block was autopsied and the corrosion damage on the sacrificial washer and steel rebar was documented. The specimens where corrosion was not detected were autopsied after the last exposure cycle (665 days). Table 8-3 and Table 8-4 summarize the autopsy results for the concrete specimens containing the NC sensors that were fabricated without the diffusion layer and had simulated cracks of widths of 0.01 and 0.04 in., respectively. All the sensors embedded in the specimens with the 0.01-in. wide cracks remained in the uncorroded state with no indication of corrosion initiation (Figure 8-22). After the autopsy, the sacrificial washers of the 0.01-in. crack specimens were found intact with no visible corrosion damage. In addition, the rebar samples had indications of localized pitting directly under the cracks. However, the observed corrosion damage on the reinforcing bars was limited.

Corrosion was detected within two of the 0.04-in. crack specimens without a diffusion layer (Figure 8-23). First, sensor NoC-4 (sensor embedded in the specimen where the crack was located at the center of the washer) reached the corroded state after only 291 days of exposure. The frequency response of that sensor was not affected by localized corrosion and the shift in resonant frequency was monotonic and lasted only two weeks. The physical autopsy confirmed the localized nature of the corrosion damage. The observed corrosion on the sacrificial washer concentrated directly under the central crack and only on one side of the washer. Evidence of pitting damage was also observed at the middle section of the reinforcing bars adjacent to the sensor.

After 610 days of exposure, sensor NoM-4 reached the corroded state. The corrosion damage was concentrated under the crack. The corrosion spread slowly until it consumed the total width of the sacrificial washer switching the response of the sensor to the corroded state. Hence, the chlorides had to diffuse through the concrete perpendicular to the crack increasing the time needed to reach the corroded state. Both reinforcing bars in specimen NoM-4 exhibited evidence of corrosion damage in the vicinity of the artificial crack.

Table 8-3: The state of the sacrificial washers and steel reinforcement of the NC sensors fabricated without a diffusion layer after the autopsy of the blocks with the 0.01-in. simulated cracks

	NoC-1	**NoM-1**	**NoE-1**
Crack location	Center of washer	Edge of washer	Edge of NC sensor
Crack size	0.01 in.	0.01 in.	0.01 in.
Days to corrosion	No Corrosion	No Corrosion	No Corrosion
Sacrificial washer corrosion			
Rebar corrosion			

Table 8-4: The state of the sacrificial washers and steel reinforcement of the NC sensors fabricated without a diffusion layer after the autopsy of the blocks with the 0.04-in. simulated cracks

	NoC-4	**NoM-4**	**NoE-4**
Crack location	Center of washer	Edge of washer	Edge of NC sensor
Crack size	0.04 in.	0.04 in.	0.04 in.
Days to corrosion	291	610	No Corrosion
Sacrificial washer corrosion			
Rebar corrosion			

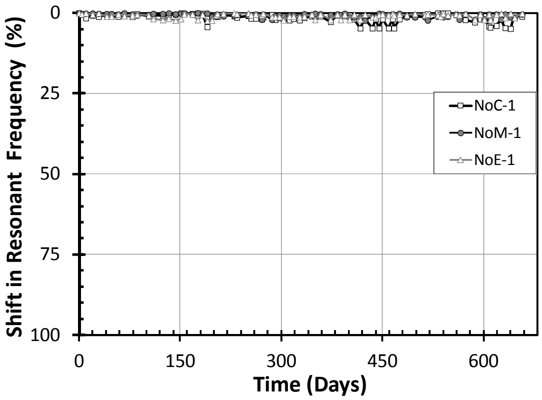

Figure 8-22: Change in the resonant frequencies of the sensors NoC-1, NoM-1, and NoE-1

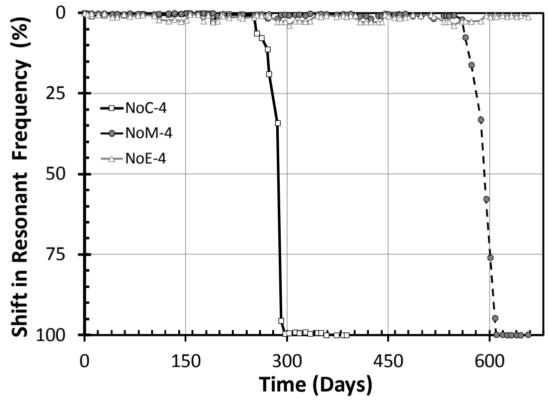

Figure 8-23: Change in the resonant frequencies of the sensors NoC-4, NoM-4, and NoE-4

In contrast, the response of sensor NoE-4 remained at the uncorroded state throughout the exposure period and the post-experiment autopsy indicated that the sacrificial washer remained intact with no evidence of corrosion. However, the rebar sections embedded in the same block showed signs of pitting corrosion underneath the artificial crack. Hence, it can be concluded that the NC sensor design in its current form is a point sensor that is highly dependent on the location of nearby cracks. If the duration of the experiment was extended, chlorides would have diffused through the porous concrete medium and reached the surface of the washer leading to a switch in frequency.

The three sensors constructed with paper diffusion layers shifted to the corroded state before the end of the exposure tests (Figure 8-24). All three sensors reached the corroded state within a ten-day period. Furthermore, the changes in the measured frequency response of each sensor followed the same pattern observed due to the formation of a uniform corrosion. The autopsy results confirmed that the paper diffusion layer successfully eliminated the localized corrosion concern (Table 8-5). It can be seen that regardless of the location of the artificial crack, all the sacrificial elements were uniformly corroded. In addition, the paper layers survived the concrete placement and remained intact during the autopsy. Unlike the polyester layer, the paper-based material did not adhere to the concrete and remained connected to the surface of the NC sensor.

The reinforcing bars in the three specimens exhibited corrosion levels that were higher than the corrosion damage observed in the specimens without diffusion layers. This can be attributed to the wrapping of the paper layer around the sensor body. In order to avoid increasing the corrosion damage on the reinforcement, the diffusion layer should only be placed on the top surface of the sensor during the curing of the mortar housing.

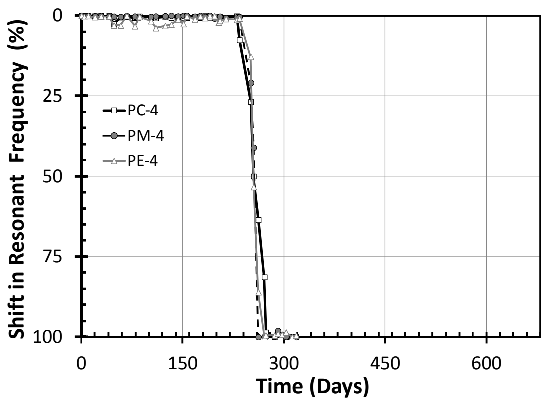

Figure 8-24: Change in the resonant frequencies of the sensors PC-4, PM-4, and PE-4

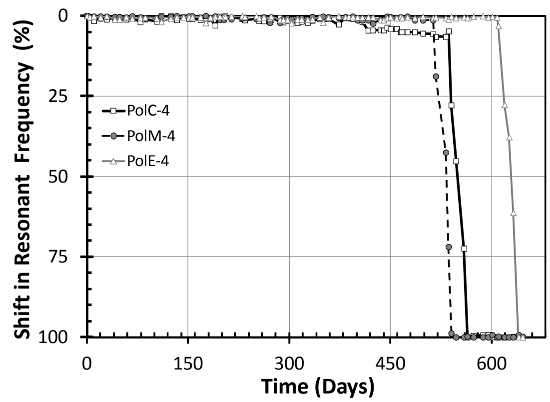

Figure 8-25: Change in the resonant frequencies of the sensors PolC-4, PolM-4, and PolE-1

The three NC sensors fabricated with the polyester diffusion layer shifted to the corroded state (Figure 8-25) and their autopsy results are summarized in Table 8-6. During autopsy, the polyester diffusion layers were found adhered firmly to the concrete. As the concrete cover was removed, the polyester layers remained attached to the concrete and detached from the sensor body. Sensors PolC-4 and PolM-4 (cracks at center and edge of the sacrificial washer) reached the corroded state after 563 and 541 days of exposure, respectively. The measured response was monotonic and gradual for both sensors. The sacrificial washers in the two specimens exhibited corrosion damage that was concentrated in the vicinity of the simulated cracks. However, the distribution of the corrosion product over the surface of these sacrificial washers was wider when compared with the NC sensors fabricated with no diffusion layers. Hence, the polyester-based diffusion layer has broadened the region of high chloride concentration exposure beyond the localized area immediately underneath the crack. However, such limited diffusion was ineffective and did not cause the sensors to reach the corroded state at similar times. Corrosion damage was observed on all the rebar sections embedded in the three blocks containing the NC sensors with polyester diffusion layers.

Sensor PolE-4 reached the corroded state approximately 3 months after the other two sensors with the polyester layer. The autopsy results have revealed a uniform distribution of corrosion damage over the entire surface of the sacrificial washer. However, breakage of sections of the washer was observed only in the side closest to the artificial crack.

Table 8-5: The state of the sacrificial washers and steel reinforcement of the NC sensors fabricated with the paper-based diffusion layers after the autopsy of the concrete blocks

	PC-4	**PM-4**	**PE-4**
Crack location	Center of washer	Edge of washer	Edge of NC sensor
Crack size	0.04 in.	0.04 in.	0.04 in.
Days to corrosion	273	262	271
Diffusion layer after autopsy*	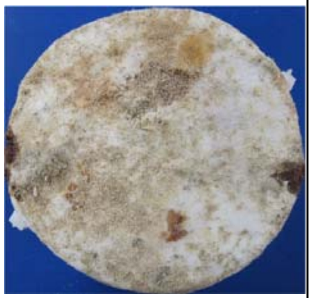		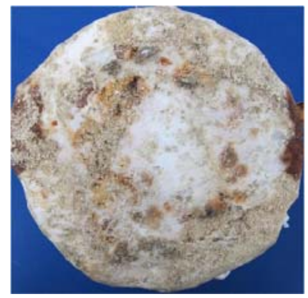
Sacrificial washer corrosion		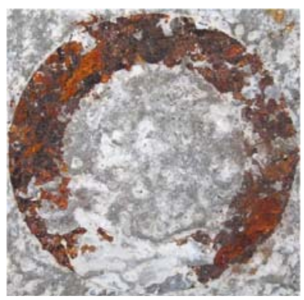	
Rebar corrosion			

* The paper-based diffusion layers remained attached to the NC sensor housing (view from above layer).

Table 8-6: The state of the sacrificial washers and steel reinforcement of the NC sensors fabricated with polyester-based diffusion layer after the autopsy of the concrete blocks

	PolC-4	**PolM-4**	**PolE-4**
Crack location	Center of washer	Edge of washer	Edge of NC sensor
Crack size	0.04 in.	0.04 in.	0.04 in.
Days to corrosion	563	540	641
Diffusion layer after autopsy*	Not available	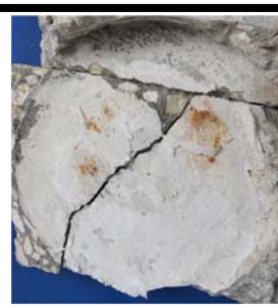	
Sacrificial washer corrosion			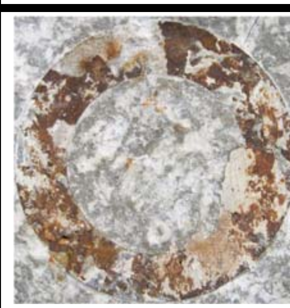
Rebar corrosion			

* The polyester-based diffusion layers remained attached to concrete (view from bottom layer).

8.6 SUMMARY

In its most basic form, the NC sensor described throughout this dissertation is a binary state sensor that shifts its response only when a corrosion threshold is exceeded. The results presented demonstrate the versatility of the sensor prototype and its ability to detect different levels of corrosion damage by changing the geometry or the material of the sacrificial element.

By introducing additional sacrificial elements of different thicknesses, it was possible to identify multiple thresholds of corrosion damage using a single sensor. The initial multi-threshold sensor design consisted of three concentric washers of different thicknesses. A major shortcoming of the concentric design was the weak coupling between the resonant circuit and the two smaller washers. An optimized design that relied on using different separation distances between the resonant circuit and the three sacrificial washers was shown to overcome the unequal inductive coupling issue. The stepped NC sensor had distinguishable and approximately equal resonant frequency steps separating four different limit states. Each step can be used to indicate a unique level of potential corrosion damage. Further optimization of the multi-threshold NC sensor design can be achieved using the Low-Frequency Electromagnetic Finite Element modeling techniques described in Chapter 3.

A modification in the NC sensor design was also developed to mitigate the issues in the sensor response associated with localized corrosion. The results of a long-term exposure test have indicated that the placement of a paper-based diffusion layer over the surface of the NC sensor during sensor fabrication can ensure uniform corrosion of the sacrificial washer. The results have shown that the adjustment allows the embedded sensor to detect corrosion at an earlier stage and in a more reliable pattern. Furthermore, the simple and inexpensive design alteration increases the actual sensing area of the NC sensor to encompass the total surface area of the mortar housing.

CHAPTER 9

Conclusions and Recommendations

The main focus of this research is to develop a class of passive wireless corrosion sensors that enable the early detection of chloride ingress and corrosion initiation within concrete bridge decks. The NC sensor design provides a simple solution that is based on a rational understanding of the complex corrosion problem in concrete bridges. The sensor output can be used to enhance the quality and reliability of the information collected during routine bridge inspections. Hence, the deployment of the NC sensor platform in ordinary reinforced concrete bridges can lead to significantly lower repair costs. It will also allow bridge owners to better allocate the ever diminishing maintenance and rehabilitation funds. Consequently, this economical investment allows for a shift in the current infrastructure management paradigms towards a more proactive approach which translates into lower overall life-cycle costs.

9.1 SUMMARY OF TEST RESULTS

The design parameters affecting the response of the NC sensor were initially identified through extensive parametric studies. The selection of the electrical components and geometric dimensions of the NC sensor prototype was based on experimental testing, circuit modeling, and finite element evaluations. In addition, the changes in the measured response of the sensor due to corrosion development were evaluated. The NC sensor primarily exhibits a binary response with two unique limit states. However, a brief transitional period between the uncorroded and corroded states exists. Thus, the selection of the final sensor design ensured that the two limit states are well-separated and can be easily distinguished. In addition, the senor parameters were tuned to ensure that the sensor signal remained detectable throughout the transition between the two states.

Chapter 4 discussed the details of an electrochemical investigation examining the suitability of the sacrificial washers as a reliable sensing transducer for corrosion of reinforcement bars. To this end, washer and reinforcement samples were examined using the linear polarization resistance and potentiodynamic polarization techniques. The electrochemical corrosion behavior of the washer and rebar samples was studied in numerous solutions that were representative of the conditions expected in reinforced concrete members. Simulated concrete and carbonated concrete pore solutions were used in the evaluation. In addition, pore solutions with and without the addition of chlorides were also examined. The results indicated that the corrosion patterns of the sacrificial washers followed closely the observed behavior of the rebar samples. However, relatively higher corrosion rates and more active corrosion potentials were observed in the low-alloy washers compared with the reinforcing steel. As a result, the NC sensors with the AISI 1010 sacrificial washers are expected to provide an early and reliable detection of adjacent rebar corrosion. In addition, the test procedures described can be used in future developments to select suitable sacrificial elements for new types of reinforcing steels or unique concrete environments.

The reliability of the NC sensor response was evaluated in two series of long-term exposure tests. In these investigations, NC sensors were embedded in reinforced concrete prisms and sections of bridge deck slabs. The sensors were exposed to cyclic exposure of either salt or tap water solutions. Established electrochemical corrosion monitoring techniques were also used to evaluate the corrosion damage within the samples. Post-experiment physical autopsies confirmed the reliability of the NC sensor response as all the embedded sensors successfully detected the state of corrosion in the adjacent rebar. In addition, the long-term exposure tests confirmed the stability of the NC sensor response and its insensitivity to the environmental variations in the surrounding environmental conditions. Temperature fluctuations of more than 80°F produced minimal to no effect on the response of the embedded sensors. Thereby, any significant shift in the sensor response was attributed to the corrosion build-up on the sacrificial element.

In contrast, the electrochemical corrosion evaluation techniques exhibited significant variability due to fluctuations in ambient temperature and moisture levels. While the half-cell method correctly identified the regions of high corrosion risk, differences in the measured potentials of more than 150 mV between consecutive wet and dry period measurements were recorded. Furthermore, the linear polarization resistance measurements exhibited differences of more than 400% between consecutive readings. The results of the LPR method were instantaneous in nature and very sensitive to the ambient temperature and moisture levels. In addition, mass loss estimations using the data from the LPR method had limited correlation with mass losses measured gravimetrically.

The potential for adjusting the design of the essentially binary NC sensor to enable the detection of multiple thresholds of corrosion damage was examined. Two multi-threshold NC sensor designs were developed and their ability to detect four different levels of corrosion damage was demonstrated. Further developments in the multi-threshold NC sensors area can be achieved using the finite element models described in Chapter 3.

Finally, the long-term prism exposure tests indicated that localized corrosion does affect the response of the NC sensor during the transition period. Such effect was expected to jeopardize the multi-threshold sensor design and introduce complexities in the interpretation of the measured signals of embedded NC sensors. To mitigate this undesirable phenomenon, a simple and inexpensive alteration to the sensor design was developed. The results of a long-term exposure test have shown that the placement of a porous paper-based diffusion layer over the surface of the NC sensor resolves the localized corrosion problem and increases the coverage area of the embedded sensor.

9.2 NC SENSOR DESIGN RECOMMENDATIONS

The development of the NC sensor design is a multivariable problem with numerous design components affecting the behavior and response of the embedded sensor. The work in this research was limited by the commercial availability of the different components. Based on the results of the parametric studies and the observations from the long-term exposure tests, the major design components are identified in the following paragraphs. Furthermore, general recommendations that are expected to optimize the sensor design and improve its behavior are listed.

9.2.1 Resonant Circuit

The electric components of the resonant circuit determine the operating frequency of the NC sensor and significantly influence the degree of mutual inductive coupling with the external reader. Resonant frequencies higher than 2 MHz are generally preferable as they prevent measuring ambient noise from AM radio frequencies. The geometry of the resonant circuit coil affects the inductance of the circuit and the coefficients of mutual coupling with the reader and sacrificial washer. The diameter of the sensing coil can be reduced to minimize the overall size of the NC sensor without significantly affecting the sensor behavior. In addition, high-quality ceramic capacitors are recommended for future production because these capacitors were found to be insensitive to the variations in temperature and produced signals with deeper phase dips.

9.2.2 Sacrificial Corroding Element

The selection of an appropriate sacrificial element is one of the most critical aspects in the development of a reliable NC sensor. The sacrificial element should exhibit electrochemical properties that are similar to the reinforcement steel while being able to shield the magnetic fields connecting the resonant circuit and the reader coil. Hence, the transduction layer of the NC sensor is versatile with an infinite range of alternatives that can be used as sacrificial transducers. To ensure reliable detection, each sacrificial element should be examined using the electrochemical procedures described in Chapter 4. Such tests can eliminate the possibility of erroneous sensor signals and unreliable performance. Generally, low-carbon steels provide a good electrochemical match to the typical steel reinforcement. In addition, sacrificial elements that require bimetallic connection through the soldering of different metals should be avoided.

The geometry of the sacrificial element and its position relative to the resonant circuit were found to have a significant influence on the shielding level. The largest level of shielding was achieved when the sacrificial element was placed directly over a resonant circuit with a matching outer diameter. High level of shielding can restrict the signal of the sensor making it undetectable. Hence, a tradeoff between the larger more desirable dynamic range and the signal strength need to be achieved. A minimum phase dip of approximately 2° and a minimum difference in the resonant frequencies of the corroded and uncorroded states larger than 0.25 MHz are recommended. For a washer element with an outside diameter equal to that of the circuit, a separation distance equal to 0.2 in. was found to produce a desirable response.

While the thickness of the sacrificial element was found to have a limited influence on the signal of the embedded sensor, it was demonstrated to be directly proportional to the threshold level of corrosion damage detected. The detection of multiple corrosion damage levels using a single sensor circuit can be achieved using several sacrificial elements that are simultaneously placed on the surface of the NC sensor. However, the geometries and locations of the different elements relative to the circuit need to be examined carefully. Each element needs to induce a significant shift in the frequency response in order to ensure an easy interpretation of the sensor state. Low-frequency electromagnetic finite element modeling can be use to optimize the design of the multi-threshold sensor.

The use of a porous diffusion layer as part of the sensing layer is critical and was found to mitigate the deleterious effects of localized corrosion. It also allows for the reliable implementation of the multi-threshold NC sensor designs. Paper-based diffusion layers were found to improve the sensitivity of the NC sensor to chloride ingress and induce uniform corrosion on the surface of the sacrificial element. It is recommended that the diffusion layer be placed on the top surface of the sensor only and not be wrapped around the mortar housing.

9.2.3 NC Sensor Protective Housing

The protective housing used in this research was developed initially by Puryear (2007) and later improved by Chou (2010). The housing includes two layers of protection. Structural epoxy is first used to cover the electric components of the resonant circuit. The hermetic impermeable seal prevents moisture and contaminants infiltration to the circuit components ensuring its durability and signal reliability. The second layer employs a fiber-reinforced mortar mix that encases the resonant circuit and provides protection against physical damage due to concrete placement. None of the sensors used in this research indicated any sign of infiltration or was exposed to significant damage during casting. Thus, the performance protective housing design is dependable and it is recommended for future development and manufacturing.

9.2.4 External Reader

The selection of the geometry of the reader coil should be optimized based on the embedment depth of the NC sensor. Pasupathy (2010) demonstrated that the optimum coupling between the system components is achieved when the radius of the reader coil is equal to read distance. Furthermore, the parametric studies have shown that the sensor response is ideal when its resonant frequency is within the inductive baseline of the reader coil. A separation of more than 1.0 MHz between the self-resonant frequencies of the reader coil and resonant circuit is recommended. The reflectometer interrogation technique was developed by Travidi et. al (2012) and was used to extract the resonant frequency of the NC sensors embedded in the reinforced concrete slabs. Unlike the impedance spectroscopy technique, the reflectometer technology allows for rapid interrogations and direct extraction of the resonant frequencies. The rapid acquisition of the sensor response is imperative for the adoption of the NC sensor technology in bridge monitoring applications. Hence, it is recommended that the reflectometer method be used in field applications. A scan window of 2.0 MHz with a scan interval of 10 kHz was found to capture the sensor response accurately.

9.3 RECOMMENDATIONS FOR FUTURE RESEARCH

The work described in this dissertation has demonstrated the reliability and potential for the NC sensor platform in corrosion detection applications. In the following paragraphs, potential areas for future research are briefly discussed. The topics include design alterations and a potential field where the use of the NC sensor can be beneficial.

9.3.1 RFID NC Sensors

The current NC sensor design employs a passive resonant LC circuit for data transfer. While the interrogation techniques developed were able to reach read distances of approximately 12 in., the LC resonant circuits have limited read ranges. Furthermore, at high interrogation speeds, the signal of the NC sensor can become hard to detect. To this end, the use of RFID tags to replace the resonant circuit can be beneficial. RFID technology has matured over the last decade and became less expensive. Furthermore, it has been used extensively in numerous monitoring and tracking applications and has shown great potential. The placement of a sacrificial inductive element in the vicinity of an RFID tag shall induce similar inductive effects as those observed in the NC sensor. An investigation of the potential benefits of utilizing RFID tags and the effect of the introduction of the sacrificial element on the read range and possible interrogation speeds of embedded NC RFID sensors is recommended.

9.3.2 Spatial Distribution in Bridge Deck Applications

By definition, the embedded NC corrosion sensor is a point sensor that is only capable of providing information regarding the conditions at its immediate location. Point sensors are common in structural health monitoring applications and include strain gages, crack propagation gauges, and accelerometers. However, due to the random and complex nature of the reinforcement corrosion problem, the response of few strategically placed sensors cannot be used to approximate the extent of the corrosion damage in the entire structure. In addition, regions of higher risk to corrosion damage cannot be known a priori. Hence, the deployment of multiple sensors over the bridge deck is necessary for accurate early detection. Due to the low per-unit, installation, and operation costs of the NC sensor, the embedment of hundreds or even thousands NC sensors in a bridge deck remains an extremely low fraction of the initial construction costs. However, in order to reduce the inspection times and further encourage the adoption of the NC sensor technology in the field, an investigation of the optimum spatial NC sensor distribution is recommended.

Generally, the sensors can be placed at a uniform spacing of approximately 3 feet, which is the average spacing of half-cell measurements typically taken during bridge deck investigations. Furthermore, a higher number of sensors can be installed near negative moment regions where structural cracks on the top surface of the concrete bridge deck are expected. Furthermore, more sensors should be placed near the shoulders of the roadway and near the curbs. The latter regions of the deck are expected to experience corrosion damage earlier due to the higher salt concentrations generated from snow removal and road clearing operations. In addition, rain water and contaminant runoff are expected to collect at the shoulders of the roadway and accelerate the corrosion activity.

9.3.3 Detection of Corrosion in Post-Tensioned Concrete Members

The versatile use of the inductively coupled transducer in the design of the NC senor can be tailored for its deployment in numerous corrosion detection applications. The NC sensor can be extremely beneficial in the detection of chloride ingress and corrosion initiation within post-tensioning ducts. Corrosion of the steel strands used in the post-tensioned members can result in catastrophic results. In modern post-tensioning construction, the strands are shielded from chloride ingress by three layers of protection; the concrete medium of the structure, the impervious post-tensioning duct surrounding the strands, and the mortar grout within the ducts. However, due to either the use of deleterious grouting materials or inappropriate grouting, excessive corrosion and fracture of the post-tensioning strands can occur which can lead to structural damage.

Due to the severity of the consequences of such corrosion-induced failures, the need for a reliable corrosion detection system is critical. However, the protective plastic ducts exhibit high inherent electrical resistance. Thereby, traditional electrochemical techniques cannot be used to evaluate the corrosion risk within the grout. The NC sensor platform can be a viable solution for this structural health monitoring application. The sensors can be embedded within the ducts during its manufacturing and the sensors can be interrogated during routine inspections. Since the mere presence of chlorides within the grout material can lead to serious damage, the change in response of any embedded sensors can be used to alert bridge owners of the corrosion problem. Further research that examines the adjustments needed to the NC sensor geometry to allow its embedment within the plastic ducts is recommended. In addition, the development of suitable attachment schemes is necessary and an examination of the influence of the sensor placement on the manufacturing processes and cost of the plastic ducts is needed.

APPENDIX A

Noncontact Sensor Fabrication

A.1 RESONANT CIRCUIT FABRICATION

Fabrication of the resonant circuit starts with winding the inductor coil. The fabrication process is similar to the circuit fabrication described by (Dickerson 2005). The coil is fabricated using a 2.0-in. nominal diameter PVC pipe as the mold. The pipe cut using a miter saw into slices that are 0.4 in. in height (Figure A-1). Then, two 0.125-in. diameter holes are drilled in the PVC slice as shown in Figure A-2. The holes should be spaced so that there enough space for five turns of copper magnet wire. Using a spool of 18-AWG enameled copper wire, the free end is inserted through one of the holes and the wire is wound around the PVC slice such that the turns overlap between holes (Figure A-3). The wire should be wound tightly five times. To facilitate the winding process, hot glue can be used to secure the wire at a number of locations. The wire is then cut from the spool and the end is inserted inside the second hole. The enamel coating should be stripped from the surface of the wire for a length of approximately 0.5 in.

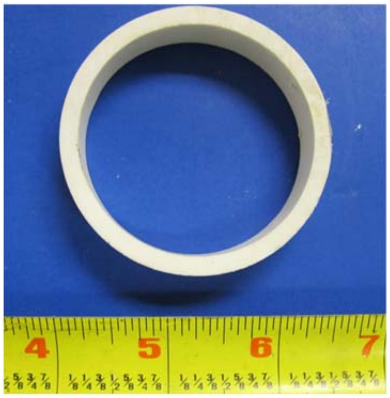

Figure A-1: 0.4-in. thick PVC slice

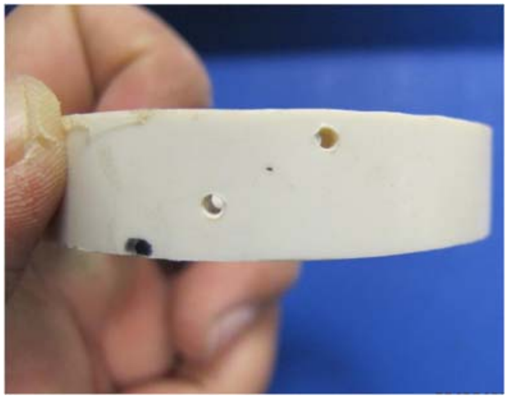

Figure A-2:Holes drilled in the PVC slice

Figure A-3: Winding inductor coil

Next, a printed circuit board should be cut such that it fits inside the PVC slice. The cut board should have at least two soldering strips to allow for connecting two circuit components in series (Figure A-4). An 820-pF ceramic capacitor is then soldered to the circuit board. The ends of the capacitor lead wires should be inserted through the side of the PC board that does not have the exposed copper strips (Figure A-5).

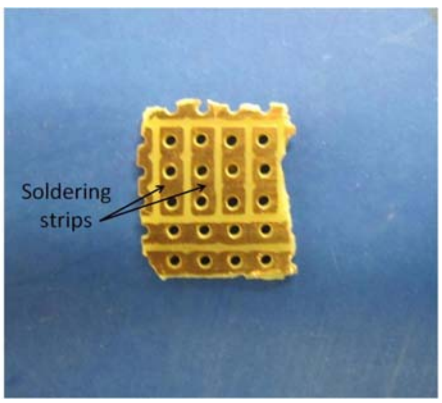

Figure A-4: Piece of PC board

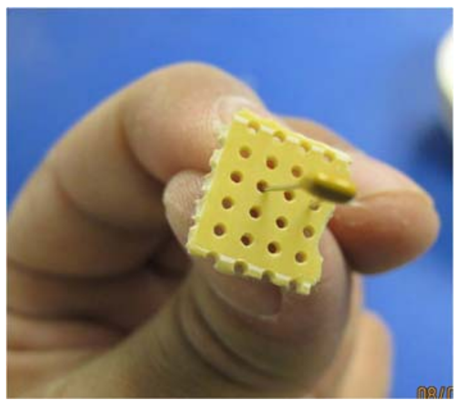

Figure A-5: Arrangement of circuit capacitor

After heating and tinning, the soldering tip is placed so that it touches both the PC board and the lead wires of the capacitor. Once the wires and board are heated, a

Kester™ 0.031-in. diameter solder wire is held at the tip of the soldering iron. The melted solder should fill the entire hole around the wire and extend a short area along the copper board. Once the soldering is complete, wires should be cut flush with the top of the solder. To complete the resonant circuit, the inductor coil should be connected to the circuit board. The stripped ends of the coil wires are inserted in the appropriated locations of the PC board. The wire ends are then soldered in the same manner used to solder the capacitor terminals (Figure A-6). The finished resonant circuit is shown in. Care should be taken to ensure that no solder remains on the circuit board that could short out the circuit.

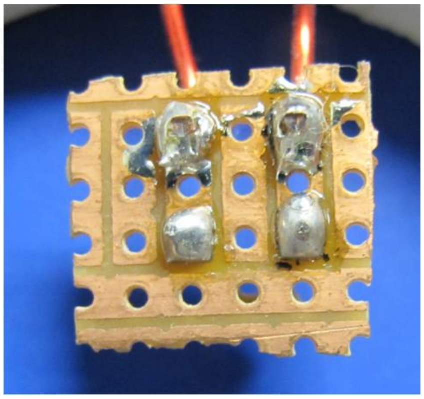

Figure A-6: Finished soldering of resonant circuit

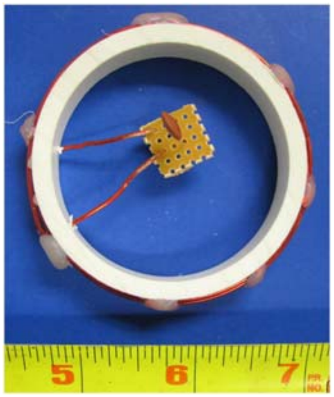

Figure A-7: Finished resonant circuit

The final step in the fabrication of the resonant circuit is protecting the circuitry and the inductor coil using a protective epoxy layer. SHEP Poxy III is used to cover the resonant circuit and provide a protective hermetic seal. The binder and resin components of the epoxy are mixed using equal volumes. The resonant circuit is then dipped in the epoxy mix and hung in air to allow the epoxy to cure and harden (Figure A-8). This process is repeated twice to eliminate any voids or accidental holes in the hermetic seal.

Figure A-8: Resonant circuit dipped in epoxy mixture and allowed to cure

A.2 MORTAR HOUSING FABRICATION

The fiber-reinforced mortar mix proposed by Chou (2010) is used to fabricate the protective housing of the NC sensor. The fiber-reinforced cement paste itself is composed of cement paste and polypropylene fibers, which are used to stabilize stucco. The potting material is produced by mixing cement, water, and the polypropylene fibers the amounts of each component to be combined for the potting material are shown in Table A-1. The water reducer is added to the mixture in order to decrease its viscosity. Low viscosity is essential to the potting material encompassing all the circuitry of the sensor.

Table A-1: Mixture components for fiber-reinforced mortar used for NC sensor housing (Chou 2010)

Component	Amount
Cement	140 g
Sand	140 g
Water	50 g
Polypropylene Fiber 500	2g
Polypropylene Fiber 150	1g
Superplasticizer	1 ml

A 4-in. diameter semi-spherical clear plastic pot is used as the mold for the mortar housing (Figure A-9). The mortar mixture is cast into the mold in two layers. The resonant circuit is positioned on top of the first mortar layer (Figure A-10). The second mortar layer is then cast to encase the circuit and fill the entire plastic mold. Hence, the depth of the mortar layers is dependent on the separation distance between the resonant circuit and sacrificial element selected for the NC sensor. The top surface of the mortar housing is then leveled and smoothed using a small piece of wood.

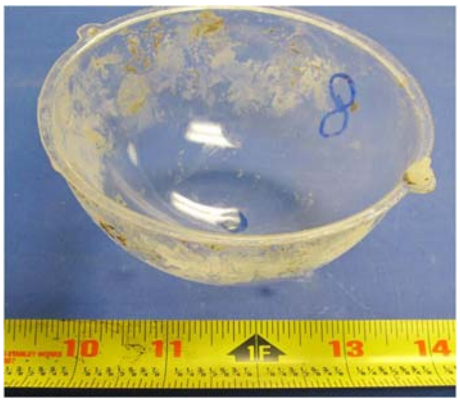

Figure A-9: Semi-spherical plastic mold

Figure A-10: First layer of mortar placed and resonant circuit positioned

Finally, the sacrificial washer(s) is placed concentrically on the top surface of the mortar housing immediately after the casting of the mortar. Then, the NC sensor housing is covered with a plastic sheet and allowed to cure for one week. The sensor assembly is later detached from the plastic mold and left to wet cure for two more weeks. Figure A-11shows a photograph of a completed NC sensor.

Figure A-11: Finished NC Sensor

APPENDIX B

Protective Epoxy Manufacturer Specifications

SHEP-poxy is a two component epoxy adhesive that is impermeable to moisture and exhibits high strength. The epoxy is suitable for numerous applications including bolt anchoring, cap sealing, crack injection, and bonding irregular surfaces. The epoxy is manufactured by Shepler’s and is distributed by CMC Construction Services. The data sheets and specifications of the product used are provided below.

Shep Poxy TX DOT Type III TWO COMPONENT, EPOXY ADHESIVE ANCHORING GELS

Shep Poxy TX DOT Type III is a high-strength, two component epoxy adhesive anchoring gel. Shep Poxy TX DOT Type III meets ASTM C 881, Types 1, 11*, IV, V* Grade 3, Classes A, B, and C. They also meet USDA specifications for use in food processing areas.

*Except Gel Time

USAGE

- Chemical anchoring for bolts, dowels, and pins.
- Cap sealing and port setting.
- Pressure-injection of cracks in structural concrete.
- Bonding irregular surfaces.

APPEARANCE

Component A - white

Component B - gray

SHELF LIFE

Two years in original unopened container.

PACKAGING

- .75 gal. (2.8 L units)
- 2 gal. (7.6 L units)
- 10 gal. (37.9 L units)
- 110 gal. (416.4 L units)

COVERAGE

75 gal. / 2.8 L of mixed epoxy yields 174 in^3 / 2851 cm^3

COMPLIANCES

- Shep Poxy TX DOT Type III - ASTM C-881: Types I, II*, IV, V*; Grade 3; Classes A, B, and C
- V.O.C. compliant
- USDA specifications for use in food processing areas
- ICBO Evaluation Report #5000 City of Los Angeles, Research Report #25220
- DOT listed
- Dade County approval
- Passed ICBO - ES AC58 (Sec. 5.3.3) ASTM E 1512
- (Sec. 7.1 and 7.5) Elevated Temperature Creep Test
- * Except Gel time

STORAGE CONDITIONS

Store at 40°- 95°F (5°- 35°C)

Precondition material to over 73° ± 2°F (23°C)

Cold weather (below 70°F/21°C): Precondition cartridges slowly to 80°-90°F (27° - 32°C) for easier gunning

Gel time: (60 g mass): 8 minutes at 73° ± 2°F (23°C)

DIRECTIONS

Bulk packaged components

Automatic Dispensing Machines: Only use CMC Construction Services approved positive displacement dispensing machines.

Hand Mixing: Pre-measure equal parts by volume of component A and component B in two separate containers. Use a third container to mix the two components together. Do not use one tapered container such as a Dixie paper cup, filling it half full of A and half full of B; the correct ratio (1:1) cannot be achieved due to tapered feature of container. Thoroughly mix for three minutes, scraping sides of container until uniform grey color is achieved. Only mix the amount of epoxy that can be used within its gel time. Spread mixed epoxy out thin on a hawk to extend gel time. If you pile it up, the gel time will be shortened due to the greater mass and exotherm.

APPLICATION

To anchor bolts, dowels, and pins:

1. Drill holes to proper diameter and length.
2. Clean holes with a nylon brush.
3. Blow concrete dust from hole with oil-free compressed air from back forward.
4. After uniform color is achieved, static mixer should be placed in back of hole. Start extruding epoxy while pulling static mixer out, filling hole 1/2 full. Rotate the bolt slightly as it is inserted to the back of the hole. Refer to tables for annular space, embedment depth, and edge distances.

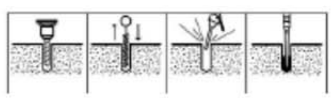

To set ports and capseal cracks: Select Shep Poxy Hi-Mod Gel or Shep Poxy Hi-Mod Fast Gel according to the desired gel time. Shep Poxy Hi-Mod Gel provides longer working time. Shep Poxy Hi-Mod Fast Gel should be selected for cooler weather applications and when faster setup of capseal is desired. Dab a small amount of epoxy to the back of a port and carefully center port over the crack. A centering nail may be helpful. Do not apply so much epoxy to back of port that it could close off the hole. After setting port, carefully butter the shoulder of the port and extend epoxy to 1/2 in (1.28 cm) on either side of the crack. Continue placement of epoxy by buttering crack between ports. To avoid leaks under pressure, the epoxy should be applied to approximately 1/4 in (.64 cm) thick. Do not place epoxy once it starts curing or getting hot or sticky, as this will compromise capseal and cause leaking. Once epoxy is placed, it should not be disturbed during the curing process. Cure time depends on air temperature and mass of epoxy. Normally a minimum of two hours is necessary to fully cure at 73° ± 2°F (23°C). Capseal must be fully cured prior to injection.

To bond irregular surfaces: Apply the mixed of Shep Poxy TX DOT Type III to the prepared substrates. Work into the substrate for positive adhesion. Secure or clamp the bonded surfaces firmly into place until the epoxy has cured. Glue line should not exceed 1/8 inch (.32 cm).

LIMITATIONS

- Minimum substrate temperature is 40°F.
- Do not thin. Solvents will prevent proper cure.
- Use dried aggregate only.
- Minimum age of concrete must be 3 - 7 days, depending on curing and drying conditions
- Shep Poxy TX DOT Type III is a vapor barrier after cure.
- Do not allow mixed epoxy to reside in static mixing head or mixer for more than 5 minutes or gelation and blockage may result.

CAUTION

- Component A - Irritant
- Component B - Corrosive
- Product is a strong sensitizer. Use of safety goggles and chemical resistant gloves are recommended.
- Use of a NIOSH/MSHA organic vapor respirator recommended if ventilation is inadequate.
- Avoid breathing vapors.
- Avoid skin contact.

CLEAN-UP

Uncured material can be removed with a citrus cleaner/degreaser or other approved solvent. Collect with absorbent material. Flush area with water. Dispose of in accordance with local, state, and Federal disposal regulations. Cured material can only be removed mechanically.

LIMITED WARRANTY

NOTICE-READ CAREFULLY. CONDITIONS OF SALE.

Manufacturer offers this product for sale subject to, and Buyer and all users are deemed to have accepted, the following conditions of sale and limited warranty which may be varied by written agreement of a duly authorized corporate officer of Manufacturer. No other representative of or for Manufacturer is authorized to grant any warranty or to waive limitation of liability set forth below.

WARRANTY LIMITATION

Manufacturer warrants this product to be free of manufacturing defects. If the product when purchased was defective and was within use period indicated on container or carton, when used, Manufacturer will replace the defective product with new product without charge to the purchaser.

Manufacturer makes NO OTHER WARRANTY, either expressed or implied, concerning this product. There is NO WARRANTY OF MERCHANTABILITY. In no case shall Manufacturer be liable for special, indirect or consequential damages resulting from the use or handling of the product, and no claim of any kind shall be greater in amount than the purchase price of the product in respect of which damages are claimed.

INHERENT RISK

MANUFACTURER MAKES NO WARRANTY TO THE PERFORMANCE OF THE PRODUCT AFTER IT IS APPLIED BY THE PURCHASER, AND PURCHASER ASSUMES ALL RISKS ASSOCIATED WITH THE USE OR APPLICATION OF THE PRODUCT.

Shep Poxy TX DOT Type III TWO COMPONENT, EPOXY ADHESIVE ANCHORING GELS

Continued from previous page

SHEAR AND TENSION VALUES FOR SMOOTH DOWELS*						
DOWEL DIAMETER	BIT DIAMETER	EMBEDMENT	ULTIMATE BOND STRENGTH (IBS)		ALLOWABLE STEEL STRENGTH	
			TENSION 3000 PSI	SHEAR 2500 PSI	TENSION 3000 PSI	SHEAR 2500 PSI
1/2"	9/16"	4-1/2"	6040	8560	3750	1930
5/8"	3/4"	5-5/8"	6760	13140	5880	3030
3/4"	7/8"	6-3/4"	12000	18920	8460	4360
7/8"	1"	7-7/8"	14220	25720	11500	5930
1"	1-1/8"	9"	23280	33600	15020	7740

*1. The tabulated shear and tension values are for anchors installed in normal weight concrete having reached the designated ultimate compressive strength at the time of installation. Linear interpolation may be used for concrete strengths between those listed.

2. Spacing and edge distance shall be in accordance with appropriate table.

3. Allowable load must be the lesser of the allowable steel strength and that allowable bond strength. Typically, allowable bond strength is equal to the ultimate bond strength divided by the safety factor of four.

4. Allowable loads may be Increased by 33 1/3% for short term loading due to earthquakes or wind.

5. Shep Poxy TX DOT Type III is recognized for installation in water filled or moist holes, for use in locations subject to severe exterior weathering conditions, and for resisting tension and shear loads due to earthquake and wind.

ALLOWABLE ANCHOR SPACING AND EDGE DISTANCE*			
	FULL ANCHOR CAPACITY CRITICAL DISTANCE (CCR)	REDUCED ANCHOR CAPACITY DISTANCE (CM IN)	REDUCTION FACTOR
Spacing Between Anchors	24 D	8 D	.90
Edge Distance: Tension Loads	12 D	See Following Chart	See Following Chart
Shear Loads -Threaded Rod	12 D	4 D	.21
Shear Loads - Smooth Dowels	12 D	4 D	.21
Shear Loads - Rebar	16 D	4 D	.15

ALLOWABLE SHEAR VALUES FOR THREADED ROD IN 2000 PSI CONCRETE*					
			ALLOWABLE STEEL STRENGTH (IBS)		
ANCHOR DIAMETER	BIT DIAMETER	EMBEDMENT	A36 / A307	A193 B7	300 SERIES STAINLESS
3/8"	7/16"	3-3/8"	1080	2345	1870
1/2"	9/16"	4-1/2"	1930	4170	3330
5/8"	3/4"	5-5/8"	3030	6520	5220
3/4"	7/8"	6-3/4"	4360	9390	6390
7/8"	1"	7-7/8"	5930	12780	8680
1"	1-1/8"	9"	7740	16690	11340
1-1/4"	1-3/8"	11-1/4"	12100	26070	17730

*See notes on previous page.

CURE TIMES FOR ADHESIVE ANCHORS*				
MINIMUM SUBSTRATE TEMP	CURE TIME		MINIMUM CURE TIME	
	SHEP-POXY HI-MOD GEL	SHEP-POXY HI-MOD FAST GEL	SHEP-POXY HI-MOD GEL	SHEP-POXY HI-MOD FAST GEL
40°F (5°C)	F	48 hrs	F	24 hrs
65°F (18°C)	48 hrs	36 his	24 hrs	8 hrs
70°F (21°C)	36 hrs	24 hrs	12 hrs	2.5 hrs
80°F (27°C)	24 hrs	12 hrs	6 hrs	2 hrs
100°F (38°C)	12 hrs	6 hrs	4 his	1 hrs

*1. F indicates Pro-Foxy Shep Poxy Hi-Mod Fast Gel is recommended.

2. Cure Time is time required before epoxy reaches ultimate strength. Minimum Cure Time is minimum time required before the design or allowable load may be applied.

3. Anchors are to be undisturbed during the minimum cure time.

EDGE DISTANCE FOR TENSION VALUES FOR ANCHORS IN CONCRETE*		
STUD SIZE	MINIMUM EDGE DISTANCE (C MIN)	REDUCTION FACTOR
3/8"	1-1/2	.70
1/2"	1-3/4	.66
5/8"	1-3/4	.70
3/4"	1-3/4	.70
7/8"	3-1/2	.70
1"	4	.70
1-1/4"	5	.70

*1. The listed values are the minimum distances required to obtain the load values in the tables above and to the left. D = anchor diameter. When adjacent anchors are different sizes or embedments, use the largest value for D.

2. The listed values are the minimum distances at which the anchor can be installed when load values are adjusted in accordance with reduction factor.

3. Load values in the table are multiplied by the reduction factor when anchors are installed at the minimum spacing listed. Use linear interpolation for spacing between critical and minimum distances. Multiple reduction factors for more than one spacing or edge distance are calculated separately and multiplied.

Shep-Poxy TX DOT Type III TWO COMPONENT, EPOXY ADHESIVE ANCHORING GELS

Continued from previous page

SHEAR AND TENSION VALUES FOR REINFORCING STEEL*

ANCHOR DIAMETER	BIT DIAMETER	EMBEDMENT	TENSION ULTIMATE BOND STRENGTH (IBS) CONCRETE STRENGTH_(RC)			ALLOWABLE STEEL STRENGTH TENSION OR SHEAR (LB.)	
			2500 PSI	4000 PSI	5500 PSI	GRADE 40	GRADE 60
# 3	1/2"	3-3/8"	7080	9050	11020	2200	2640
# 4	5/8"	4-1/2"	12300	14730	17160	4000	4800
# 5	3/4"	5-5/8"	16000	18810	21620	6200	7440
# 6	1"	6-3/4"	39035			8800	10560
# 7	1-1/8"	7-7/8"	36740			12000	14400
# 8	1-1/4"	9"	42670			15600	18720

* See notes on previous page. NOTE: Values for Threaded Rod in Hollow and Grout Filled Block available on request.

ESTIMATING GUIDE FOR NUMBER OF HOLES PER CARTRIDGE

		HOLE DEPTH (IN)																		
		2	3	4	5	6	7	8	9	10	11	12	13	14	15	16	17	18	19	20
THREADED ROD IN CONCRETE		NUMBER OF HOLES PER CARTRIDGE																		
ROD SIZE	HOLE SIZE																			
3/8"	7/16"	192	128	96	77	64	55	48	43	39	35	32	30	28	26	24	23	22	21	20
1/2"	9/16"	136	91	68	55	46	39	34	29	28	25	23	21	19	18	17	16	15	15	14
5/8"	3/4"	70	47	35	28	24	20	18	16	14	13	12	11	10	10	9	9	8	8	7
3/4"	7/8"	56	37	28	23	19	16	14	13	11	10	10	9	8	8	7	7	7	6	6
7/8"	1"	47	31	24	19	16	12	12	11	10	9	8	8	7	7	6	6	6	5	5
1"	1-1/8"	38	26	19	16	13	11	10	9	8	7	7	6	6	5	5	5	5	4	4
1-1/8"	1-1/4"	34	23	17	14	12	10	9	8	7	7	6	6	5	5	5	4	4	4	4
1-1/4"	1-3/8"	29	20	15	12	10	9	8	7	6	6	5	5	5	4	4	4	4	3	3
1-1/2"	1-5/8"	23	16	12	10	8	7	6	5	5	5	4	4	4	3	3	3	3	3	3
REBAR IN CONCRETE																				
REBAR SIZE	HOLE SIZE																			
No. 3	1/2"	163	109	82	66	55	47	41	37	33	30	28	26	24	22	21	20	19	18	17
No. 4	5/8"	127	85	64	51	43	37	32	29	26	24	22	20	19	17	16	15	15	14	13
No. 5	3/4"	103	69	52	41	35	30	26	23	21	19	17	16	15	14	13	12	12	11	11
No. 6	7/8"	82	55	41	32	28	24	21	19	17	15	14	13	12	11	11	10	10	9	9
No. 7	1"	72	48	36	29	24	21	18	16	15	13	12	11	11	10	9	9	8	8	8
No. 8	1-1/8"	62	41	31	25	21	18	16	14	13	12	11	10	9	9	8	8	7	7	7
No. 9	1-3/8"	31	21	16	13	11	9	8	7	7	6	6	5	5	4	4	4	4	4	3
No. 10	1-1/2"	30	20	15	12	10	9	8	7	6	6	5	5	5	4	4	4	4	4	3
SMOOTH DOWEL IN CONCRETE																				
DOWEL SIZE	HOLE SIZE																			
3/4"	7/8"	83		42	34	28	24	21	19	17	15	14	13	12	11	11	10	10	9	9
7/8"	1"	72	48	36	29	24	21	18	16	15	13	12	11	11	10	9	9	8	8	8
1"	1-1/8"	61	41	31	25	21	18	16	14	12	11	10	10	9	8	8	8	7	7	6
1-1/4"	1-3/8"	50	33	25	20	17	14	13	11	10	9	9	8	7	7	7	6	6	6	5
1-1/2"	1-5/8"	42	28	21	17	14	12	11	10	9	8	7	7	6	6	6	5	5	4	4

ULTIMATE TENSION VALUES FOR THREADED ROD IN CONCRETE *

ANCHOR DIA.	BIT DIA.	EMBEDMENT	ULTIMATE BOND STRENGTH IN CONCRETE F'C				ALLOWABLE STEEL STRENGTH (IBS)		
			2500 PSI	3000 PSI	4000 PSI	5500 PSI	A36 / A307	A193 B7	300 SERIES STAINLESS
3/8"	7/16"	1-11/16"		5450			2100	4550	3630
3/8"	7/16"	3-3/8"	7300		8250	9200	2110	4550	3630
3/8"	9/16"	3-3/8"	9560				2110	4550	3630
3/8"	7/16"	5-5/8"	10980		11360	11740	2110	4550	3630
1/2"	9/16"	2-1/4"		7495			3750	8100	6470
1/2"	9/16"	4-1/2"	10540		11730	12920	3750	8100	6470
1/2"	11/16"	4-1/2"	14640				3750	8100	6470
1/2"	9/16"	7-1/2"	14660		17010	19360	3750	8100	6470
5/8"	3/4"	2-13/16"		13665			5870	12655	10130
5/8"	3/4"	5-5/8"	14800		18870	22940	5870	12655	10130
5/8"	7/8"	5-5/8"	23340				5870	12655	10130
5/8"	3/4"	9-3/8"	21560		26260	30960	5870	12655	10130
3/4"	7/8"	3-3/8"		17825			8460	18220	12400
3/4"	7/8"	6-3/4"	22380		25870	29360	8460	18220	12400
3/4"	1"	6-3/4"	29850				8460	18220	12400
3/4"	7/8"	11-1/4"	30320		34340	38360	8460	18220	12400
7/8"	1"	3-15/16"		21390			11500	24800	16860
7/8"	1"	7-7/8"	43280				11500	24800	16860
1"	1-1/8"	4-1/2"		27419			15020	32400	22020
1"	1-1/8"	9"	55650				15020	32400	22020
1 1/4	1 3/8	11 1/4	77860				23480	50610	34420

APPENDIX C

Sensitivity of Noncontact Sensor Response to Environmental Conditions

C.1 OVERVIEW

The reliability of any structural health monitoring (SHM) technique relies primarily on the sensitivity of the measured response to the variations in the environmental conditions. Thus, the sensor platform should only be affected by the criterion being monitored and its signal needs to be independent of the inadvertent changes in the surrounding medium. However, a number of monitoring tools that are widely used by inspection technicians and engineers are affected by the natural changes in the environment. For example, systematic drifts in the measured strains due to ambient temperature fluctuations remain a big challenge in the field of bridge monitoring. The unfavorable effect of temperature and moisture level fluctuations on the results of the traditional electrochemical corrosion evaluation techniques has been demonstrated in Chapter 5 and Chapter 7 of this dissertation and by other researchers (ACI 222R 2010). The traditional and modern methods used to conduct delamination surveys are also affected by presence of moisture within the bridge deck (ACI 201.1R 2008).

The NC sensor, in it is most basic form, acts as a binary state sensor with two unique limit states (corroded/ uncorroded). The sensor also exhibits a short transition period between the two states. However, the response of the sensor is expected to remain mainly at either the initial uncorroded state or the final fully corroded state. Hence, any shift in the measured response from the initial state is indicative of corrosion initiation in the surrounding concrete. Consequently, the reliable deployment of the NC sensor platform requires that any noticeable change in the response should be the result of corrosion accumulation on the sacrificial element only and the environmentally-induced noise should be small in comparison and limited in magnitude.

Slight shifts in the measured resonant frequency and phase dip of the NC sensor that are not caused by corrosion can be observed. These shifts can be attributed to numerous factors including variations in temperature and the moisture content. The capacitance of the resonant circuit can be affected by the increase in the concrete temperature. However, the selection of high-quality ceramic capacitors to fabricate the circuit was found to limit the magnitude of these errors (Dickerson 2005). The presence of moisture in the vicinity of the inductor coil can also affect the measured response. However, the impervious, hermetic, epoxy seal used to protect the sensor circuitry limits the likelihood of moisture infiltration. In addition, there are a number of factors that are not environment-induced but still can affect the accuracy of the measured sensor response. The deterioration in the reader coil, the stability of the AC source powering the Impedance/Phase analyzer, the precision of the read distance, and the lateral location of the reader coil relative to the sensor are all factors that can cause unexpected shifts in the measured response.

To this end, the collected data of the 32 NC corrosion sensors embedded in the reinforced concrete slabs (Chapter 6 and Chapter 7) were used to evaluate the sensitivity of the prototype NC sensor to the environmental variation. During the test, the embedded sensors were exposed to different levels of exposure to chloride and moisture based on their location. The continuous exposure to wet and dry cycles of either a salt water solution or tap water lasted for more than 19 months. In addition, the slab specimens were stored in an unheated building where ambient temperature fluctuations of more than 70°F were recorded. In the last three months of the exposure period, infrared heaters were used to hold the surface temperature at 105°F during the dry cycles while the recorded temperature during the wet cycles dropped to approximately 50°F. Hence, the embedded sensors experienced extreme exposure conditions that are representative of the conditions expected in the field.

Furthermore, seven of the embedded sensor shifted to the corroded state prior to the end of the exposure period. Hence, the sensitivity of the sensor response in both the uncorroded and corroded limit states can be evaluated.

C.2 STATISTICAL ANALYSIS OF MEASURED SENOR RESPONSE

Based on the findings of Chapter 3, the resonant frequency of the NC sensor is the most stable parameter extracted from the measured frequency response. In addition, the shift of the resonant frequency during transition is monotonic and gradual providing a simple indication of corrosion initiation. A statistical analysis of all the measured resonant frequencies for each of the embedded sensors was conducted. For the twenty five sensors that remained in the uncorroded state, all the resonant frequent data collected during the 19-month exposure period were examined. For the seven sensors that shifted to the corroded state, two separate statistical analyses were conducted. The first included the data recorded while the sensor in the initial uncorroded state while the second included the corroded state resonant frequencies measured. The signals collected during sensor transition were omitted for all the corroded NC sensors. The use of two separate analyses for the uncorroded and corroded states allows for identifying the sources of frequency shifts. Shifts observed in the corroded state can be attributed to the resonant circuitry. In contrast, shifts measured in the uncorroded state are a combination of the environment effect on the circuit components, the sacrificial element, and the interaction between the two elements.

Table C-1 summarizes the results of the statistical analyses for sensors corresponding in the uncorroded state. It can be seen that the standard deviations of the measured resonant frequencies ranged between 0.69 to 7.47 kHz for all the sensors considered. The average standard deviation for the uncorroded state measurements was approximately 4.5 kHz.

There results indicate that there is no clear correlation between the level of chloride exposure and the variation in the measured sensor output. Similar degrees of statistical deviation were calculated for the slabs exposed to salt or tap water. Furthermore, the sensors embedded in the splash zone did not exhibit higher variations compared with the sensors placed in the slab sections that were kept dry throughout the test period. Hence, changes in the moisture content do not seem to have a major influence on the inherent resonant frequency of the NC sensors. The results of the uncorroded state analysis suggest that the observed frequency variations can only be attributed to either temperature fluctuations or factors unrelated to the environmental conditions.

Table C-1: Statistical summary of the NC sensors responding in their uncorroded state

Slab	**Sensor**	**$f_{se(avg)}$**	**σ**	**COV**	**Slab**	**Sensor**	**$f_{se(avg)}$**	**σ**	**COV**
		MHz	**kHz**	**%**			**MHz**	**kHz**	**%**
S1	1	3.35	4.76	0.14	**T1**	1	3.49	5.53	0.21
	2	3.39	0.69	0.02		2	3.65	5.30	0.15
	3	3.38	4.29	0.13		3	3.45	4.59	0.10
	4	3.43	2.23	0.07		4	3.39	4.30	0.13
	5	3.44	2.74	0.08		5	3.52	5.77	0.16
	6	3.35	3.60	0.11		6	3.57	5.05	0.14
	7	3.48	7.47	0.22		7	3.57	5.60	0.16
	8	3.50	4.95	0.14		8	3.57	5.18	0.15
	Avg.	**-**	**3.84**	**0.11**		**Avg.**	**-**	**5.29**	**0.15**
S2	1	3.58	5.63	0.16	**T2**	1	3.46	4.69	0.14
	2	3.46	5.81	0.17		2	3.51	4.96	0.14
	3	3.55	3.03	0.09		3	3.60	4.13	0.11
	4	3.55	2.18	0.06		4	3.78	6.01	0.16
	5	3.52	3.40	0.10		5	3.45	2.62	0.08
	6	3.35	6.27	0.19		6	3.54	3.47	0.10
	7	3.58	4.62	0.13		7	3.54	4.19	0.12
	8	3.63	5.42	0.15		8	3.63	5.42	0.15
	Avg.	**-**	**4.55**	**0.13**		**Avg.**	**-**	**4.44**	**0.12**

Table C-2 summarizes the results of the statistical analysis for the measured corroded state resonant frequencies for the seven sensors that shifted to the corroded state. The measured variations were generally less than those observed for the uncorroded state frequencies. The calculated standard deviations ranged between 2.2 and 4.5 kHz and had an average of approximately 2.9 kHz, which is only 63% of the average deviation for the frequencies measured during the uncorroded stage. Hence, the presence of the sacrificial washer increases the amount of environmentally-induced frequency shifts. In addition, the location of the sensor did not seem to have a significant effect on the frequency shifts.

Table C-2: Statistical summary of the NC sensors responding in their corroded state

Slab	**Sensor**	**$f_{rc(avg)}$**	**σ**	**COV**
		MHz	**kHz**	**%**
S1	2	3.18	2.22	0.07
	3	3.12	2.13	0.07
	4	3.20	2.13	0.07
	Avg.	-	**2.16**	**0.07**
S2	3	3.21	3.11	0.10
	4	3.13	4.47	0.17
	5	3.19	4.29	0.13
	6	3.13	1.86	0.06
	Avg.	-	**3.68**	**0.12**

The maximum recorded standard deviation for any of the 32 NC sensors at either the corroded or uncorroded stages was less than 7.5 kHz. This level of change is very small compared to the available range of resonant frequencies separating the two limit states. For sensor S1-7, the difference between the uncorroded and corroded resonant frequencies is approximately 350 kHz. Thus, shifts in the measured resonant frequency induced by environmental conditions constitute less than 3.7% of the available range for sensor S1-7.

C.3 SUMMARY

The results of the statistical analyses conducted on the measured resonant frequencies of the NC sensors embedded in the slabs suggest that the response of the NC sensor is insensitive to environmental variations. The observed shifts in frequencies are mostly attributed to temperature drifts and reader related irregularities. Changes in the moisture levels and chloride ion concentrations did not seem to impose significant effect on the measured resonant frequencies. Most importantly, the level of environmentally-induced drifts were generally less than 5% of the available range of frequencies separating the two limit states of response.

APPENDIX D

Monitoring Results for the Long-Term Exposure Test

The data collected during the long-term exposure test for the reinforced concrete slab specimens, which are described in Chapter 6 and Chapter 7, are presented in this appendix. For each of the 32 embedded NC sensors, the following information are provided:

(a) the location of the sensor in the slab and relative to the points where electrochemical measurements were conducted,

(b) photographs of the NC sensor prior to concrete placement,

(c) photographs of the concrete surface above the embedded sensor indicating the location of flexural cracks,

(d) the shift in the measured resonant frequency of the NC sensor with time,

(e) the measured phase response of the NC sensor in selected days,

(f) the measured current density values collected using the GECOR® equipment,

(g) the average half-cell potentials measured at the location of the NC sensor with time,

(h) photograph of the NC sensor and the sacrificial element after the physical autopsy,

(i) and the reinforcing bar sections that were adjacent to the NC sensor.

In addition, post-experiment autopsy results are tabulated and include the mass losses measured for the rebar sections and the acid-soluble chloride ion concentrations measured for concrete samples taken near the embedded sensor.

D.1 SENSORS EMBEDDED IN SLAB T1

D.1.1 Sensor T1-1

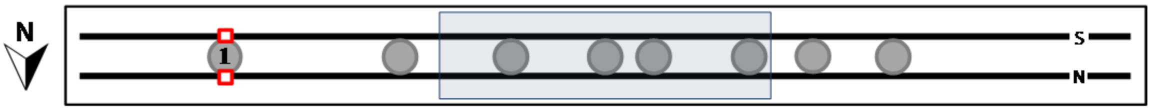

a) Locations of sensor T1-1 and half-cell and LPR measurement points

b) Sensor T1-1 before concrete casting

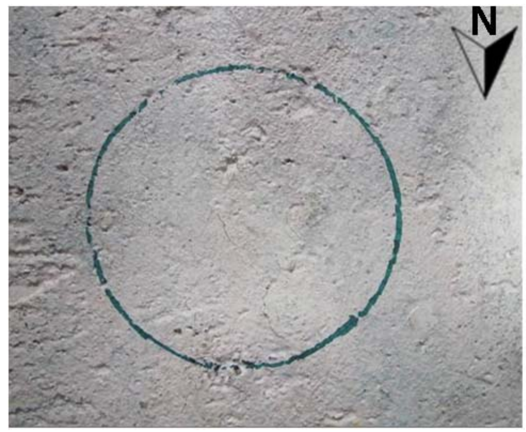

c) Surface Cracks in vicinity of T1-1

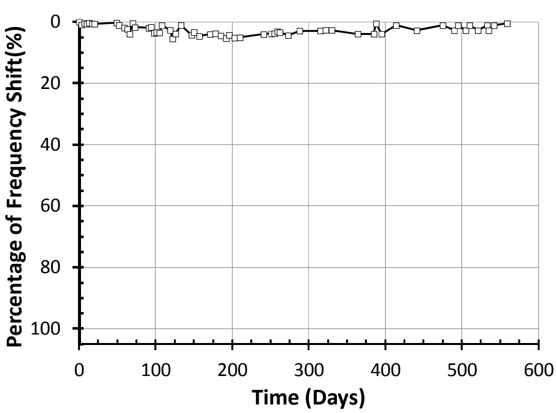

d) Shift in resonant frequency of T1-1

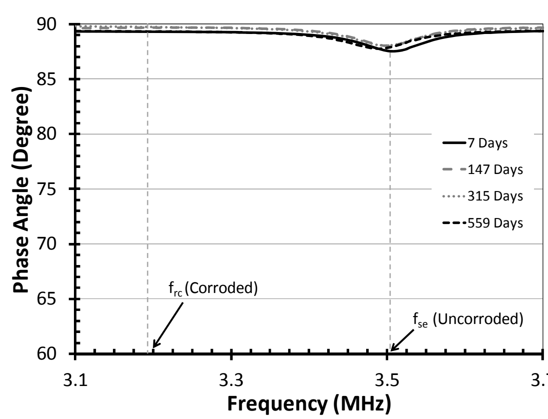

e) Measured phase response of T1-1 in selected days

Figure D-1: Details of sensor T1-1

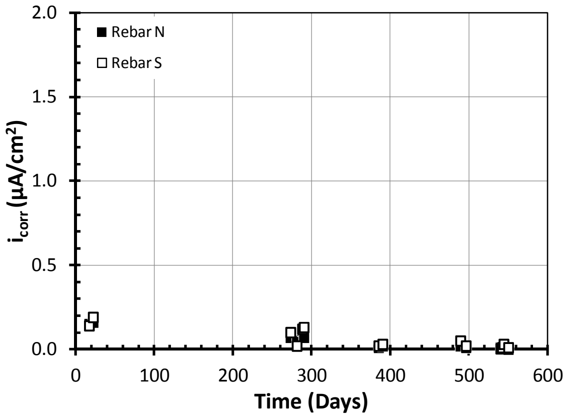

f) Measured corrosion current densities

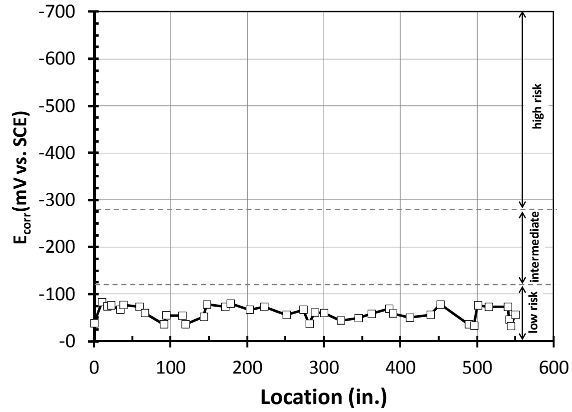

g) Average measured half-cell potentials

h) Sacrificial element of sensor T1-1 after autopsy

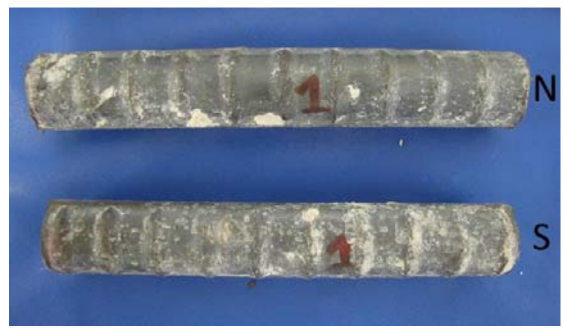

i) Rebar sections at vicinity of sensor T1-1

Figure D-1(Continued): Details of sensor T1-1

Table D-1: Post-autopsy results of sensor T1-1

Time to corrosion of sacrificial washer (Days)		Uncorroded
Max. width of crack crossing the embedded sensor (in.)		None
Rebar mass loss (%)	North	0.29
	South	0.15

D.1.2 Sensor T1-2

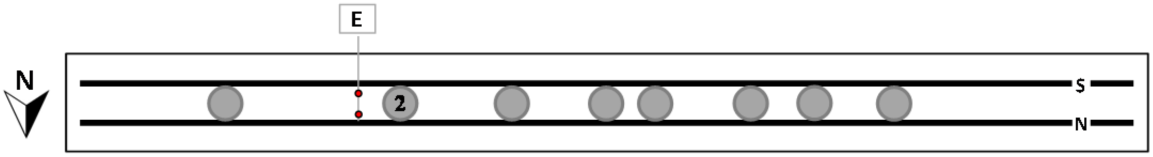

a) Locations of sensor T1-2, half-cell and LPR measurement points, and concrete powder samples

b) Sensor T1-2 before concrete casting

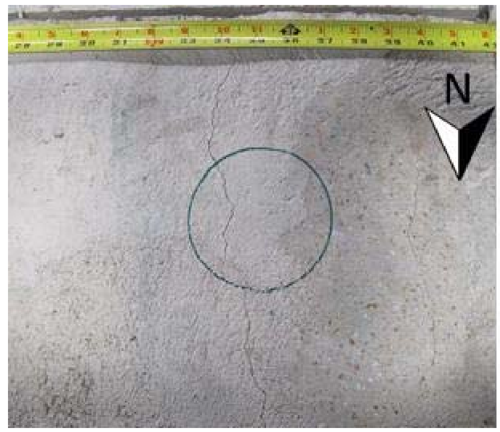

c) Surface Cracks in vicinity of T1-2

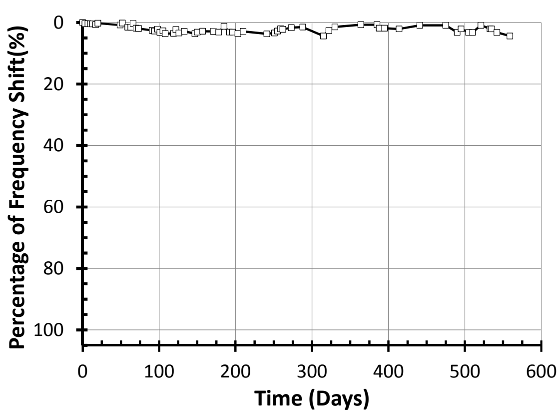

d) Shift in resonant frequency of T1-2

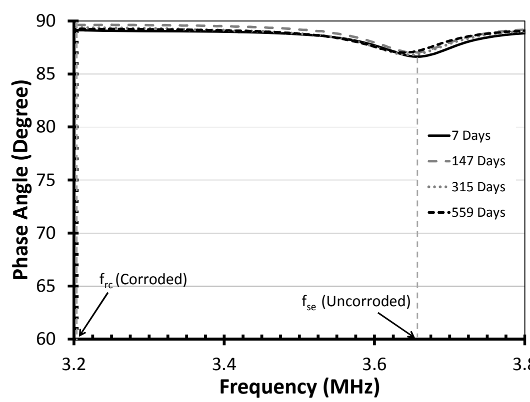

e) Measured phase response of T1-2 in selected days

Figure D-2: Details of sensor T1-2

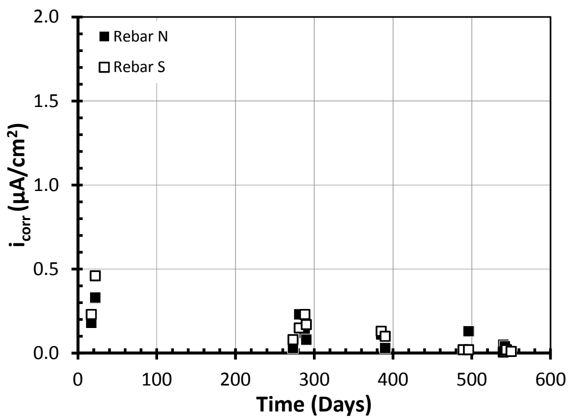

f) Measured corrosion current densities

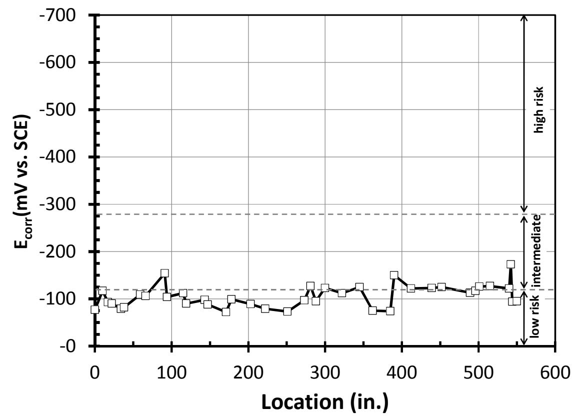

g) Average measured half-cell potentials

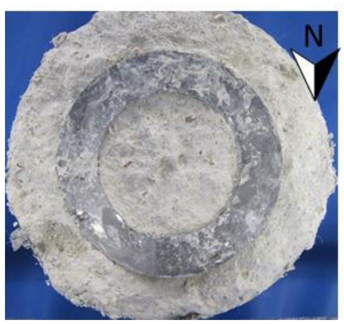

h) Sacrificial element of sensor T1-2 after autopsy

i) Rebar sections at vicinity of sensor T1-2

Figure D-1(Continued): Details of sensor T1-2

Table D-2: Post-autopsy results of sensor T1-2

Time to corrosion of sacrificial washer (Days)		Uncorroded
Max. width of crack crossing the embedded sensor (in.)		0.025
Rebar mass loss (%)	North	0.62
	South	0.52
Chloride ion concentration (ppm)	Line E	47
	-	-

D.1.3 Sensor T1-3

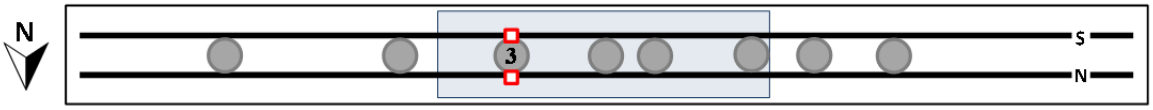

a) Locations of sensor T1-3and half-cell and LPR measurement points.

b) Sensor T1-3 before concrete casting

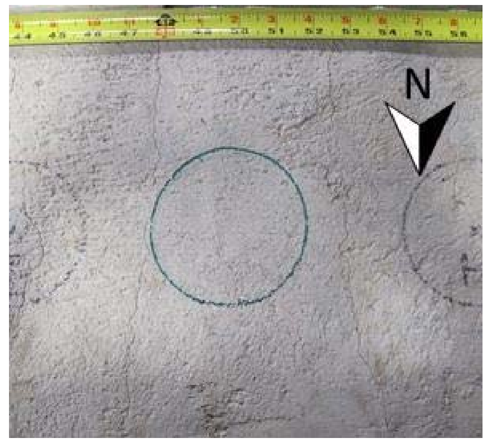

c) Surface Cracks in vicinity of T1-3

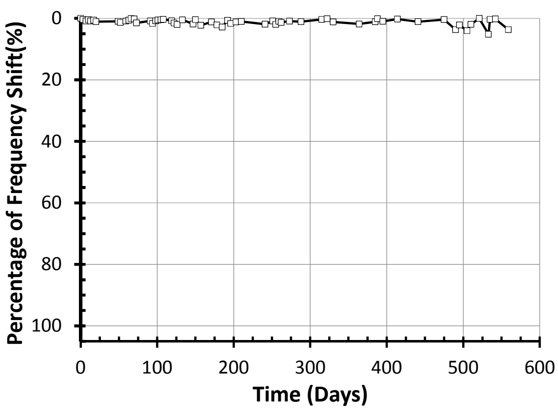

d) Shift in resonant frequency of T1-3

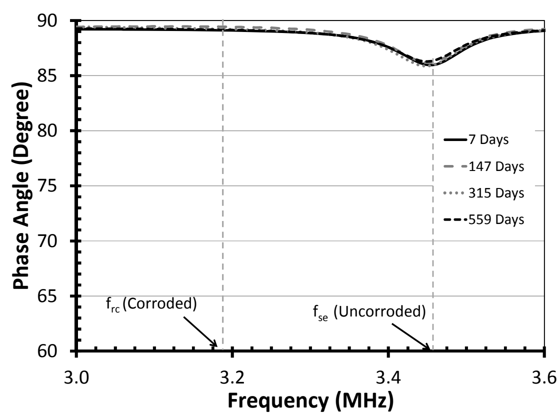

e) Measured phase response of T1-3 in selected days

Figure D-3: Details of sensor T1-3

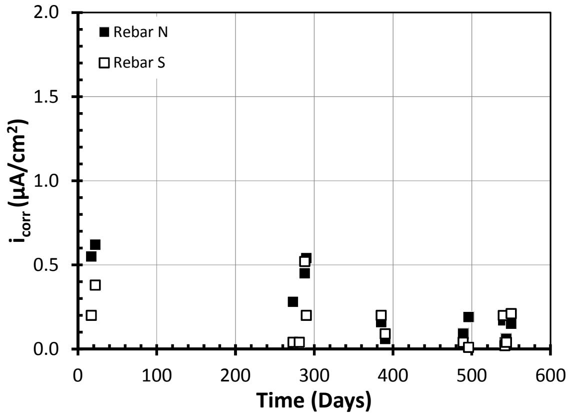

f) Measured corrosion current densities

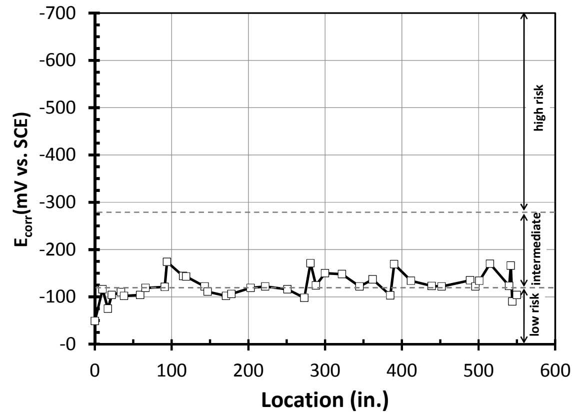

g) Average measured half-cell potentials

h) Sacrificial element of sensor T1-3 after autopsy

i) Rebar sections at vicinity of sensor T1-3

Figure D-3(Continued): Details of sensor T1-3

Table D-3: Post-autopsy results of sensor T1-3

Time to corrosion of sacrificial washer (Days)		Uncorroded
Max. width of crack crossing the embedded sensor (in.)		0.016
Rebar mass loss (%)	North	0.45
	South	0.60

D.1.4 Sensor T1-4

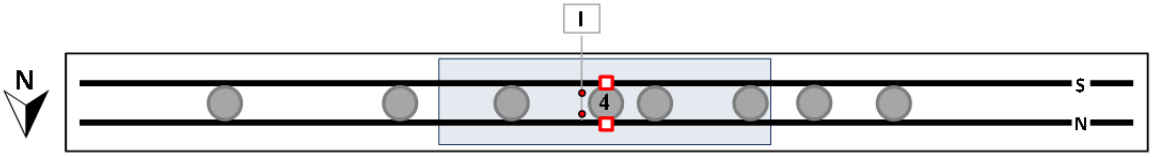

a) Locations of sensor T1-4, half-cell and LPR measurement points, and concrete powder samples

b) Sensor T1-4 before concrete casting

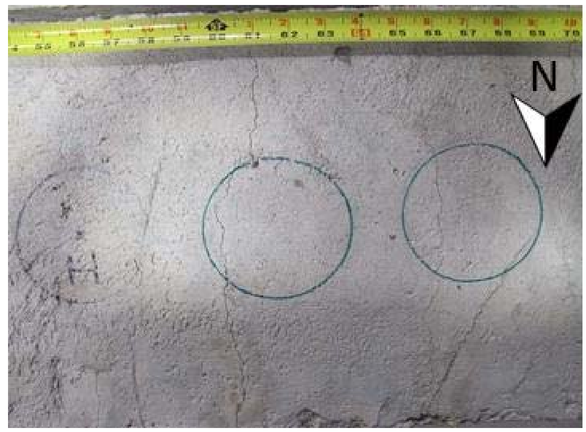

c)Surface Cracks in vicinity of T1-4

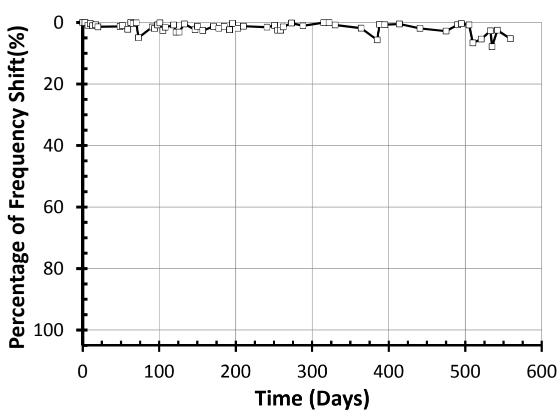

d) Shift in resonant frequency of T1-4

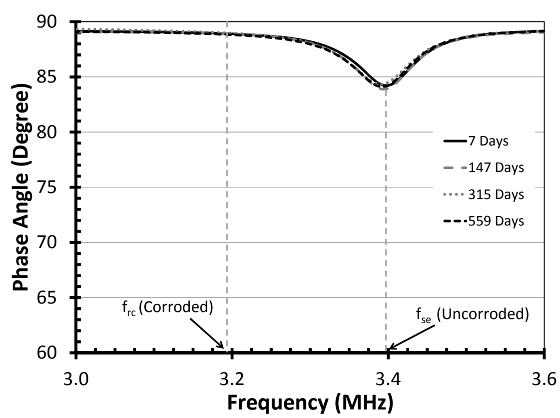

e) Measured phase response of T1-4 in selected days

Figure D-4: Details of sensor T1-4

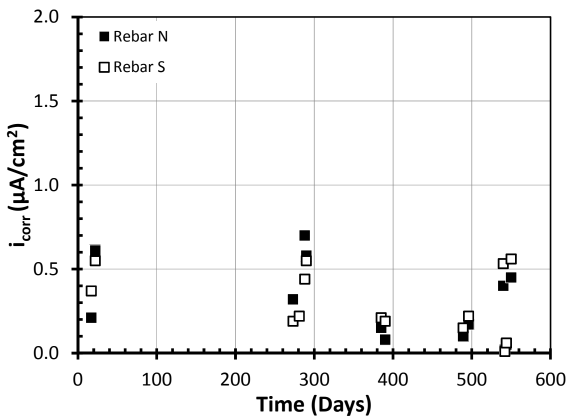

f) Measured corrosion current densities

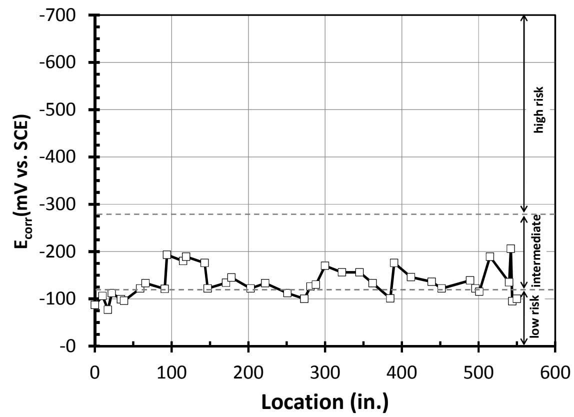

g) Average measured half-cell potentials

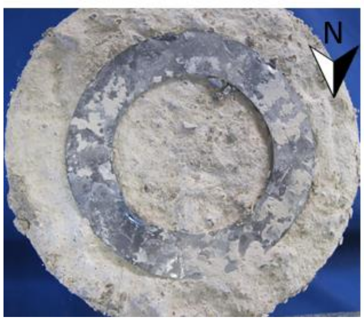

h) Sacrificial element of sensor T1-4 after autopsy

i) Rebar sections at vicinity of sensor T1-4

Figure D-4(Continued): Details of sensor T1-4

Table D-4: Post-autopsy results of sensor T1-4

Time to corrosion of sacrificial washer (Days)		Uncorroded
Max. width of crack crossing the embedded sensor (in.)		0.025
Rebar mass loss (%)	North	0.26
	South	0.22
Chloride ion concentration (ppm)	Line I	97
	-	-

D.1.5 Sensor T1-5

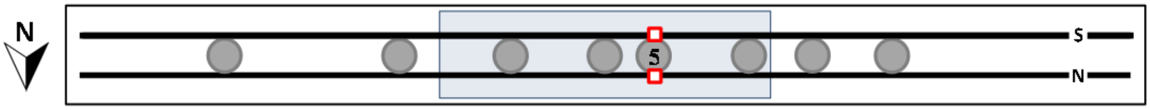

a) Locations of sensor T1-5, and half-cell and LPR measurement points

b) Sensor T1-5 before concrete casting

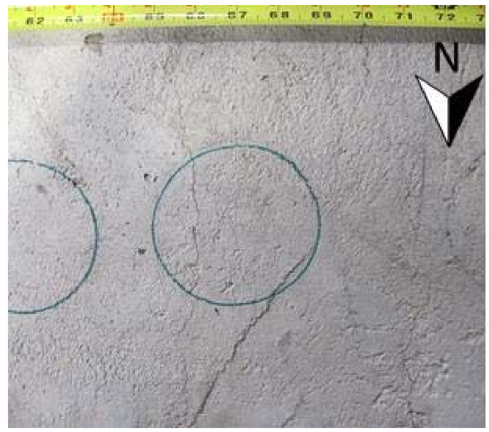

c)Surface Cracks in vicinity of T1-5

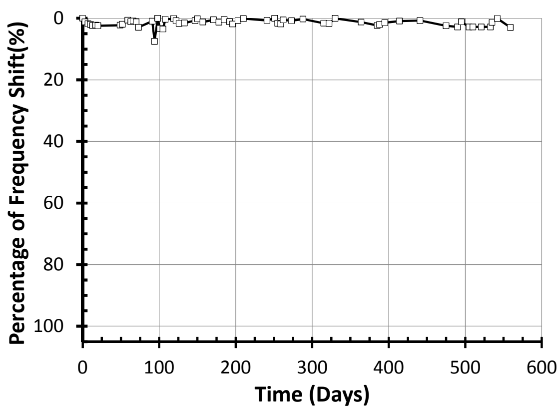

d) Shift in resonant frequency of T1-5

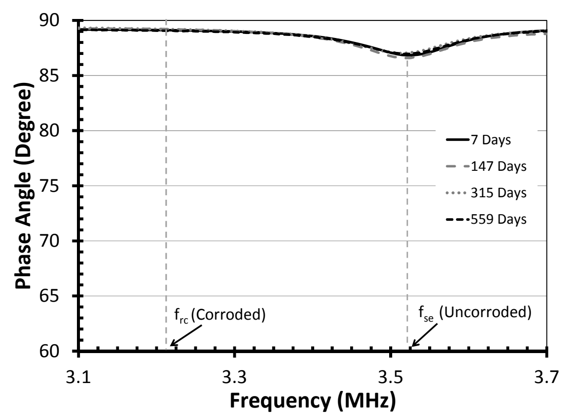

e) Measured phase response of T1-5 in selected days

Figure D-5: Details of sensor T1-5

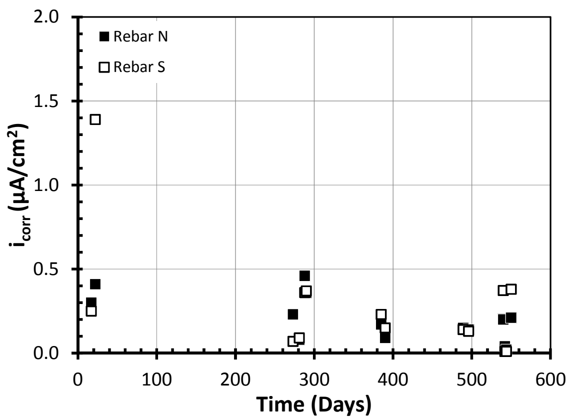

f) Measured corrosion current densities

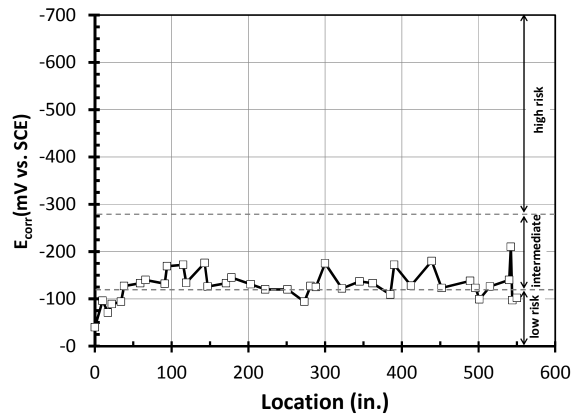

g) Average measured half-cell potentials

h) Sacrificial element of sensor T1-5 after autopsy

i) Rebar sections at vicinity of sensor T1-5

Figure D-5(Continued): Details of sensor T1-5

Table D-5: Post-autopsy results of sensor T1-5

Time to corrosion of sacrificial washer (Days)		Uncorroded
Max. width of crack crossing the embedded sensor (in.)		0.013
Rebar mass loss (%)	North	0.26
	South	0.22

D.1.6 Sensor T1-6

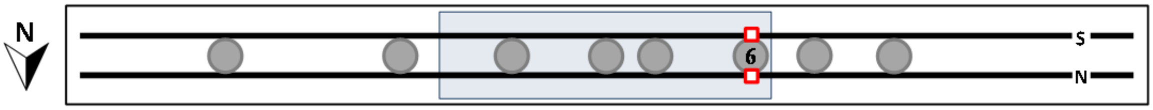

a) Locations of sensor T1-6, and half-cell and LPR measurement points

b) Sensor T1-6 before concrete casting

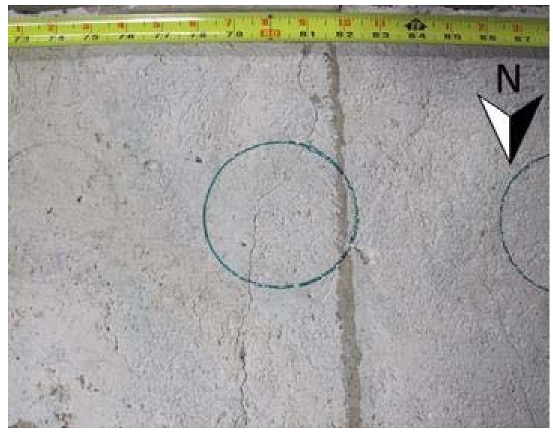

c)Surface Cracks in vicinity of T1-6

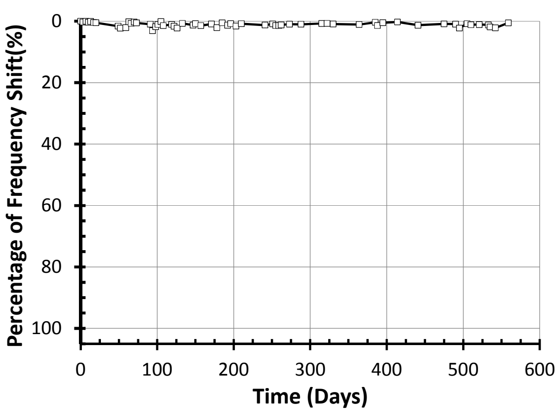

d) Shift in resonant frequency of T1-6

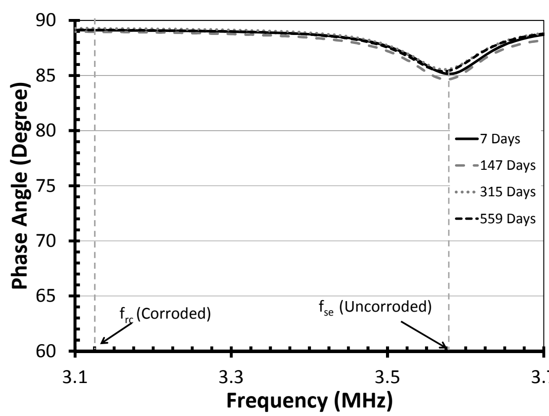

e) Measured phase response of T1-6 in selected days

Figure D-6: Details of sensor T1-6

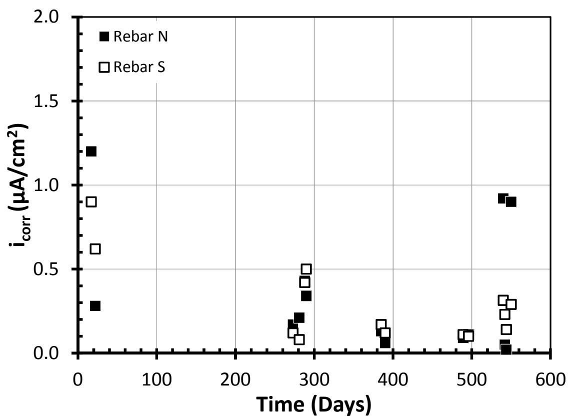

f) Measured corrosion current densities

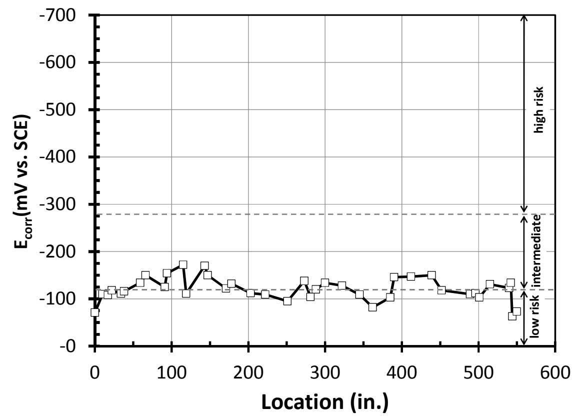

g) Average measured half-cell potentials

h) Sacrificial element of sensor T1-6 after autopsy

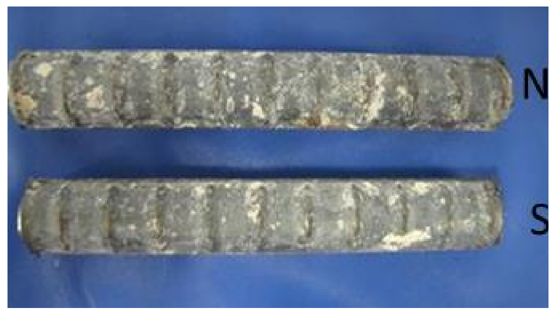

i) Rebar sections at vicinity of sensor T1-6

Figure D-6(Continued): Details of sensor T1-6

Table D-6: Post-autopsy results of sensor T1-6

Time to corrosion of sacrificial washer (Days)		Uncorroded
Max. width of crack crossing the embedded sensor (in.)		0.020
Rebar mass loss (%)	North	0.29
	South	0.24

D.1.7 Sensor T1-7

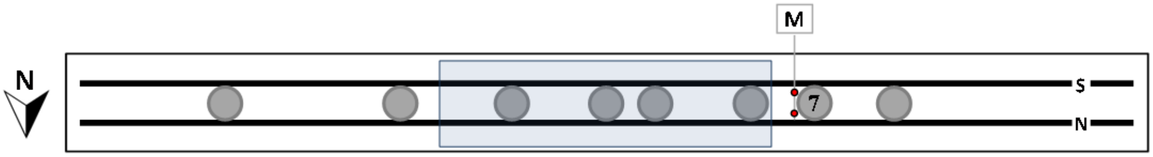

a) Locations of sensor T1-7, half-cell and LPR measurement points, and concrete powder samples

b) Sensor T1-7 before concrete casting

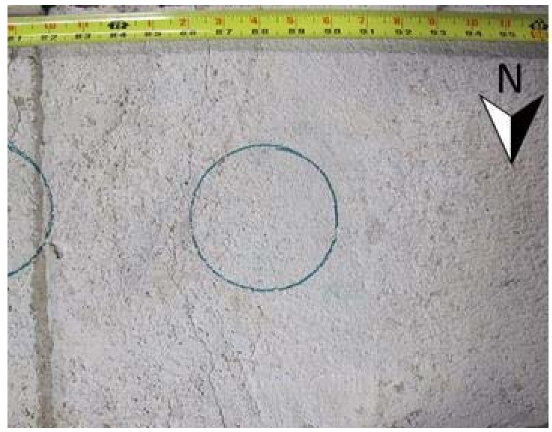

c)Surface Cracks in vicinity of T1-7

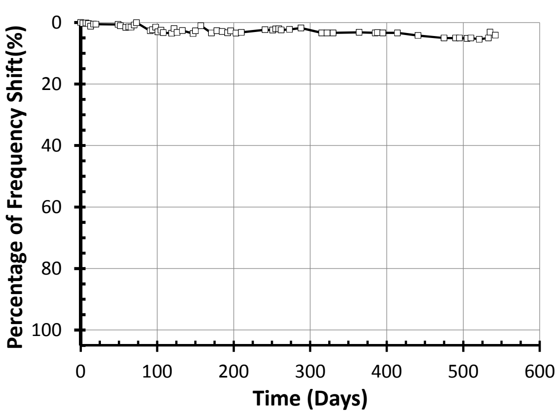

d) Shift in resonant frequency of T1-7

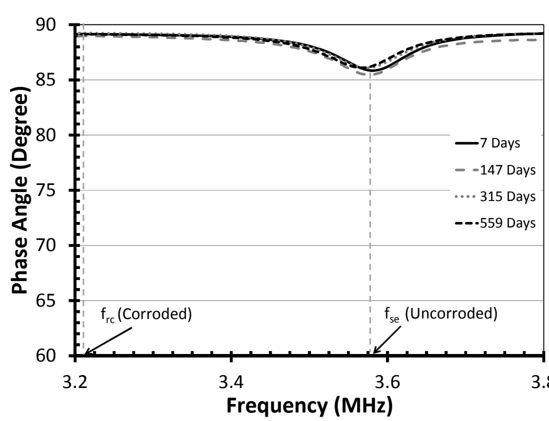

e) Measured phase response of T1-7 in selected days

Figure D-7: Details of sensor T1-7

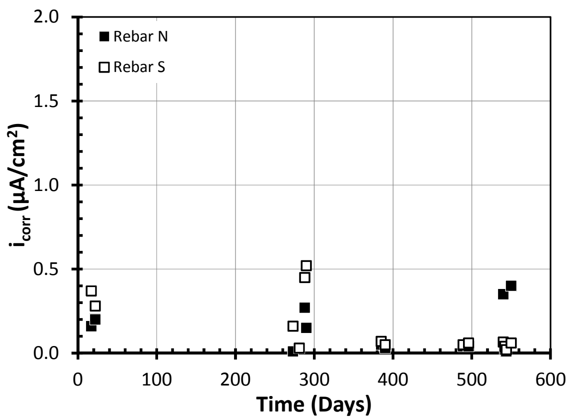

f) Measured corrosion current densities

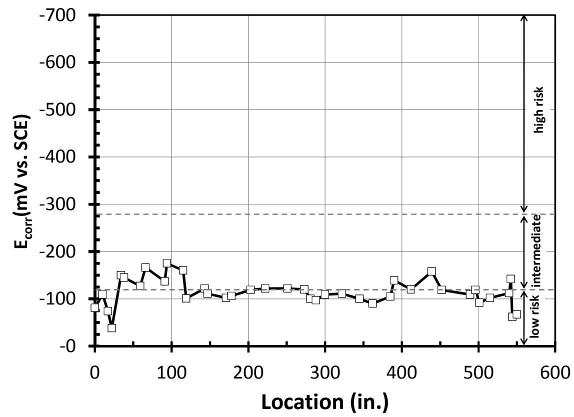

g) Average measured half-cell potentials

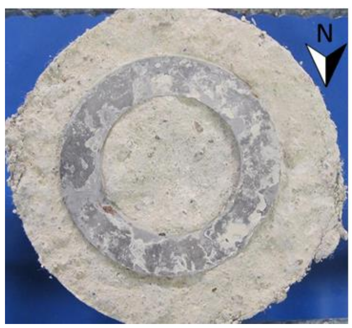

h) Sacrificial element of sensor T1-7 after autopsy

i) Rebar sections at vicinity of sensor T1-7

Figure D-7 (Continued): Details of sensor T1-7

Table D-7: Post-autopsy results of sensor T1-7

Time to corrosion of sacrificial washer (Days)		Uncorroded
Max. width of crack crossing the embedded sensor (in.)		0.013
Rebar mass loss (%)	North	0.24
	South	0.18
Chloride ion concentrations (ppm)	Line M	79
	-	-

D.1.8 Sensor T1-8

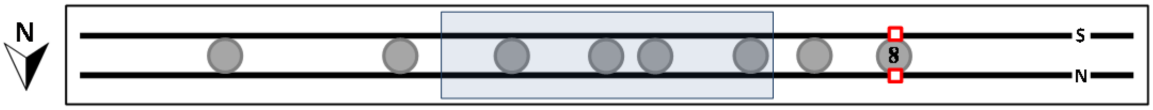

a) Locations of sensor T1-8, and half-cell and LPR measurement points

b) Sensor T1-8 before concrete casting

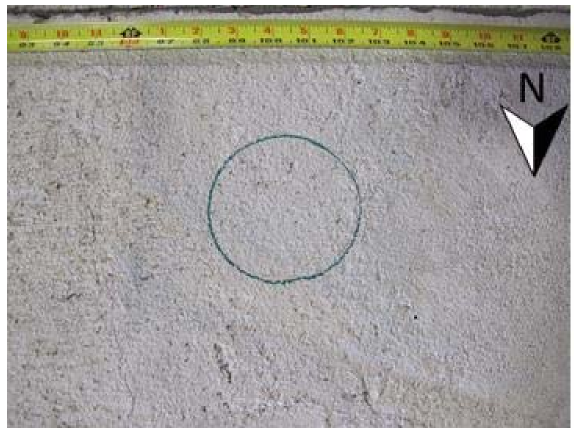

c)Surface Cracks in vicinity of T1-8

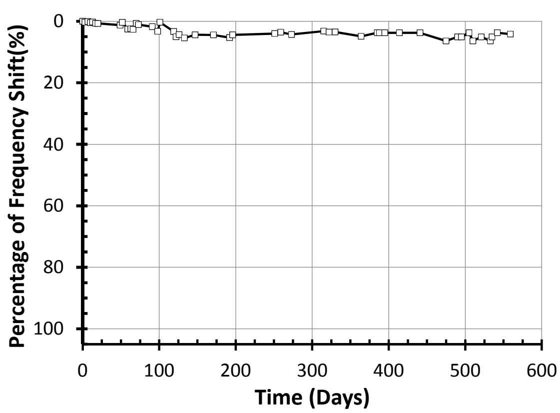

d) Shift in resonant frequency of T1-8

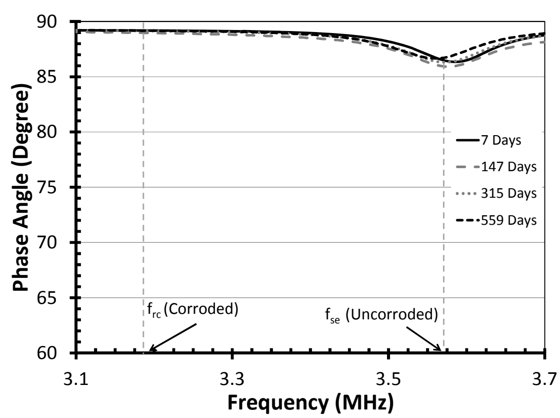

e) Measured phase response of T1-8 in selected days

Figure D-8: Details of sensor T1-8

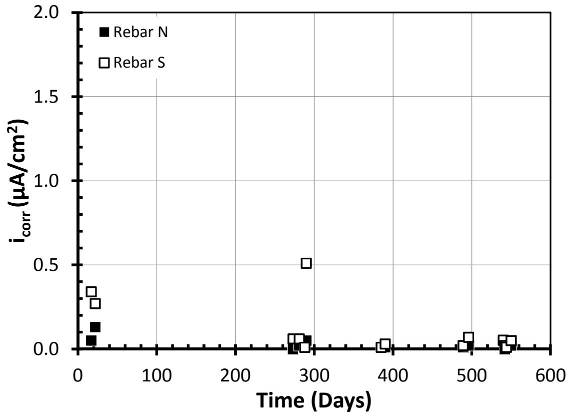

f) Measured corrosion current densities

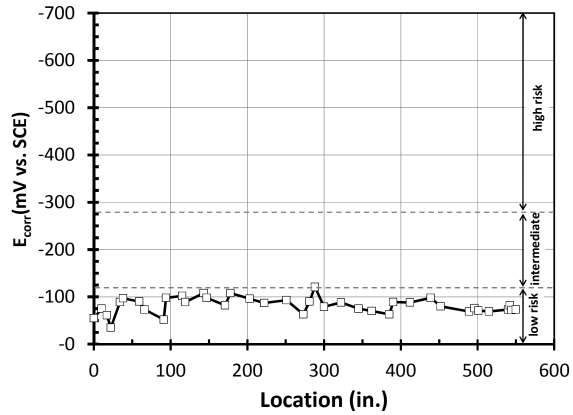

g) Average measured half-cell potentials

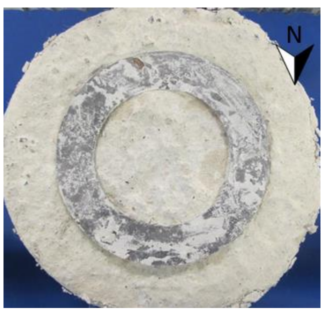

h) Sacrificial element of sensor T1-8 after autopsy

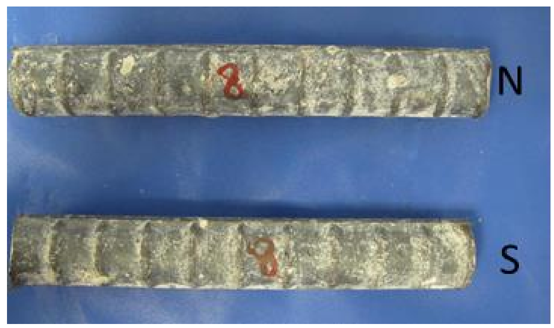

i) Rebar sections at vicinity of sensor T1-8

Figure D-8 (Continued): Details of sensor T1-8

Table D-8: Post-autopsy results of sensor T1-8

Time to corrosion of sacrificial washer (Days)		Uncorroded
Max. width of crack crossing the embedded sensor (in.)		None
Rebar mass loss (%)	North	0.28
	South	0.13

D.2 Sensors Embedded in Slab T2

D.2.1 Sensor T2-1

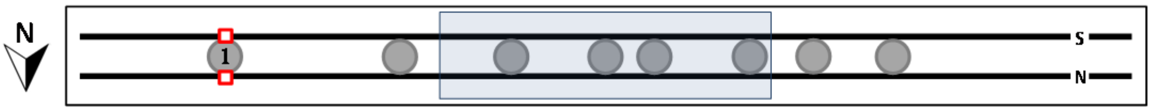

a) Locations of sensor T2-1, and half-cell and LPR measurement points

b)Sensor T2-1 before concrete casting

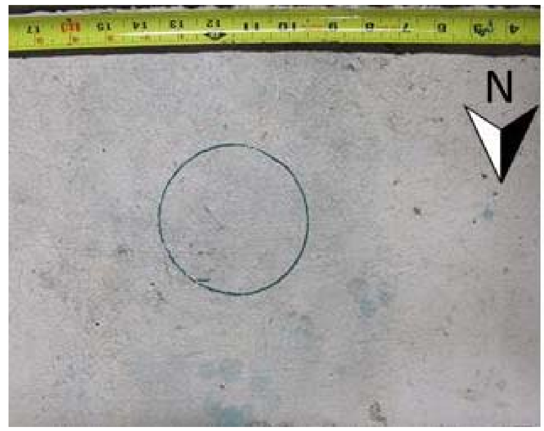

c)Surface Cracks in vicinity of T2-1

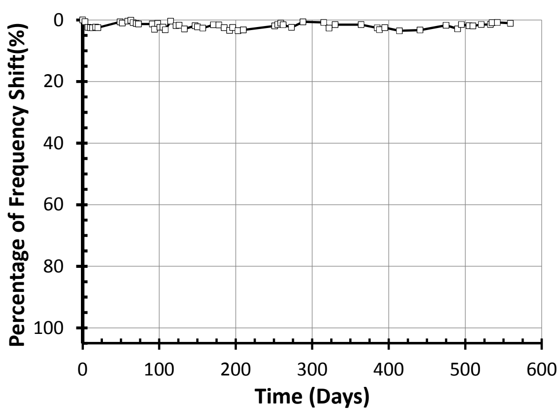

d) Shift in resonant frequency of T2-1

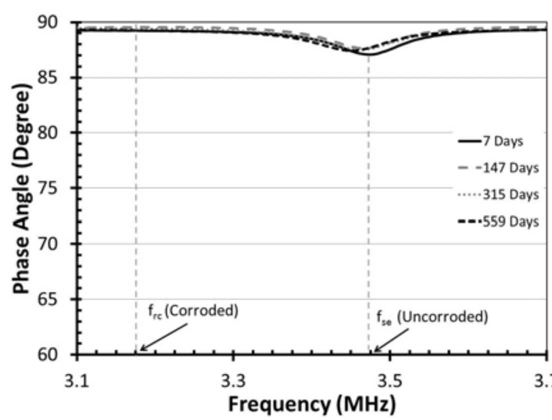

e) Measured phase response of T2-1 in selected days

Figure D-9: Details of sensor T2-1

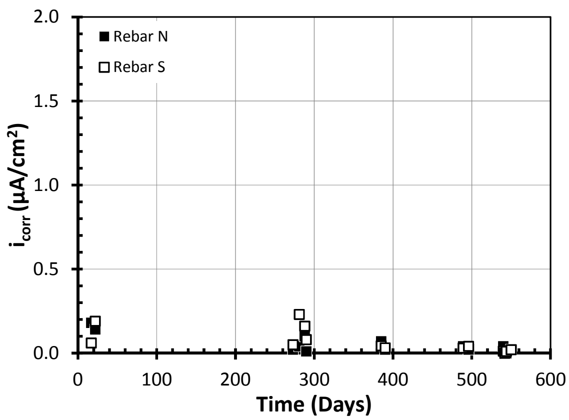

f) Measured corrosion current densities

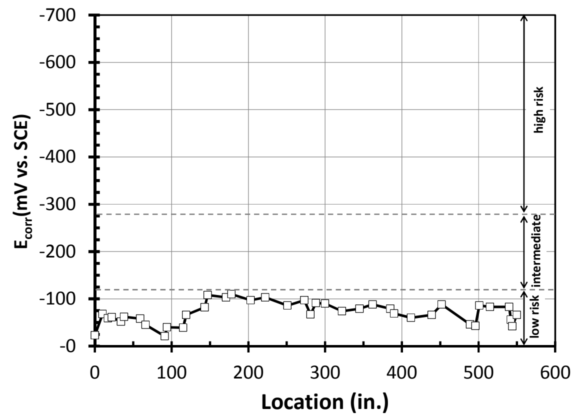

g) Average measured half-cell potentials

h) Sacrificial element of sensor T2-1 after autopsy

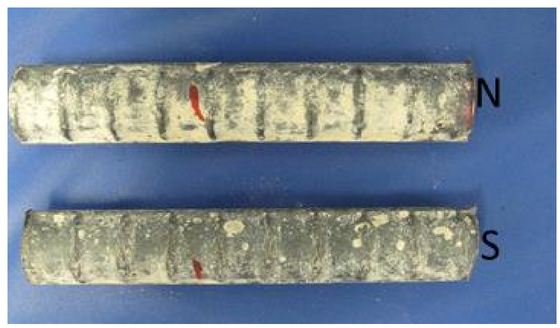

i) Rebar sections at vicinity of sensor T2-1

Figure D-9(Continued): Details of sensor T2-1

Table D-9: Post-autopsy results of sensor T2-1

<table>
<tr><td colspan="2">Time to corrosion of sacrificial washer (Days)</td><td>Uncorroded</td></tr>
<tr><td colspan="2">Max. width of crack crossing the embedded sensor (in.)</td><td>0.005</td></tr>
<tr><td rowspan="2">Rebar mass loss (%)</td><td>North</td><td>0.11</td></tr>
<tr><td>South</td><td>0.09</td></tr>
</table>

D.2.2 Sensor T2-2

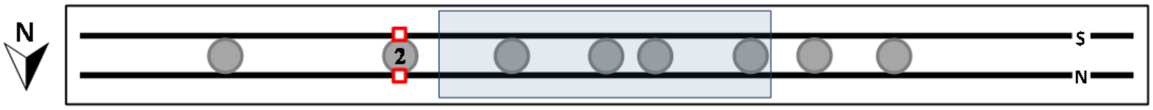

a) Locations of sensor T2-2, and half-cell and LPR measurement points

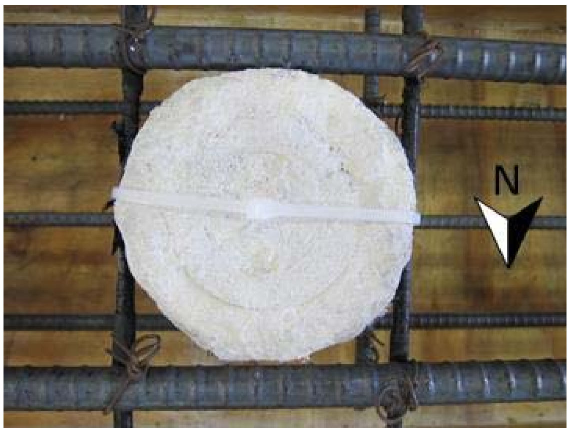

b)Sensor T2-2 before concrete casting

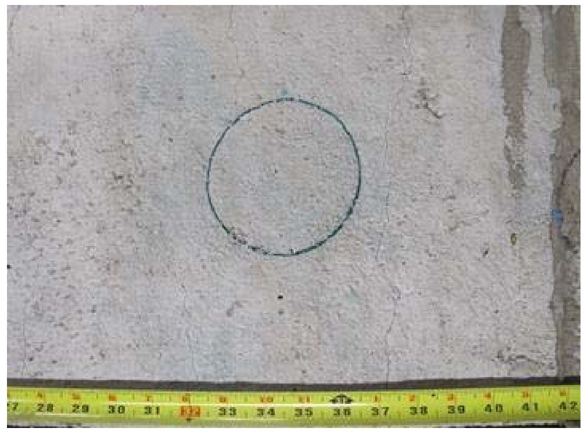

c)Surface Cracks in vicinity of T2-2

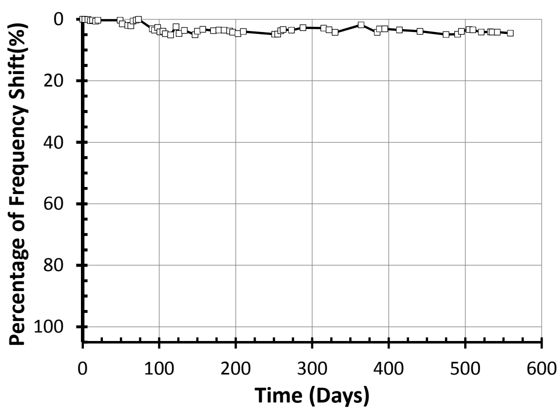

d) Shift in resonant frequency of T2-2

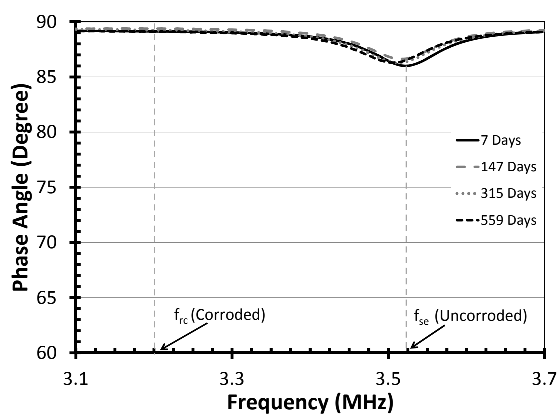

e) Measured phase response of T2-2 in selected days

Figure D-10: Details of sensor T2-2

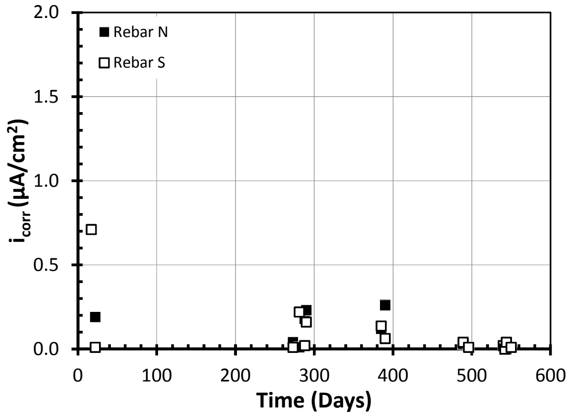

f) Measured corrosion current densities

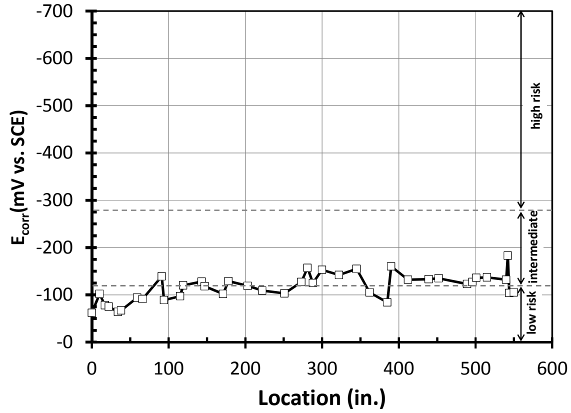

g) Average measured half-cell potentials

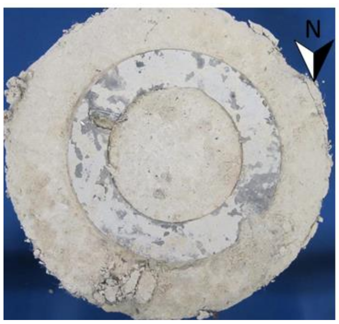

h) Sacrificial element of sensor T2-2 after autopsy

i) Rebar sections at vicinity of sensor T2-2

Figure D-10(Continued): Details of sensor T2-2

Table D-10: Post-autopsy results of sensor T2-2

Time to corrosion of sacrificial washer (Days)		Uncorroded
Max. width of crack crossing the embedded sensor (in.)		0.002
Rebar mass loss (%)	North	0.18
	South	0.12

D.2.3 Sensor T2-3

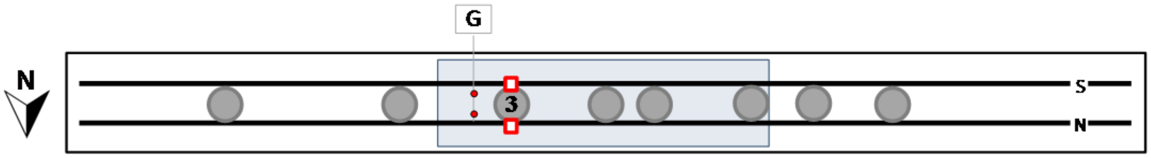

a) Locations of sensor T2-3, half-cell and LPR measurement points, and concrete powder samples

b)Sensor T2-3 before concrete casting

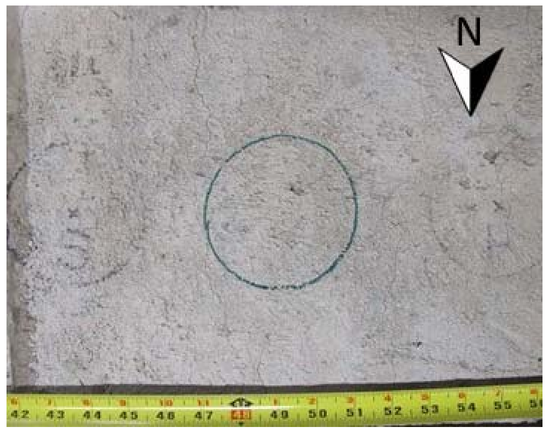

c)Surface Cracks in vicinity of T2-3

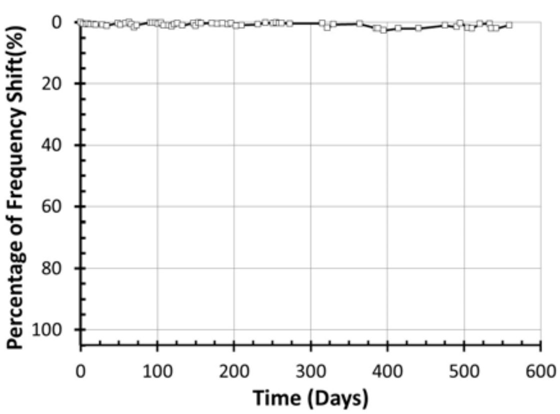

d) Shift in resonant frequency of T2-3

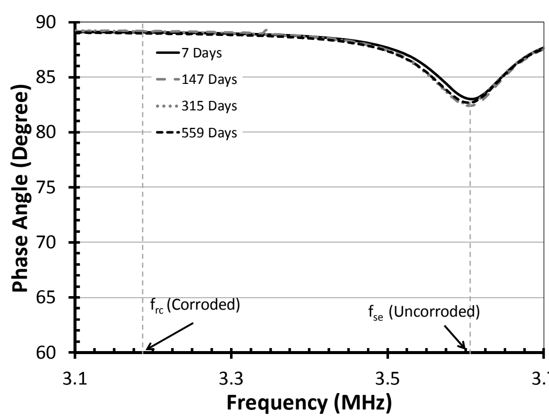

e) Measured phase response of T2-3 in selected days

Figure D-11: Details of sensor T2-3

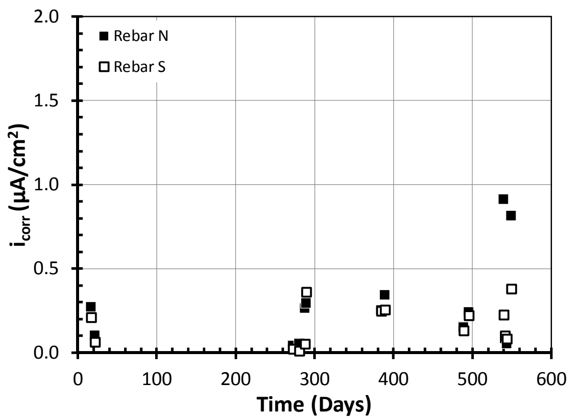

f) Measured corrosion current densities

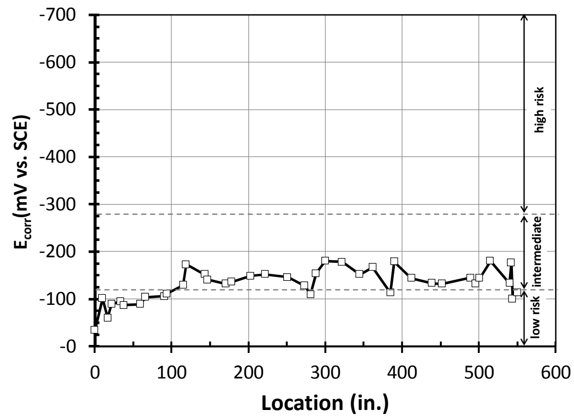

g) Average measured half-cell potentials

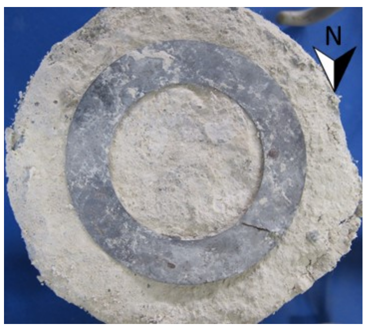

h) Sacrificial element of sensor T2-3 after autopsy

i) Rebar sections at vicinity of sensor T2-3

Figure D-11(Continued): Details of sensor T2-3

Table D-11: Post-autopsy results of sensor T2-3

Time to corrosion of sacrificial washer (Days)		Uncorroded
Max. width of crack crossing the embedded sensor (in.)		0.013
Rebar mass loss (%)	North	0.21
	South	0.30
Chloride ion concentrations (ppm)	Line G	69

D.2.4 Sensor T2-4

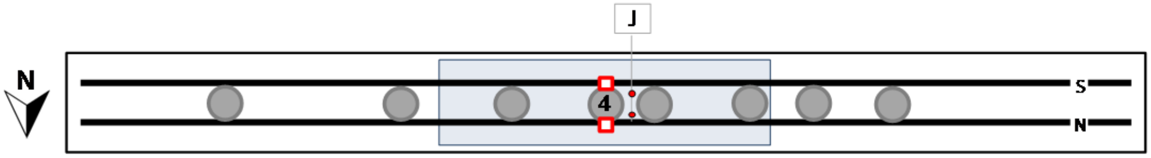

a) Locations of sensor T2-4, half-cell and LPR measurement points, and concrete powder samples

b)Sensor T2-4 before concrete casting

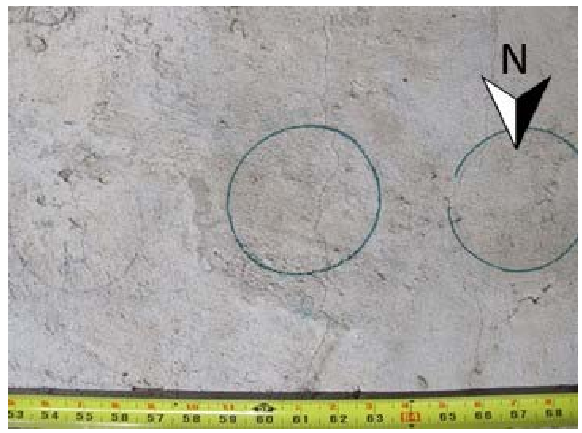

c)Surface Cracks in vicinity of T2-4

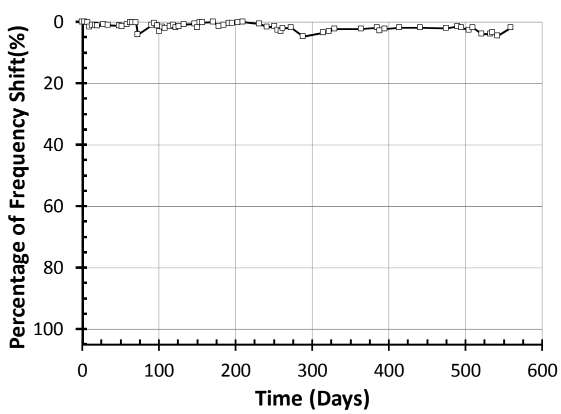

d) Shift in resonant frequency of T2-4

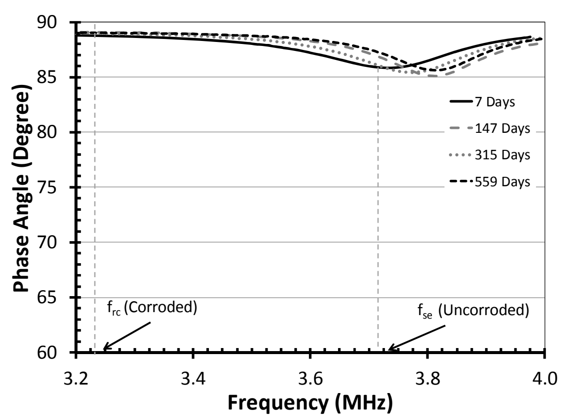

e) Measured phase response of T2-4 in selected days

Figure D-12: Details of sensor T2-4

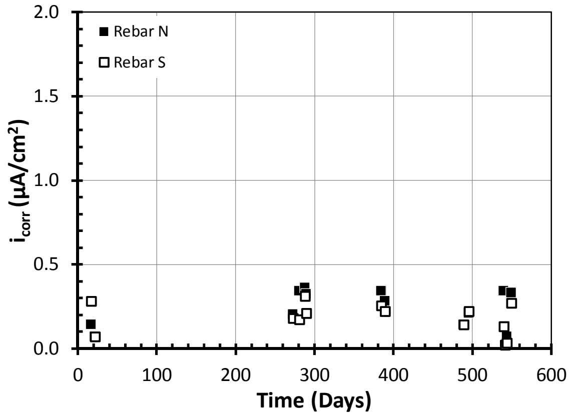

f) Measured corrosion current densities

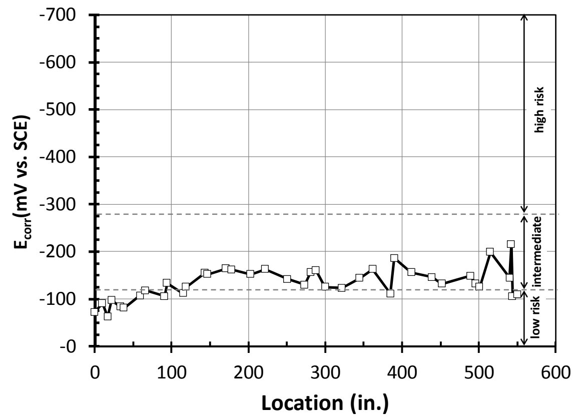

g) Average measured half-cell potentials

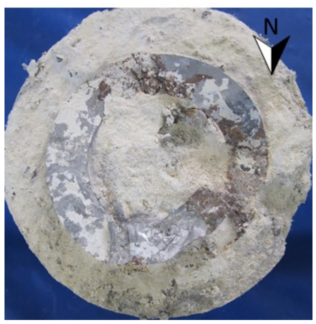

h) Sacrificial element of sensor T2-4 after autopsy

i) Rebar sections at vicinity of sensor T2-4

Figure D-12(Continued): Details of sensor T2-4

Table D-12: Post-autopsy results of sensor T2-4

Time to corrosion of sacrificial washer (Days)		Uncorroded
Max. width of crack crossing the embedded sensor (in.)		0.020
Rebar mass loss (%)	North	0.52
	South	0.33
Chloride ion concentration (ppm)	Line J	64

D.2.5 Sensor T2-5

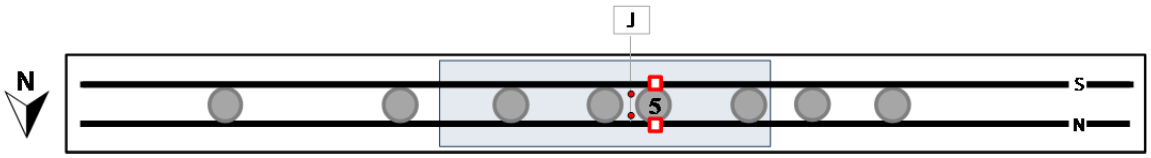

a) Locations of sensor T2-5, half-cell and LPR measurement points, and concrete powder samples

b)Sensor T2-5 before concrete casting

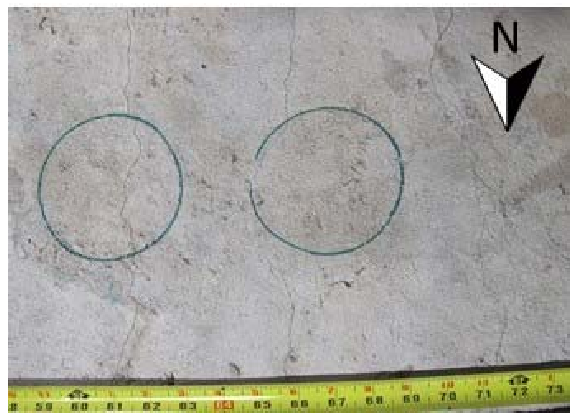

c)Surface Cracks in vicinity of T2-5

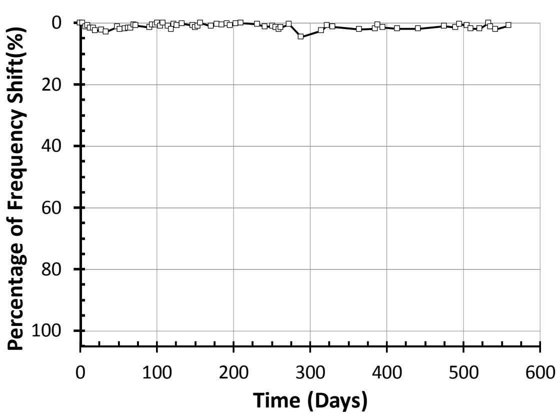

d) Shift in resonant frequency of T2-5

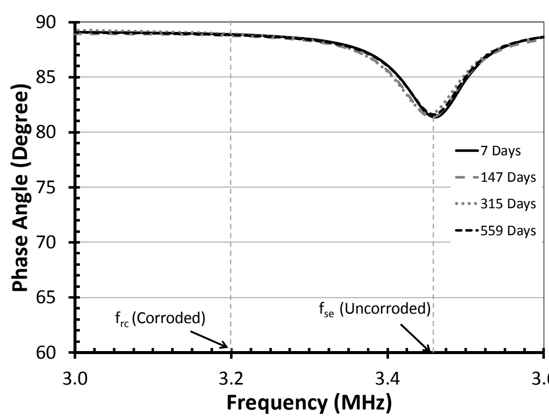

e) Measured phase response of T2-5 in selected days

Figure D-13: Details of sensor T2-5

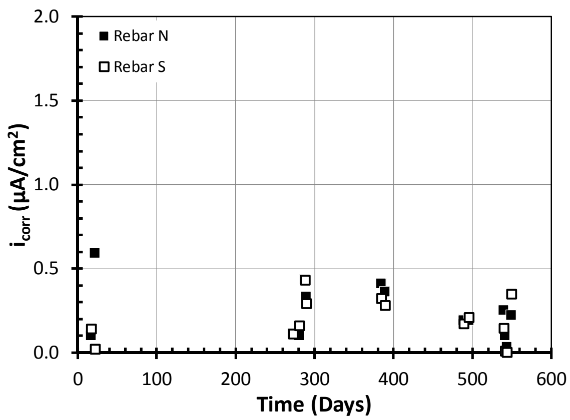

f) Measured corrosion current densities

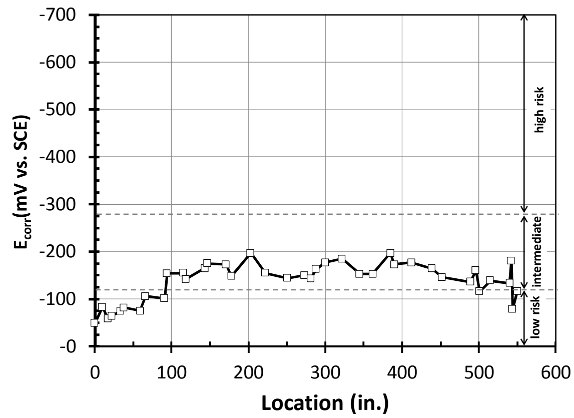

g) Average measured half-cell potentials

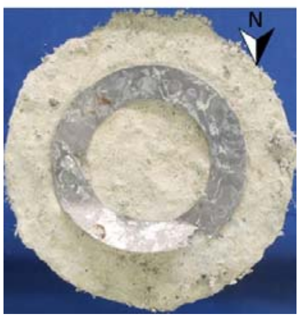

h) Sacrificial element of sensor T2-5 after autopsy

i) Rebar sections at vicinity of sensor T2-5

Figure D-13 (Continued): Details of sensor T2-5

Table D-13: Post-autopsy results of sensor T2-5

Time to corrosion of sacrificial washer (Days)		Uncorroded
Max. width of crack crossing the embedded sensor (in.)		0.013
Rebar mass loss (%)	North	0.27
	South	0.25

D.2.6 Sensor T2-6

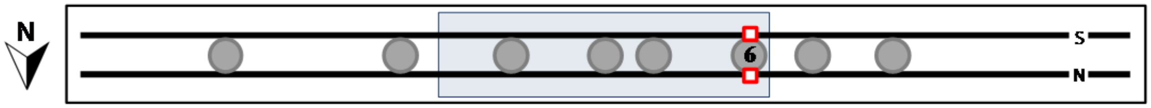

a) Locations of sensor T2-6, and half-cell and LPR measurement points

b)Sensor T2-6 before concrete casting

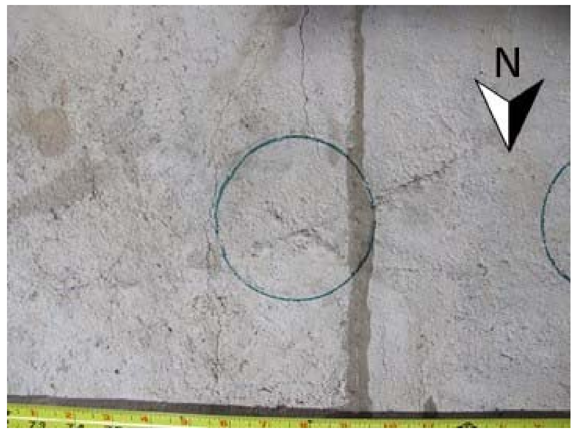

c)Surface Cracks in vicinity of T2-6

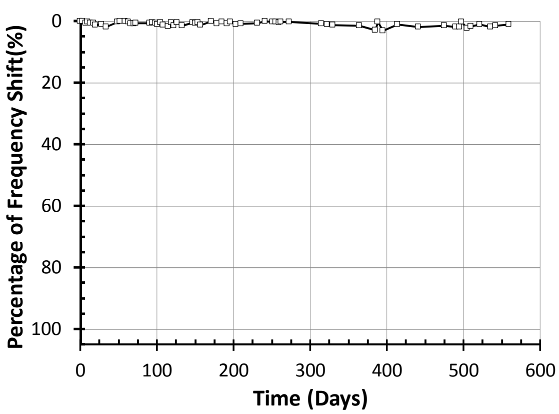

d) Shift in resonant frequency of T2-5

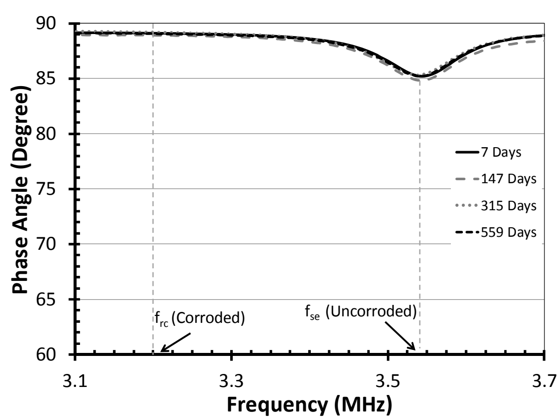

e) Measured phase response of T2-6 in selected days

Figure D-14: Details of sensor T2-6

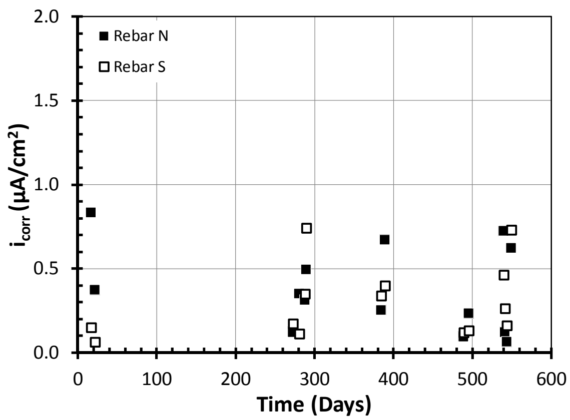

f) Measured corrosion current densities

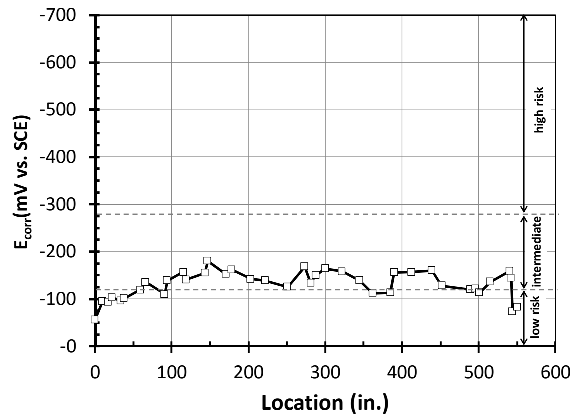

g) Average measured half-cell potentials

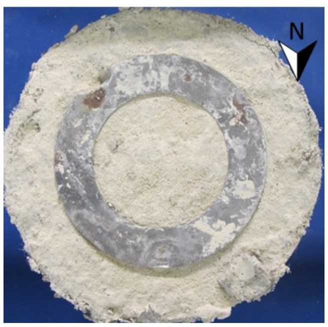

h) Sacrificial element of sensor T2-6 after autopsy

i) Rebar sections at vicinity of sensor T2-6

Figure D-14(Continued): Details of sensor T2-6

Table D-14: Post-autopsy results of sensor T2-6

Time to corrosion of sacrificial washer (Days)		Uncorroded
Max. width of crack crossing the embedded sensor (in.)		0.025
Rebar mass loss (%)	North	0.09
	South	0.07

D.2.7 Sensor T2-7

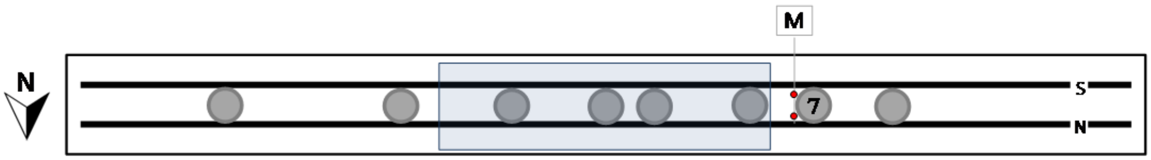

a) Locations of sensor T2-7, half-cell and LPR measurement points, and concrete powder samples

b)Sensor T2-7 before concrete casting

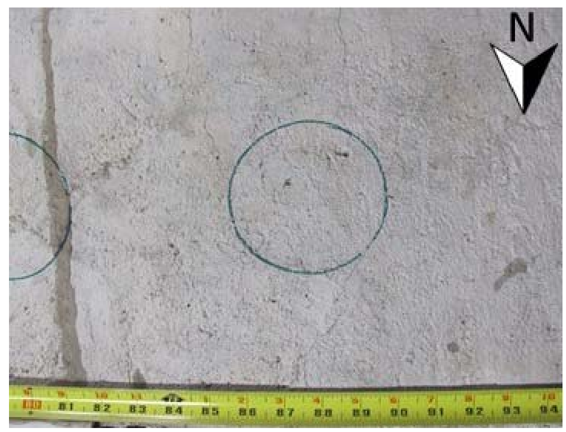

c)Surface Cracks in vicinity of T2-7

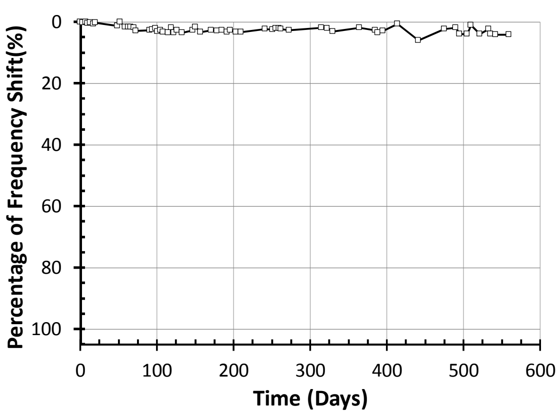

d) Shift in resonant frequency of T2-7

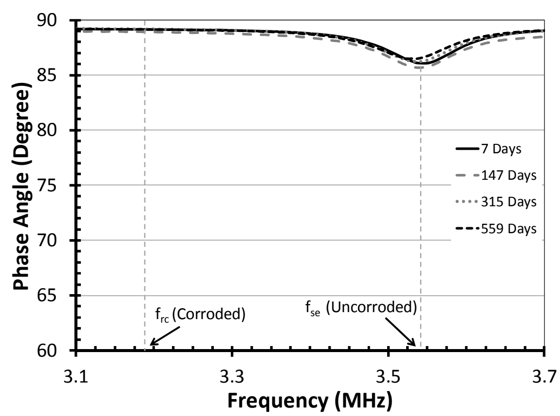

e) Measured phase response of T2-7 in selected days

Figure D-15: Details of sensor T2-7

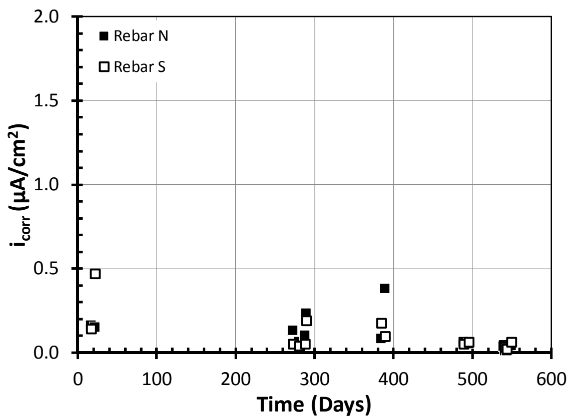

f) Measured corrosion current densities

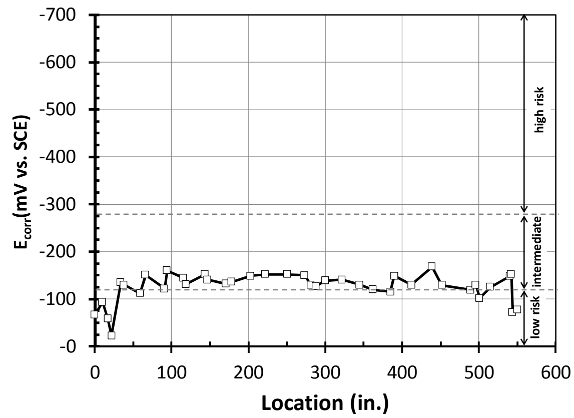

g) Average measured half-cell potentials

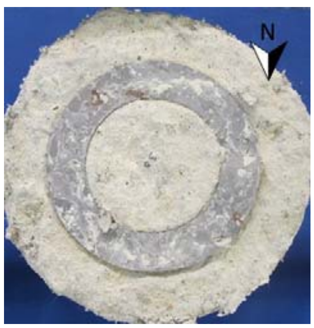

h) Sacrificial element of sensor T2-7 after autopsy

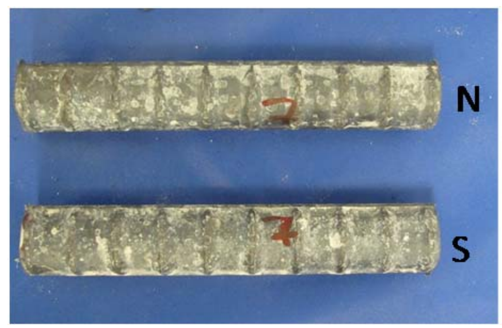

i) Rebar sections at vicinity of sensor T2-7

Figure D-15(Continued): Details of sensor T2-7

Table D-15: Post-autopsy results of sensor T2-7

Time to corrosion of sacrificial washer (Days)		Uncorroded
Max. width of crack crossing the embedded sensor (in.)		0.002
Rebar mass loss (%)	North	0.07
	South	0.07
Chloride ion concentration (ppm)	Line M	71

D.2.8 Sensor T2-8

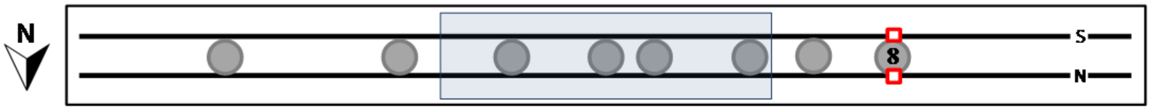

a) Locations of sensor T2-8, and half-cell and LPR measurement points

b)Sensor T2-8 before concrete casting

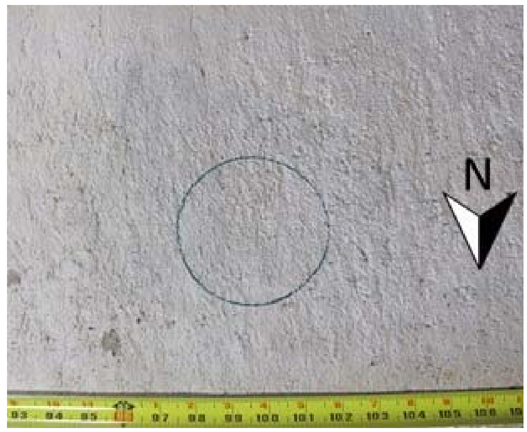

c)Surface Cracks in vicinity of T2-8

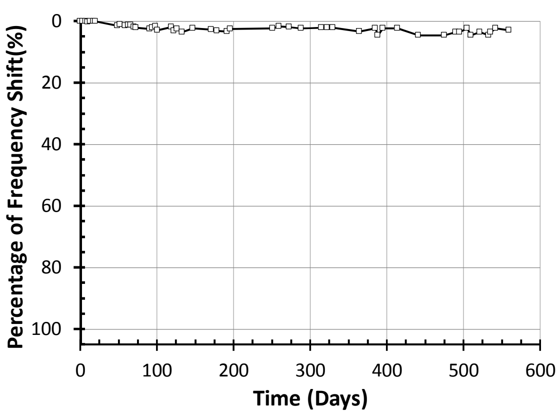

d) Shift in resonant frequency of T2-8

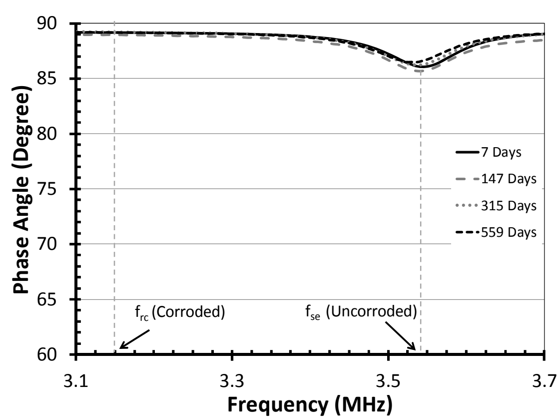

e) Measured phase response of T2-8 in selected days

Figure D-16: Details of sensor T2-8

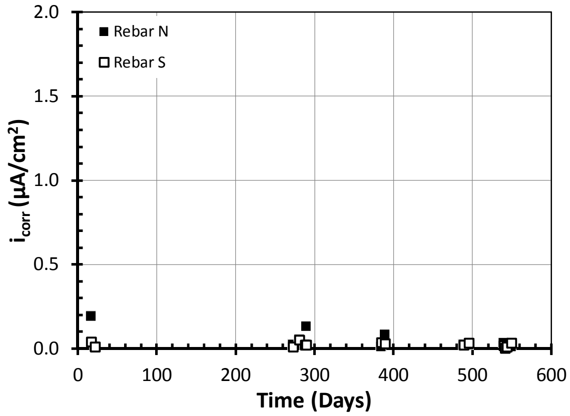

f) Measured corrosion current densities

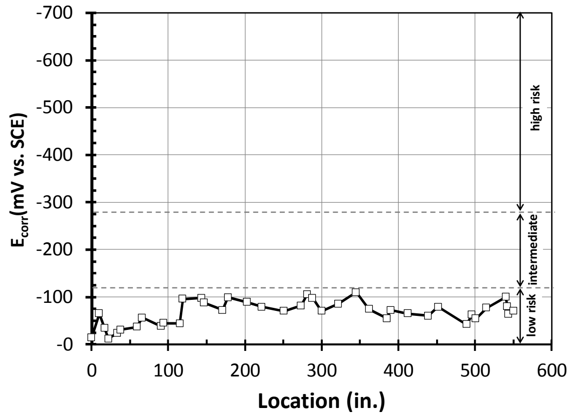

g) Average measured half-cell potentials

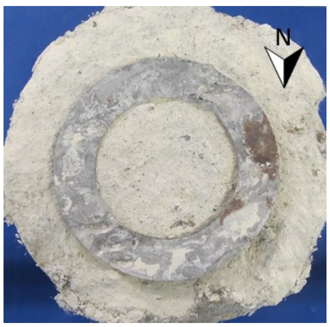

h) Sacrificial element of sensor T2-8 after autopsy

i) Rebar sections at vicinity of sensor T2-8

Figure D-16(Continued): Details of sensor T2-8

Table D-16: Post-autopsy results of sensor T2-8

Time to corrosion of sacrificial washer (Days)		Uncorroded
Max. width of crack crossing the embedded sensor (in.)		None
Rebar mass loss (%)	North	0.03
	South	0.07

D.3 Sensors Embedded in Slab S1

D.3.1 Sensor S1-1

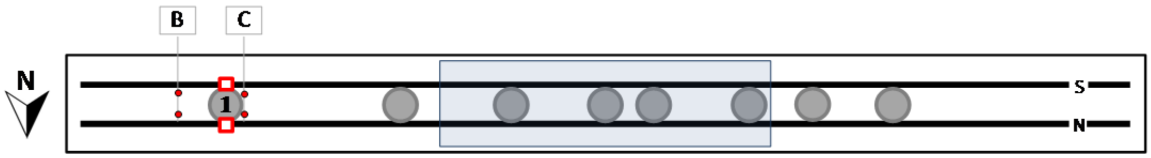

a) Locations of sensor S1-1, half-cell and LPR measurement points, and concrete powder samples

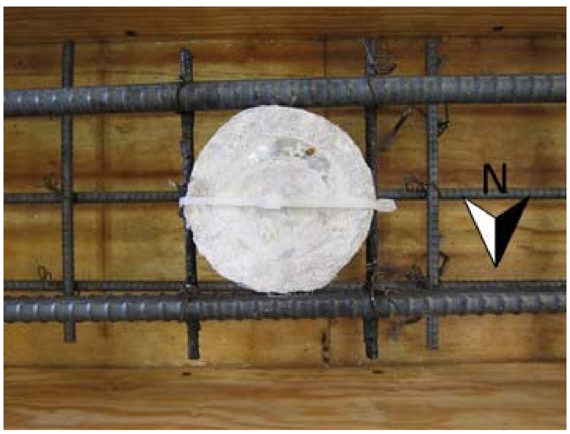

b)Sensor S1-1 before concrete casting

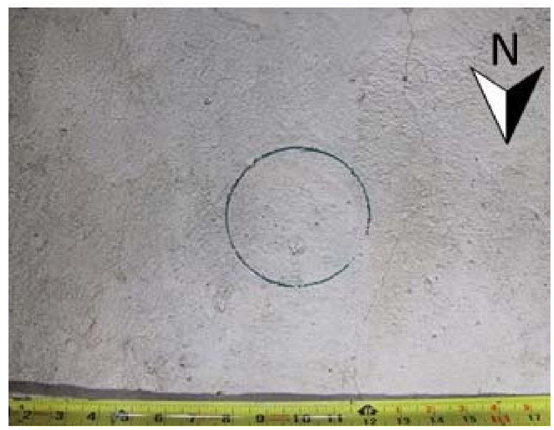

c)Surface Cracks in vicinity of S1-1

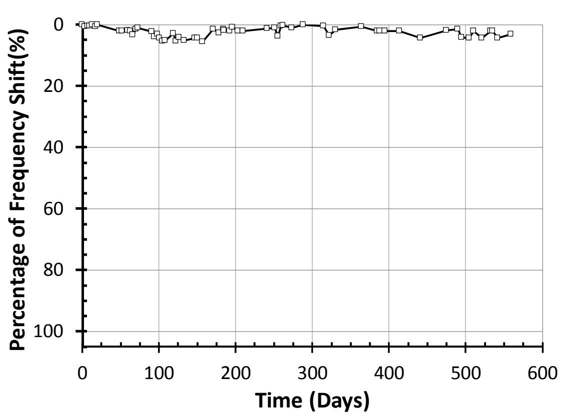

d) Shift in resonant frequency of S1-1

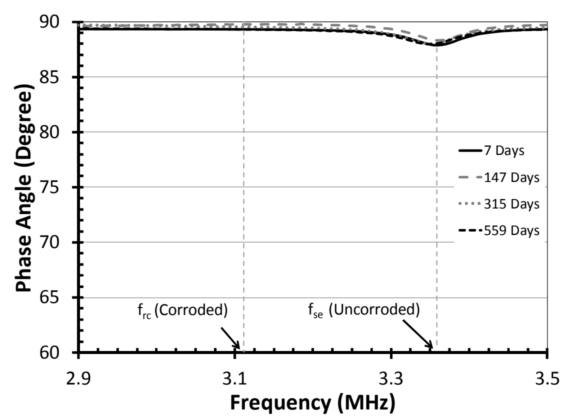

e) Measured phase response of S1-1 in selected days

Figure D-17: Details of sensor S1-1

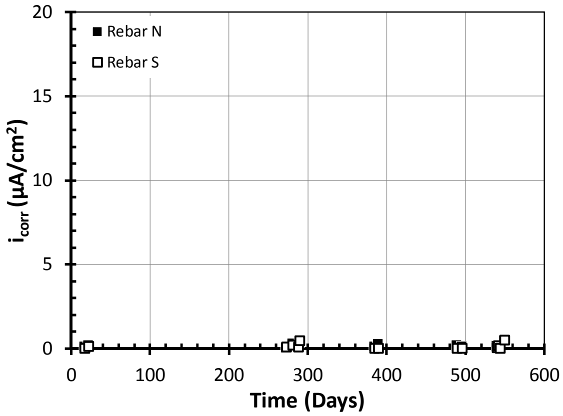

f) Measured corrosion current densities

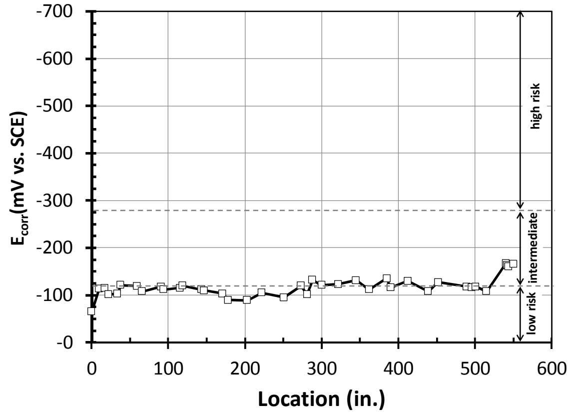

g) Average measured half-cell potentials

h) Sacrificial element of sensor S1-1 after autopsy

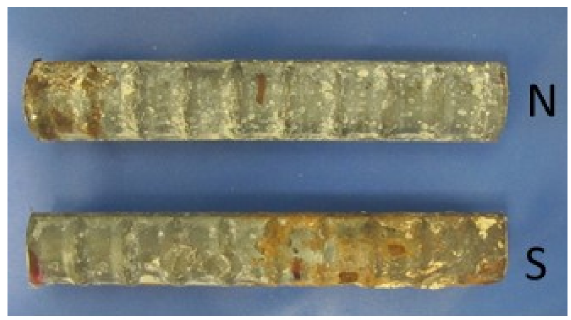

i) Rebar sections at vicinity of sensor S1-1

Figure D-17 (Continued): Details of sensor S1-1

Table D-17: Post-autopsy results of sensor S1-1

Time to corrosion of sacrificial washer (Days)		Uncorroded
Max. width of crack crossing the embedded sensor (in.)		0.016
Rebar mass loss (%)	North	0.09
	South	1.37
Chloride ion concentration (ppm)	Line B	1886
	Line C	2547

D.3.2 Sensor S1-2

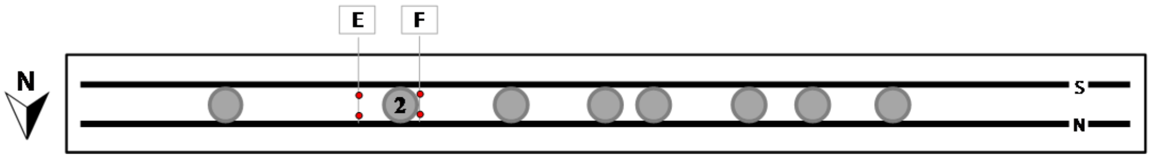

a) Locations of sensor S1-2, half-cell and LPR measurement points, and concrete powder samples

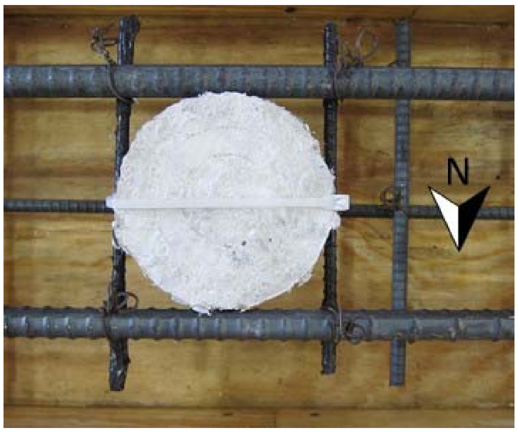

b)Sensor S1-2 before concrete casting

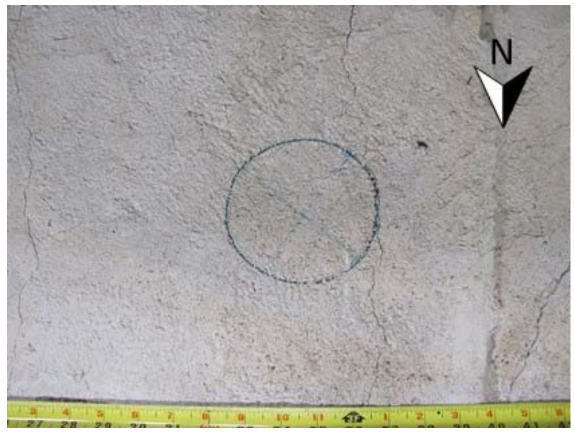

c)Surface Cracks in vicinity of S1-2

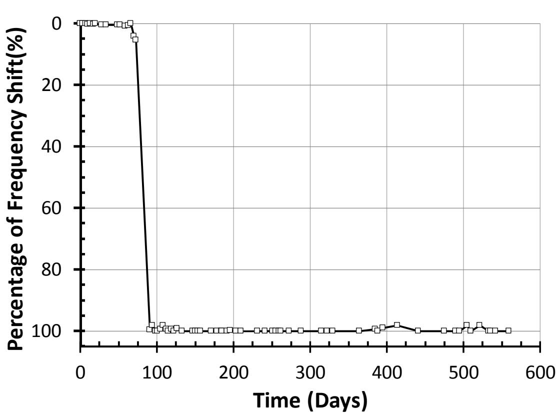

d) Shift in resonant frequency of S1-2

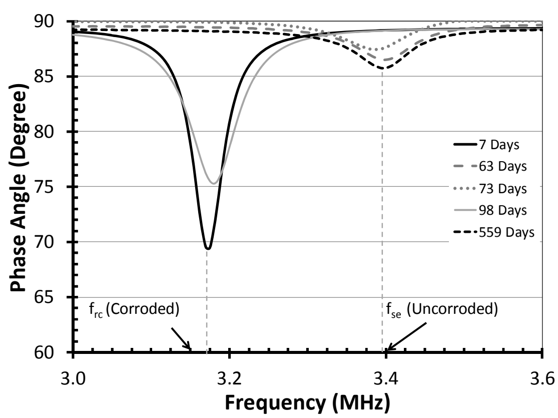

e) Measured phase response of S1-2 in selected days

Figure D-18: Details of sensor S1-2

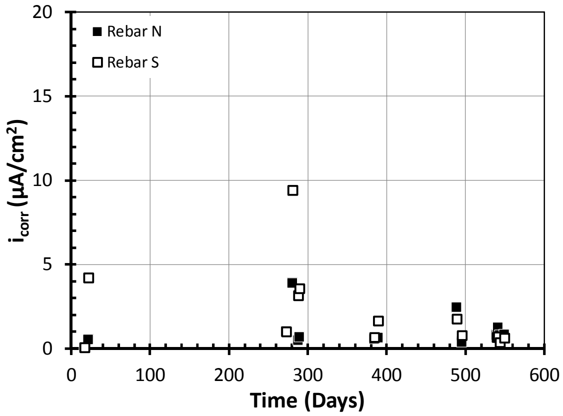

f) Measured corrosion current densities

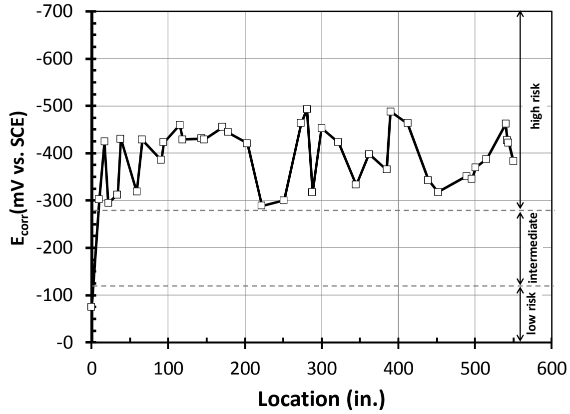

g) Average measured half-cell potentials

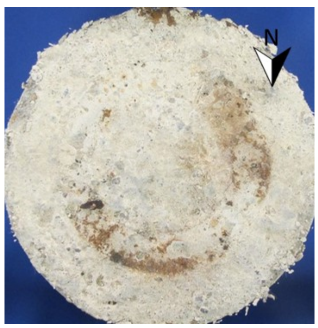

h) Sacrificial element of sensor S1-2 after autopsy

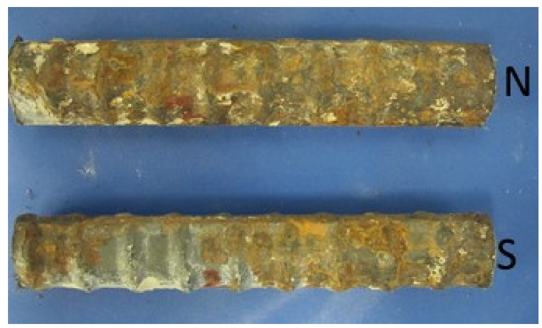

i) Rebar sections at vicinity of sensor S1-2

Figure D-18(Continued): Details of sensor S1-2

Table D-18: Post-autopsy results of sensor S1-2

Time to corrosion of sacrificial washer (Days)		98
Max. width of crack crossing the embedded sensor (in.)		0.04
Rebar mass loss (%)	North	2.35
	South	4.48
Chloride ion concentration (ppm)	Line E	2286
	Line F	1769

D.3.3 Sensor S1-3

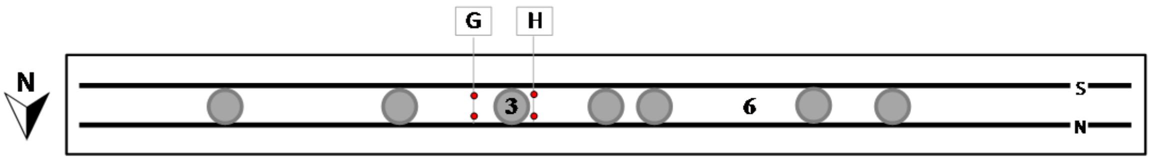

a) Locations of sensor S1-3, half-cell and LPR measurement points, and concrete powder samples

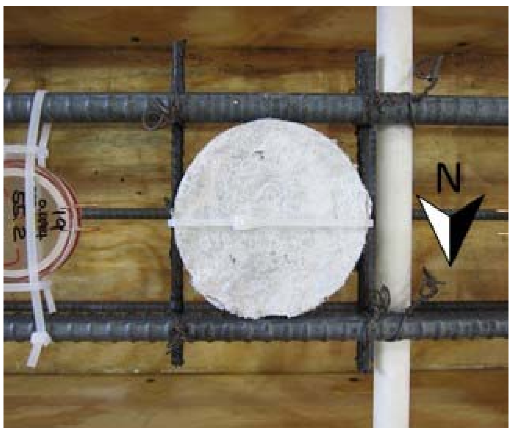

b)Sensor S1-3 before concrete casting

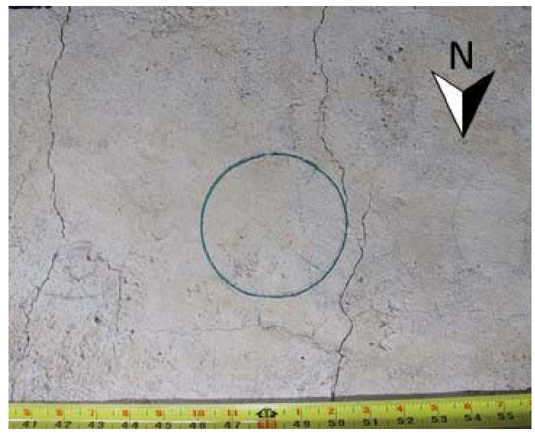

c)Surface Cracks in vicinity of S1-3

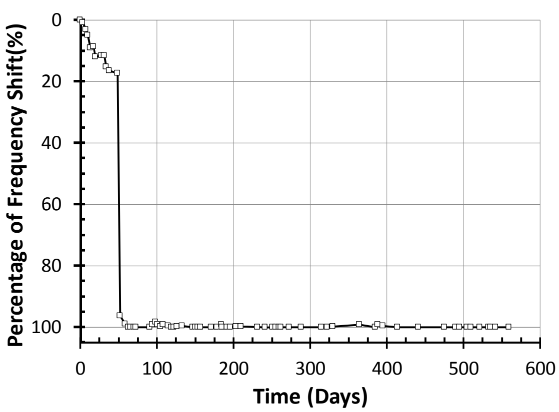

d) Shift in resonant frequency of S1-3

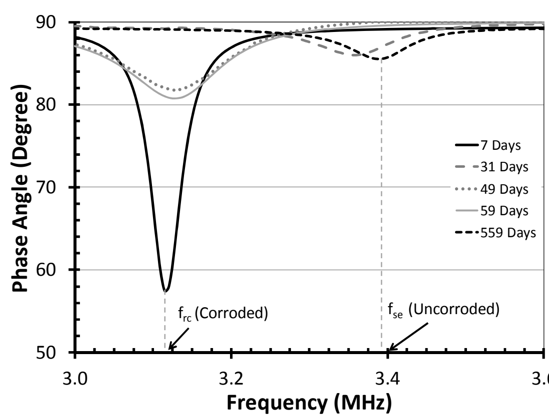

e) Measured phase response of S1-3 in selected days

Figure D-19: Details of sensor S1-3

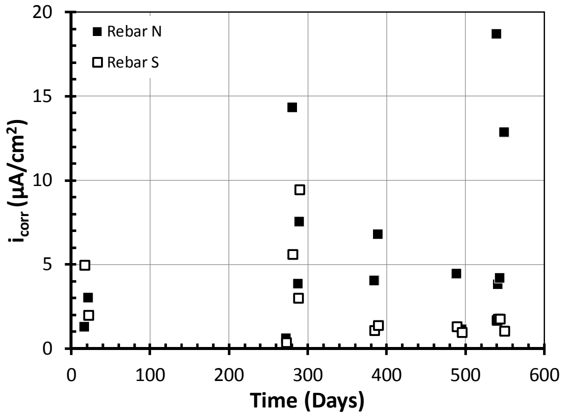

f) Measured corrosion current densities

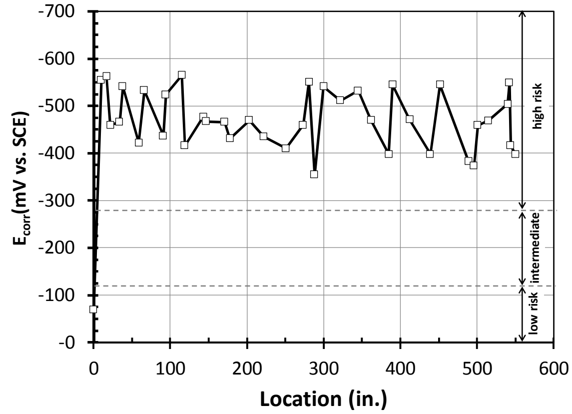

g) Average measured half-cell potentials

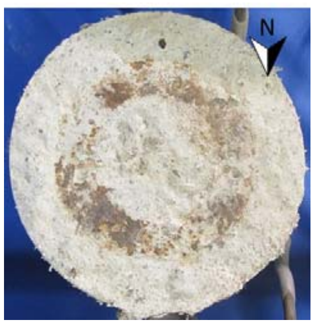

h) Sacrificial element of sensor S1-3 after autopsy

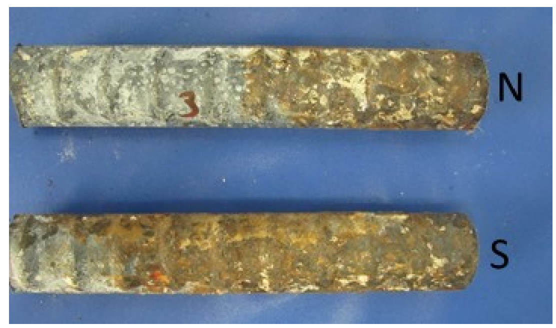

i) Rebar sections at vicinity of sensor S1-3

Figure D-19(Continued): Details of sensor S1-3

Table D-19: Post-autopsy results of sensor S1-3

Time to corrosion of sacrificial washer (Days)		59
Max. width of crack crossing the embedded sensor (in.)		0.04
Rebar mass loss (%)	North	3.71
	South	2.37
Chloride ion concentration (ppm)	Line G	2198
	Line H	3046

D.3.4 Sensor S1-4

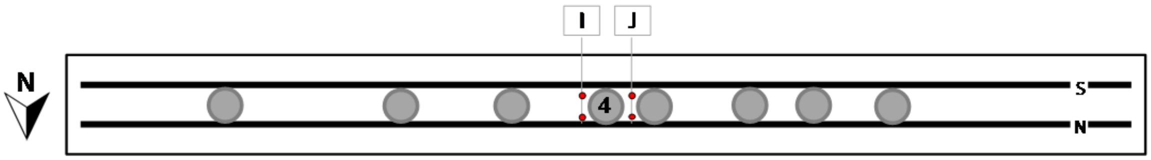

a) Locations of sensor S1-4, half-cell and LPR measurement points, and concrete powder samples

b)Sensor S1-4 before concrete casting

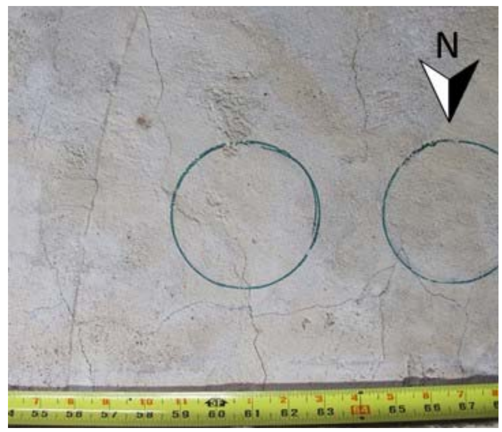

c)Surface Cracks in vicinity of S1-4

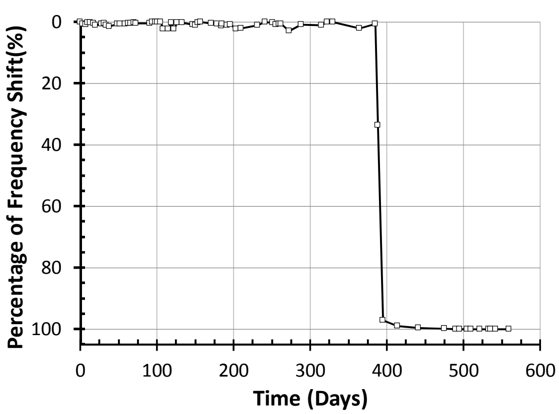

d) Shift in resonant frequency of S1-4

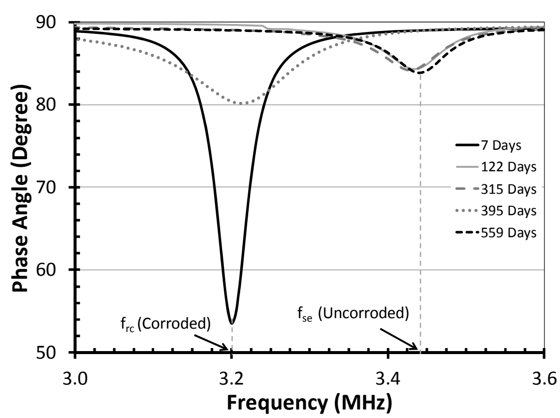

e) Measured phase response of S1-4 in selected days

Figure D-20: Details of sensor S1-4

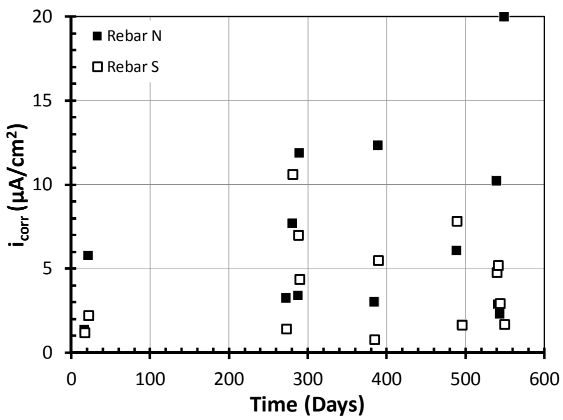

f) Measured corrosion current densities

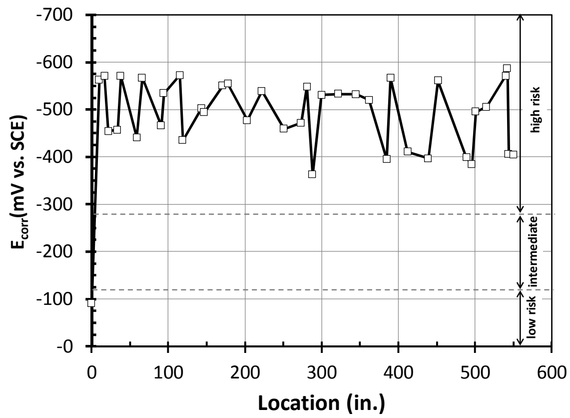

g) Average measured half-cell potentials

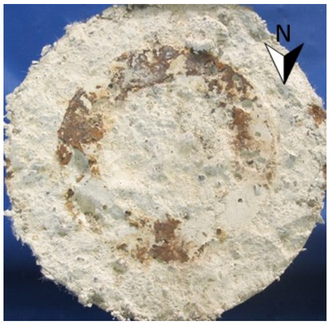

h) Sacrificial element of sensor S1-4 after autopsy

i) Rebar sections at vicinity of sensor S1-4

Figure D-20(Continued): Details of sensor S1-4

Table D-20: Post-autopsy results of sensor S1-4

Time to corrosion of sacrificial washer (Days)		414
Max. width of crack crossing the embedded sensor (in.)		0.02
Rebar mass loss (%)	North	3.20
	South	2.57
Chloride ion concentration (ppm)	Line I	2018
	Line J	1783

D.3.5 Sensor S1-5

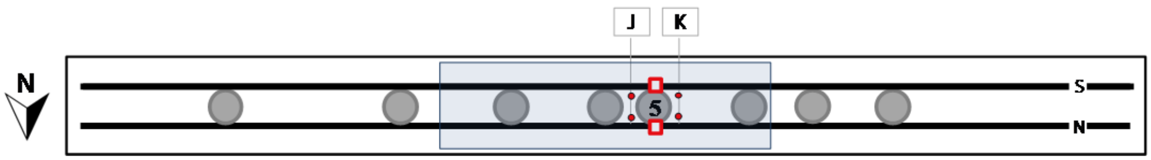

a) Locations of sensor S1-5, half-cell and LPR measurement points, and concrete powder samples

b)Sensor S1-5 before concrete casting

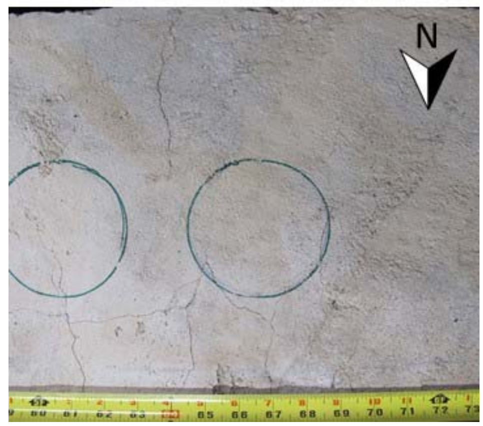

c)Surface Cracks in vicinity of S1-5

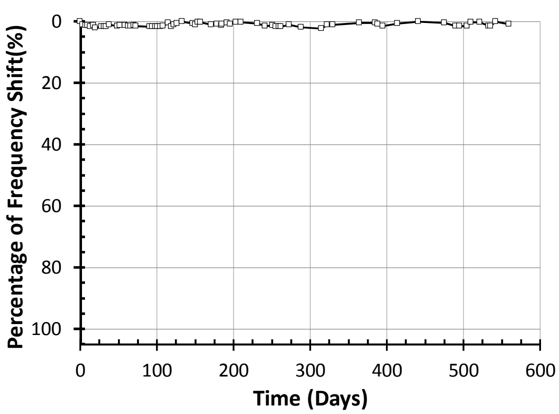

d) Shift in resonant frequency of S1-5

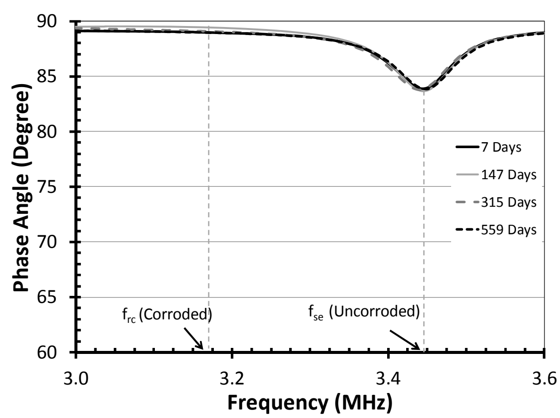

e) Measured phase response of S1-5 in selected days

Figure D-21: Details of sensor S1-5

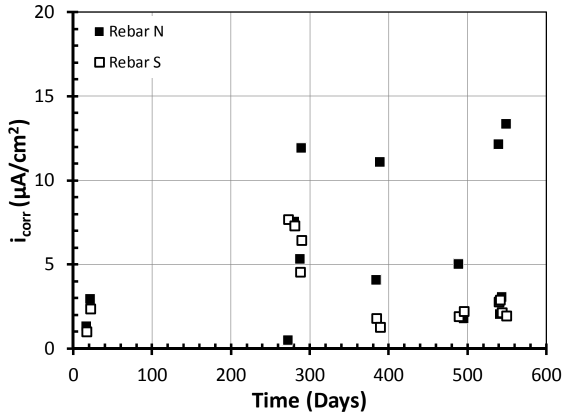

f) Measured corrosion current densities

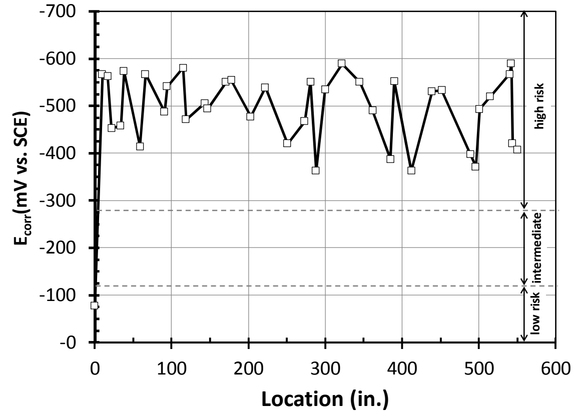

g) Average measured half-cell potentials

h) Sacrificial element of sensor S1-5 after autopsy

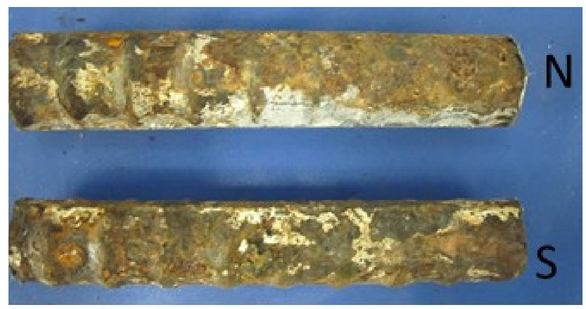

i) Rebar sections at vicinity of sensor S1-5

Figure D-21(Continued): Details of sensor S1-5

Table D-21: Post-autopsy results of sensor S1-5

Time to corrosion of sacrificial washer (Days)		Uncorroded
Max. width of crack crossing the embedded sensor (in.)		None
Rebar mass loss (%)	North	4.41
	South	2.93
Chloride ion concentration (ppm)	Line J	1783
	Line K	3098

D.3.6 Sensor S1-6

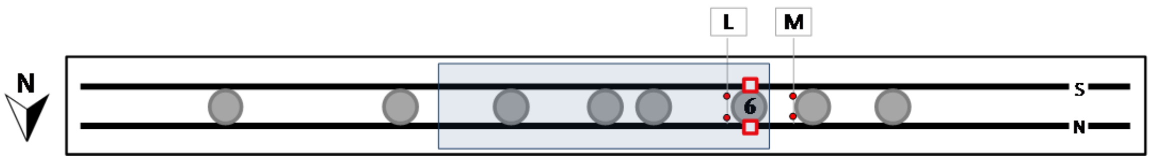

a) Locations of sensor S1-6, half-cell and LPR measurement points, and concrete powder samples

b)Sensor S1-6 before concrete casting

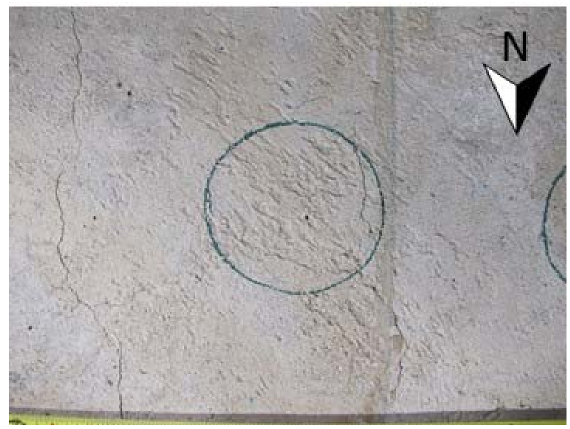

c)Surface Cracks in vicinity of S1-6

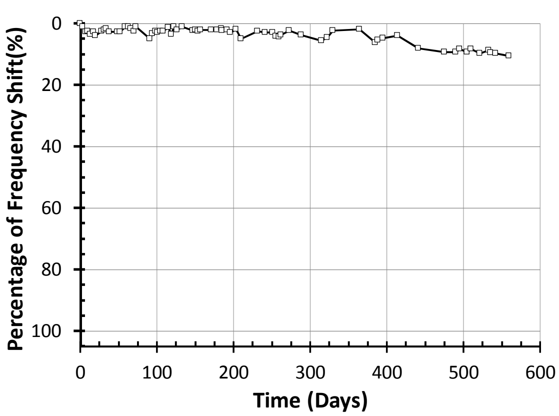

d) Shift in resonant frequency of S1-6

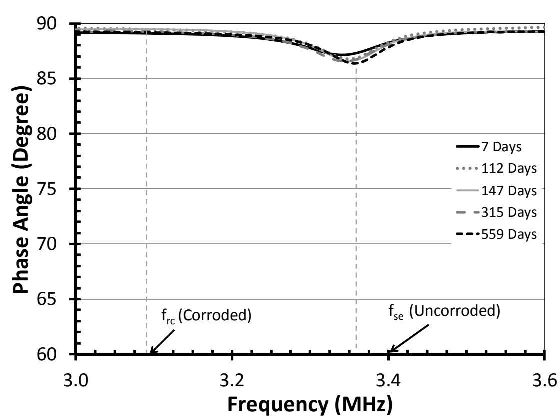

e) Measured phase response of S1-6 in selected days

Figure D-22: Details of sensor S1-6

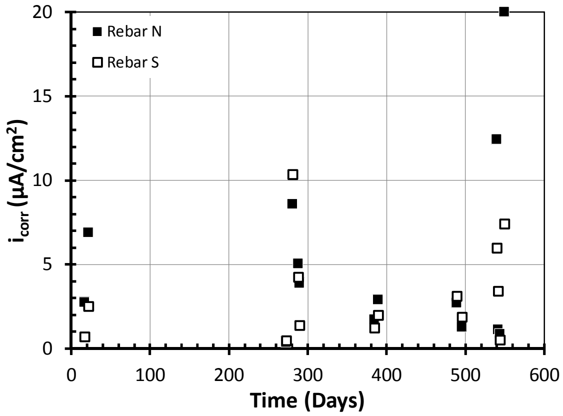

f) Measured corrosion current densities

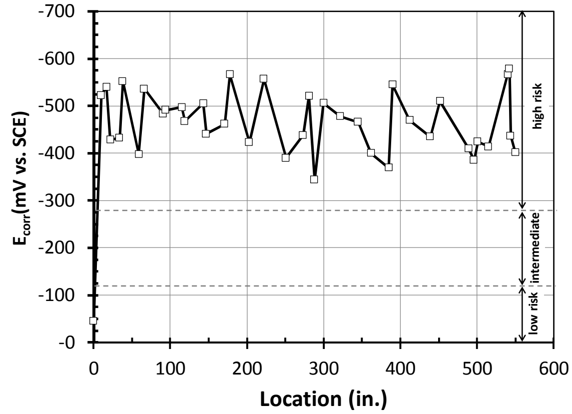

g) Average measured half-cell potentials

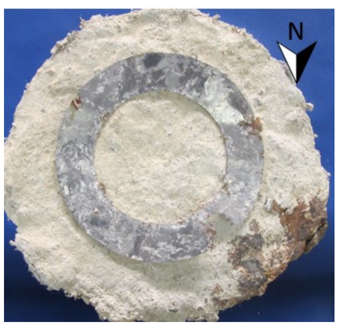

h) Sacrificial element of sensor S1-6 after autopsy

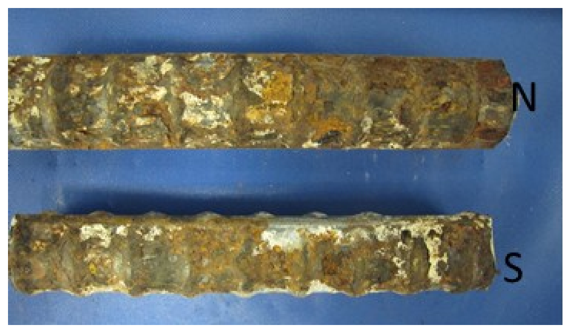

i) Rebar sections at vicinity of sensor S1-6

Figure D-22(Continued): Details of sensor S1-6

Table D-22: Post-autopsy results of sensor S1-6

Time to corrosion of sacrificial washer (Days)		In transition
Max. width of crack crossing the embedded sensor (in.)		0.02
Rebar mass loss (%)	North	4.28
	South	1.01
Chloride ion concentration (ppm)	Line L	2772
	Line M	2637

D.3.7 Sensor S1-7

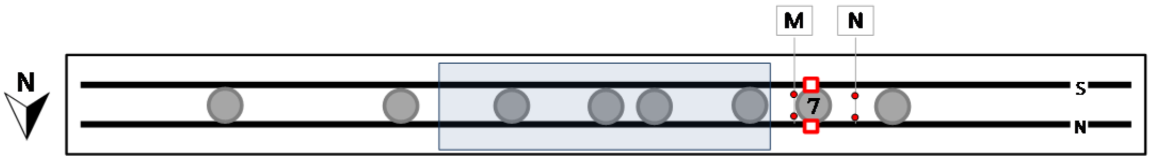

a) Locations of sensor S1-7, half-cell and LPR measurement points, and concrete powder samples

b)Sensor S1-7 before concrete casting

c)Surface Cracks in vicinity of S1-7

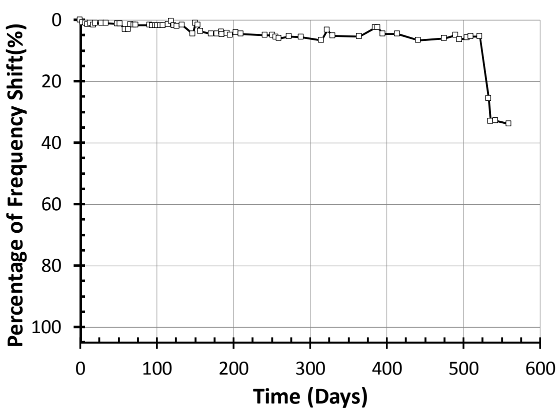

d) Shift in resonant frequency of S1-7

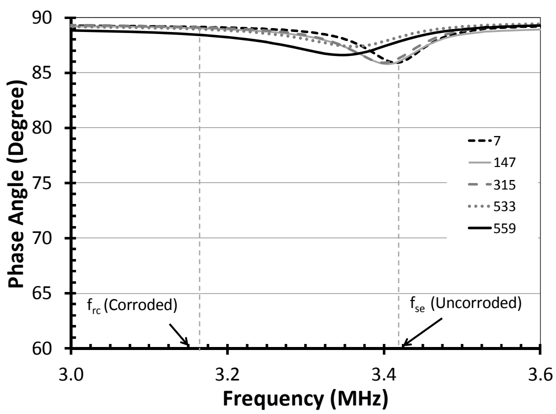

e) Measured phase response of S1-7 in selected days

Figure D-23: Details of sensor S1-7

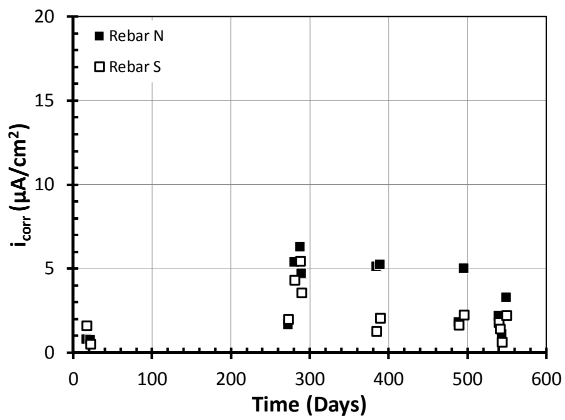

f) Measured corrosion current densities

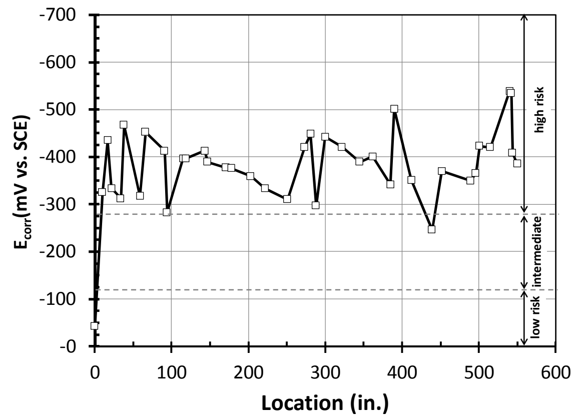

g) Average measured half-cell potentials

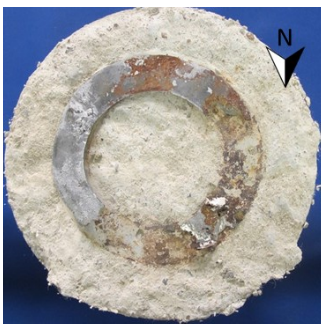

h) Sacrificial element of sensor S1-7 after autopsy

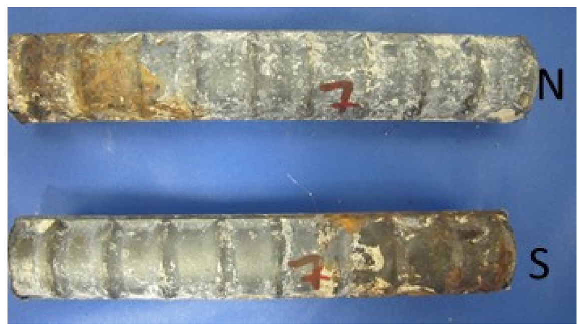

i) Rebar sections at vicinity of sensor S1-7

Figure D-23 (Continued): Details of sensor S1-7

Table D-23: Post-autopsy results of sensor S1-7

Time to corrosion of sacrificial washer (Days)		In transition
Max. width of crack crossing the embedded sensor (in.)		0.02
Rebar mass loss (%)	North	1.58
	South	0.88
Chloride ion concentration (ppm)	Line M	2637
	Line N	1499

D.3.8 Sensor S1-8

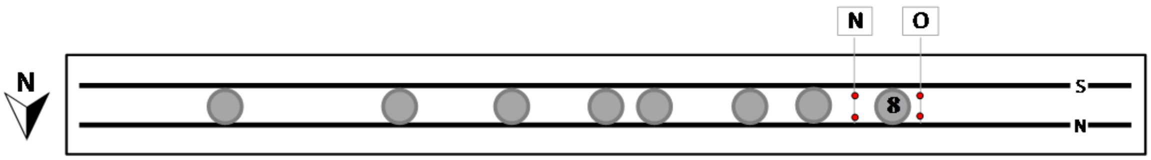

a) Locations of sensor S1-8, half-cell and LPR measurement points, and concrete powder samples

b)Sensor S1-8 before concrete casting

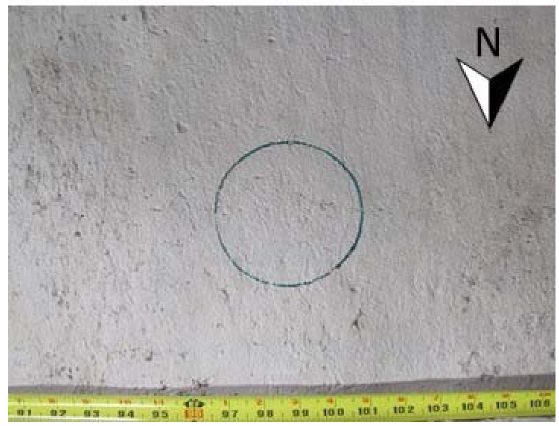

c)Surface Cracks in vicinity of S1-8

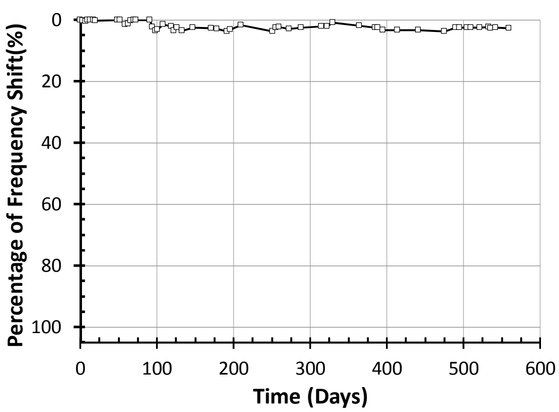

d) Shift in resonant frequency of S1-8

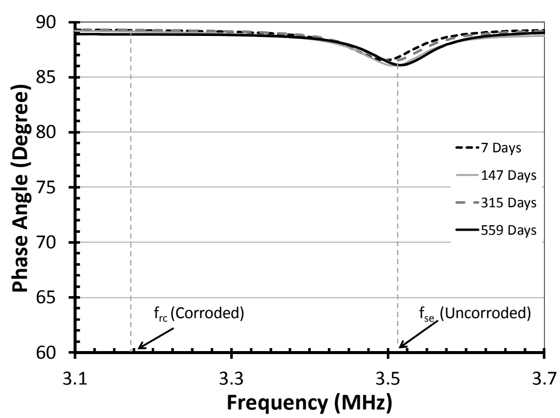

e) Measured phase response of S1-8 in selected days

Figure D-24: Details of sensor S1-8

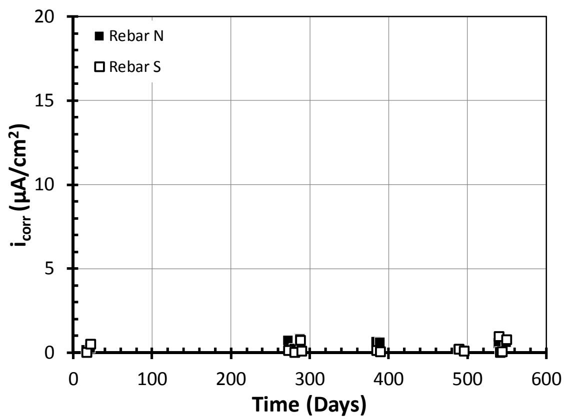

f) Measured corrosion current densities

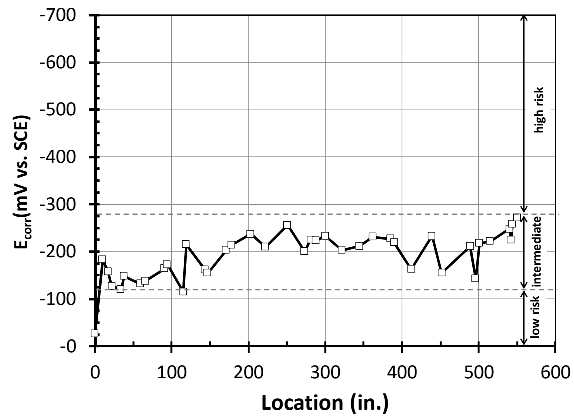

g) Average measured half-cell potentials

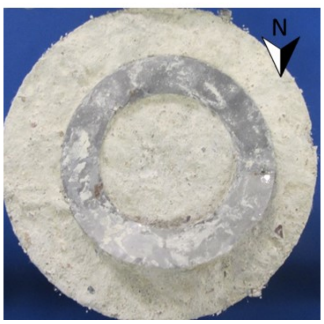

h) Sacrificial element of sensor S1-8 after autopsy

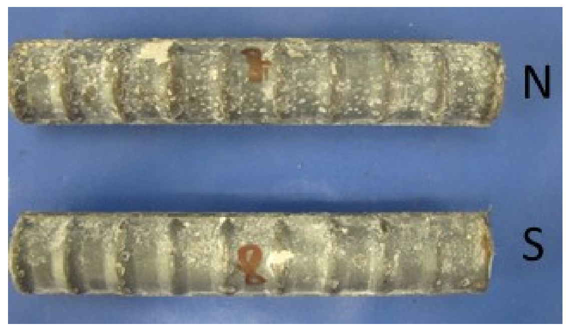

i) Rebar sections at vicinity of sensor S1-8

Figure D-24 (Continued): Details of sensor S1-8

Table D-24: Post-autopsy results of sensor S1-8

Time to corrosion of sacrificial washer (Days)		Uncorroded
Max. width of crack crossing the embedded sensor (in.)		0.002
Rebar mass loss (%)	North	0.12
	South	0.18
Chloride ion concentration (ppm)	Line N	1499
	Line O	746

D.4 SENSORS EMBEDDED IN SLAB S2

D.4.1 Sensor S2-1

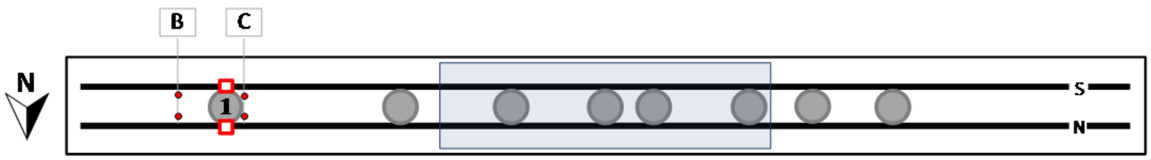

a) Locations of sensor S2-1, half-cell and LPR measurement points, and concrete powder samples

b)Sensor S2-1 before concrete casting

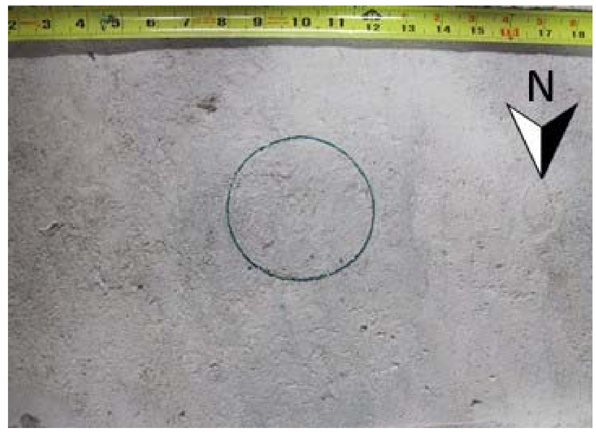

c)Surface Cracks in vicinity of S2-1

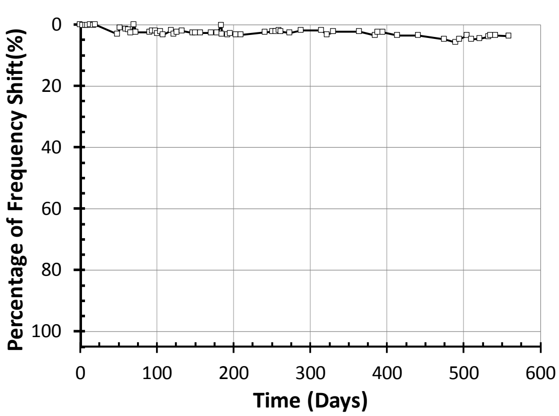

d) Shift in resonant frequency of S2-1

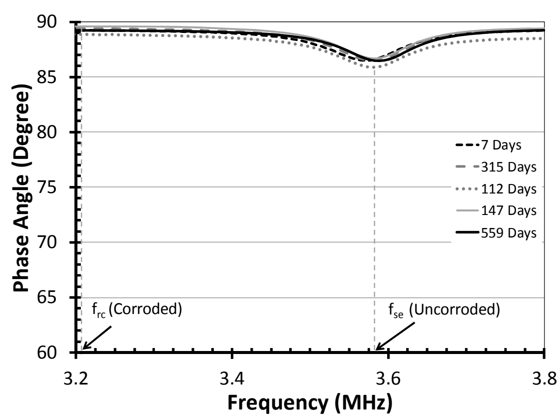

e) Measured phase response of S2-1 in selected days

Figure D-25: Details of sensor S2-1

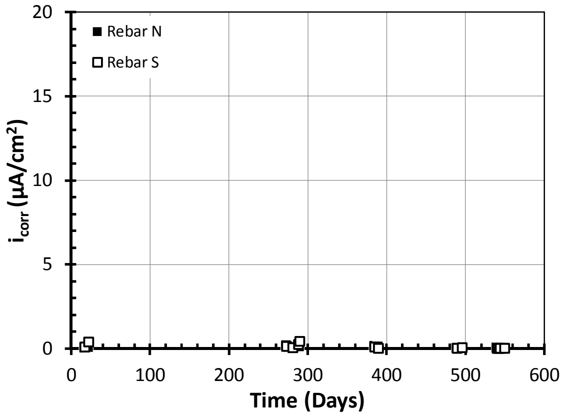

f) Measured corrosion current densities

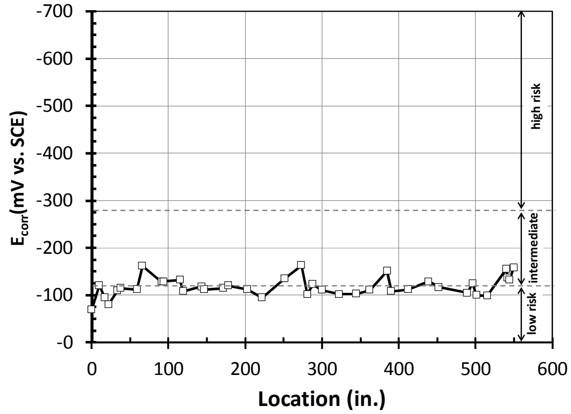

g) Average measured half-cell potentials

h) Sacrificial element of sensor S2-1 after autopsy

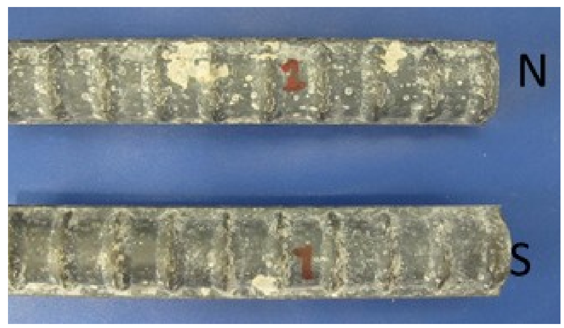

i) Rebar sections at vicinity of sensor S2-1

Figure D-25(Continued): Details of sensor S2-1

Table D-25: Post-autopsy results of sensor S2-1

Time to corrosion of sacrificial washer (Days)		Uncorroded
Max. width of crack crossing the embedded sensor (in.)		0.002
Rebar mass loss (%)	North	0.13
	South	0.14
Chloride ion concentration (ppm)	Line B	128
	Line C	144

D.4.2 Sensor S2-2

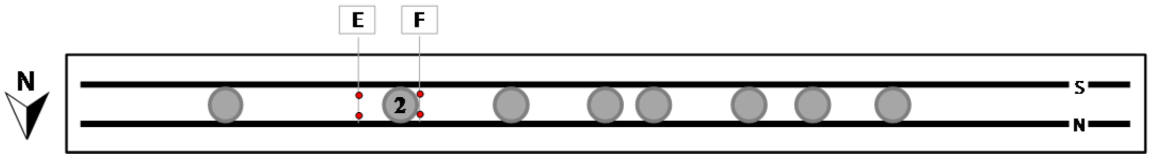

a) Locations of sensor S2-2, half-cell and LPR measurement points, and concrete powder samples

b)Sensor S2-2 before concrete casting

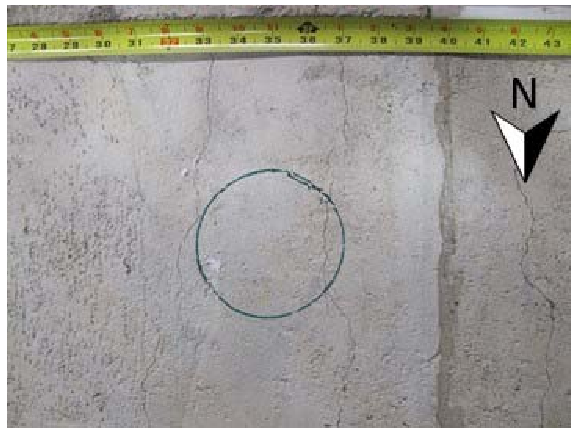

c)Surface Cracks in vicinity of S2-2

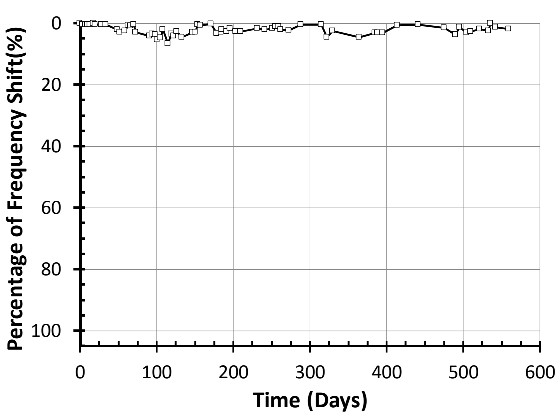

d) Shift in resonant frequency of S2-2

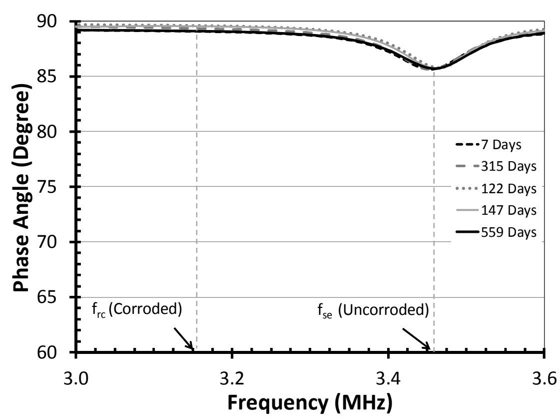

e) Measured phase response of S2-2 in selected days

Figure D-26: Details of sensor S2-2

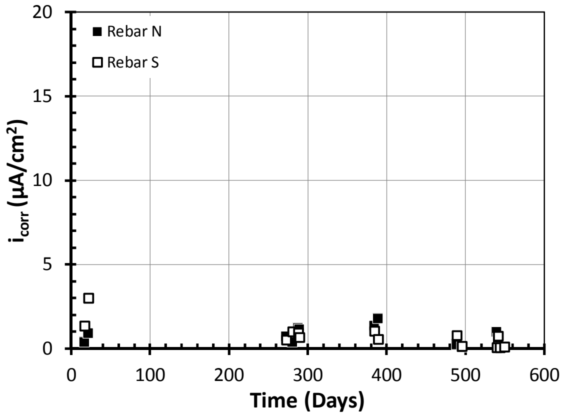

f) Measured corrosion current densities

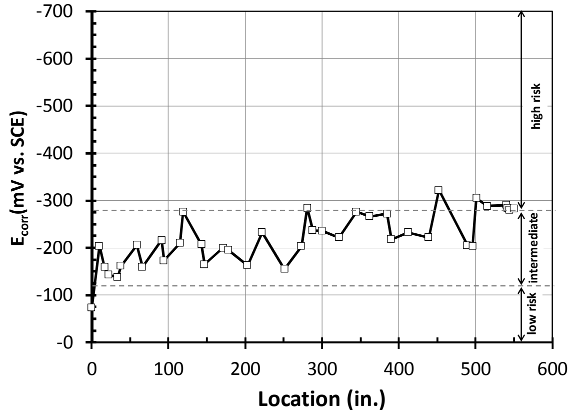

g) Average measured half-cell potentials

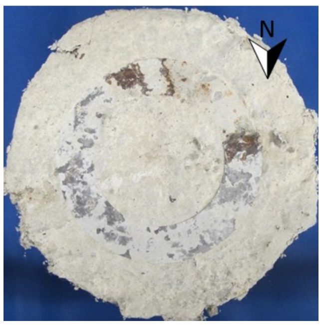

h) Sacrificial element of sensor S2-2 after autopsy

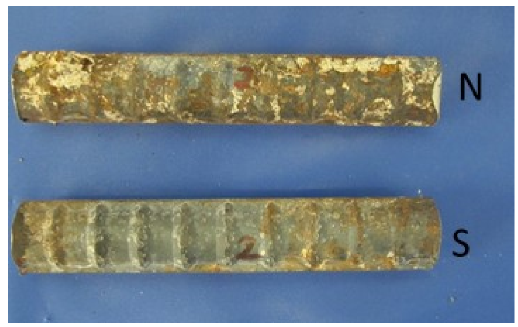

i) Rebar sections at vicinity of sensor S2-2

Figure D-26 (Continued): Details of sensor S2-2

Table D-26: Post-autopsy results of sensor S2-2

Time to corrosion of sacrificial washer (Days)		Uncorroded
Max. width of crack crossing the embedded sensor (in.)		0.025
Rebar mass loss (%)	North	0.93
	South	0.47
Chloride ion concentration (ppm)	Line E	1152
	Line F	1531

D.4.3 Sensor S2-3

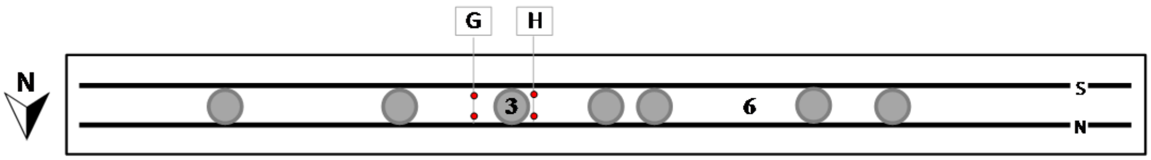

a) Locations of sensor S2-3, half-cell and LPR measurement points, and concrete powder samples

b)Sensor S2-3 before concrete casting

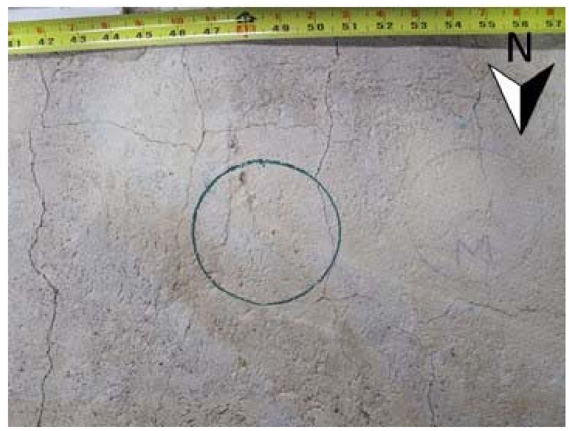

c)Surface Cracks in vicinity of S2-3

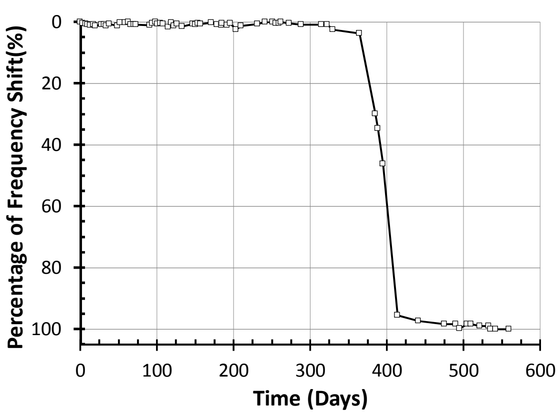

d) Shift in resonant frequency of S2-3

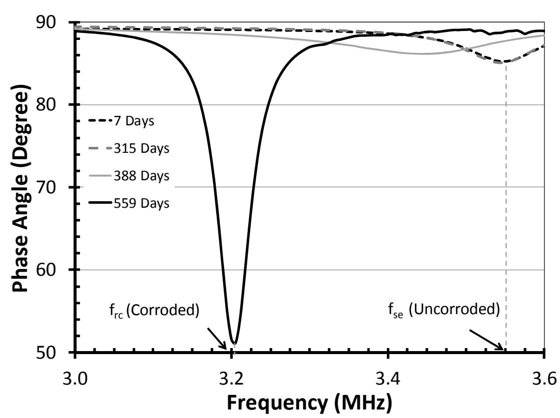

e) Measured phase response of S2-3 in selected days

Figure D-27: Details of sensor S2-3

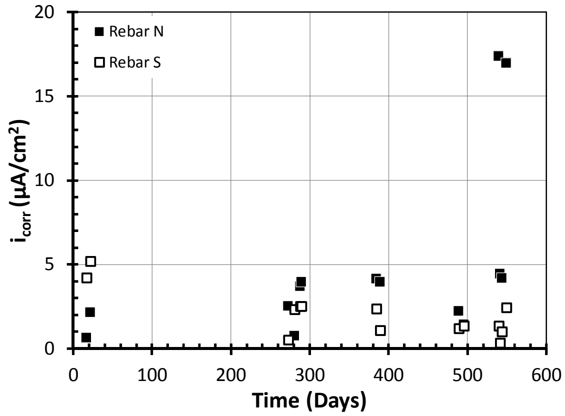

f) Measured corrosion current densities

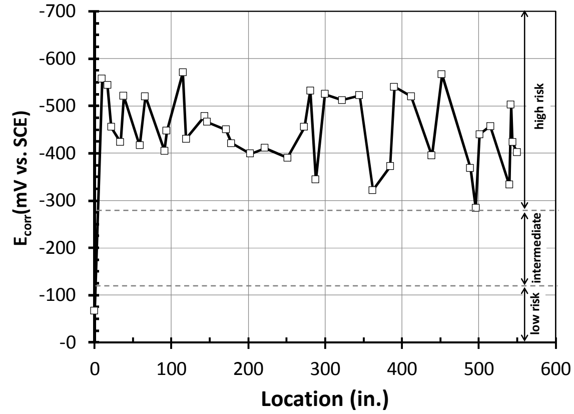

g) Average measured half-cell potentials

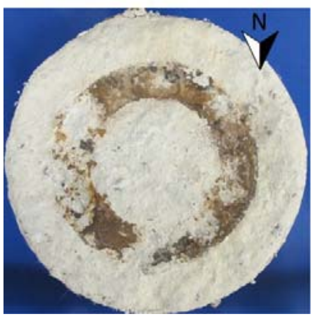

h) Sacrificial element of sensor S2-3 after autopsy

i) Rebar sections at vicinity of sensor S2-3

Figure D-27 (Continued): Details of sensor S2-3

Table D-27: Post-autopsy results of sensor S2-3

Time to corrosion of sacrificial washer (Days)		441
Max. width of crack crossing the embedded sensor (in.)		0.03
Rebar mass loss (%)	North	2.57
	South	2.86
Chloride ion concentration (ppm)	Line G	2141
	Line H	2146

D.4.4 Sensor S2-4

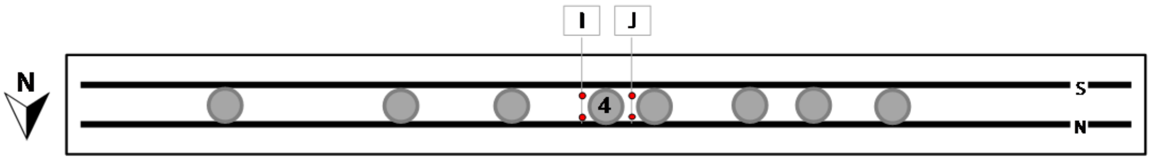

a) Locations of sensor S2-4, half-cell and LPR measurement points, and concrete powder samples

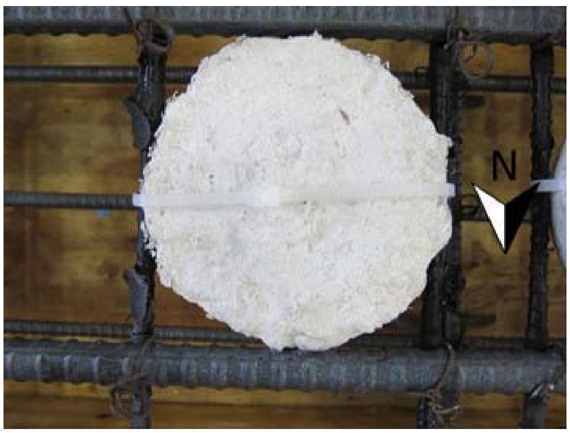

b)Sensor S2-4 before concrete casting

c)Surface Cracks in vicinity of S2-4

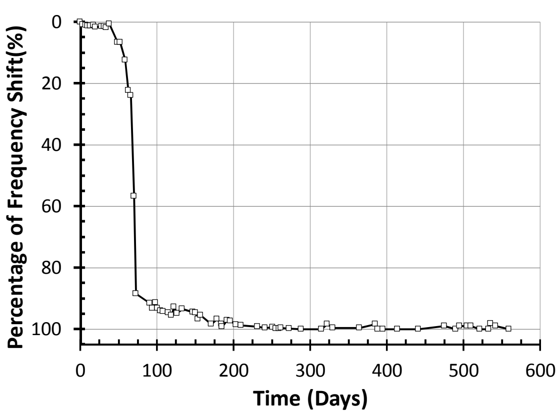

d) Shift in resonant frequency of S2-4

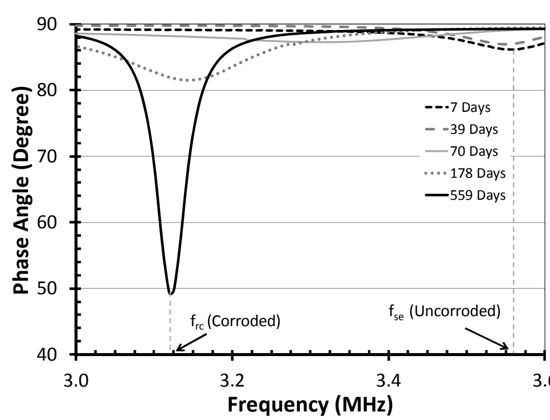

e) Measured phase response of S2-4 in selected days

Figure D-28: Details of sensor S2-4

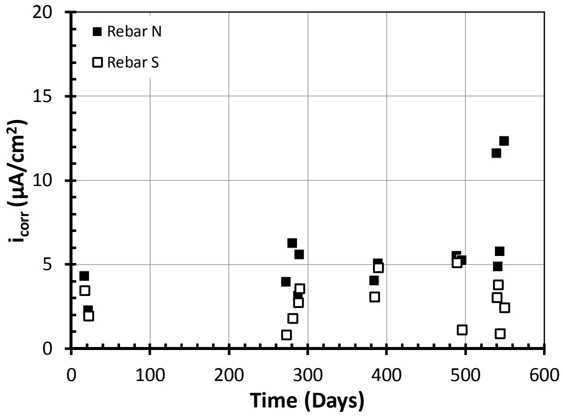

f) Measured corrosion current densities

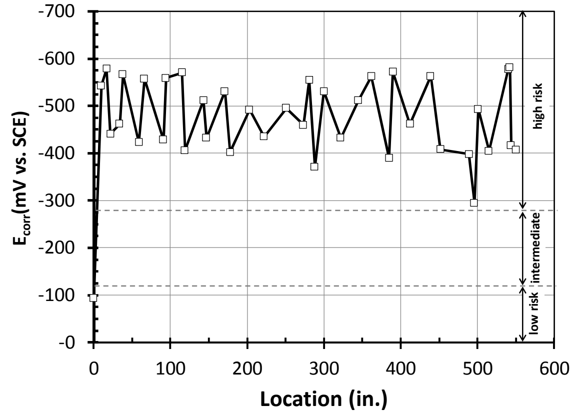

g) Average measured half-cell potentials

h) Sacrificial element of sensor S2-4 after autopsy

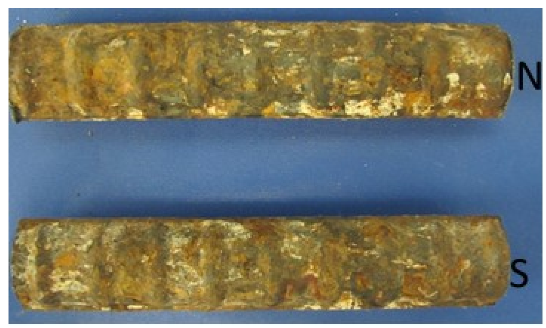

i) Rebar sections at vicinity of sensor S2-4

Figure D-28(Continued): Details of sensor S2-4

Table D-28: Post-autopsy results of sensor S2-4

Time to corrosion of sacrificial washer (Days)		171
Max. width of crack crossing the embedded sensor (in.)		0.03
Rebar mass loss (%)	North	5.70
	South	3.93
Chloride ion concentration (ppm)	Line I	1593
	Line J	1902

D.4.5 Sensor S2-5

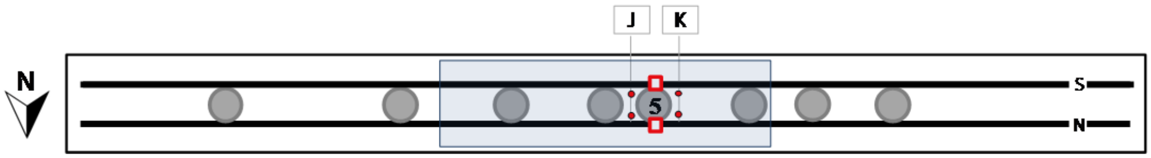

a) Locations of sensor S2-5, half-cell and LPR measurement points, and concrete powder samples

b) Sensor S2-5 before concrete casting

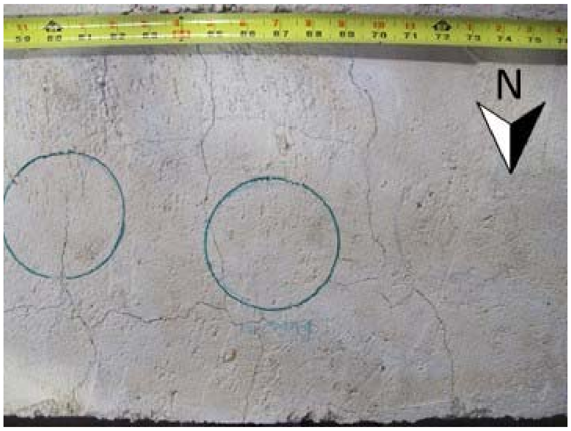

c)Surface Cracks in vicinity of S2-5

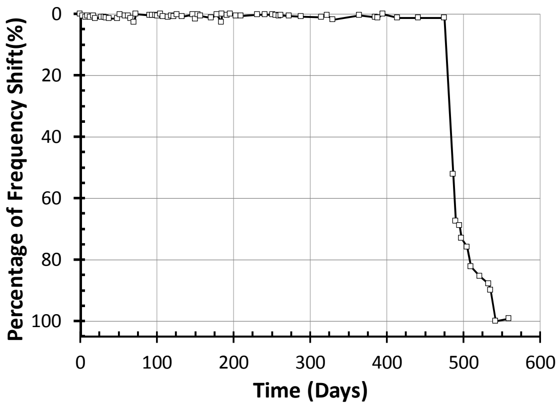

d) Shift in resonant frequency of S2-5

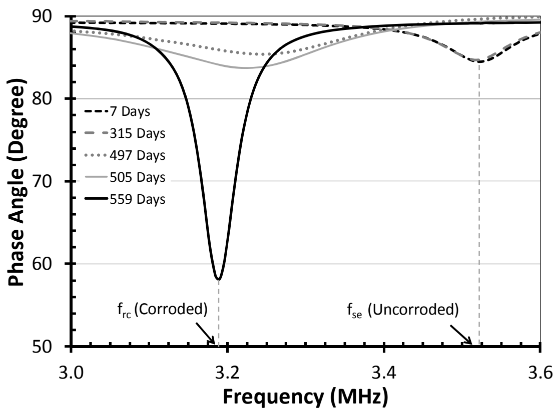

e) Measured phase response of S2-5 in selected days

Figure D-29: Details of sensor S2-5

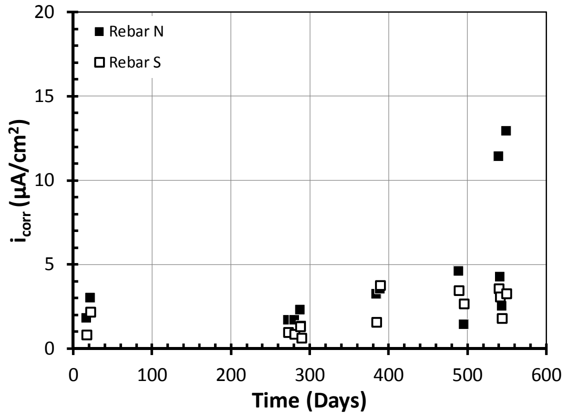

f) Measured corrosion current densities

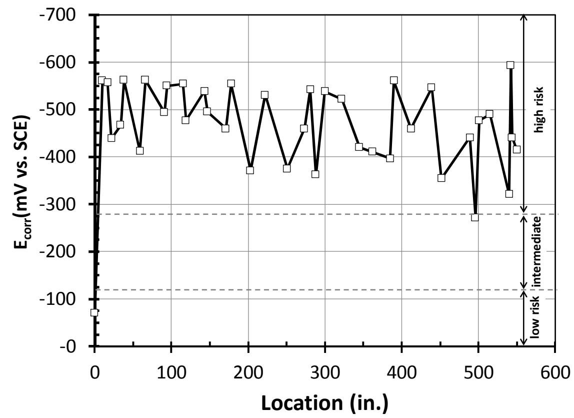

g) Average measured half-cell potentials

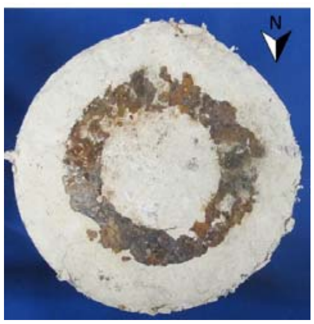

h) Sacrificial element of sensor S2-5 after autopsy

i) Rebar sections at vicinity of sensor S2-5

Figure D-29 (Continued): Details of sensor S2-5

Table D-29: Post-autopsy results of sensor S2-5

Time to corrosion of sacrificial washer (Days)		559
Max. width of crack crossing the embedded sensor (in.)		0.02
Rebar mass loss (%)	North	4.0
	South	2.27
Chloride ion concentration (ppm)	Line J	1902
	Line K	2728

D.4.6 Sensor S2-6

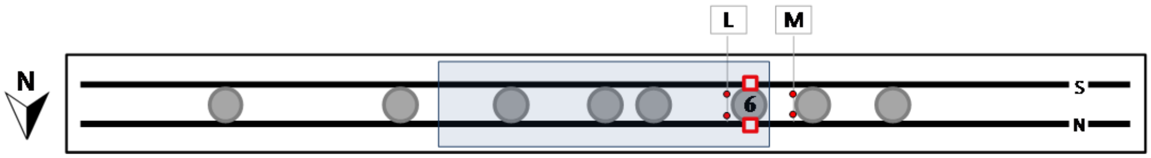

a) Locations of sensor S2-6, half-cell and LPR measurement points, and concrete powder samples

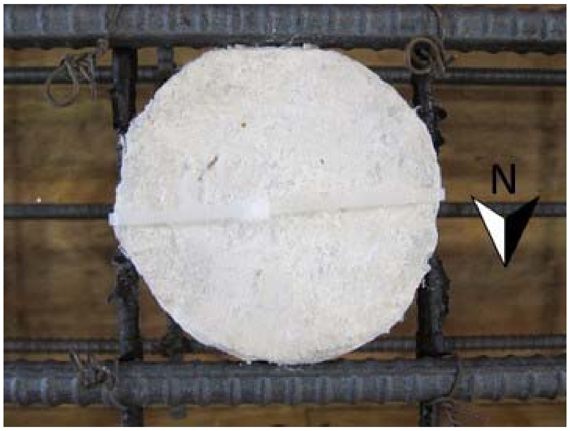

b)Sensor S2-6 before concrete casting

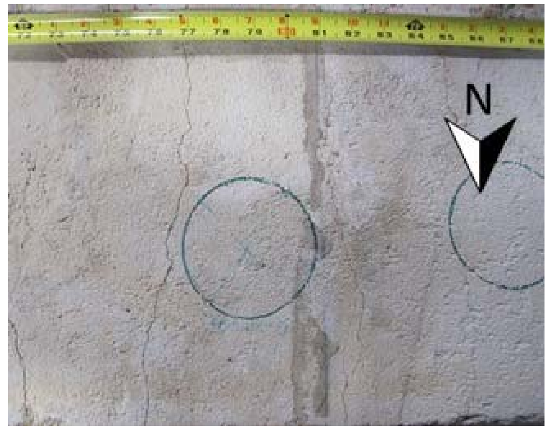

c)Surface Cracks in vicinity of S2-6

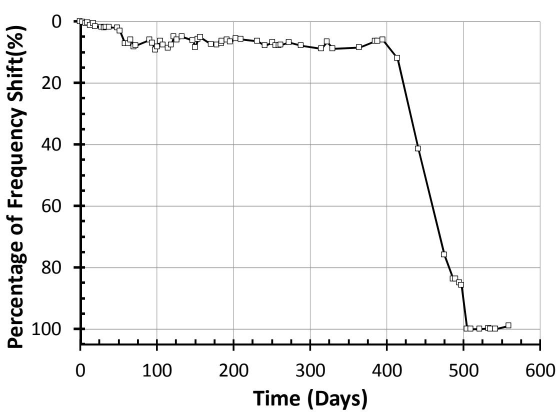

d) Shift in resonant frequency of S2-6

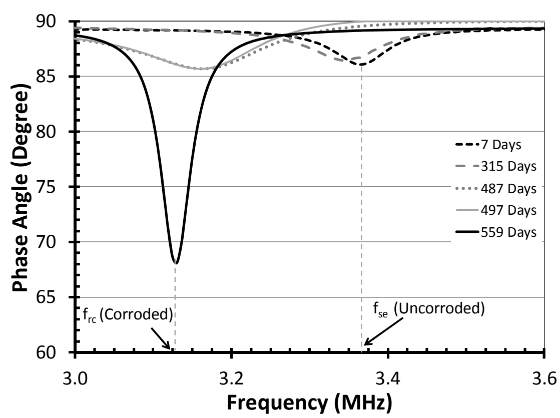

e) Measured phase response of S2-6 in selected days

Figure D-30: Details of sensor S2-6

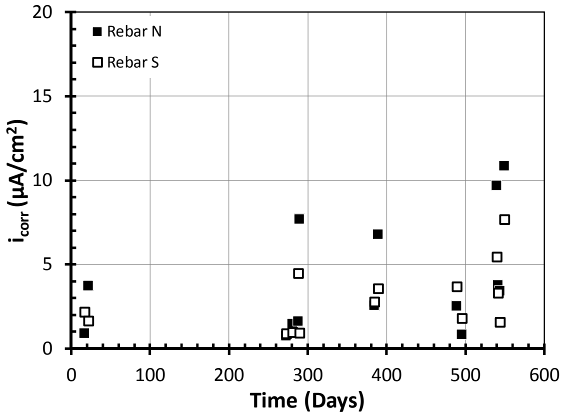

f) Measured corrosion current densities

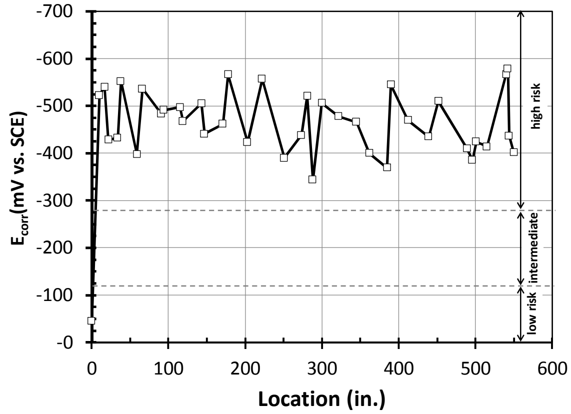

g) Average measured half-cell potentials

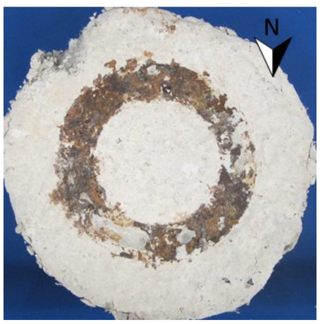

h) Sacrificial element of sensor S2-6 after autopsy

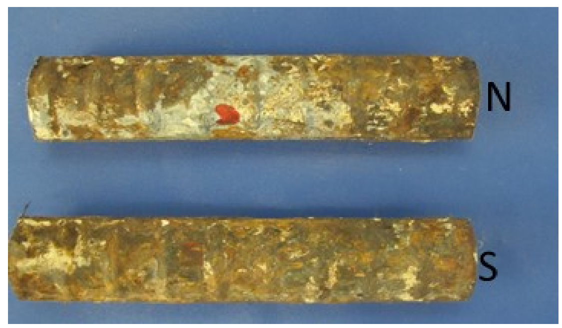

i) Rebar sections at vicinity of sensor S2-6

Figure D-30 (Continued): Details of sensor S2-6

Table D-30: Post-autopsy results of sensor S2-6

Time to corrosion of sacrificial washer (Days)		510
Max. width of crack crossing the embedded sensor (in.)		0.03
Rebar mass loss (%)	North	0.9
	South	1.5
Chloride ion concentration (ppm)	Line L	2160
	Line M	1525

D.4.7 Sensor S2-7

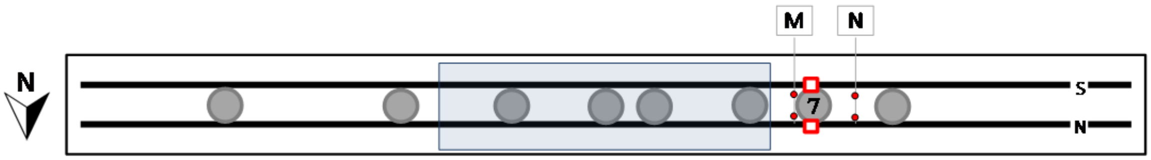

a) Locations of sensor S2-7, half-cell and LPR measurement points, and concrete powder samples

b)Sensor S2-7 before concrete casting

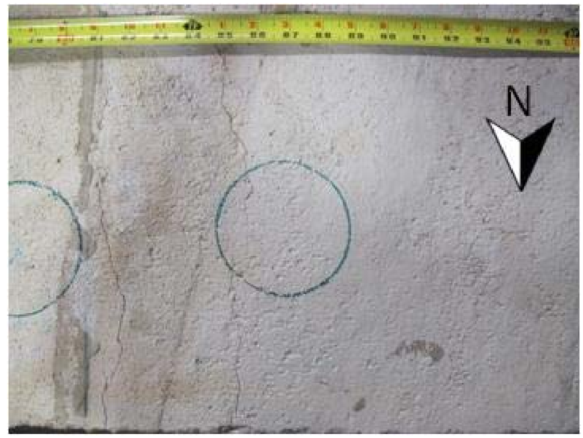

c)Surface Cracks in vicinity of S2-7

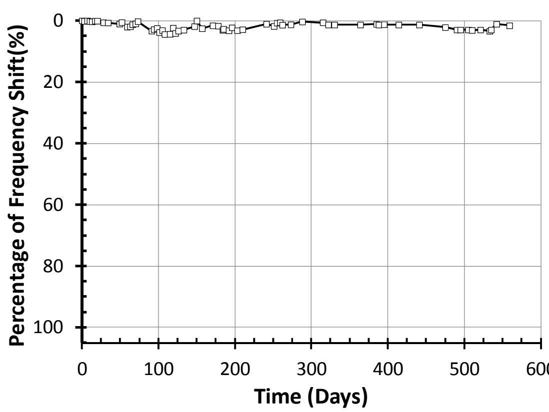

d) Shift in resonant frequency of S2-7

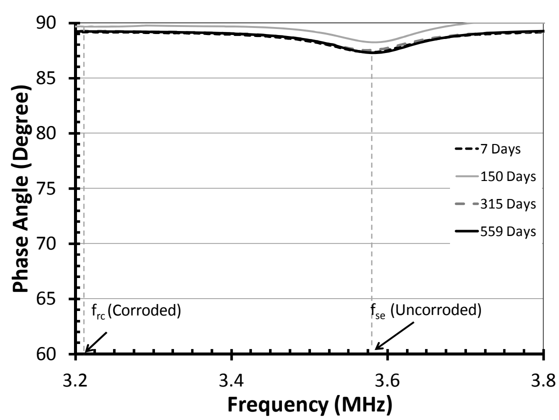

e) Measured phase response of S2-7 in selected days

Figure D-31: Details of sensor S2-7

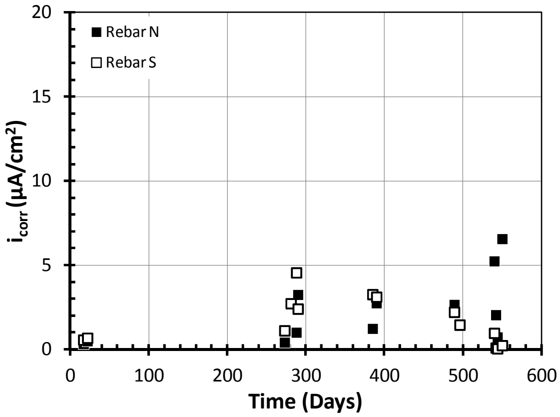

f) Measured corrosion current densities

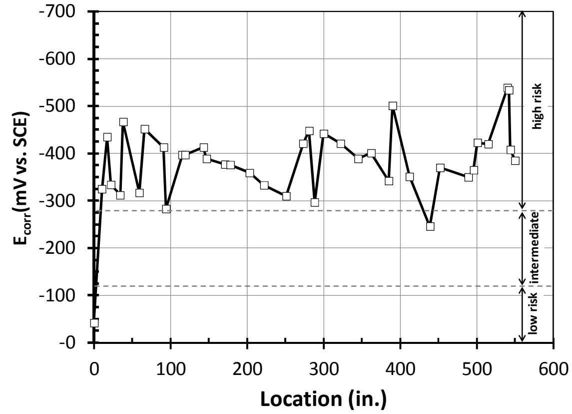

g) Average measured half-cell potentials

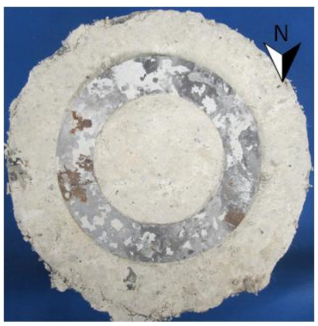

h) Sacrificial element of sensor S2-7 after autopsy

i) Rebar sections at vicinity of sensor S2-7

Figure D-31(Continued): Details of sensor S2-7

Table D-31: Post-autopsy results of sensor S2-7

Time to corrosion of sacrificial washer (Days)		Uncorroded
Max. width of crack crossing the embedded sensor (in.)		0.016
Rebar mass loss (%)	North	0.81
	South	0.58
Chloride ion concentration (ppm)	Line M	1525
	Line N	1223

D.4.8 Sensor S2-8

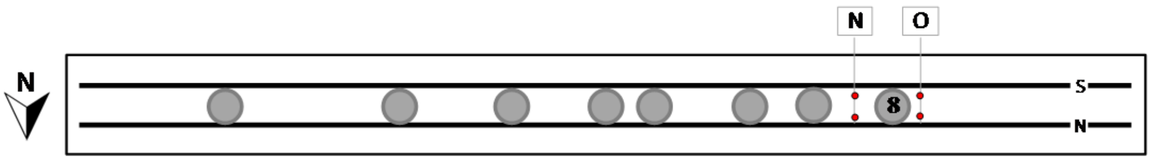

a) Locations of sensor S2-8, half-cell and LPR measurement points, and concrete powder samples

b)Sensor S2-8 before concrete casting

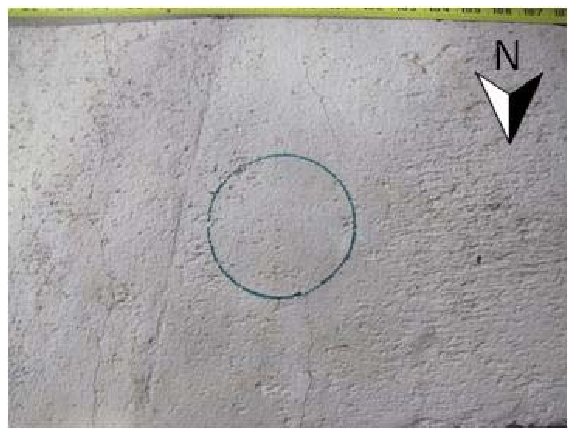

c)Surface Cracks in vicinity of S2-8

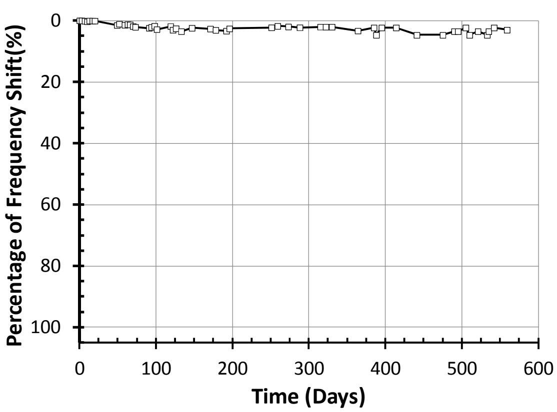

d) Shift in resonant frequency of S2-8

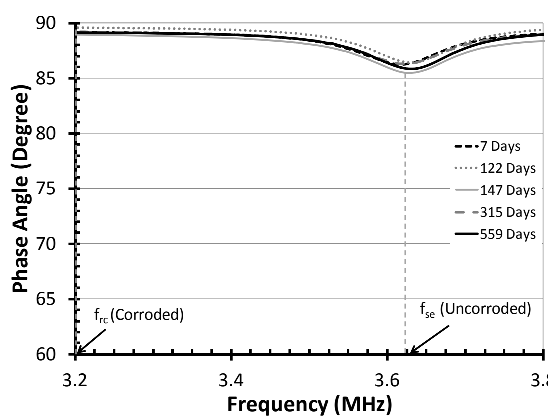

e) Measured phase response of S2-8 in selected days

Figure D-32: Details of sensor S2-8

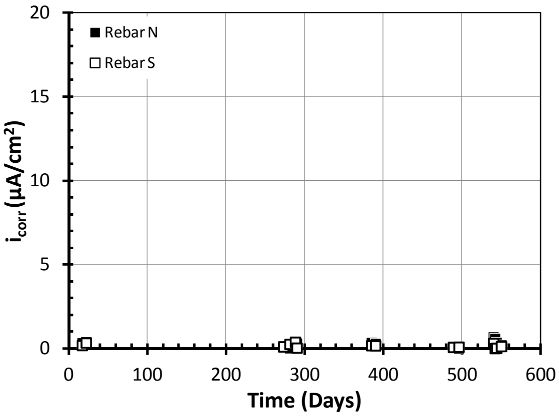

f) Measured corrosion current densities

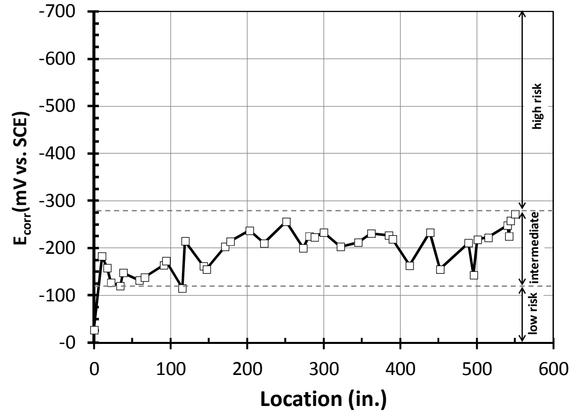

g) Average measured half-cell potentials

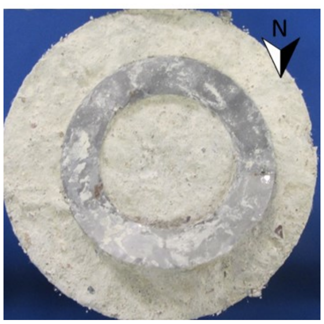

h) Sacrificial element of sensor S2-8 after autopsy

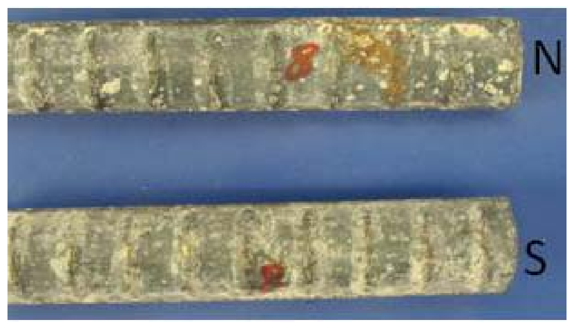

i) Rebar sections at vicinity of sensor S2-8

Figure D-32 (Continued): Details of sensor S2-8

Table D-32: Post-autopsy results of sensor S2-8

Time to corrosion of sacrificial washer (Days)		Uncorroded
Max. width of crack crossing the embedded sensor (in.)		0.002
Rebar mass loss (%)	North	0.17
	South	0.18
Chloride ion concentration (ppm)	Line N	1223
	Line O	1057

References

Abu Yosef, Ali, Praveenkumar Pasupathy, Sharon Wood, and Dean Neikirk. "Detection of multiple corrosion thresholds in reinforced concrete structures using passive sensors." *Proc. SPIE 8347*. San Diego, CA: Society of Photo-Optical Instrumentation Engineers, 2012.

Abu Yousef, Ali E., Praveenkumar Pasupathy, Sharon L. Wood, and Dean P. Neikirk. "Low-cost passive sensors for monitoring corrosion in concrete structures." *Sensors and Smart Structures Technologies for Civil, Mechanical, and Aerospace Systems*. San Diego, California: International Society for Optical Engineering, 2011.

Abu Yousef, Ali, Praveenkumar Pasupathy, Sharon L. Wood, and Dean P. Neikirk. "Resonant sensors for detecting corrosion in concrete bridges." *Transportation Research Record: Journal of the Transportation Research Board* (Transportation Research Board of the National Academies) 2201/2010 (December 2010): 19-26.

ACI 222R. *Protection of Metals in Concrete Against Corrosion.* American Concrete Institute, 2010.

Agrawal, A., et al. "Remote Corrsion Monitoring Systems for Highway Bridges." *Practice Periodical on Structural Design and Construction* 14, no. 4 (2009): 152-158.

Andrade, C., and A. Castillo. "Evolution of reinforcment corrosion due to climatic variations." *Materials and Corrosion* 54 (2003): 379-386.

Andrade, C., C. Alonso, and J. Sarria. "Corrosion rate evaluation in concrete structures exposed to the atmosphere." *Cement and Concrete Composites* (24) 1 (2002): 55-64.

Andrade, C., et al. "Recommendations of RILEM TC-154-EMC:"Electrochemical techniques for measuring metallic corrosion"." *Materials and Structures*, 2004: 623-643.

Andringa , Mathew M. *Unpowered wireless sensors for structural health monitoring.* Austin, TX: Department of Electrical and Computer Engineering, Univeristy of Texas at Austin, 2006.

Angst, U., B. Elsener, C. Larsen, and O. Vennesland. "Chloride induced reinforcment corrosion: electrochemical monitoring of initiation stage and chloride threshold values." *Corrosion Science* 53 (2011): 1451-1464.

Ansuini, Frank, and James Dimond. "Factors affecting the accuracyof reference electrodes." *Materials performance* 33, no. 11 (November 1994): 14-17.

ANSYS Inc. "Maxwell 3D User's Guidel." Canonsburg, PA: Southpointe, 2010.

ANSYS Inc. "Simplorer 11.0 User's Guide." Canonsburg, PA, 2012.

ASCE. *Report card for America's infrastructure*. Washington, D.C.: Ameican Society of Civil Engineers, 2013.

ASTM C1152/C1152M. *Standard test method for acid-soluble chloride in mortar and concrete.* Standard, West Conshohocken: ASTM International, 2004, pp.4.

ASTM C876. *Standard Test Methods for Corrosion Potentials of Uncoated Reinforcing Steel in Concrete.* West Conshohocken: ASTM International, 2009, pp. 7.

ASTM D 4580. *Standard practice for measuring delaminations in concrete bridge decks by sounding.* Standard, West Conshohocken, PA: ASTM International, 2007, 4 pp.

ASTM G1. *Standard practice for preparing, cleaning, and evaluating corrosion test specimens.* Standard, West Conshohocken, PA: ASTM International, 2003.

Bertolini, Luca, Bernhard Elsener, Pietro Pedeferri, and Rob Polder. *Corrosion of steel in concrete.* Weinheim: Wiley-VCH, 2004.

Bhadra, S., D. Thomson, and G. Bridges. "A wireless embedded passive sensor for monitoring the corrosion potential of reinforcing steel." *Smart materials and structures* 22 (2013): 10 pp.

Birdsell, Edward, Jinwoo Park, and Mark Allen. "Wireless ceramic sensors operating in high temprature environments." *40 th AIAA/ASME/SAE/ASEE Joint Propulsion Conference. 2004.* Fort Lauderdale, FL: American Institute of Aeronautics and Astronautics, 2004.

Branco, Fernando, and Jorge De Brito. *Handbook of concrete bridge management.* ASCE Publications, 2004.

British Cement Association. *Development of an holistic approach to ensure the durability of new concrete construction.* Camberley, UK: BCA, 1997, 81.

Broomfield, J. *Corrosion of steel in concrete : understanding, investigation and repair.* Second. New York: Taylor and Francis, 2007.

Broomfield, J., J. Rodriguez, L. Ortega, and A. Garcia. "Corrosion rate measurements in reinforced concrete structures by a linear polarization device." *ACI Special Publication 151*, 1994: 163-181.

Broomfield, J., K. Davies, and K. Hladky. "The use of permenant corrosion monitoring in new and existing reinforced cocncrete structures." *Cement and Concrete Composites* 24 (2002): 27-34.

Brownjohn, J. "Structural health monitoring of civil infrastructure." *Philosophical transactions of the royal society A* 365 (2007): 589-622.

Cain, R., B. Carkhuff, P. Pandolfini, and F. Weiskopf. *Smart Aggregate Sensor Suite for Bridge Deck Measurements.* Baltimore, MD: Maryland State Highway Administration, 2003, 48 pp.

Carino, N. "Nondestructive techniques to investigate corrosion status in concrete structures." *Journal of performance of constructed facilities*, 1999: 96-106.

Chase, S., and J Laman. "Dynamics and field testing of bridges." *TRB Transportation in the new millennium*, 2000.

Chou, C. *Improvements to wireless, passive sensors for monitoring conditions within reinforced concrete structures.* M.S. Thesis, Department of Civil, Architectural and Environmental Engineering, University of Texas at Austin, 2010.

Chuang, J., D. Thomson, and G. Bridges. "Embeddable wireless strain sensor based on resonant RF cavities." *Review of scientific instruments* 76 (2005): 7.

Clark, M., D. McCann, and M. Forde. "Application of infrared thermography to the non-destructive testing of concrete and masonary bridges." *NDT & E International* 36, no. 4 (2003): 265-275.

Code of Federal Regulations, National Bridge Inspection Standards – 23CFR650. U.S. Government Printing Office via GPO Access, revised December 14, 2004, pp. 74419-74439.

Covino, B., S. Cramer, G. Holcomb, S. Bullard, and H. Laylor. "Postmortem of a failed bridge." *Concrete International* 21, no. 2 (1999): 39-45.

Dickerson, N. P. "Wireless corrosion sensors for reinforced concrete structures." M.S. Thesis, Department of Civil, Architectural and Environmental Engineering, University of Texas at Austin, 2005.

Dickerson, N. P., M. M. Andringa, J. M. Puryear, S. L. Wood, and D. P. Neikirk. "Wireless threshold sensors for detecting corrosion in reinforced concrete structures." *Smart Structures and Materials 2006: Sensors and Smart Structures Technologies for Civil, Mechanical, and Aerospace Systems* (International Society for Optical Engineering) 6174 (2006): 8 pp.

Dierks, E. *Design of electromagnetic vibration energy harvester for structural health monitoring of bridges employing wireless sensor networks.* MS Thesis, Austin, TX: The University of Texas at Austin, 2011.

Elsener, B., C. Andrade, J. Gulikers, R. Podler, and M. Raupach. "Half-cell potential measurements-potential mapping on reinforced cocncrete structures." *Materials and Structures*, 2003: 461-471.

Emmons, P, and D Sordyl. "The state of the concrete idustry, ana a vision for its future." *Concrete Repair bulletin*, 2006: 7-14.

Emmons, P. *Concrete repair and maintenance illustrated: Problem analysis, Repair strategy, Techniques.* 1993.

Engel, Thomas G, and Stacy Rohe. "A comparison of single-layer coaxial coil mutual inducatance calculations using finite-element and tabulated methods." *IEEE Transatcions on Magnetics* 42, no. 9 (2006): 2159-2163.

Farrar, Charles, and Keith Worden. "An introduction to structural health monitoring." *Philosophical transactions of the royal societ A* 365 (2007): 303-315.

Fasl, Jeremiah. "Estimating the Remaining Fatigue Life of Steel Bridges Using Field Measurements." PhD Dissertation, Department of Civil, Architechtural, and Environmental Engineering, University of Texas at Austin, Austin, TX, 2013.

Felic, Klaric, D Ng, and E. Skafidas. "Investigation of frequency dependent effects in inductive coils for implantable electronics." *IEEE Transactions on Magnetics* 49, no. 4 (2013): 1353-1360.

Feliu, S., J. Gonzalez, and C. Andrade. "Electochemical methods for on-site determinations of corrosion rates of rebars." In *Techniques to assess the corrosion activity of steel reinforced concrete structures,* edited by N S Berke, E Escalante, CK Nmai and D Whiting, 107-118. ASTM, 1996.

Feliu, Sebastian, Jose Gonzalez, and Carmen Andrade. "Electochemical methods for on-site determinations of corrosion rates of rebars." In *Techniques to assess the corrosion activity of steel reinforced concrete structures*, edited by N S Berke, E Escalante, CK Nmai and D Whiting, 107-118. ASTM, 1996.

FHWA. *Deficient bridges by state and highway system.* 2012. http://www.fhwa.dot.gov/bridge/deficient.cfm (accessed July 4, 2012).

Finkenzeller, K. *RFID handbook: Fundamentals and applications in contactless smart cards and identification.* London, UK: John Wiley & Sons Ltd., 2003.

Foroulis, Z., and H. Uhlig. "Effect of cold-work on corrosion of iron and steel in hydrochloric acid." *Journal of Electrochemical Society*, 1964: 552-528.

Fortner, B. "Technology: Embedded miniature sensors detect chloride in bridge decks." *Civil Engineering* (ASCE) 73, no. 6 (2003): 42-43.

French, C., C. Shield, H. Stolarski, B. Hedegaard, and B. Jilk. *Instrumentation, monitoring, and modeling of the I-35W bridge.* St. Paul, MN: Minnesota Department of Transportation, 2012, 352 pp.

Freytag, D., K. Kesner, R. Poston, and K. Bondy. "When bad things happen to good buildings." *ACI Special Publication 291*, 2012: 14 pp.

Gannon, Edward, and Philip Cady. "Condition Evaluation of Concrete Bridges Relative to Reinforcment Corrosion." Stratigic Highway Research Program, Washington, DC, 1992, 125 pp.

Garcia-Canton, J., A. Merlos, and A. Baldi. "A wireless LC chemical sensor based on high quality factor EIS capacitor." *Sensors and Actuators B* 126 (2007): 648-654.

Gowers, K., and S. Millard. "Measurement of concrete resistivity for assessment of corrosion severity of steel using Wenner technique." *ACI Materials Journal* 96, no. 5 (1999): 536-541.

Grantham, M. G., B. Herts, and J Broomfield. "The use of linear polarization corrosion rate measurements in aiding rehabilitation options for the deck slab of a reinforced concrete underground car park." *Construction and Building Materials* (Elsevier Science Ltd) 11, no. 4 (1997): 215-224.

Grizzle, K. M. "Development of a Wireless Sensor Used to Monitor Corrosion in Reinforced Concrete." MS Thesis, Department of Civil, Architectural, and Environmental Engineering, University of Texas at Austin, Austin, TX, 2003.

Grover, Frederick. *Inductance calculations, working formulas and tables.* New York, NY: Dover Publications, 1946.

Gu, P., and J. Beaudoin. "Obtaining effective half-cell potential measurements in reinforced concrete structures." *Construction Technology Update*, 1998: 4.

Gu, P., P. Carter, J. Beaudoin, and M. Arnott. "Validation of half-cell potential data from bridge decks." *Constrction repair*, 1996: 18-20.

Gucunski, Nenad, Francisco Romero, Sabine Kruschwitz, Ruediger Feldmann, Ahmed Abu-Hawash, and MArk Dunn. "Multiple Complementary Nondestructive Evaluation Technologies for Condition Assessment of Concrete Bridge Decks." *Journal of the Transportation Research Board* 2201 (2010): 34-44.

Halabe, Udaya, Hung-Liang Chen, Vasudev Bhandarkar, and Zahid Sami. "Detection of sub-surface anomalies in concrete bridge decks using ground penetrating radar." *ACI Materials Journal* 94, no. 5 (September-October 1997).

Hansson, Carolyn. "Comments on electrochemical measurements of the rate of corrosion of steel in concrete." *Cement and Concrete Research* 14 (1984): 574-584.

Hearn, George, Ronald Purvis, Paul Thompson, William Bushman, Kevin McGhee, and Wallace McKeel. *Bridge maintenance and management- A look to the future.* A3C06: Committee on Structures Maintenance and Management, Washington, DC: Transportation Research Board, 2002.

Huang, Ran, Jiang-Jhy Chang, and Jiann-Kuo Wu. "Correlation between corrosion potential and polarization resistance of rebar in concrete." *Materials Letters* 28 (1996): 445-450.

Jia, Y., and K. Sun. "Thick film wirless and powerless strain sensor." *SPIE Proceedings 6174.* San Diego, CA, 2006. 11 pp.

Johnson, P, A Couture, and R Nicolet. *Commission of inquiry into the collapse of a portion of the de la Concorde overpass.* Quebec: Library and National Archives, 2007.

Jones, Denny. *Principles and prevention of corrosion.* Prentice Hall, 1996.

Kee, S., T. Oh, J. Popovics, R. Arndt, and J. Zhu. "Nondestructive bridge deck testing with air-coupled impact-echo and infrared thermography." *Journal of Bridge Engineering* (American Society of Civil Engineers) 17 (2012): 928-939.

Kim, Jin-Young. "Structural and Material Health Monitoring of Cementitious Materials Using Passive Wireless Conductivity Sensors." PhD Dissertation, Department of Civil, Archetictural, and Environmental Engineering, University of Texas at Austin, 2013.

Kliethermes, J. "Repair of spalling bridge decks." *Highway Research Record* 1, no. 400 (1972): 83-92.

Ko, J. M., and Y. Q. Ni. "Technology developments in structural health monitoring of large-scale bridges." *Engineering Structures* 27 (2005): 1715-1725.

Koch, G. H,, M. Brongers, N. Thompson, Y. Virmani, and J. Payer. *Corrosion Cost and preventive stratigies in the United States.* Office of infrastructure research and development: Federal Highway Administration, 2001.

Kujur, Jitu, and B. Bhattacharjee. "Potentiodynamic Linear Sweep Test for Evaluation of Performance of Steel." *International Journal of Earth Sciences and Engineering* 04 (October 2011): 592-595.

LePatner, Barry B. *Too big to fall: America's failing infrastructure and the way forward.* New York, NY: Foster Publishing, 2010.

Lu, S., and H. Ba. "Corrosion risk assessment of chloride-contaminated concrete structures using embeddable multi-cell system." *Journal of Central South University of Technology*, 2011: 230-237.

Lynch, Jerome, and Kenneth Loh. "A summary review of wirless sensors and srnsor networks for structural health monitoring." *The Shock and Vibration Digest* 38, no. 2 (2006): 91-130.

Mammoliti, L., L. Brown, C. Hansson, and B. Hope. "The influence of surface finish of reinforcing steel and pH of the test solution on the chloride threshold concentration for corrosion initiation in synthetic pore solutions." *Cement and Concrete Research* 26, no. 4 (1996): 545-550.

Marschner, U., S. Reitz, P. Schneider, and W. Fischer. "Simulation-based planar coil design optimization for resonance sensors." Dresden, Germany: Proceedings Eurosensors, 2008.

Martinez, I., C. Andrade, N. Rebolledo, v. Bouteiller, E. Marie-Victoire, and G. Oliver. "Corrosion Characterization of Reinforced Concrete Slabs with Different Devices." *Coorosion* (NACE International) 64, no. 2 (2008): 107-123.

Maser, Kenneth, Nicole Martino, Jeff Doughty, and Ralf Birken. "Understanding and detecting bridge deck deterioration with Ground-Penetrating Radar." *Journal of the Transportation Research Board* (Transportation Research Board of the National Academies) 2313 (2012): 116-123.

Materer, N., A. Apblett, and T. Ley. *Passive, wireless corrosion sensors for transportation infrastructure.* Midwest City, OK: Oklahoma Transportation Center, 2011, 43 pp.

Mays, G. *Durability of concrete structures: Investigation, repair, protection.* London: E & FN SPON, 1992.

McCarter, W., and O. Vennesland. "Sensor systems for use in reinforced concrete structures." *Construction and building materials* 18 (2004): 351-358.

Mehta, Kumar, and Richard Burrows. "Building durable structures in the 21st century." *Concrete International* 23, no. 3 (2001): 57-63.

Melchers, R., and C. Li. "Reinforcement corrosion initiation and activation times in concrete structures exposed to severe marine environments." *Cement and Concrete Research*, 2009: 1068-1076.

Millard, S. G., D. Law, J. H. Bungey, and J. Cairns. "Environmental influences on linear polarisation corrosion rate measurement in reinforced concrete." *NDT & E International* 34, no. 6 (2001): 409-417.

Mita, A., and S. Takahira. "Health monitoring of smart structures using damage index sensors." *Smart Structures and Materials 2002: Smart systems for bridges, structures, and highways.* San Diego, CA: SPIE, 2002. 8 pp.

Moore, Mark, Brent Phares, Benjamin Graybeal, Dennis Rolander, and Glenn Washer. *Reliability of visual inspection for highway bridges.* McLean, VA: Federal Highway Administration, 2001.

Moreno, M, W Morris, M. Alvarez, and G Duffo. "Corrosion of reinforcing steel in simulated concrete pore solutions: Effect of carbonation and chloride content." *Corrosion Science* 46 (2004): 2681-2699.

National Instruments. *Multisim 11.0.1 User Manual.* Austin, TX: NI, 2010.

NCHRP. *Concrete Bridge Deck Performance: A Synthesis of Highway Practice.* National Cooperative Highway Research Program, Washington, D.C.: Transportation Research Board, 2004.

Nilsson, James, and Susan Riedel. *Electric circuits.* 5th. Addison-Wesley Publishing Company, 1996.

Novak, L., K. Grizzle, S. Wood, and D. Neikirk. "Development of state sensors for civil engineering structures." *Proceedings of SPIE 5057.* San Diego, CA, 2003. 6 pp.

Nygaard, P., M. Geiker, and B. Elsener. "Corrosion rate of steel in concrete: evaluation of confinement techniques for on-site corrosion rate measurements." *Materials and Structures* 42 (2009): 1059-1076.

Ong, J., Z. You, J. Mills-Beale, E. Tan, B. Pereles, and K. Ong. "A wireless passive embedded sensors for real-time monitoring of water content in civil engineering materials." *IEEE Sensors Journal* 8, no. 12 (2008): 2053-2058.

Ong, K., J. Bitler, C. Grimes, L. Puckett, and L. Bachas. "Remote Query Resonant-Circuit Sensors for Monitoring of Bacteria Growth: Application to food quality control." *Sensors*, 2002: 219-232.

Ota, Y., Y. Takura, F. Sato, and H. Matsuki. "Wireless power transfer by low coupling electromagnetic induction-LC booster." *Microwave Workshop Series on Innovative Wireless Power Transmission: Technologies, Systems, and Applications.* Kyoto, Japan: IEEE, 2012.

Otieno, Mike, MArk Alexander, and Hans Beushausen. "Suitability of various measurement techniques for assessing corrosion in cracked concrete." *ACI Materials Journal* 107, no. 5 (2010): 481-489.

Pasupathy, P. *Coupled passive resonant circuits as battery-free wirelless sensors.* Austin: University of Texas, 2010.

Pasupathy, P., S. Munukutla, D. Neikirk, and S. Wood. "Verstile wireless sacrificial transducers for electronic structural surveillance sensors." *IEEE Sensors 2009.* Christchurch, New Zealand: Institute of Electrical and Electronics Engineers, 2009.

Pease, B., M. Geiker, H. Stang, and J. Weiss. "The design of an instrumented rebar for assessment of corrosion in craced reinforced concrete." *Materials and structures* 44 (2011): 1259-1271.

Polder, R. B., W. Peelen, M. Raupach, and K. Reichling. "Economic effects of full corrosion surveys for aging concrete structures." *Materials and corrosion* 63 (2012): 1-6.

Poston, R., and J. West. "Investigation of the Charlotte motor speedway bridge collapse." *Structures Congress 2005: Metropolis and Beyond.* ASCE, 2005. 1-11.

Pourbaix, Marcel. *Lectures on Electrochemical Corrosion.* New York: Plenum Press, 1973.

Poursaee, A. "Corrosion of steel bars in saturated $Ca(OH)_2$ and concrete pore solution." *Concrete research letters* 1, no. 3 (2010).

Poursaee, A. "Determining the approprite scan rate to perform cyclic polarization test on the steel bars in concrete." *Electrochimica Acta* 55 (2010): 1200-1206.

Poursaee, A., and C. Hansson. "Potential pitfalls in assessing chloride-induced corrosion of steel in concrete." *Cement and Concrete Research* 39, no. 5 (May 2009): 391-400.

Puryear, John. *Passive Wireless Corrosion Sensors for Reinforced Concrete Structures.* M.S. Thesis, Department of Civil, Architectural and Environmental Engineering, University of Texas at Austin, 2007.

Raupach, M., and P. Schiebl. "Macrocell sensor systems for monitoring of the corrosion risk of the reinforcment in concrete structures." *NDT & E International* 34 (2001): 435-442.

Raupach, M., et al. "Inspection stratigies for reinforcment corrosio surveys." *Materials and Corrosion* 63 (2012): 5.

Reis, R., and M. Gallaher. *Evaluation of the VTI ECI-1 Embedded Corrosion Instrument.* Sacramento, CA: California Department of Transportation, 2006, 58 pp.

Richardson, M. *Fundamentals of durable reinforced concrete.* New York, NY: Tylor & Francis Group, 2002.

RocTest. *RocTest Group.* 5 12, 2013. http://www.roctest-group.com/node/866.

Russell, H. *Concrete Bridge Deck Performance: A Synthesis of Highway Practice.* National Cooperative Highway Research Program, Washington, D.C.: Transportation Research Board National Research, 2004.

Ryan, Thomas, Eric Mann, Zachary Chill, and Brayan Ott. *Bridge Inspector's Reference Manual.* Arlington, VA, Federal Highway Administration, 2012.

Sandler, Steven, and Charles Hymowitz. *SPICE Circuit Handbook.* New York: McGraw-Hill, 2006.

Scott, M., et al. "A comparison of nondestructive evaluation methods for bridge deck assessment." *NDT & E International*, 2003: 245-255.

Scully, J. "Polarization resistance method for determination of instantaneous corrosion rates." *Corrosion* 56, no. 2 (2000): 199-218.

Seim, C. "Bridge maintenance and safety: A practitioner's view." *5th International Conference on Bridge maintenance, Safety and Management.* Philadelphia, PA: IABMAS, 2010. 5 pp.

Simonen, Jarkko T., Matthew M. Andringa, Kristin M. Grizzle, and Sharon L. Wood. "Wireless sensors for monitoring corrosion in reinforced concrete members." *Smart Structures and Materials: Proceedings of SPIE 5391*. San Diego, CA: International Society for Optics and Photonics, 2004. 587-596.

Somerville, George. *Management of deteriorating concrete structures.* New York: Taylor and Francis, 2008.

Staszewski, W, C Boller, and G Tomlinson. *Health monitoring of aerospace structures: smart sensor technologies and signal processing.* Chichester, England: John Wiley & Sons, 2004.

Steinberg, I., and M. Steinberg. "Radio-frequency tag with optoelectronic interface for distributed wireless chemical and biological sensor applications." *Sensors and Actuators B*, 2009: 120-125.

Stern, M, and A. Geary. "Electrochemical Polarization : I. A Theoritical analysis of the shape of polarization curves." *Journal of the electrochemical society*, 1957: 56-63.

Tait, William S. *An introduction to electrochemical corrosion testing for practicing engineers and scientists.* Racine, WI: PairODocs Publications, 1994.

Thompson, Neil, and Joe Payer. *DC Electrochemical Test Methods.* Edited by Barry Syrett. Houston, TX: NACE International, 1998.

Trivedi, Tanuj, Praveen Pasupathy, Ali Abu-Yousef, Ye Chen, Dean Neikirk, and Sharon Wood. "A reflectometer-based reader for passive wireless electronic structural surveillance sensors ." *Proc. SPIE 8347.* San Dieg, CA: Society of Photo-Optical Instrumentation Engineers, 2012.

USDOT. "2004 Status of the Nation's Highways, Bridges, and Transit: Conditions & Performance." 2006. http://www.fhwa.dot.gov/policy/2004cpr/.

Vaghefi, K., et al. "Evaluation of commercially available remote sensors for highway bridge condition assessment." *Journal of bridge engineering*, 2012: 886-895.

Virginia Technologies Inc. *Embedded Corrosion Instrument.* 2013. http://www.vatechnologies.com/eciIndex.htm (accessed May 10, 2013).

Watters, D., A. Bahr, P. Jayaweera, and D. Huestis. *SMART PEBBLES: Passive embeddable wireless sensors for chloride ingress monitoring in bridge decks.* Sacramento, CA: California Department of Transportation, 2003, 60 pp.

Weyers, R, B Prowell, M Sprinkel, and M Vorster. *Concrete bridge protection, repair, and rehabilitation relative to reinforcment corrosion: a methods application manual.* Washington, DC: National Research Council, 1993, 269.

Wood, S., and D. Neikirk. "Passive sensors for infrastructure monitoring." *Proc. SPIE 7292.* San Diego, 2009.

Woodward, R, and F Williams. "Collapse of Ynys-y-Gwas bridge, West Glamorgan." *Proceedings of the Inistute of Civil Engineers Part 1* (ICE) 84 (1988).

Yehia, S., O. Abudayyeh, I. Fazal, and D. Randolph. "A decision support system for concrete bridge deck maintenance." *Advances in engineering software* 39 (2008): 202-210.

Yi, X., T. Wu, Y. Wang, and R. Leon. "Passive wireless smart-skin sensor using RFID-based folded batch antena." *International Journal of Smart and Nano Materials* 2, no. 1 (2011): 22-38.

Yoon, D., J. Weiss, and S. Shah. "Detecting the extent of corrosion with acoustic emissions." *Transportation Research Record: Journal of the Transportation Research Board* 1698, no. 1 (2000): 54-60.

Zhang, S., P. Pasupathy, and D. Neikirk. "Microfabricated self-resonant structures as a passive wireless chemical sensors." *SPIE Proceedings.* San Diego, CA, 2011. 8 pp.

Vita

Ali Emad Abu Yosef, the son of Emad Abu Yosef and Rachida Al-Telimsani, was born in Zarka, Jordan on September 2, 1984. After living in Taza, Morroco for 4 years, he moved to Doha, Qatar with his family where he graduated from Omar Bin Al-Khattab Scientific School in June 2002. He received his Bachelor of Science in Civil Engineering degree from The University of Jordan in December 2006. During his undergraduate studies, he worked as an undergraduate research assistant in the Department of Civil and Environmental Engineering of the University of Illinois at Urbana-Champaign. He worked in the Structural Engineering group of MZ and Partners in Doha, Qatar, and in August 2007, he enrolled in the graduate structural engineering program The University of Texas at Austin.

Email Address: abuyousef@utexas.edu

This dissertation was typed by the author.